



**HAL**  
open science

# Theoretical and experimental study of fully grouted rockbolts and cablebolts under axial loads

Laura Blanco Martin

► **To cite this version:**

Laura Blanco Martin. Theoretical and experimental study of fully grouted rockbolts and cablebolts under axial loads. Other. Ecole Nationale Supérieure des Mines de Paris, 2012. English. NNT : 2012ENMP0010 . pastel-00711490

**HAL Id: pastel-00711490**

**<https://pastel.hal.science/pastel-00711490>**

Submitted on 25 Jun 2012

**HAL** is a multi-disciplinary open access archive for the deposit and dissemination of scientific research documents, whether they are published or not. The documents may come from teaching and research institutions in France or abroad, or from public or private research centers.

L'archive ouverte pluridisciplinaire **HAL**, est destinée au dépôt et à la diffusion de documents scientifiques de niveau recherche, publiés ou non, émanant des établissements d'enseignement et de recherche français ou étrangers, des laboratoires publics ou privés.

École doctorale n°398  
Géosciences et Ressources Naturelles

**Doctorat ParisTech**

**T H È S E**

pour obtenir le grade de docteur délivré par

**l'École nationale supérieure des mines de Paris**

**Spécialité**

**« Techniques et Économie de l'Exploitation du Sous-sol »**

*présentée et soutenue publiquement par*

**Laura BLANCO MARTÍN**

le 29 mars 2012

**Étude théorique et expérimentale du boulonnage à ancrage réparti  
sous sollicitations axiales**

**Theoretical and experimental study of fully grouted rockbolts  
and cablebolts under axial loads**

Directeur de thèse : **Michel TIJANI**

Co-encadrement de thèse : **Faouzi HADJ-HASSEN**

**Jury**

**M. Jack-Pierre PIGUET**, Docteur d'État, Professeur, Ecole des Mines de Nancy  
**M. Alain MILLARD**, Professeur, École Polytechnique, Directeur de recherches, CEA Saclay  
**M. Rod STACE**, Associate Professor, Faculty of Engineering, The University of Nottingham  
**M. Behrouz GATMIRI**, Docteur, Direction scientifique, ANDRA  
**M. Faouzi HADJ-HASSEN**, Docteur, Centre de Géosciences, MINES-ParisTech  
**M. François LAIGLE**, Docteur, Centre d'Ingénierie Hydraulique, EDF-DPIH  
**M. Michel TIJANI**, Directeur de recherches, Centre de Géosciences, MINES-ParisTech

Président  
Rapporteur  
Rapporteur  
Examineur  
Examineur  
Examineur

**T  
H  
È  
S  
E**

**MINES ParisTech**

**Centre de Géosciences**

35, rue Saint-Honoré - 77305 Fontainebleau Cedex - France



*A Pilar, Armando y Lucía. Por estar siempre cerca, estando lejos. Esta tesis es de los cuatro, a partes iguales.*

*Y a mi abuela, la ti'María. Por todos los momentos inolvidables de mi infancia en un lugar de Castilla, de cuyo nombre siempre querré acordarme. Y por esos minutos semanales de conversación en los últimos años que, aunque escasos, han sido imprescindibles para no olvidar el verdadero valor de las cosas...*

*...Gracias a todos*



## ACKNOWLEDGEMENTS

My first acknowledgements in English are addressed to Professor Rod Stace, who kindly accepted to review this work. I am grateful for his presence at my *viva* and for his comments on my manuscript.

I would like to thank as well our colleagues in the PROSAFECOAL project (EU Research Fund for Coal and Steel, RFCS). One of the aims of this project is to increase the productivity and safety of European underground coal mines by gaining insight into the effect of fully grouted rockbolts and cablebolts on the face-roadway junction. The collaborations, discussions and knowledge exchanged between partners, in addition to the technical visits attended during the coordination meetings have invaluable contributed to the fulfilment of this thesis and to the understanding of the industrial issues of the subject.

Mes premiers remerciements francophones s'adressent au Professeur Jack-Pierre Piguet, qui m'a fait l'honneur de présider le jury. Je remercie également le Professeur Alain Millard, non seulement d'avoir accepté de rapporter sur cette thèse, mais aussi (et surtout!) des remarques, toujours pertinentes, qu'il a faites sur mon travail. Je ne pourrais pas oublier dans ces lignes François Laigle, que je remercie de m'avoir accueillie au sein du groupe du travail sur le boulonnage GT30 de l'AFTES et d'avoir accepté de faire partie du jury, malgré son agenda souvent chargé.

En parallèle au projet européen PROSAFECOAL financé par le RFCS, cette recherche a été menée en collaboration avec l'Andra, dans le cadre du projet MIBOULAND. Le but de ce projet est de compléter l'étude *in situ* effectuée par l'Andra sur les ancrages passifs par une étude approfondie à l'échelle du laboratoire. Je remercie Gilles Armand, Behrouz Gatmiri et Aurélien Noiret d'avoir suivi ce travail et d'avoir mis à notre disposition les résultats des essais *in situ* et une partie du matériel nécessaire pour la réalisation des essais en laboratoire. Je remercie également Behrouz d'avoir accepté de participer au jury.

Je tiens à remercier mes encadrants, Michel Tijani et Faouzi Hadj-Hassen, de m'avoir proposé ce sujet et de la confiance qu'ils m'ont accordée au cours de la thèse, en plus des connaissances apportées. J'exprime également ma gratitude à Jacques Schleifer, qui est intervenu activement pour l'aboutissement de la partie expérimentale de ce travail. Je suis très reconnaissante envers l'ensemble du personnel de la Halle d'essais du Centre de Géosciences pour leur aide, le temps qu'ils m'ont consacré, leurs conseils et leur bonne humeur et soutien dans les moments difficiles. Aucun essai n'aurait fonctionné sans leur présence, et je garderai un très bon souvenir des moments vécus autour du banc d'arrachement.

Je voudrais de même remercier les personnes de l'équipe Géologie de l'Ingénieur Géomécanique -et

du Site de Fontainebleau plus globalement- qui ont contribué d'une façon ou d'une autre à l'avancement de cette recherche. J'exprime aussi ma gratitude envers mes camarades de thèse Khouzama, Manon, Ha, Florent, Anis, Xinyu, Malek, Dhaker et Salim (et les déjà docteurs Gilles et Mario-Luis), auprès desquels c'était très agréable de travailler. Un grand merci est réservé à Rima, avec qui les liens ont largement dépassé les murs de l'École ; je ne saurais pas trouver ici les mots pour condenser ces années d'amitié, que j'espère ne sont que le début d'un long et riche chemin.

Enfin, je veux remercier Frédéric, qui, étant arrivé lorsque le tunnel était sombre et non bouloigné, a eu le courage de rester à mes côtés et m'accompagner jusqu'à la sortie. Et parce que toute histoire a un début, je remercie Bruno, José Héctor et Carlos ; tout simplement parce que, sans leurs conseils et leur aide, ce voyage se serait fini il y a bien, bien longtemps...

Rockbolting and cablebolting are two ground reinforcement techniques broadly used not only in mining but also in civil engineering applications. As of today, hundred of millions of bolts are installed each year worldwide.

This study focuses on the behaviour of fully grouted rockbolts and cablebolts subjected to tensile axial loads, in static conditions. Under these circumstances, the system equilibrium relates the bolt axial load with the shear stress developed at the bolt outer surface, in contact with the grouting material. Experience throughout the world has proven that failure of fully grouted bolts is more likely to take place by a decoupling mechanism at the bolt-grout interface, as a result of the axial load on the bolt. The interface behaviour of fully grouted bolts, before and after the peak strength, is the core of this thesis. The research comprises two principal parts: a theoretical investigation and an experimental study.

The theoretical investigation consists of the following:

- a one-dimensional analysis of the radial and axial responses of the grout and surrounding ground annuli, carried out assuming a generalized plane stress state and rotational invariance. The classic framework of the linear theory of elasticity is adopted. The radial study aims at understanding the pressure transmission from the annuli outside to the bolt-grout interface. As for the axial analysis, it is useful to estimate the interface shear stress before decoupling occurs;
- a new analytical tool to predict the full range behaviour of a fully grouted rockbolt subjected to a tensile load. This tool is of particular interest to predict the pull-out response of a long rockbolt (in terms of axial displacement, axial load and shear stress along the embedded length), for which the shear stress is not uniformly distributed. The innovation of the new approach consists in using boundary conditions that are solely related to the bolt free end. This new tool is limited to monotonic loadings and is only valid if the bolt remains in the elastic range during the whole loading process. To use it, the embedment length and the bolt radius and Young's modulus are required, as well as the interface shear stress-slip relationship,  $\tau_b(W)$ . A complete development of the solution is explained in the case of a classic tri-linear  $\tau_b(W)$  model. However, the relationship  $\tau_b(W)$  is of experimental nature, and is not necessarily tri-linear; it can be obtained through pull-out tests, which justifies the experimental investigation undertaken during the current research.

The experimental study has been conducted at two different scales, although most of it has been undertaken in the laboratory. Pull-out tests have been carried out using a new experimental bench,

designed before the beginning of this thesis, but tuned and put into operation during the Ph.D. The tests have been conducted under constant outer radial confinement and constant outer radial stiffness conditions. The tested samples are composed of a rock sample, a grouting material, a bolt and a metallic tube that is grouted along the bolt length that protrudes from the rock borehole. The bench design is flexible enough to investigate a wide range of parameters, but in this study, attention has been focused on the embedment length (short enough to ensure a uniform distribution of the shear stress), the confining pressure and the bolt type and profile. Three types of rockbolts (25 mm diameter HA25 and FRP rebars and also smooth bars) and 23 mm diameter Flexible cablebolts have been tested. Additionally, to prevent the unscrewing phenomenon that could arise when testing cablebolts grouted along short lengths, a new set-up has been designed. The majority of the tests have been conducted on rockbolts, while the tests on cablebolts have been mainly used to verify the effectiveness of the new set-up.

In the field, pull-out tests have been conducted in ANDRA's URL in North-Eastern France. Due to the great embedment lengths used and in order to preserve the bolt elastic behaviour, the tests were stopped before the advent of any significant displacement. For this reason, the  $\tau_b(W)$  relationships have only been derived partially from the experimental field data. On the other hand, since short embedment lengths are more accurate to examine the interface behaviour, it is proposed to design the *in situ* pull-out tests according to the laboratory-scale findings; the comparison between the field and the modelled results for great lengths will help evaluate the laboratory, small-scale research.

The analysis of the results issued from laboratory-scale pull-out tests on rockbolts has therefore been directed towards the definition of an interface behaviour model. Such model, which depends on the bolt-grout combination chosen, is defined by the relationships  $\tau_b(W, p_b)$  and  $\Delta u_{rb}(W, p_b)$ , in which  $\tau_b$  is the interface shear stress,  $W$  is the axial displacement,  $p_b$  is the bolt-grout interface normal pressure and  $\Delta u_{rb}$  is the radial opening. While  $\tau_b$  and  $W$  can be easily obtained experimentally,  $p_b$  needs a supplementary analysis. The analytical approach developed to compute  $p_b$  from the measured data is described. Then, from the data available, a semi-empirical model for  $\tau_b(W, p_b)$  and  $\Delta u_{rb}(W, p_b)$  is defined using the tests held at constant radial stiffness. A method to obtain an interface behaviour model from experimental measurements is thereby proposed. Finally, the ability of the defined semi-empirical model to reproduce the tests held at constant confinement is explored. This is an important aspect with a view to the construction of a constitutive law; however, insufficient data are available so far. In the future, the samples instrumentation in the radial direction will let gain more insight into the interface behaviour. This perspective and other improvements are proposed at the end of this thesis.

**Keywords:** analytical approach, bolt-grout interface, boundary conditions, cablebolt, pull-out test, rockbolt, semi-empirical method

Le boulonnage et le câblage sont deux techniques de renforcement du terrain couramment utilisées dans l'industrie minière et dans le génie civil. A titre d'exemple pour quantifier l'importance de ces deux techniques, des centaines de millions de boulons sont installés chaque année dans les mines du monde entier.

Cette recherche s'intéresse au comportement des boulons et des câbles à ancrage réparti, soumis à des chargements axiaux de traction en régime statique. Dans ces conditions, l'équilibre du système relie la force axiale agissant sur la barre à la contrainte de cisaillement développée sur sa surface latérale, en contact avec le matériau de scellement. Diverses expériences ont montré que la rupture des boulons et des câbles à ancrage réparti se produit le plus fréquemment à l'interface tige-scellement, par un processus de décohésion qui commence dès que la force axiale sur la barre dépasse une valeur limite. Le comportement de l'interface, avant et après rupture, constitue le sujet principal de cette thèse, qui comprend deux volets principaux : une étude théorique et une étude expérimentale.

La partie théorique comporte deux sections :

- premièrement, une analyse unidimensionnelle des réponses radiale et axiale de l'anneau de scellement et du terrain environnant, effectuée en élasticité linéaire supposant un état de contraintes planes généralisé et une configuration axisymétrique. D'une part, l'étude radiale permet de comprendre la transmission de la pression de l'extérieur vers l'interface barre-scellement. D'autre part, l'étude axiale s'avère particulièrement utile pour déterminer la contrainte de cisaillement à l'interface avant le début du phénomène de décohésion ;
- deuxièmement, le développement d'un outil analytique capable de prédire la réponse complète, pendant tout le processus de désolidarisation de l'interface, d'un boulon à ancrage réparti soumis à une force axiale de traction. L'intérêt principal de cet outil consiste à prédire le résultat d'un essai d'arrachement (en termes de déplacement axial, force axiale et contrainte de cisaillement le long de la partie ancrée) effectué sur une longue tige, pour laquelle on ne peut pas admettre que le cisaillement soit uniformément distribué. Par rapport aux solutions existantes du même problème, l'innovation a consisté à utiliser des conditions aux limites ne concernant que l'extrémité libre de la barre. Ce nouvel outil est limité à des chargements monotones et ne peut être utilisé que lorsque la tige reste dans le domaine élastique. Les données nécessaires pour l'utiliser sont le rayon de la barre, son module de Young, la longueur d'ancrage et la relation contrainte de cisaillement-glisement,  $\tau_b(W)$ , de l'interface boulon-scellement. Le développement complet de la solution est décrit dans le cas d'une relation  $\tau_b(W)$  tri-linéaire, traditionnellement utilisée ;

cependant, une telle forme n'est pas forcément réaliste. La vraie forme de la relation  $\tau_b(W)$  est expérimentale et peut être déterminée *via* des essais d'arrachement, ce qui justifie l'étude expérimentale menée.

L'étude expérimentale a été effectuée à deux échelles, *in situ* et en laboratoire, la plupart du travail ayant été réalisée à l'échelle du laboratoire. Des essais d'arrachement ont été exécutés en utilisant un nouveau banc expérimental, conçu au préalable et mis au point pendant la thèse. Les tests ont été menés soit à pression de confinement constante, soit à rigidité radiale extérieure constante. Les échantillons se composent d'une carotte de roche pourvue d'un trou borgne dans lequel on scelle un boulon ou un câble à l'aide d'un matériau de scellement. Un tube métallique est ancré à la barre le long de la partie dépassant le trou borgne. La conception du banc expérimental est suffisamment flexible pour tester un grand nombre de paramètres. Dans cette étude, la longueur d'ancrage (petite pour assurer une distribution uniforme de  $\tau_b$ ), la pression de confinement et le type et profil de la barre ont été étudiés plus en détail. Trois types de boulons (des barres crénelées en acier HA25, des boulons en fibres de verre et des tiges lisses, tous de 25 mm de diamètre) et des câbles Flexibles de 23 mm de diamètre ont été testés. Afin d'empêcher le phénomène de dévissage du câble par rapport à l'anneau de scellement qui pourrait fausser les résultats dans le cas de petites longueurs, de nouvelles pièces ont été conçues. La plupart des essais d'arrachement a été effectuée sur les boulons, les essais sur les câbles ayant pour objectif principal de vérifier l'efficacité de ces nouvelles pièces.

Les essais *in situ* ont été réalisés au laboratoire de recherche souterrain de l'ANDRA en Meuse/Haute-Marne. En raison des grandes longueurs de scellement, et dans le but de ne pas plastifier les tiges, les essais étaient arrêtés avant l'obtention d'un glissement important entre la barre et le milieu environnant. Pour cette raison, les relations  $\tau_b(W)$  ont été déduites seulement partiellement à partir des données de terrain. D'autre part, étant donné que les petites longueurs d'ancrage sont mieux adaptées pour étudier le comportement de l'interface, il est proposé comme perspective de dimensionner les essais *in situ* à partir des résultats obtenus à l'échelle du laboratoire ; la comparaison entre les résultats expérimentaux et ceux issus de la modélisation pour de grandes longueurs pourra alors aider à évaluer la recherche menée à échelle réduite en laboratoire.

L'analyse des résultats des essais d'arrachement effectués en laboratoire sur les boulons a donc été orientée vers la définition d'une loi de comportement pour l'interface boulon-scellement. Cette loi, variable pour chaque combinaison tige-scellement, est définie par les relations  $\tau_b(W, p_b)$  et  $\Delta u_{rb}(W, p_b)$ , où  $\tau_b$  est la contrainte de cisaillement,  $W$  est le déplacement axial,  $p_b$  est la pression normale à l'interface et  $\Delta u_{rb}$  est l'ouverture normale du joint. Les données expérimentales donnent facilement accès à  $\tau_b$  et  $W$  ; néanmoins, la pression  $p_b$  requiert davantage d'analyse. Une approche analytique a été développée pour calculer  $p_b$  à partir des mesures. Ensuite, le modèle semi-empirique pour  $\tau_b(W, p_b)$  et  $\Delta u_{rb}(W, p_b)$  obtenu à partir des essais effectués à rigidité radiale constante est présenté. L'ensemble de cette analyse constitue une méthode pour déduire le comportement de l'interface à partir d'une série d'essais. La capacité du modèle semi-empirique à reproduire un essai à confinement constant est également évaluée ; en effet, cette évaluation s'avère nécessaire vis-à-vis de la définition d'une loi de comportement. Les données disponibles pour le moment sont insuffisantes pour pouvoir tirer des conclusions. L'instrumentation des essais pour étudier la réponse radiale permettra de mieux comprendre le comportement du contact boulon-scellement. Cette perspective et d'autres améliorations sont proposées à la fin de ce mémoire de thèse.

**Mots-clés** : approche analytique, boulon, câble, conditions aux limites, essai d'arrachement, interface boulon-scellement, méthode semi-empirique

# NOMENCLATURE AND ACRONYMS

## Material properties

| Symbol     | Description                  | Unit  |
|------------|------------------------------|-------|
| $E_b$      | Bolt elastic modulus         | [MPa] |
| $\nu_b$    | Bolt Poisson's ratio         | [-]   |
| $E_g$      | Grout elastic modulus        | [MPa] |
| $\nu_g$    | Grout Poisson's ratio        | [-]   |
| $R_{t,g}$  | Grout tensile strength       | [MPa] |
| $E_r$      | Rock elastic modulus         | [MPa] |
| $\nu_r$    | Rock Poisson's ratio         | [-]   |
| $R_{t,r}$  | Rock tensile strength        | [MPa] |
| $E_{bl}$   | Bladder elastic modulus      | [MPa] |
| $\nu_{bl}$ | Bladder Poisson's ratio      | [-]   |
| $E_c$      | Biaxial cell elastic modulus | [MPa] |
| $\nu_c$    | Biaxial cell Poisson's ratio | [-]   |

## Geometry

| Symbol     | Description               | Unit |
|------------|---------------------------|------|
| $R_b$      | Bolt radius               | [mm] |
| $R_g$      | Borehole radius           | [mm] |
| $R_r$      | Rock sample outer radius  | [mm] |
| $R_{pl}$   | End plate inner radius    | [mm] |
| $R_{pist}$ | Upper piston inner radius | [mm] |
| $R_{bl}$   | Bladder outer radius      | [mm] |
| $R_c$      | Biaxial cell inner radius | [mm] |
| $H$        | Rock sample height        | [mm] |
| $L$        | Embedment length          | [mm] |
| $h_{pl}$   | End plate height          | [mm] |

## Axial direction

| Symbol       | Description                                     | Unit  |
|--------------|---|-------|
| $F$          | Bolt axial force                                | [kN]  |
| $\tau_b$     | Bolt-grout interface shear stress               | [MPa] |
| $W$          | Bolt axial displacement at $Z = L$ (loaded end) | [mm]  |
| $T$          | Bolt axial displacement at $Z = kT$ (free end)  | [mm]  |
| $(w_i, f_i)$ | Bond-slip model parameters                      | [-]   |

## Radial direction

### Interface $R_b$

| Symbol     | Description               | Unit  |
|------------|---------------------------|-------|
| $u_{rb^-}$ | Bolt radial displacement  | [mm]  |
| $u_{rb^+}$ | Grout radial displacement | [mm]  |
| $p_b$      | Radial pressure           | [MPa] |

### Interface $R_g$

| Symbol     | Description               | Unit  |
|------------|---------------------------|-------|
| $u_{rg^-}$ | Grout radial displacement | [mm]  |
| $u_{rg^+}$ | Rock radial displacement  | [mm]  |
| $p_g$      | Radial pressure           | [MPa] |

### Interface $R_r$

| Symbol     | Description              | Unit  |
|------------|--------------------------|-------|
| $u_{rr^-}$ | Rock radial displacement | [mm]  |
| $p_r$      | Radial pressure          | [MPa] |

### Bladder outer surface, $R_{bl}$

| Symbol      | Description                 | Unit  |
|-------------|-----------------------------|-------|
| $u_{rbl^-}$ | Bladder radial displacement | [mm]  |
| $p_{bl}$    | Radial pressure             | [MPa] |

|   |             |
|---|-------------|
| <b>Abstract</b>   | <b>vii</b>  |
| <b>Résumé</b>   | <b>ix</b>   |
| <b>Nomenclature and acronyms</b>  | <b>xi</b>   |
| <b>Table of Contents</b>  | <b>xiii</b> |
| <b>Introduction</b>   | <b>1</b>    |
| <b>1 Rockbolting and cablebolting: state-of-the-art</b>                                     | <b>5</b>    |
| 1.1 Introduction . . . . .  | 9           |
| 1.2 Technological Background . . . . .  | 11          |
| 1.2.1 Rockbolting . . . . .   | 12          |
| 1.2.2 Cablebolting . . . . .  | 17          |
| 1.2.3 General aspects of fully grouted rockbolts and cablebolts . . . . .                   | 19          |
| 1.2.4 Design of rockbolting and cablebolting systems . . . . .                              | 22          |
| 1.2.5 Failure of fully grouted rockbolts and cablebolts . . . . .                           | 24          |
| 1.2.6 Performance of passive reinforcement systems . . . . .                                | 27          |
| 1.3 Scientific Background . . . . .   | 29          |
| 1.3.1 The pull-out test . . . . .   | 30          |
| 1.3.2 Analytical and experimental studies . . . . .   | 33          |
| 1.3.3 Numerical modelling of passive reinforcement elements . . . . .                       | 50          |
| 1.4 Conclusions . . . . .   | 56          |
| <b>2 Analytical tools</b>   | <b>59</b>   |
| 2.1 Introduction . . . . .  | 60          |
| 2.2 Radial response of the grout and ground annuli . . . . .                                | 61          |
| 2.3 Axial response of the grout and ground annuli . . . . .                                 | 63          |
| 2.4 New analytical solution to the behaviour of grouted bolts under tensile loads . . . . . | 64          |
| 2.4.1 Resolution method . . . . .   | 66          |
| 2.4.2 Analytical solution using a tri-linear bond-slip model . . . . .                      | 67          |
| 2.4.3 Determination of the bond-slip model . . . . .  | 70          |

|          |   |            |
|----------|---|------------|
| 2.4.4    | Comparison of analytical predictions with experimental results . . . . .  | 71         |
| 2.4.5    | Influence of the embedment length . . . . .   | 74         |
| 2.5      | Conclusions . . . . .   | 77         |
| <b>3</b> | <b>Experimental methods and results</b>   | <b>79</b>  |
| 3.1      | Introduction . . . . .  | 80         |
| 3.2      | Laboratory pull-out test campaign . . . . .   | 81         |
| 3.2.1    | Equipment: new experimental bench . . . . .   | 81         |
| 3.2.2    | Samples preparation . . . . .   | 88         |
| 3.2.3    | Experimental campaign conducted . . . . .   | 93         |
| 3.3      | Analysis of the laboratory pull-out test results . . . . .  | 97         |
| 3.3.1    | Pull-out tests on rockbolts . . . . .   | 97         |
| 3.3.2    | Pull-out tests on cablebolts . . . . .  | 105        |
| 3.3.3    | Comparison of pull-out test results on rockbolts and cablebolts . . . . .   | 107        |
| 3.3.4    | Application of analytical and numerical tools to interpret and understand the results . . . . .                     | 107        |
| 3.3.5    | Bench calibration . . . . .   | 109        |
| 3.3.6    | Effect of the grout and rock annuli boundary conditions on the radial pressure along the embedment length . . . . . | 112        |
| 3.4      | <i>In situ</i> pull-out test campaign . . . . .   | 113        |
| 3.4.1    | General context . . . . .   | 113        |
| 3.4.2    | Analysis of the results . . . . .   | 115        |
| 3.5      | Comparison of pull-out test results in the laboratory and the field . . . . .                                       | 118        |
| 3.6      | Conclusions . . . . .   | 118        |
| <b>4</b> | <b>Analysis of the results and modelling</b>  | <b>121</b> |
| 4.1      | Introduction . . . . .  | 122        |
| 4.2      | Preliminary analysis . . . . .  | 123        |
| 4.2.1    | HA25 rockbolts . . . . .  | 125        |
| 4.2.2    | FRP rockbolts . . . . .   | 126        |
| 4.2.3    | Smooth bars . . . . .   | 127        |
| 4.2.4    | Conclusions . . . . .   | 128        |
| 4.3      | Interface radial pressure determination . . . . .   | 129        |
| 4.3.1    | Framework . . . . .   | 129        |
| 4.3.2    | Pressure $p_b$ determination: general principle . . . . .   | 130        |
| 4.4      | Analysis of the tests conducted at constant radial stiffness . . . . .  | 131        |
| 4.4.1    | Pressure $p_b$ determination: procedure . . . . .   | 131        |
| 4.4.2    | Pressure $p_b$ determination: examples . . . . .  | 133        |
| 4.4.3    | A model for the shear stress . . . . .  | 135        |
| 4.4.4    | A model for the joint opening . . . . .   | 138        |
| 4.5      | Analysis of the tests conducted at constant radial pressure . . . . .   | 139        |
| 4.6      | Conclusions . . . . .   | 140        |
|          | <b>Conclusions and Perspectives</b>   | <b>143</b> |
|          | <b>Bibliography</b>   | <b>151</b> |

---

|   |            |
|---|------------|
| <b>Appendix</b>   | <b>157</b> |
| A Laboratory pull-out test campaign on rockbolts . . . . .  | 157        |
| A.1 Pull-out tests on HA25 rockbolts . . . . .              | 158        |
| A.2 Pull-out tests on FRP rockbolts . . . . .               | 172        |
| A.3 Pull-out tests on smooth steel bars . . . . .           | 184        |
| B Laboratory pull-out test campaign on cablebolts . . . . . | 188        |
| B.1 Pull-out tests on Flexible cablebolts . . . . .         | 189        |
| C Field pull-out test campaign on HA25 rockbolts . . . . .  | 191        |



## INTRODUCTION

*Le boulonnage et le câblage (boulonnage de façon générale) à ancrage réparti sont deux techniques de renforcement du terrain couramment utilisées dans l'industrie minière et dans le génie civil. Au fil de cette recherche, on s'intéresse à la réponse de ces éléments sous des sollicitations axiales de traction, en régime statique. Dans ces conditions, l'équilibre du système relie la force axiale agissant sur la barre à la contrainte de cisaillement qui se développe sur sa surface extérieure, en contact avec le matériau de scellement. L'expérience montre que la rupture de ce type de soutènement se produit le plus fréquemment à l'interface boulon-scellement via un processus de décohésion qui commence dès que la force sur la barre atteint une valeur limite. L'objectif de cette thèse est de mieux comprendre le comportement de cette interface, dans les directions tangentielle et normale. Ce comportement, qui peut s'exprimer en termes d'une loi intrinsèque, permet de déterminer la capacité de l'ancrage et les facteurs qui la régissent.*

*Ce sujet est loin d'être nouveau : de nombreuses recherches, thèses et publications y sont consacrées, comme le montre l'étude bibliographique effectuée, qui est en conséquence assez vaste. Cette étude a justement montré la pertinence de la présente thèse et en a guidé tant la démarche que la structure. Ainsi, ce mémoire se compose de quatre chapitres comme suit.*

*Dans le **chapitre 1**, on présente l'étude bibliographique effectuée. D'abord, on décrit quelques aspects de la technologie du boulonnage, en se focalisant sur les boulons et les câbles à ancrage réparti. Les barres et les matériaux de scellement les plus habituels sont présentés. On explique le principe de transfert de charge entre le renforcement et le terrain environnant, ainsi que les modes d'action du boulonnage à ancrage réparti et ses rôles principaux. Les outils disponibles à ce jour pour établir les schémas de boulonnage sont commentés brièvement. Ensuite, on expose les modes de rupture possibles du boulonnage à ancrage réparti et les facteurs qui en régissent la performance. La dernière partie du chapitre est consacrée à la revue scientifique. On présente et explique les principaux travaux expérimentaux et théoriques menés afin d'étudier le comportement de l'interface. D'une part, les études expérimentales consistent en la réalisation d'essais d'arrachement, effectués la plupart des cas en laboratoire. La finalité de ces essais est de déterminer l'influence de plusieurs paramètres sur la capacité de l'ancrage. D'autre part, les études théoriques se focalisent sur la réponse tangentielle de l'interface ; de fait, une seule loi complète, comprenant les directions tangentielle et normale, a été trouvée pour les câbles. Enfin, on s'intéresse à la façon dont les boulons et les câbles à ancrage réparti sont modélisés dans quelques codes de calcul numérique d'usage répandu. Le but est de comprendre la façon avec laquelle l'interaction soutènement-terrain est prise en compte ;*

Dans le **chapitre 2**, on présente des outils analytiques permettant de comprendre la réponse d'un boulon/câble à ancrage réparti soumis à une force axiale de traction. D'abord, la réponse élastique de l'anneau de scellement et du terrain est étudiée séparément dans les directions radiale et axiale. D'une part, la réponse radiale est utile pour évaluer l'effet de la pression de confinement externe sur la pression normale à l'interface barre-scellement. Cet effet est important parce que la contrainte de cisaillement a une composante frictionnelle. D'autre part, la réponse axiale s'avère pratique afin d'évaluer le cisaillement à l'interface à partir du comportement en cisaillement de l'anneau de scellement et du terrain, mais seulement avant que l'ancrage ne soit endommagé. La dernière partie du chapitre décrit un nouvel outil analytique capable de déterminer la réponse complète d'un boulon à ancrage réparti soumis à une force axiale de traction. Cet outil fournit la distribution du déplacement axial, de la force axiale et de la contrainte de cisaillement pendant un essai d'arrachement et s'avère très avantageux dans le cas des grandes longueurs d'ancrage, pour lesquelles la contrainte de cisaillement n'est pas uniforme. Enfin, on explore et souligne l'influence de la longueur d'ancrage sur la réponse à l'arrachement. A cette fin, on utilise le nouvel outil pour déterminer le résultat, en termes de force-déplacement axial, de six essais effectués dans les mêmes conditions mais avec des longueurs très différentes ;

Dans le **chapitre 3**, on s'intéresse aux études expérimentales en laboratoire et in situ. En laboratoire, des essais d'arrachement ont été effectués sur des boulons (HA25, fibres de verre et tiges lisses en acier) et sur des câbles (type Flexible). Un nouveau banc expérimental a été employé. Ce banc et les procédures de préparation des échantillons sont présentés. De plus, on décrit les modifications effectuées progressivement dans le but de s'approcher au mieux des conditions optimales permettant d'étudier l'interface tige-scellement. La plupart des essais a été réalisée sur les boulons. Les paramètres les plus étudiés sont la longueur d'ancrage, la pression de confinement et le type et profil de la barre. L'effet des conditions aux limites dans les résultats des essais est aussi analysé. Concernant les essais d'arrachement sur les câbles, leur objectif principal a été de vérifier l'efficacité des pièces conçues pour éviter le phénomène de dévissage qui pourrait fausser les résultats. Une analyse exhaustive du nouveau banc a été effectuée pour bien comprendre son fonctionnement et pour déterminer comment obtenir les données nécessaires à l'étude de l'interface. In situ, les essais ont été réalisés au laboratoire de recherche souterrain de l'ANDRA en Meuse/Haute-Marne. A cause des grandes longueurs de scellement utilisées, les essais ont été arrêtés à de faibles valeurs de déplacement. Les données disponibles ont été analysées grâce à l'outil analytique décrit dans le chapitre 2. Enfin, on expose les aspects qui doivent être pris en compte avant de comparer les données de laboratoire et de terrain ;

Dans le **chapitre 4**, on présente l'analyse des résultats des essais effectués sur les boulons, en laboratoire. D'abord, les résultats sont étudiés en termes des données disponibles : déplacement axial, force axiale et pression de confinement externe. Les paramètres caractéristiques de la relation expérimentale contrainte de cisaillement-déplacement axial sont étudiés en fonction de cette pression. Les tendances générales observées pour chaque type de boulon sont identifiées et interprétées par rapport aux constats faits après les essais, présentés dans le chapitre 3. La deuxième partie du chapitre est consacrée à l'étude du comportement de l'interface boulon-scellement. Cette étude requiert la connaissance de la pression normale à l'interface. La procédure analytique développée pour calculer ladite pression à partir des variables mesurées est présentée. Elle s'applique à la configuration particulière des essais effectués. Ensuite, on présente les modèles semi-empiriques d'interface définis pour les boulons HA25 et en fibres de verre, scellés à la résine. Ces modèles ont été établis moyennant les essais effectués à rigidité radiale constante. Finalement, en vue de la définition d'une loi de comportement intrinsèque, on évalue la capacité de ces nouveaux modèles à reproduire les essais réalisés à confinement constant.

---

This research deals with fully grouted rockbolts and cablebolts subjected to tensile axial loads, in static conditions. Rockbolting and cablebolting are two ground reinforcement techniques widely used in mining and civil engineering. Under axial loadings, the bolt equilibrium relates the tensile load with the shear stress developed at the bolt outer surface, in contact with the grouting material. Experience proves that failure of fully grouted bolts usually takes place at the bolt-grout interface, *via* a decoupling mechanism that is activated if the axial load on the bolt exceeds a critical value. The objective of this thesis is to gain more insight into the behaviour of the bolt-grout interface, defined along the tangential and normal directions. Knowledge of the interface behaviour, that can be expressed in terms of a constitutive law, provides access to the reinforcement anchoring capacity and the factors that influence it.

To date, many research works (projects, thesis, articles, *etc.*), have been carried out in the same context. The literature review clearly proves this statement. On the one hand, this justifies the extension of the background revision; on the other hand, the literature review itself not only proves the relevance of this thesis, but also motivates the work sequence and the structure of this manuscript, as follows.

In **chapter 1**, the literature review is presented. First, some technological aspects of bolting are described, with emphasis on fully grouted bolts. The most common tendons and grouting materials are briefly exposed and the load transfer mechanism between the reinforcement and the surrounding ground is explained, together with the different ways these bolts can come into operation and their main roles. The principal tools available at present to design bolting patterns are concisely presented, as well as a review of the different failure modes of this type of reinforcement. The major factors that influence the performance of fully grouted rockbolts and cablebolts are also described. The last part of the chapter is devoted to the examination of the scientific background. The most important analytical and experimental investigations undertaken to study the interface behaviour are presented and explained. The experimental investigations consist mainly of laboratory pull-out tests carried out to ascertain the influence of several parameters on the anchoring capacity. As for the theoretical studies, most of them focus on the interface tangential behaviour, while only one complete constitutive law, including the tangential and normal directions, has been detailed for cablebolts. Finally, a review of some common numerical programs that propose models to simulate fully grouted rockbolts is presented, with emphasis on the way the reinforcement-ground interaction is accounted for.

In **chapter 2**, analytical tools that may help understand the response of a fully grouted bolt subjected to a tensile axial load are gathered together. First, the elastic response of the grout and ground annuli is explored in the radial and axial directions, separately. The radial response is useful to examine the pressure transmission from the annuli outside to the bolt-grout interface. This examination is helpful because the interface shear stress has a frictional component. As for the axial response, it is useful to estimate the interface shear stress from the annuli shear behaviour, but only before decoupling starts. The last part of this chapter describes a new analytical tool able to predict the full range response of a fully grouted rockbolt subjected to a tensile axial load. This tool provides the distribution of the axial displacement, the axial load and the shear stress during a pull-out test, and proves to be particularly useful for long embedment lengths, along which the shear stress is not uniformly distributed. At the end of the chapter, the influence of the embedment length on the pull-out response is explored and highlighted through the use of the new analytical tool to predict the load-displacement curves of six pull-out tests conducted under identical conditions except for the length used.

In **chapter 3**, the laboratory and field experimental work is presented. In the laboratory, pull-

out tests have been carried out on rockbolts (HA25 rebars, FRP rockbolts and smooth steel bars) and cablebolts (Flexible) using a new experimental bench. The bench and the samples preparation procedure are described, together with the modifications introduced progressively in order to study the bolt-grout interface as accurately as possible. The majority of the tests have been conducted on rockbolts, and attention has been focused on the embedment length, the confining pressure and the bolt type and profile. The influence of the boundary conditions on the test results is also discussed. As for cablebolts, the main objective of the executed pull-out tests has been to verify the effectiveness of the set-up designed to prevent the well-known problem of unscrewing. Additionally, an exhaustive examination of the bench to completely understand the way it works and to determine how to get the data required to study the bolt-grout interface has been accomplished. The next part of the chapter is devoted to the field pull-out test campaign, that has been carried out in ANDRA's URL in North-Eastern France. In this case, due to the great embedment lengths used, the tests were stopped at low values of axial displacement. The data available have been analyzed using the analytical tool described in chapter 2. At the end of the chapter, the aspects that should be taken into account before comparing laboratory and field data are exposed.

In **chapter 4**, the analysis of the results issued from laboratory pull-out tests on rockbolts is presented. First, the results are analyzed in terms of the data available, which are the axial displacement, the axial force and the radial outer pressure. The characteristic parameters of the experimental shear stress-slip relationship are studied as a function of the outer pressure and the general trends observed for each type of rockbolt are identified and interpreted with respect to the observations made after the tests, exposed in chapter 3. The second part of the chapter concentrates on the interface behaviour. To assess it, the interface pressure and not the outer pressure is needed. The analytical procedure to determine such pressure from the measured data, in the particular configuration of the pull-out tests described in chapter 3, is explained. Then, using the tests held at constant radial stiffness, a semi-empirical interface behaviour model is proposed for resin-grouted HA25 and also for FRP rockbolts. Finally, the ability of the proposed model to reproduce the tests held at constant confinement is explored. This is an important aspect with a view to the definition of a constitutive law.

# CHAPTER 1

## ROCKBOLTING AND CABLEBOLTING: STATE-OF-THE-ART

*Dans ce premier chapitre, une revue bibliographique du boulonnage-câblage est exposée. Après une présentation générale de ce type de renforcement, on se concentre sur le sujet principal de cette recherche, qui est l'étude des boulons et des câbles à ancrage réparti soumis à des sollicitations axiales de traction, en régime statique. L'objectif de cette revue technologique et scientifique est de parcourir l'état de l'art actuel afin de bien comprendre le principe de fonctionnement de ces boulons, de faire le point des avancées et d'identifier les aspects non bien compris jusqu'à présent.*

*Le boulonnage et le câblage sont deux techniques de renforcement du terrain couramment utilisées dans l'industrie minière et dans le génie civil. A titre d'exemple pour quantifier l'importance de ces techniques, environ cent millions de boulons sont installés chaque année dans les mines de charbon en Amérique du Nord.*

*Les avantages du boulonnage-câblage sont multiples : installation facile et mécanisable, encombrement très réduit dans la section droite de l'ouvrage, faible coût par rapport aux autres techniques de renforcement, souplesse pour être combiné à d'autres techniques et capacité pour soutenir de grands espaces souterrains, entre autres. Toutefois, pour qu'un système de renforcement par boulonnage-câblage soit efficace, le temps de pose vis-à-vis de la déformation du terrain environnant est très important.*

*Le principe de ces deux techniques est le même (de fait, on tend à parler d'une façon générale de boulonnage pour se référer soit à l'une, soit à l'autre) : on fore un trou dans le terrain, on y insère une tige et on l'ancre de façon à ce qu'elle soit solidaire du milieu environnant. D'après Windsor et Thompson [Windsor1996], le boulonnage est composé de quatre éléments principaux : la tige (i.e., un boulon ou un câble), le terrain environnant (du sol ou de la roche), la fixation externe à la surface de l'excavation (une plaque et un écrou en général) et la fixation interne à la paroi du trou borgne. Se basant sur le type et l'extension de la fixation interne, Windsor et Thompson [Windsor1993] ont défini trois types de boulons : boulons à ancrage ponctuel ou DMFC (Discretely Mechanically or Frictionally Coupled), pour lesquels l'ancrage est effectué en fond du trou borgne sur seulement une partie de la longueur de la barre, moyennant un outil mécanique ou un court scellement ; boulons à friction ou CFC (Continuously Frictionally Coupled), pour lesquels l'ancrage est fait par contact direct de la barre avec le milieu environnant, sur toute la longueur de la tige ; boulons à ancrage réparti ou CMC (Continuously Mechanically Coupled), pour lesquels l'ancrage se fait sur toute la longueur de la barre grâce à un matériau de scellement, préparé à base de résine ou de ciment dans la plupart des cas. Les boulons à ancrage réparti et les boulons à friction appartiennent à la famille des ancrages passifs,*

car c'est le mouvement du terrain environnant qui leur transmet l'effort ; en revanche, les boulons à ancrage ponctuel sont des ancrages actifs, parce qu'ils doivent être mis en tension lors de l'installation afin de pouvoir limiter le mouvement du terrain. Pour ce qui est des différences entre le boulonnage et le câblage, la principale distinction vient de la propre structure de la barre : les boulons sont des tiges pleines, tandis que les câbles sont composés d'un nombre de torons plus ou moins torsadés autour d'un fil central. Même si les câbles ont une faible rigidité torsionnelle qui fait qu'ils puissent se "dévisser" du scellement, en particulier pour de faibles longueurs d'ancrage, ils offrent une résistance à la traction beaucoup plus importante que les boulons à section droite identique.

La recherche qui fait l'objet de cette thèse est axée sur le comportement des boulons et des câbles à ancrage réparti, soumis à des forces axiales de traction. L'étude met l'accent sur leur comportement à la rupture. Sous des forces de traction, la rupture d'un système de soutènement par boulonnage à ancrage réparti peut se produire à plusieurs endroits : dans la barre elle-même si la résistance à la traction du matériau constituant le boulon est dépassée ; dans le matériau de scellement ; dans le terrain environnant ; à l'interface barre-scellement, ou à l'interface scellement-terrain. L'expérience montre que c'est le contact tige-scellement qui cède en premier le plus fréquemment. En conséquence, l'étude se focalise sur les facteurs qui régissent le comportement de cette interface. Il est à noter qu'en général, les barres sont soumises à des efforts combinés, axiaux et de cisaillement, comme le montrent de nombreuses études telles que celles de Ludvig, Bawden et al. et Li [Ludvig1983, Bawden1994, Li2010a], par exemple ; cependant, le sujet principal de cette étude ne concerne que les efforts axiaux.

La rupture commence à l'endroit où la force est maximale, qui peut être soit au droit d'une discontinuité, soit le long de la partie ancrée du boulon (ou en paroi d'excavation) dans le cas des terrains déformables, comme le montrent les travaux pionniers de Freeman [Freeman1978], qui étudia le processus de charge et la distribution de la force axiale le long de la partie ancrée des boulons passifs. Dès que la force sur la barre dépasse une valeur limite, un processus de *décohésion* commence à l'interface boulon-scellement et se propage sur la longueur ancrée au fur et à mesure que la force axiale augmente. Aujourd'hui, différentes méthodes d'instrumentation existent pour les boulons à ancrage réparti afin de mieux comprendre leur mode de fonctionnement et le processus de décohésion.

D'un point de vue plus scientifique, il est important de remarquer que la recherche en cours se limite à des conditions statiques. La situation étudiée est montrée dans la figure 1.15, où le boulon, sans fixation externe, est ancré sur deux longueurs différentes séparées par une discontinuité proche de la paroi de l'excavation ; cette discontinuité définit ainsi un bloc susceptible de glisser sous l'effet de la force axiale,  $F$ . La longueur scellée au-dessus de la discontinuité est supposée suffisamment importante pour que l'ancrage soit assuré dans cette partie. D'autre part, on suppose également que la barre reste en phase élastique pendant tout le processus de chargement. L'étude se focalise ainsi sur la longueur inférieure, où un processus de décohésion ou détérioration du contact scellement-tige aura lieu si la force dans la barre, qui est maximale au droit de la discontinuité, dépasse une certaine limite. Ce processus de décohésion pourrait éventuellement entraîner le glissement du bloc, provoquant sa chute.

L'équilibre d'une longueur infinitésimale de boulon dans cette partie est défini par l'équation (1.1) : la force axiale dans la barre est équilibrée par une contrainte de cisaillement qui se développe sur la surface extérieure de la tige. La contrainte de cisaillement  $\tau_b$  est définie donc comme le taux de transfert de la force axiale sur la longueur scellée. On en déduit que si l'on connaît le cisaillement, on peut connaître la force supportée par la barre, ce qui constitue une donnée très importante pour la définition des schémas de soutènement par boulonnage. La contrainte de cisaillement  $\tau_b$  peut être connue sous deux formes différentes : en tant que distribution sur la longueur de scellement,  $\tau_b(Z)$ , où  $Z$  est la direction de l'axe du boulon, ou bien en fonction du déplacement axial du boulon,  $\tau_b(W)$ .

Plusieurs chercheurs ont remarqué que, dans le but de déterminer le comportement de l'interface, il est préférable de connaître la relation  $\tau_b(W)$  (ou éventuellement  $\tau_b(W, p_b)$  où  $p_b$  est la pression normale à l'interface), car elle ne change pas au cours du processus de chargement (loi intrinsèque).

Le but de cette recherche est plus précisément de mieux comprendre le comportement de l'interface, avec l'objectif futur de déterminer sa loi de comportement. Cette loi comporte non seulement la réponse dans la direction tangentielle, définie par les variables  $\tau_b$  et  $W$ , mais aussi la réponse dans la direction normale à l'interface, définie par la pression et l'ouverture normales, respectivement  $p_b$  et  $\Delta u_{r,b}$ . La loi est complétée par un critère, relation entre  $\tau_b$  et  $p_b$ .

Le comportement de l'interface peut être étudié expérimentalement moyennant l'essai d'arrachement. Cet essai consiste à ancrer une longueur de barre dans un matériau et à appliquer un effort de traction sur la longueur qui dépasse la longueur d'ancrage. Afin d'exploiter les résultats, la force axiale et le déplacement axial en sortie de la longueur ancrée doivent être mesurés. D'autre part, pour pouvoir étudier le comportement post-pic, il est préférable d'effectuer les essais à déplacement contrôlé et non à force contrôlée. Les essais d'arrachement peuvent être réalisés en laboratoire et *in situ*; dans le but d'étudier l'interface et le phénomène de décohesion, les essais en laboratoire sont préférés parce qu'ils sont plus faciles à mettre en œuvre et plus faciles à contrôler. Du fait de leur réalisation habituelle dans de nombreux endroits, une standardisation existe dans plusieurs pays. En même temps, depuis les premiers essais d'arrachement effectués par Fuller et Cox [Fuller1975] sur des câbles à sept torons scellés au ciment et confinés par des tubes creux (essais à rigidité radiale constante en paroi du trou), la technologie a beaucoup évolué et depuis les années 90 des cellules d'arrachement qui permettent l'application d'un confinement externe et la prise de multiples mesures (notamment pression et déplacement radiaux) sont disponibles. D'autre part, les travaux de Hagan [Hagan2004] ont analysé l'influence du principe de fonctionnement des bancs expérimentaux sur les résultats. En général, les échantillons sont composés de la barre, de l'anneau de scellement et dans certaines études d'un anneau de roche ou béton pour simuler le terrain environnant. Les résultats des essais montrent l'effet prépondérant de la pression de confinement, aussi bien pour les boulons que pour les câbles. Ce constat s'explique par la composante frictionnelle de l'arrachement. Néanmoins, la réponse en termes de force-déplacement axial obtenue pour les boulons et les câbles est assez différente : après le pic de force, les boulons ne peuvent résister qu'à de très faibles efforts résiduels, tandis que dans les mêmes conditions, un câble présente une phase post-pic très résistante, rappelant un comportement plastique parfait. En ce qui concerne le critère, Moosavi et al. [Moosavi2005] ont obtenu pour des boulons ancrés au ciment une relation non linéaire entre le cisaillement au pic et la pression de confinement appliquée autour de l'anneau de scellement,  $p_g$  (la pression importante pour l'interface est  $p_b$ , mais elle ne peut pas être mesurée directement).

Concernant l'approche théorique, une des premières études du phénomène d'arrachement fut réalisée par Farmer [Farmer1975], qui annonça une décroissance exponentielle de la force axiale et de la contrainte de cisaillement sur la longueur ancrée. La relation  $\tau_b(W)$  utilisée par Farmer est déduite du comportement élastique en cisaillement du matériau de scellement (il a supposé le terrain rigide). La comparaison entre les prédictions théoriques et les résultats expérimentaux issus de boulons instrumentés montre un bon accord lorsque l'ancrage tige-scellement n'est pas endommagé. Dans le même esprit, Li et Stillborg [Li1999] ont défini le comportement de l'interface non endommagée à partir de celui de l'ensemble scellement-terrain environnant. Ils ont complété leur étude en tenant compte de la décohesion progressive de l'interface avec l'augmentation de la force axiale. Pour ce faire, ils ont établi un modèle de distribution de la contrainte de cisaillement sur la longueur d'ancrage,  $\tau_b(Z)$ , à partir des résultats d'essais d'arrachement effectués sur des boulons instrumentés. D'autre part, sur la base des

résultats expérimentaux obtenus pour des boulons et des câbles, Benmokrane et al. [Benmokrane1995] ont proposé une relation  $\tau_b(W)$  tri-linéaire, cf. figure 1.21, pour reproduire le processus de décohé- sion de l'interface. Toujours partant d'un modèle tri-linéaire, Ren et al. [Ren2010] ont décrit en détail toutes les étapes du processus d'endommagement de l'interface. Quant aux câbles, Yacizi et Kaiser [Yacizi1992] ont proposé un modèle pour expliquer la résistance à l'arrachement des câbles classiques. Pour étudier le comportement radial de l'interface, ils se sont basés sur le comportement de l'anneau de scellement et du terrain environnant, qui est complété par une relation totalement empirique pour limiter le déplacement radial maximum. Le comportement axial est déduit des essais d'arrachement (effectués à rigidité radiale constante en paroi du trou), sous l'hypothèse d'un comportement uniforme sur toute la longueur ancrée. Hyett et al. [Hyett1995] ont proposé une loi d'interface pour décrire le comportement post-pic des câbles classiques. Dans leur modèle pour reproduire des essais d'arrache- ment, l'effet de la rotation est pris en compte, et le comportement radial de l'interface, adapté de celui des joints rocheux, est plus complet que dans le modèle de Yacizi et Kaiser, mais on ne donne pas de justification pour une telle adaptation. La comparaison entre les résultats des essais (effectués à pression de confinement constante et à rigidité radiale constante en paroi du trou) et les prédictions du modèle donne des résultats satisfaisants, comme le montre la figure 1.29 (essais à confinement constant). La loi d'interface proposée est apte pour implémentation dans un code de calcul, mais elle ne tient pas compte du comportement avant la rupture.

Pour finir ce chapitre bibliographique, une revue des modèles proposés dans quelques codes de calcul numérique bidimensionnel (FLAC, Phase<sup>2</sup>, Plaxis, VIPLEF et CESAR-LCPC) pour simuler les boulons à ancrage réparti est présentée. Les modélisations numériques s'avèrent particulièrement utiles non seulement pour prédire la réponse des ouvrages complexes (au moins en termes de ten- dances d'évolution), mais aussi pour aider à la conception des schémas de soutènement. La façon dont l'interaction terrain-renforcement est prise en compte est en conséquence très importante. Laigle [Laigle2004] a montré que l'effet du boulonnage passif peut être mis en évidence numériquement. L'exa- men approfondi des modèles proposés montre d'une part que les tiges sont discrétisées sans épaisseur non seulement pour réduire les besoins informatiques mais surtout pour éviter la distorsion des mailles (provoquée par la différence d'échelle entre l'ouvrage et le soutènement), et d'autre part que l'inter- face de contact n'est prise en compte que dans quelques cas. Par ailleurs, seule l'interface qui risque de casser est discrétisée afin de ne pas alourdir les calculs. Son comportement tangentiel est souvent élastique-parfaitement plastique et sa réponse normale est linéaire, en général très rigide. Lorsque l'interface n'est pas discrétisée, on utilise le comportement en cisaillement du matériau de scellement pour approximer la réponse du contact; cependant, dans ces conditions le glissement relatif ne peut pas être simulé. Quant à la comparaison 2D-3D, il est important de remarquer qu'en 2D l'ensemble tige-interface est remplacé par une plaque continue dans la direction normale au plan. Les modèles 3D surmontent cette limitation, ce qui conduit à des résultats plus précis, mais au détriment de la taille et le temps des calculs. En outre, la représentation tridimensionnelle de l'interface de contact (cylin- drique) oblige à donner une épaisseur aux tiges, rendant alors le choix du maillage très compliqué. Pour ces raisons, la plupart des simulations comprenant des boulons à ancrage réparti sont faites en deux dimensions.

En résumé, la revue bibliographique montre que le comportement de l'interface tige-scellement n'est pas totalement maîtrisé. L'objectif des chapitres suivants de ce mémoire est d'essayer d'améliorer les connaissances actuelles, aussi bien d'un point de vue théorique qu'expérimental.

## 1.1 Introduction

Rockbolting and cablebolting are two ground reinforcement techniques broadly used not only in mining but also in civil engineering applications. In fact, according to Stillborg [Stillborg1986], rockbolting is the most effective and the most economical means of supporting excavations in rock. As of today, hundred of millions of bolts are installed each year worldwide: only roof bolting applications in coal mining in North America represent annually about  $100 \cdot 10^6$  of bolts (*cf.* [Mark2003]). Likewise, in several countries around the world, the only way to maintain at present longwall coal mining operations profitable is through the use of bolts in the roadways.

Although the first bolts were installed in the 19<sup>th</sup> century, the extensive use of rockbolts began in the late 1950s, nearly a century after the patent for reinforced concrete was granted in 1867. Coal mines were the first users of rockbolts, which came to replace timber props. Similarly, the application of cablebolts began in the 1960s, some 70 years after the patent for prestressed concrete was awarded. As one could imagine, the first rockbolts were identical to the elements used in reinforced concrete and the first cablebolts were identical to the elements used in prestressed concrete. In the recent years, the spectrum of applications has widened significantly, which has brought about the development of new and versatile bolt concepts to tackle a various range of ground problems. On average, a new bolt design is launched in the market every 5-10 years.

In general terms, a rockbolt or cablebolt consists of a bar inserted in a borehole that is drilled into the surrounding soil or rock mass and anchored to it by means of a fixture. Thus, the reinforcement element is installed *inside* the ground, thereby reinforcing and mobilizing the inherent strength of the soil or rock mass. On the other hand, support techniques such as steel arches and shotcrete restrict the ground movements from the excavation surface. Historically, this difference favoured an early development of support elements rather than reinforcement elements because in the former case, it is easier to visually follow the rock mass deformation; actually, rock and cablebolting prompted some skepticism at the beginning because of the absence of a visual reaction force on the excavation sidewalls. But today, any distrust in bolting has been overcome and not only engineers but also workers are convinced of the advantages of rock reinforcement elements.

The main assets of rock and cablebolting are:

- an easy and fast installation as compared to other techniques: fully mechanized bolting rigs are able to combine drilling and bolting in a one-pass operation, increasing productivity, safety and cost efficiency. Moreover, self-drilling anchors provided with a sacrificial drill bit are also available and are particularly useful for unstable conditions (silt, clay, soft to medium fractured rock formations, ...);
- the minimization of the obstruction in the excavated cross-section: the usable space is equal to the designed space (in any case, the obstruction is much smaller than that of any other technique);
- the possibility to reinforce large underground openings such as power plants or storage facilities;
- the possibility to be easily combined with supplementary support systems (wire mesh, shotcrete, concrete lining, *etc.*);
- the bolting pattern can be easily modified if so is required by the local rock mass conditions;
- their price: in regular situations, the cost of bolting is remarkably cheaper than that of other technologies (see table 1.1 below).

**Table 1.1:** cost of support technologies (adapted from Alejano *et al.* [Alejano2010]).

| Technology                       | Price (€/m) |
|----------------------------------|-------------|
| Advance (drilling&blasting)      | 335         |
| Bolting (1bolt/4m <sup>2</sup> ) | 115         |
| Shotcrete 2"                     | 190         |
| Shotcrete 4"                     | 380         |
| Mesh                             | 95          |
| Steel arch&Layer                 | 465         |

In addition, rockbolts and cablebolts can be used not only as temporary but also as permanent rock mass reinforcement. Apart from extremely weak rock conditions or extremely cracked rock masses, bolts can be used in a wide range of situations. As a way to illustrate the efficiency of bolting, a case study where the use of rockbolts was essential to maintain the stability of an underground opening is shortly presented here. The relevant information is displayed in figure 1.1.

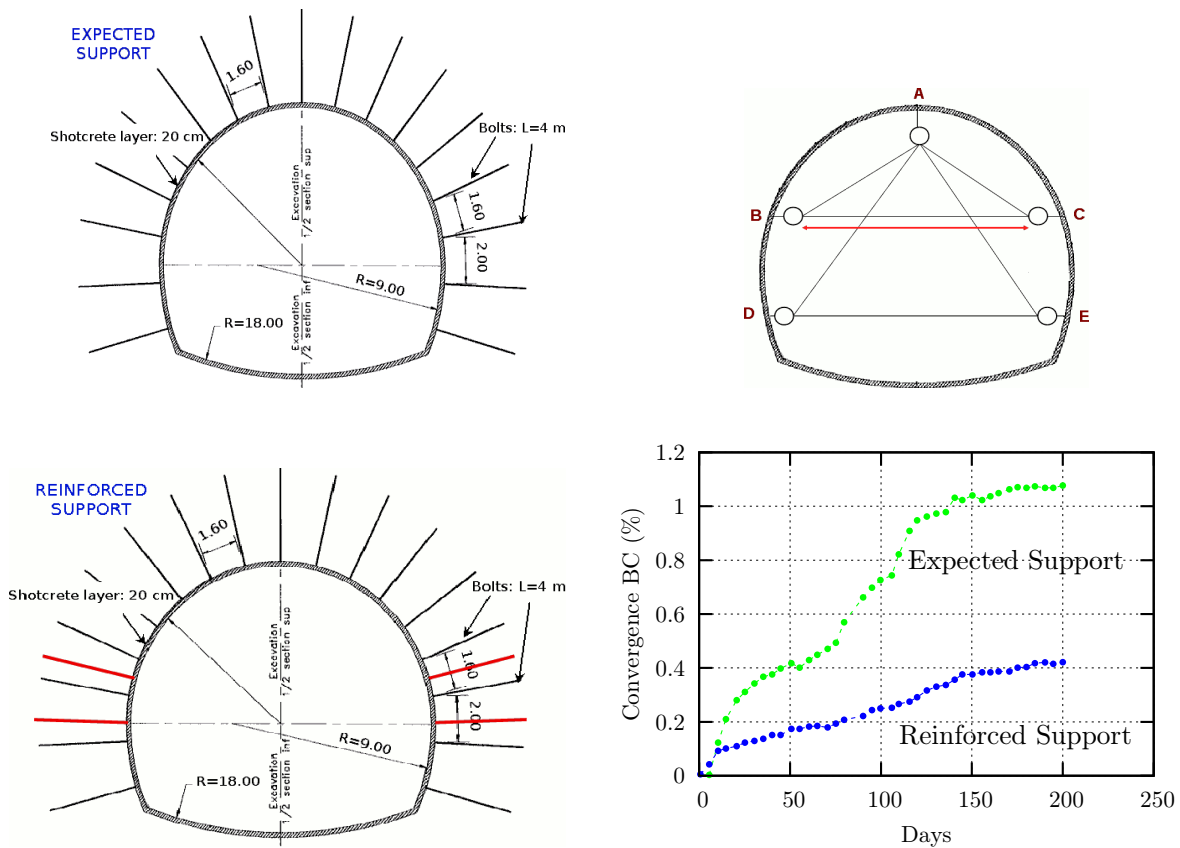


**Figure 1.1:** the Tartaguille tunnel. Effect of rockbolts on the convergence (adapted from Laigle [Laigle2004]).

The study concerns the Tartaguille tunnel, excavated in the South of France within the extension project of the high speed train network from Lyon to Marseille. This tunnel is about 2400 m long and has a 180 m<sup>2</sup> cross-section (average radius of 7.5 m). Its average and maximum depths are 75 and 137 m, respectively. Along 1150 m from the South end, the tunnel goes through the Aptien marl layer, whose mechanical properties are weak (Young's modulus  $E \approx 1270$  MPa and uniaxial compressive strength  $UCS \approx 12.5$  MPa) and moreover it presents a creep behaviour. The initial support for this tunnel consisted of a 20 cm thick shotcrete layer and 17 radial rockbolts (*Super-Swellex* 4 m long)

spaced between 1.6 and 2 m around the tunnel with the closer spacing in the roof and upper sidewalls, see the first illustration in figure 1.1. During the excavation phase, the convergence between different bases on the tunnel surface was monitored as shown in the upper right drawing in the figure. Through the Aptien marl layer, the excavation was carried out in two phases: driveage of the upper section first and afterwards excavation of the lower part. The rockbolts were installed when the deconfinement ratio was  $\lambda = 0.7$ . Monitoring revealed that, during the excavation of the sill plate, roof convergence increased threefold and consequently the vault was likely to collapse. Numerical simulations assuming the marl to be elastoplastic also indicated high rock damage and potential to collapse in this zone. In order to overcome this problem, the bolt pattern was reinforced by four supplementary bolts per cross-section when  $\lambda = 0.9$ , as indicated by the red lines in the lower left illustration in figure 1.1. It can be seen in the lower right graph in the figure that the reinforced bolt pattern let the convergence measurements go back to reasonable values (the thickness of the concrete layer was not changed).

After this brief introduction to get straight to the matter in hand, the current chapter is dedicated to describe the most common types of rockbolts and cablebolts. Among the different bolting technologies available today, the present study focuses on fully grouted rockbolts and cablebolts; therefore, this technology will be explained in detail. More precisely, the core of this research is the behaviour of grouted bolts under tensile axial loads. Accordingly, the last part of the chapter reviews the research undertaken in the past years on this topic. The objective is to understand the work done and to ascertain the limitations encountered in order to try to improve the knowledge acquired through these previous works.

## 1.2 Technological Background

As stated by Windsor and Thompson [Windsor1996], rockbolts and cablebolts consist of four principal components:

- the rock or soil: simply, the host ground where the bolt will be installed. It is important to note that the proper drilling of the borehole is a critical part of rockbolting, since the bar is anchored to the borehole walls;
- the reinforcing bar: metallic in most cases, its main function is to restrain (but not to prevent) the surrounding ground deformation, by being stiffer. Reinforcing bars that allow for larger deformations before failure are more satisfactory. Furthermore, the use of a plain bar or a several-wire strand yields the principal difference between rockbolts and cablebolts;
- the internal fixture to the borehole wall: in other words, the way the rod is anchored to the rock or soil (*i.e.*, the way they are coupled together). As it will be explained later, this element is used to classify the different bolting systems;
- the external fixture to the excavation surface: namely, a plate and a nut. In order to screw the nut that holds the plate, bolts are usually provided with a threaded part about 20-25 cm long at one of their ends. The basic roles of the external fixture are to reduce the rock fracturation around the borehole collar (*i.e.*, spalling), to improve the loading of the reinforcing bar and, in some bolts, to maintain the tension on the bar, see part 1.2.1.

Rockbolts and cablebolts are designed to help the rock mass support itself (*cf.* [Rabczewicz1964]). This is practically achieved by means of a load transfer mechanism that takes place between the ground

and the reinforcing element *via* the fixture. In this context, the nature of the internal fixture and the coupling conditions provided at its interfaces with the bar and the ground play an important role.

As for the differences between rockbolts and cablebolts, they are mainly associated with the scale and standards of design and installation. As indicated by Barley and Windsor [Barley2000], cablebolts are most commonly used in mining engineering applications, whereas rockbolts are used in both mining and civil engineering projects.

### 1.2.1 Rockbolting

Rockbolts are characterized by the use of a plain bar to reinforce the rock or soil. Probably the most famous classification of reinforcement systems is the one proposed by Windsor and Thompson [Windsor1993], who, taking into account the aforementioned load transfer concept, defined three types of systems according to the degree and extent of the coupling between the components of the reinforcement:

- discretely mechanically or frictionally coupled (DMFC) systems;
- continuously frictionally coupled (CFC) systems, and
- continuously mechanically coupled (CMC) systems.

The current investigation deals with fully grouted rockbolts, which belong to the CMC system; therefore, more details will be given for this type of rockbolt.

#### Discretely mechanically or frictionally coupled (DMFC) systems

DMFC rockbolts are the earliest (and hence, the simplest) system to come into widespread use. They are anchored to the rock at the borehole far end, just over a small length, while the rest of the bar is free (and consequently the axial load along this part is constant). Figure 1.2 shows the main components of a DMFC rockbolt.

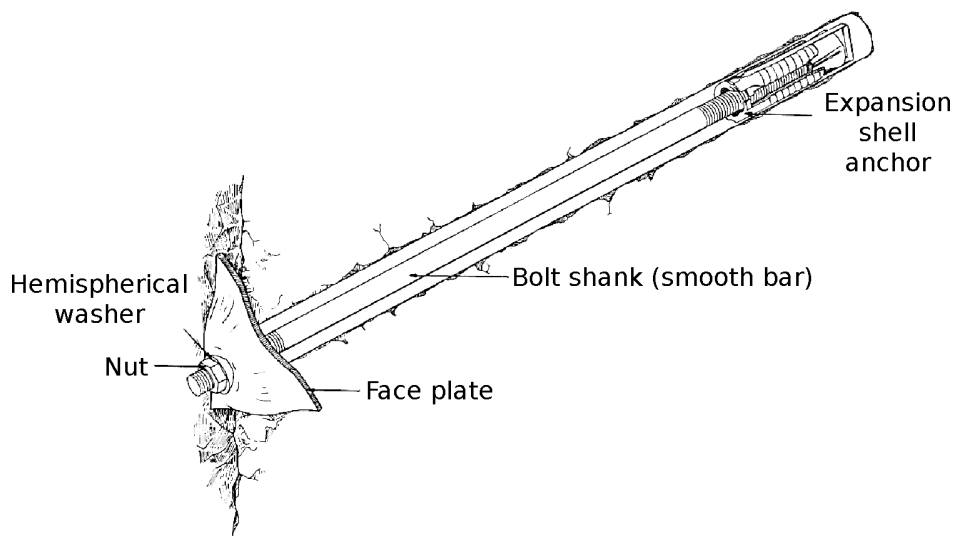


**Figure 1.2:** main components of a DMFC rockbolt (adapted from Stillborg [Stillborg1986]).

The anchoring can be achieved using a fast-set resin grout or alternatively a slot-and-wedge mechanism or an expansion shell. When using resin, the required number of cartridges is inserted into

the borehole and afterwards the spinning of the rod mixes and distributes the grout around the bar. In the second case, the anchor consists of a tapered, threaded cone attached to the bolt far end and surrounded by 2-3 wedges held in place by a bail. After installation in the borehole, a strong pull is applied on the rockbolt head, so that the cone is forced into the wedges, which grip consequently the borehole wall (the external surface of the wedges is threaded as well). In order to maintain the applied tension (otherwise the rockbolt is useless), a plate and a nut must be fixed on the excavation surface and should be checked regularly. This tension is usually about 70 % of the bar yield strength.

As a result of the pretension in the bar, the surrounding ground between the plate and the anchored end is confined. In general, 16-24 mm diameter smooth ductile steel bars are used for this type of rockbolt, *cf.* [Fine1998]. DMFC systems can handle tensile, compressive and bending loads, but are not able to deal with shear loads unless the shear displacement exceeds the thickness of the borehole annulus. In practice, the system response is a combination of several load modes.

The principal advantage of these rockbolts is that they provide immediate support action: they are *active* rockbolts. For long-term applications, it is recommended to post-grout the bar free length, which also reduces the risk of corrosion. Besides, the time of installation is quite short. As for their disadvantages, perhaps the most important is the need to regularly check the proper tensioning of the bar: creep behaviour, vibrations induced by blasting or loosening of the face plate can drastically reduce the load on the bar. On the other hand, DMFC systems cannot be used in neither very hard nor very soft rock conditions: in the former case, the rock would prevent the wedges from properly gripping the borehole, whereas in the latter, the wedges would sink in the borehole wall, letting the cone slip under the effect of pretension. Moreover, DMFC systems are more efficient when they are as perpendicular to the strata as possible.

### Continuously frictionally coupled (CFC) systems

CFC rockbolts rely on full length contact between the bar and the borehole wall to provide the reinforcing frictional action. Swellex and Split-set are the most popular friction bolts. In both cases, the bar is metallic. CFC rockbolts are very easy to install and can hold a combination of tensile, compressive and bending loads. In addition, they can accommodate large rock deformations, which make them suitable for deep excavation applications. However, they are unable to support large shear loadings because they are hollow structures. Friction anchored bolts are one of the latest developments in the bolting technology (they were introduced in the 1980s). Since they mainly provide support action if the surrounding ground tries to deform, they are *passive* rockbolts. Although they have gained popularity in the mining industry, they are seldom used in civil engineering projects because they are not suitable for long-term applications (due particularly to the risk of corrosion).

**Split-set rockbolts:** first manufactured by Ingersoll-Rand, the Split-set rockbolt consists of a longitudinally-slotted high strength steel tube installed by pushing it into a slightly undersized hole. The radial stress generated by the tube compression (the steel remains within the elastic range) provides friction along the entire length of the bolt. Figure 1.3 illustrates the Split-set rockbolt. Split-set's main advantages are the speed and the ease of installation. On the other hand, the risk of corrosion remains one of its main problems, and the borehole requires very specific dimensions and regularity.

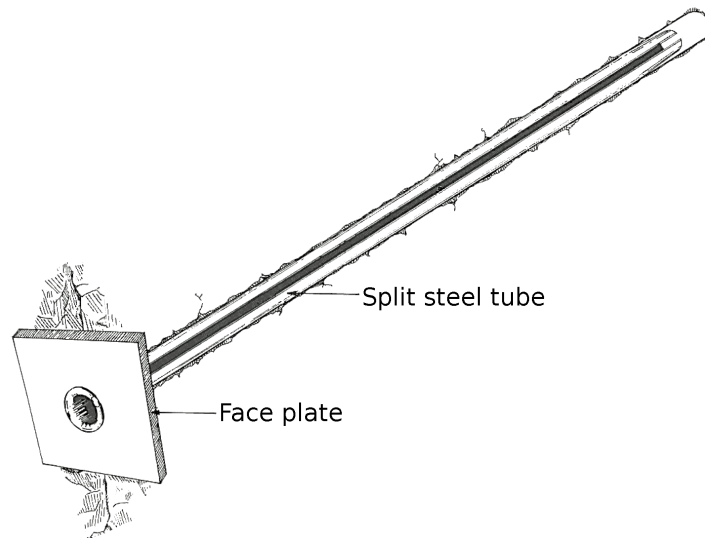


**Figure 1.3:** CFC system: Split-set rockbolt (adapted from Stillborg [Stillborg1986]).

**Swellex rockbolts:** manufactured by Atlas Copco, the classic Swellex system consists of a 42 mm diameter metallic welded tube folded on itself to create a 25-28 mm diameter unit. The tube is 2 mm thick and can be up to 7 m long. It is sealed at one extremity. *In situ*, the Swellex bolt is inserted into the borehole with the closed extremity facing the borehole end. High pressure water (approximately 30 MPa) is then injected inside the folded tube, which thereby inflates and deforms plastically, coming into contact with the borehole walls. Figure 1.4 shows several views of the Swellex rockbolt.

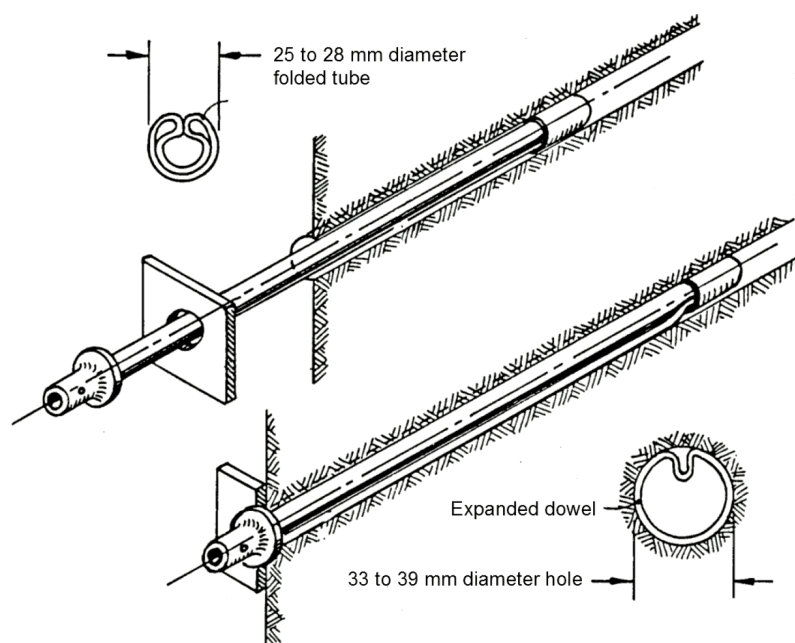


**Figure 1.4:** CFC system: Swellex rockbolt (after Hoek [Hoek2007], chapter 14, pages 1–21 ).

The major advantage of the Swellex rockbolt is that it embraces the shape of the borehole, assuring a good contact along its length. The speed of installation is another important asset. Moreover, the strength of a regular Swellex rockbolt is about 90 kN (Split-sets fail at about 50 kN according to Girard

[Girard1996]). Regarding the disadvantages, corrosion is a matter of concern in the case of permanent applications or aggressive environments; moreover, the water pressure should be predetermined to avoid the formation of cracks around the borehole, the drilling of which requires a very specific diameter. Finally, it is a quite expensive rockbolt, *cf.* [Stillborg1986].

### Continuously mechanically coupled (CMC) systems

CMC rockbolts are anchored to the rock or soil over their entire length; for this reason they are usually referred to as *fully grouted rockbolts*. This new concept came into play in the 1960s. According to Moosavi *et al.* and Li [Moosavi2005, Li2007], today the CMC rockbolt is probably the most commonly used reinforcement element. A typical CMC rockbolt is displayed in figure 1.5. The internal fixture of CMC rockbolts is either a cement mortar or a resin-based grout. Traditionally, fully anchored dowels were made of carbon steel, but since the 1980s, Fibre Reinforced Polymer (FRP) bars have been regularly used when cuttable reinforcement is required (for instance, at the tunnel face in civil and mining applications or at the sidewalls in longwall mining applications). Other assets of FRP rockbolts are: high resistance to corrosion and chemical attacks, high strength-to-weight ratio, high flexibility, electromagnetic neutrality and ease of handling. Nonetheless, for a given diameter, the shear strength of FRP bolts is about one half that of steel rockbolts.

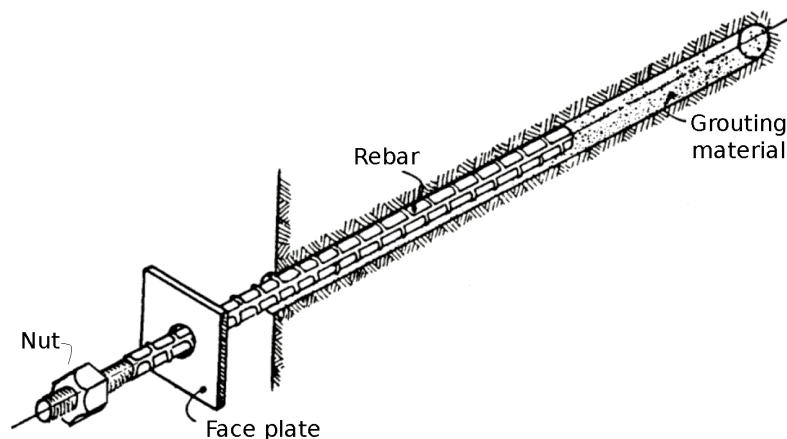


**Figure 1.5:** main components of a CMC rockbolt (adapted from Hoek [Hoek2007]).

In order to increase the mechanical anchoring between the rod and the internal fixture, bars are usually provided with ridges (and are then called REinforcing BARS or *rebars*), so that the ribs and the surrounding grouting material create a rock joint-like interface. Kilic *et al.* [Kilic2003] studied the bar shape effect on the pull-out capacity of CMC rockbolts and concluded that the bond strength associated with a ribbed bar is up to 5.5 times that associated with a smooth bar. The use of smooth bars proves to be successful in situations where larger deformabilities than that allowed by ribbed dowels are needed, such as in the case of bending of thin strata (*cf.* [Tincelin1991]). Nonetheless, the decrease in the bond capacity should not be neglected.

The main characteristic of fully grouted rockbolts is that they only provide support action if the surrounding soil or rock mass tries to deform: they are *passive* anchorage systems. Besides, since the whole length of the bar is embedded in the grouting material, the risk of corrosion is reduced. CMC rockbolts can be used either as a temporary or a permanent reinforcement, and are very popular not only in the mining industry but also in civil engineering applications. They are able to hold a combination of tensile, compressive, shear and bending loads. In the current investigation, especial

interest has been focused on their behaviour under tensile loads and on the load transfer mechanism between the rockbolt and the rock mass.

### Latest rockbolt concepts

The increase in depth of underground excavations in the recent years has introduced a challenge in the reinforcement concepts. In general, rockbolts used at depth are the same as those used in shallow excavations, but with a narrower pattern. Experience has shown that the use of conventional rockbolts does not provide a satisfactory reinforcement performance because of the small deformation capacity of those bolts; in fact, in deep openings (depth beyond 800-1000 m) the *in situ* stresses are very high and as a consequence rockbursts may occur in hard rocks and large squeezing deformations may appear in soft and weak rocks. These situations require dynamic reinforcing elements, able to sustain high loads and to accommodate important rock dilations; that is to say, able to absorb a large amount of energy.

One of the first solutions proposed was the cone bolt, invented in South Africa in the early 1990s (*cf.* [Jager1992]). This bolt consists of a smooth, high tensile strength steel bar with a flattened conical flaring forged onto one end, while the other end is fixed at the excavation surface, see figure 1.6a. Although fully grouted, the bar is coated with a layer of lubricant, so that it can easily debond under pull loads (the bar Poisson's effect also contributes to this detachment). As the rock mass between the two anchor points tries to deform, a load is induced in the bar and the cone will plough through the grout if the load exceeds a predefined value. Consequently, the bolt absorbs energy through a combination of the force required to compress the grout and the friction between the grout and the cone, *cf.* [Ansell2005]. This way, both the strength and the elongation capacity of the bolt material are used.

In the recent years, other types of energy-absorbing rockbolts have been designed and have gradually gained acceptance. Some of them are shown in figures 1.6b and 1.6c. Perhaps the latest is the D bolt, invented in 2006 (*cf.* [Li2010b]). It differs from the other energy-absorbing bolts in that it has a number of anchors along its length, as shown in figure 1.6b. These strong anchors are firmly fixed in the grout, while the smooth bar sections show a weak bonding and can elongate plastically, thereby absorbing energy. The main advantage of the D bolt is that the smooth bar sections between two adjacent anchors act independently, so that yielding of one section has only a local effect on the reinforcement capability.

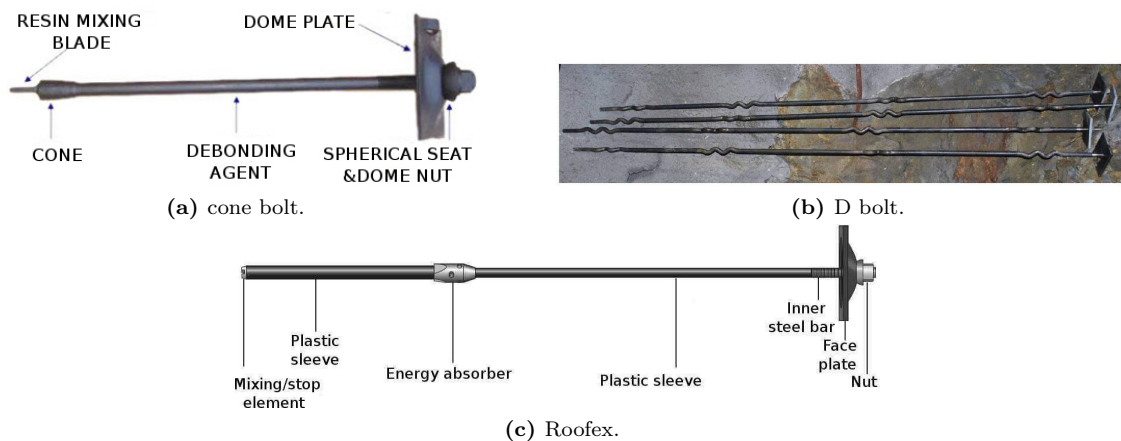


**Figure 1.6:** different types of energy-absorbing rockbolts.

Another energy-absorbing concept is the Roofex rockbolt (see figure 1.6c), developed by Atlas Copco. Its principle is as follows: when the rock starts to move, an inner steel bar slides inside a resin-grouted hollow bar by being pulled through an energy absorber device fixed to the borehole wall. This way, the energy released from rock deformation is absorbed by the friction created at the absorber.

### 1.2.2 Cablebolting

Cablebolts are based on the same principles as rockbolts. Nevertheless, with respect to the latter, cables have three particular characteristics which put them into a separate class of rock reinforcement:

- cablebolts are constructed from steel rope strands, not from plain bars. Several wires (six in the standard configuration) are wound around a central or *king* wire. The wires may be rewound to form particular structures that increase the load transfer mechanism between the cable and the grouting material;
- as a consequence of their helical structure, cablebolts have low torsional rigidities and hence they are able to hold not only tensile, compressive, shear and bending loads, but also torsional loads (and any combination of these modes);
- they exceed the capacity of traditional rockbolts: a 16 mm diameter cablebolt has a tensile strength of 250 kN, while a plain bar of the same cross-section fails at 180 kN.

The development of cablebolts came along with the move towards larger underground excavations, which needed longer and more resistant bars to be reinforced with. For general applications, when monitoring or previous experience shows that roof movement is occurring or is likely to occur above the rockbolted height, cablebolts are applied. Nowadays, cable lengths beyond 20 m are not unusual (rockbolts are rarely longer than 6-8 m). Most of their applications are in hard mining. Since cables are flexible, they can be packaged as small diameter coils (about 2 m), so that they can be easily transported and installed, even in small cross-section openings.

Cablebolts are normally fully grouted along their length. In most cases, cement is used as grouting material. The principal cablebolts used in both mining and civil engineering applications are:

- plain strand: it is the standard cablebolt, a 15.2 mm diameter and 250 kN tensile strength steel rope strand made of 7 or 19 wires (but the strand has the same nominal diameter). The outer wires are a bit smaller than the king wire (90 % of its diameter). The strand outer surface is normally profiled by rolling onto it a pattern of indents to increase the bond strength. A plain strand cablebolt is shown on top of figure 1.7. Plain strands are normally cement grouted; however, in conditions demanding fast support, resin is used and mechanical installation required. Stiffer, 23 mm diameter and 500 kN tensile strength bolts (comprising 7 or 19 wires) are utilized in such circumstances, with a limitation in the bolt length due to the fast curing time of the resin-based grouts;
- Birdcage: developed in Australia, it consists of a seven-wire steel rope strand in which the wires are unwound by hand or by machine to form a *birdcaged* structure consisting of alternate nodes and antinodes (see the second cable in figure 1.7). The aim of this modification is to increase the reinforcement bond strength and stiffness. The tensile strength of a birdcaged cablebolt is 300 kN and the cage nominal diameter is 35 mm. These cables are used with cementitious grouts, and normally supplied as double Birdcages (*i.e.*, two cables are installed in each borehole);

- Nutcage: it is a smaller version of the Birdcage cable, in which the same seven-wire, 300 kN strength strand is modified into a caged profile using nuts placed on the central king, see the third illustration in figure 1.7. The cages have a maximum diameter of 28 mm and are spaced 150 mm. Nutcage cables are normally installed into 35 mm diameter boreholes. As before, two strands are almost invariably used together;
- Mini-cage: it is a seven-wire strand axially compressed to create a bulbed profile of 25 mm maximum diameter and 160 mm bulb spacing. The Mini-cage is a derivative of the Australian Garford cablebolt. Its tensile strength is 300 kN. As with the Birdcage cablebolts, the Mini-cage strands are supplied as double cables, especially for roof bolt applications. They are used as a smaller diameter alternative to Birdcage cables, mostly in the same application areas. A Mini-cage bolt is schematically represented by the last illustration in figure 1.7;
- Megastrand: this cablebolt consists of multiple 70 kN tensile strength profiled steel wires configured as a simple strand. The 28 mm diameter standard version comprises 8 wires and has consequently a capacity of 560 kN. It is designed to be discretely anchored using polyester resin and pretensioned to provide immediate support. For long-term applications, the whole length can be grouted by means of a thixotropic cementitious grout, which is poured from a grout injection tube that runs internally through the strand until its far end. In general, the Megastrand is used in mining applications as an alternative to conventional cables in roof support patterns.

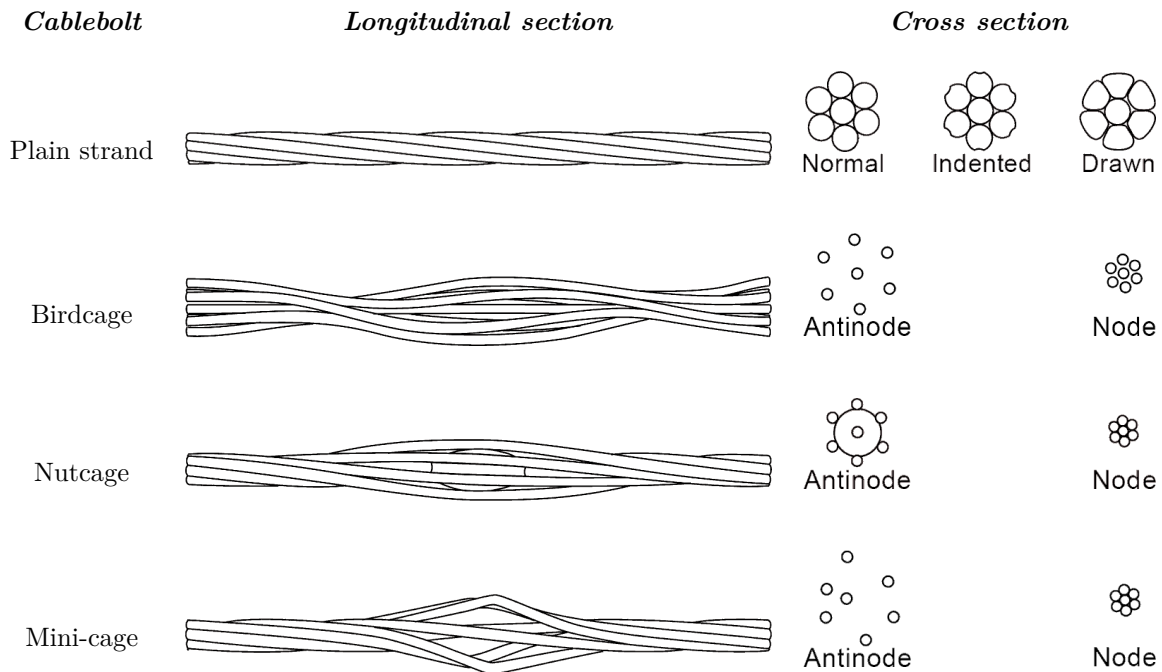


**Figure 1.7:** principal types of cablebolts (after Barley and Windsor [Barley2000]).

Modified geometry cablebolts are all recent developments of bolt technology. Experience and numerical simulations by Bawden *et al.* [Bawden1997] have shown that they are more performant than standard strands because they increase the normal pressure at the cable-grout interface, thereby increasing the

bond. Consequently, in cases where a reduction of *in situ* stresses is expected, modified geometry cablebolts are an interesting solution.

Finally, perhaps the most remarkable characteristic of cablebolts with respect to rockbolts is that, as a direct consequence of their structure, grouted cables may rotate under tensile loads. If both extremities of the cable length that is likely to fail are fixed, the cable will simply slip with respect to the rock mass; nonetheless, if one of the extremities is left free (namely, at the borehole collar), the wires of the cable will have a tendency to untwist themselves, forming an dissociated structure. This fact highlights the need to use face plates. Untwisting has been often observed, to a degree that depends on the load acting on the cablebolt. Figure 1.8 presents a comparison between the visual aspect of three cables whose structure has been partially or totally untwisted.

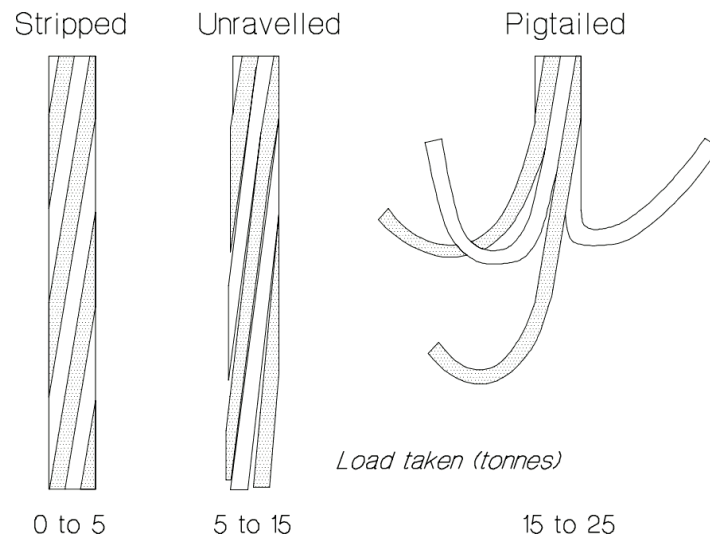


**Figure 1.8:** different degrees of untwisting of cablebolts due to their helical structure and low torsional rigidity (after Hutchinson and Diederichs [Hutchinson1996]). The tensile strength of the cables in the figure is 250 kN (25 t).

### 1.2.3 General aspects of fully grouted rockbolts and cablebolts

As for the grouting materials, the most common are:

- resin grout: in general terms, resin is used in the form of plastic cartridges that contain two separate chambers: the resin mortar, made of polyester in most cases, and the hardener (an organic peroxide). When mixed, the grout sets through an exothermic reaction and the rockbolt gets anchored to the rock mass. The higher the temperature, the shorter the curing time. Most resins have the following mechanical properties after 24 h and at 25 °C (*cf.* [Minova2009a, Minova2009b]): uniaxial compressive strength  $UCS \approx 70$  MPa, shear strength  $\tau_{\max} \approx 30$  MPa and Young's modulus  $E \approx 15$  GPa. Different setting times (from 20 s to 3 min) and cartridges dimensions are available depending upon the application: for instance, when rapid support action is required, a fast setting resin should be used. Alternatively, resin can be prepared *in situ* by mixing the two components in the good proportions and then injecting the mixture into the hole. Cartridges are usually installed using a bolter, while on-site prepared resin needs to be pumped inside the borehole. The advantages of resin are: it sets faster than cement, it is easy to handle, it does not degrade over time and it does not shrink during curing; nevertheless, it is more expensive than cementitious grouts. In addition, Campbell and Mould and Villaescusa *et*

*al.* [Campbell2005, Villaescusa2008] reported that the two most important drawbacks of resin cartridges are gloving and poor mixing, which are both caused by the presence of the plastic cartridges inside the boreholes. From experimental results, Villaescusa *et al.* [Villaescusa2008] concluded that the best resin mixing and bolt encapsulation occurs within the bolt middle region, whereas at the hole end the cartridges accumulation makes the anchorage difficult. At the same time, Campbell and Mould [Campbell2005] concluded from their analysis that 10-30 % of the reinforcement cost is wasted when poor mixing occurs;

- cementitious grouts: made of a mixture of cement, water and other substances that may reduce shrinkage, increase pumpability or improve the mixture mechanical properties (when used in the correct proportions), cement grouts are undoubtedly characterized by the water-cement mass ratio, hereafter  $w : c$ . They were the first grouting material used along with CMC rockbolts. For many decades, numerous researchers have concentrated on the study of the  $w : c$  parameter. For instance, investigations by Hyett *et al.*, Benmokrane *et al.* and Kilic *et al.* [Hyett1992a, Hyett1995, Benmokrane1995, Kilic2002] have demonstrated that the anchoring capacity increases with the decrease of the  $w : c$  ratio. According to Kilic *et al.* [Kilic2002], the physical reason for this statement is that the mixing water that is not used to hydrate the cement evaporates and creates capillary porosity, which results in an inhomogeneous internal structure of the grout, thereby reducing its performance. The conclusion of the experimental investigations undertaken by the authors above is that ratios  $w : c \in [0.35, 0.4]$  provide the best compromise between performance (*i.e.*, mechanical properties, see figure 1.9) and installation requirements (for lower ratios, the pumpability and mixability decrease because the viscosity increases). Improving the mechanical properties of the grouting material increases the bolt bearing capacity. According to Hyett *et al.* [Hyett1992b], low ratios can increase the anchoring capacity by 50 – 75 %. The principal advantages of cementitious grouts are that they are less expensive than resin-based grouts and that their composition can be adjusted easily. In addition, their components can be stored longer (as a general rule, resin cartridges do not last longer than six months). But on the other hand, to fully develop the mechanical properties of cement-based grouts, a curing time of about 28 days is needed. So when immediate support action is required, resin-based grouts are more suitable. Investigations by Kilic *et al.* [Kilic2002] have revealed that the grout strength develops rapidly within the first seven days and continues to increase at a slower rate thereafter.

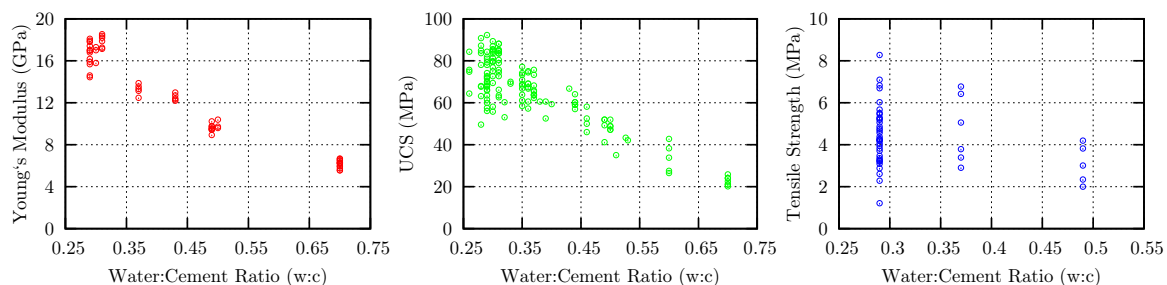


**Figure 1.9:** important mechanical properties of cementitious grouts pertaining to bolting (after Hyett *et al.* [Hyett1992a]). For ratios  $w : c < 0.35$ , only the Young's modulus continues to increase. Any trend in the strength data is overshadowed by the scatter due to the *incomplete compaction* phenomenon (insufficient water available to saturate capillary voids & entrapment of air pockets). On the other hand, Moosavi *et al.* [Moosavi2005] have reported that the same type of cement produced by different factories may result in different strengths.

As for the rockbolts installation procedure, it depends on the grouting material in use: in the case of resin, the predetermined number of cartridges is inserted into the borehole before the bolt is introduced. During its installation, the bar is spinned, so that the resin mortar and the hardener are mixed together. In the case of cement grouts, the mortar is pumped into the hole by means of a grout tube that is slowly withdrawn as the grout is pumped in. The bar is then pushed into the hole. In either case, it is quite difficult to ensure that the bar is properly centered in the borehole and that the grout is uniformly distributed along the embedment length. Finally, once the grouting material has set, the plate and the nut are tightly installed at the borehole collar.

The installation of cablebolts is not very different from the installation of rockbolts, *cf.* [Hoek2007]; however, it should be noticed that, since cables are longer, more attention needs to be paid to the pumpability of the grout in use: if the grout is injected into the borehole bottom and the air is bled from the hole end (the *breather tube method*), a ratio  $w : c \geq 0.4$  is normally used, but when the grout is injected into the borehole end (the *grout tube method*), very viscous grouts ( $w : c \in [0.30, 0.35]$ ) are preferred to reduce slump voids. On the other hand, in order for the grout to be able to penetrate into the modified geometries created along the cables enumerated in part 1.2.2, the use of a 0.35 – 0.4  $w : c$  grout is recommended. Therefore, the *breather tube method* is more suitable for these types of cables.

From a more technical point of view, there are two principal ways of inducing a load on a fully grouted bolt depending on the *in situ* stresses and the surrounding rock mass properties and degree of damage:

- in jointed rock masses, block separation will induce a load in the bar. The load reaches its maximum value at a discontinuity. Such a load can be a combination of axial and shear, as shown in figure 1.10;

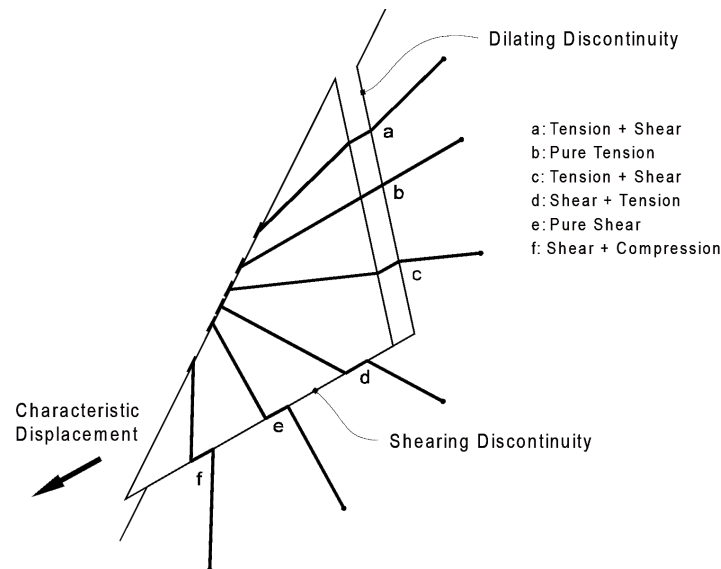


**Figure 1.10:** loading cases of CMC bolts in a jointed rock mass (after Barley and Windsor [Barley2000]).

- in the case of continuous media (homogenous or highly fractured ground), the largest ground movement occurs normally at the excavation surface. Under these circumstances, the bolt is in general most loaded at the borehole collar, and the axial load in the bar is maximum in this zone

(cf. [Hyett1996, Li1999, Li2010a]). The use of a face plate is important here because as the rock tends to move, the plate will get charged. The load on the face plate will be transferred to the bolt through the nut and the thread. Thus, more load will be transferred to the bar thanks to the presence of the plate, thereby increasing the reinforcement effect (however, as reported by Li [Li2007], especial attention should be paid to the threaded part tensile strength when large rock deformations are likely to happen).

As a result of the mentioned features, three main roles can be elucidated for CMC bolts:

- rock mass mechanical properties improvement: this role is characteristic of CMC bolts. In highly stratified or damaged ground, these bolts are able to clamp the rock layers together, making them move more as a unity. This way, the rock mass actual strength and performance increase. This function represents the pure *reinforcement* role, displayed in the first illustration in figure 1.11;
- rock confinement: as the bolt is progressively loaded, a compressive zone appears around the opening, which contributes to the use of the damaged rock belt to confine the stable rock mass. This corresponds to the *confining* role illustrated in the second drawing in figure 1.11;
- jointed rock mass stabilization: provided the bar far end is anchored to a stable zone, the bar is able to support unstable rock blocks that are likely to either fall or slip, with no consequence to the stability of the opening. This corresponds to the *load-bearing* role, see the last illustration in figure 1.11 (this role is common for all types of bolts).

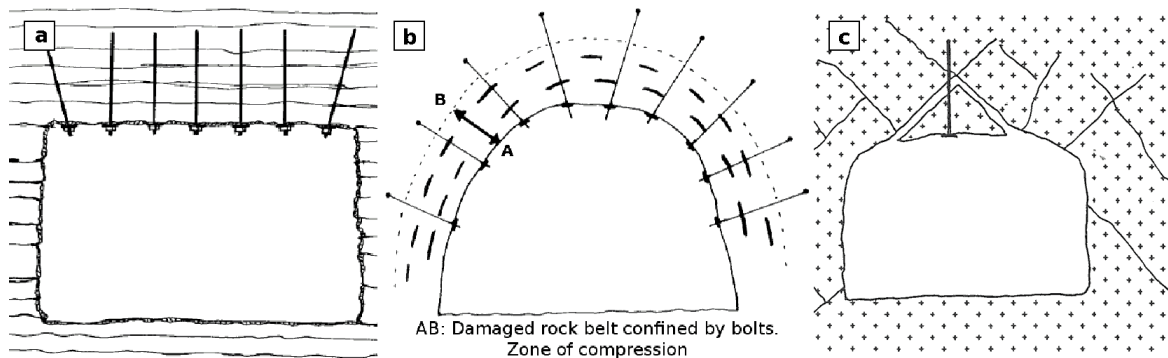


**Figure 1.11:** main roles of CMC bolts. a: rock mass mechanical properties improvement (from Stillborg [Stillborg1986]); b: rock confinement (from Tincelin [Tincelin1991]); c: jointed rock mass stabilization (from Fine [Fine1998]).

#### 1.2.4 Design of rockbolting and cablebolting systems

As with the design of any type of rock support, the design of a cable or rockbolting system depends on the state, properties and failure modes of the surrounding ground, the *in situ* stresses, the excavation geometry and the support requirements (in terms of acceptable deformation and lifetime of the excavation). To design reinforcement patterns, it is considered that the reinforcing elements do not reach failure. In most cases (apart from the support of unstable rock blocks, where the bolts are designed to hold the dead weight of the blocks), the load taken by the bolts is small compared with the loads acting in the rock, cf. [Stillborg1986]. This emphasizes the way bolts enable the rock mass to be self supporting.

For a bolting pattern to be properly designed, the following parameters must be determined:

- bolt type;
- bolt diameter and load-carrying capacity;
- bolt length;
- spatial array on the opening cross-section and along its axis;
- need for pretension (and magnitude), particularly for DMFC bolts.

The bolt type selection demands a thorough understanding of the performance and possible failure mode of each type of bolt in a specific situation. Numerous guidelines exist, as those proposed by Stillborg and Smith [Stillborg1986, Smith1993]: they describe the advantages and drawbacks of each bolt type, the conditions they best suit and the situations in which they should not be used. Some of these guidelines have been exposed in 1.2.1 and 1.2.2. In general, design work and verification of the performance of the bolts in use (by means of the analysis of the monitoring results) continue throughout the lifetime of the opening, so that the necessary adaptations can be introduced.

There are at present four principal techniques to help the engineer define a bolting pattern:

- analysis of structural stability (*i.e.*, limit equilibrium analysis): this technique aims at preventing unstable wedges, blocks or rock layers from falling, sliding or collapsing. Minimum required bolt length and spacing to reach this target are estimated from the unstable rock mass density and volume, the sliding surface properties (dip and friction angles, cohesion, area, *etc.*), the bolt load bearing capacity and a safety factor. Three different approaches exist depending on the rock mass:
  - the beam or slab concept for bedded rock: in the case of horizontally-bedded rocks, flat or haunched roofs are habitual, see the first illustration in figure 1.11. If the horizontal stresses are high, buckling of the beds may occur. In such circumstances, the use of bolts contributes to the formation of a structural beam,
  - the rock arch concept: in the case of jointed rock masses, curved roofs are normally excavated, as shown in the second illustration in figure 1.11. In this case, a natural arch is formed above the roof at some depth into the rock mass due to the stress redistribution following the excavation. Bolts are in general applied to maintain the stability of the loose zone,
  - limited rock block stability analysis: it refers to blocks formed in massive rocks as a result of natural or induced discontinuities, that may fall or slide without compromising the stability of the excavation. This situation is displayed in the last drawing in figure 1.11. Bolts are used to retain such blocks;
- standards and empirical approaches: based on the use of rock mass classification systems (RMR, Q-system, *etc.*) or on past experience, they provide empirical rules to determine the length and spacing of a predefined bolt type. As an example, Gagnon [Gagnon1996] recommends the following formulae:
  - $L/S > 2$  and  $S/B < 4$ , where  $L$  is the bolt length,  $S$  is the bolt spacing (in the cross-section) and  $B$  is the characteristic size of the blocks (namely, the joint spacing),
  - $L = 1.4 + 0.18x$  [m], where  $x$  is the tunnel width,

- $L = e + 1$  [m], where  $e$  is an estimate of the thickness of the unstable strata above the opening;

Empirical assessments are frequently used because they provide fast and easy guidance; however, they should be accompanied by other design tools;

- closed form solutions: they consist of analytical approaches able to predict the load acting on one or several bolts. To do so, they assume a number of hypotheses in order to obtain a simplified mathematical formulation compatible with an analytical development. Some closed form solutions are based on homogenization approaches (*i.e.*, the periodically reinforced ground is converted into a homogeneous, anisotropic continuum). The parameters needed to define the bolting pattern may be derived from the predicted load;
- numerical models: numerical tools may help predict the response (at least, the general trends) of an excavation reinforced by bolts. Different bolting patterns may be tested to identify the most suitable one. There are currently several programs that propose different structural elements to model rockbolts or cablebolts. Some of the most popular are described in section 1.3.

As a whole, given the complex interaction between the excavation geometry, the stress level and the rock mass properties, no design method has gained widespread acceptance, simply because none fits every possible situation. Consequently, experience and corroboration using several methods are common practices to design bolting configurations.

### 1.2.5 Failure of fully grouted rockbolts and cablebolts

Within the vast domain of fully grouted bolts, this research focuses on their behaviour under tensile axial loads. Experience throughout the world reported by many researchers, *cf.* [Stillborg1984, Goris1990, Reichert1991, Kaiser1992, R. Pakalnis1994, Hyett1995, Benmokrane1995, Bawden1997, Moosavi2005, Ivanovic2009] for example, has shown that, in real field situations and under tensile loads, it is the bolt-grout interface that fails in most cases, creating a relative slip between the reinforcing bar and the surrounding media. But strictly, any of the following could happen:

- failure of the bar, if the axial load on it exceeds locally the bolt material tensile strength;
- failure of the grout-ground interface, if for any reason this interface is weaker than the bolt-grout interface;
- failure of the grouting material itself;
- failure of the surrounding ground.

Failure of the grout-ground interface and failure of the bolt itself are also common. A combination of different failure modes could also befall. In practice, it is very difficult to predict where failure will occur because it depends upon a large number of parameters, which include not only the intrinsic properties of the materials involved but also factors like the riffling of the borehole wall, the quality of grouting or the stress changes *in situ*. In this study, the most reported failure mechanism has been considered and therefore it has been assumed in the theoretical and experimental studies developed respectively in chapters 2 and 3 that failure takes place at the bolt-grout interface. This hypothesis is supported by the fact that solid materials are in general more resistant than the interfaces in between. Under these assumptions, a decoupling process may occur between the bar and the grouting material

as the axial load on the bar increases. The interface behaviour and the factors that influence it are the core of the current investigation.

With the aim of gaining some understanding in the way rockbolts work, Freeman [Freeman1978] monitored for the first time in the 1970s the loading process of a fully grouted bolt and the distribution of the axial load along its length (Kielder experimental tunnel, UK). On the basis of his results, he suggested that the embedment length of a CMC rockbolt can be divided into three different parts:

- *neutral point*: at this point, the axial load on the rockbolt reaches a maximum and the shear stress is zero. At the neutral point, there is no relative movement between the rock and the bolt. If during the loading process decoupling occurs, the position of the neutral point may change;
- *anchoring length*: it is the length between the neutral point and the bolt far end. Along this part, the shear stress anchors the bar to the rock. Thus, it corresponds to the resistant, load-carrying part of the rockbolt. In the *anchoring length*, the load on the bar is transferred *via* the grout to the stable rock mass;
- *pick-up length*: it is the length between the neutral point and the excavation surface. This part, shorter than the *anchoring length*, is likely to fail by a decoupling process if the shear stress developed is insufficient to equilibrate the axial force on the rockbolt.

These three parts are displayed in the two illustrations in figure 1.12, which correspond to two CMC rockbolts naturally loaded. In figure 1.12a, the face plate is absent, while in figure 1.12b, the washer plate is installed at the excavation surface.

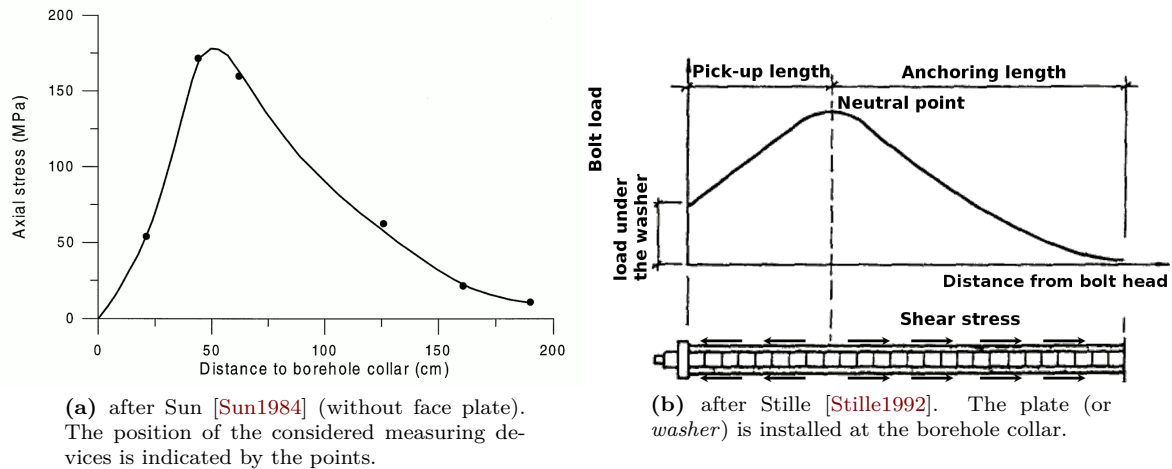


**Figure 1.12:** load distribution along a fully grouted rockbolt *in situ*.

As one could expect, failure will start where the load is maximum and will propagate along the embedded length with an increasing load. It is important to note that, in real situations, bolts are not only subjected to axial but also to shear and bending loads. Moreover, a combination of shearing and tensioning enhance the bearing capacity of rockbolts, as demonstrated in the laboratory by Ludvig [Ludvig1983]. Li [Li2010a] reported several field observations in which a mixed mode of pull, shear and bending led to the failure of passive reinforcement elements. Some of them are shown in figure 1.13. While in the first case the rebar could handle the applied loads, the bolt itself broke in the last two cases.

At laboratory scale, it is very difficult to simulate combined axial and lateral loads, which justifies the limited number of publications on this topic. One of such studies was led by Bawden *et al.*

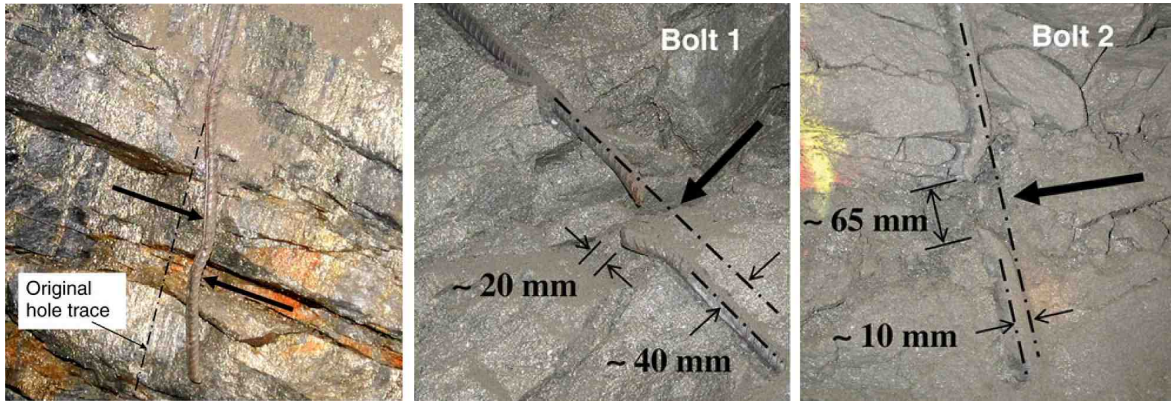


**Figure 1.13:** field observations in mining reported by Li [Li2010a]. Rebars exposed to shear, bending and axial loads. The arrows show the direction of possible shear movements in the rock mass.

[Bawden1994], who conducted a series of pull-out tests on standard and modified geometry cablebolts to evaluate their load-displacement characteristic as a function of their orientation with respect to rock joint displacement. To do so, the authors designed a testing rig that allowed for changes in the pull angle  $\alpha$  (*i.e.*, the angle between the joint displacement and the bolt axis), while the tendon was installed perpendicular to the discontinuity. The pull angle was varied from  $0^\circ$  to  $60^\circ$ ; under these circumstances, the bolts were subjected to a combined axial and shear load (excepting  $\alpha = 0^\circ$ ). A schematic view of the apparatus is illustrated in the left-hand side of figure 1.14. The results, displayed in the top right-hand side of the figure, show that the bond strength increases with the pull angle, whereas the anchorage stiffness decreases.

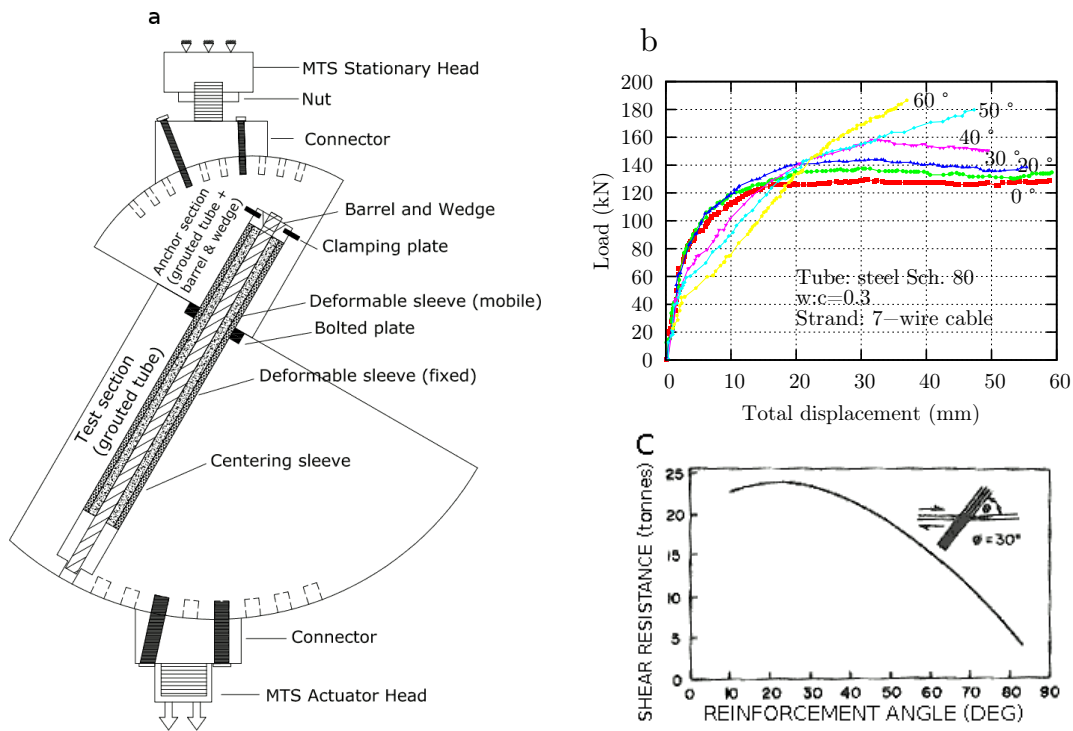


**Figure 1.14:** a, b: study of the response of standard cablebolts under combined axial and lateral loads. Laboratory bench and experimental results obtained (adapted from Bawden *et al.* [Bawden1994]); c: effect of the cable inclination with respect to the shear plane on the resistance to joint shearing, for a shear displacement of 1.8 mm (after Fuller [Fuller1983]).

Additionally, Fuller and Durville *et al.* [Fuller1983, Durville2006] have conducted shear tests on rockbolts installed at different inclinations with respect to the shear plane. Results from both studies confirm that the maximum contribution to the shear resistance is obtained for bolt inclinations comprised between 20 ° and 60 ° following the direction of shearing, see graph *c* in figure 1.14. Furthermore, the contribution increases with the bolt diameter approximately in a linear fashion. Beyond the range 20 °- 60 °, the shear displacement may increase but the contribution to the shear resistance decreases. It has also been observed that joint opening is best restricted by placing the bolts normal to the joint plane. Pellet [Pellet1993] has conducted similar tests (he has also included several discontinuities) and highlighted not only the influence of the bar inclination, but also the importance of both the joint friction angle and the adjacent ground mechanical properties.

In the context of this investigation, it will be assumed that the bolt is subjected to a pure tensile axial load and that failure takes place at the bolt-grout interface. This choice will let understand the effect of the axial load on the bolt and the load transfer mechanism between the reinforcement element and the surrounding media. The effect of mixed loading modes will not be studied.

### 1.2.6 Performance of passive reinforcement systems

Fuller *et al.* [Fuller1996] declared that the performance of a rockbolt or cablebolt reinforcement system depends on three factors: the bolt type, the internal and external fixtures properties and the surrounding ground condition (*i.e.*, type, mechanical properties and degree of damage). As a consequence of the influence of local parameters, no general rules but rather guidelines (see part 1.2.4) exist to know which bolting system is most appropriate for a particular application. As stated by Tincelin [Tincelin1991], the most important aspect is to ensure that the bolt and the rock mass are properly coupled together; otherwise, the bolt reinforcement system is useless. In this context, bolts should be tested *in situ* to know whether the reinforcement in use is compatible with the actual characteristics of the considered rock.

At the same time, in order to comprehend the interaction between the reinforcement and the surrounding ground, field monitoring, laboratory and *in situ* testing, analytical approaches and numerical modelling techniques are available to the engineer. The last three will be further discussed later in this chapter, *cf.* section 1.3. As for field monitoring, different methods exist to ascertain the stress or load distribution along the embedded length of CMC-CFC rockbolts and cablebolts (in general, the bolt material strain is deduced from the measurements [resistance, frequency, *etc.*] and converted into load *via* the tendon stiffness). Monitoring is a practical field and laboratory research tool because it provides information on the bolts behaviour through the estimate of the axial strain and the axial stress along the bars. Such information may be used to fulfil several purposes:

- determine if the bolts are being loaded, and to what extent with respect to their capacity;
- change the bolt pattern: number, spatial array and length of the bars in use;
- change the bolt type if the current bars do not provide the expected reinforcing action;
- provide insight into the load transfer mechanism along the embedded length. This aspect will be detailed in section 1.3.

Nevertheless, since the instrumentation of bolts is a specialized and expensive task, the bolt loads are often estimated from rock movement data obtained by the use of tell-tales or classic extensometers

(cheaper and better known instruments). Anyway, the most popular monitoring devices for CMC bolts are:

- strain gauges: mounted externally along the bar axis, they provide a measurement of the bolt strain, and thus the bolt axial force. The closer the gauges are, the more accurate the load estimate is. Electrical resistance strain (*ers*) gauges are the most common measurement system. The axial force distribution is useful to comprehend the location and extent of the loosened zones, which will in turn help the engineer design the most suitable reinforcement pattern. The two major disadvantages of strain gauges are that they are not reliable for long term applications (particularly in the field, due to the environmental conditions) and that, since they are externally installed on the bar, they interfere with the bar-grout bond;
- internal strain gauges: Mitri [Mitri2011] has recently proposed an instrumentation design which is based on the installation of a strain gauge inside a coupler by drilling a blind hole along its axis. The coupler is then fixed onto the bolt threaded length, so that monitoring of the axial load on the bar is possible (although only at the head);
- SMART bolts: the SMART (Stretch Measurement to Assess Reinforcement Tension) bolt is a classic seven strand rope in which the king wire has been replaced by a six-wire extensometer. Each wire is attached at a discrete user-specified location along the bolt, as explained in Bawden and Lausch [Bawden2000]. The other end of each wire is attached to a spring-loaded wiper that passes across a linear potentiometer in the readout head, so that as the cable stretches, the displacements at the anchor points are determined through the movement of the wiper across the potentiometer. The main asset of the SMART cable is that, since the measuring system is inside the bolt, any possible bond interference is avoided;
- CTMD: the Cable Tension Measuring Device (CTMD) has been developed at Sherbrooke University by Benmokrane and Chekired [Benmokrane1996] to instrument steel strands and rockbolts. It consists of a vibrating wire strain gauge mounted on two holding anchors fixed on the tendon using epoxy resin and spaced 12 cm. The device is protected by a mastic pad, making the measuring system reliable for long term applications. In the case of cablebolts, one of the holding anchors comprises a bearing as a rotative system to avoid the twisting effect of the cable.

It is important to notice that, to be efficient, rockbolts and cablebolts should be installed before considerable movement in the rock mass occurs. Thus, the timing of installation is a crucial aspect. The rock mass-rock reinforcement interaction concept (*cf.* [Rabcewicz1964]) is a very helpful tool to determine the most suitable timing of installation. It is well known that near the face of the excavation the stress field is high, but that the face confining action is important. In this zone, flexible reinforcement is required. However, behind the tunnel face, at a distance of 2 – 3 times the excavation diameter, the face influence is attenuated, and hence a stiffer reinforcement may be used because less movement will occur. Accordingly, DMFC or CFC rockbolts are normally used close to the face and CMC rockbolts are installed behind the front. Alternatively, with the aim of simplifying the rockbolt pattern, DMFC bolts may be installed close to the face; in this case, the rest of their length is anchored using a cementitious grout, which will set slowly as the the face moves forward. Investigations by Langille *et al.* [Langille1996] have shown the advantages of this hybrid technique, but to date this possibility has only been considered in a few cases.

### 1.3 Scientific Background

As it was stated in part 1.2.5, this research aims at a better understanding of the bolt-gout interface behaviour. The literature review proves that many authors have already been interested in this topic, and as a result a large number of experimental and theoretical investigations are available. In this section, the most significant related studies carried out in the past years are described and examined. The objective is to understand and assimilate the existing advances and to identify the lacking aspects.

It is worth noting that almost all the published research on rockbolting and cablebolting has been directed towards mining applications rather than civil engineering works, *cf.* [Stillborg1983]. The main reason is that, in general, civil engineering projects do not rely on bolting as the primary support technique. Because bolts are prominently used in the mining industry, it is not surprising that most of the research is found in the context of mining.

In the following, only static conditions are taken into account, which means that phenomena such as rockbursts, rock squeezing and earthquakes are disregarded. Moreover, only monotonic loadings are considered. Typically, the scenario under study corresponds to that shown in the left-hand side diagram in figure 1.15, where the rock block close to the excavation surface may slide or fall, should the axial load on the unplated bar exceed a critical value. The bolt length embedded on the upper rock mass, longer than the portion underneath, is supposed to remain anchored during the process (it is the load-carrying part, Freeman's *anchoring length*). It is also assumed that the bolt yield strength is not reached and that the bolt material and the surrounding media are stiffer than the interface itself; these conditions make the study of that interface easier. Taking a look at a bigger scale in this diagram, one gets the stress distribution in an infinitesimal length  $dZ$  shown in the right-hand side drawing in figure 1.15.

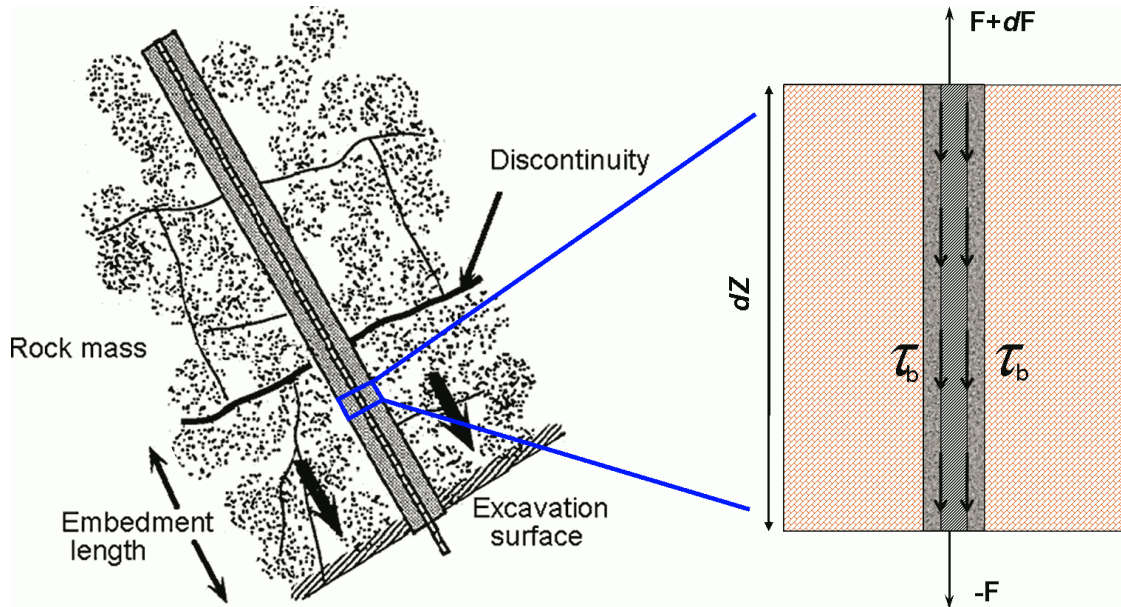


**Figure 1.15:** left: load situation under study (after Bawden *et al.* [Bawden1992]). The discontinuity at which joint displacement occurs and which defines the embedment length may be either natural or stress-induced; right: stress distribution in an infinitesimal length  $dZ$  within the *embedment length*.

As it can be inferred from the drawing, the equilibrium of the lower part reads

$$dF = 2\pi R_b \tau_b dZ \quad (1.1)$$

where  $R_b$  is the bar radius. Hereafter, either  $Z$  or  $x$  will be used to designate the bolt axis. According to equation (1.1), the shear stress  $\tau_b$  at the interface is defined as the change in the axial force  $dF$  along the embedment length  $dZ$ ; that is to say, the rate of load transfer along such length. This equation points out that the knowledge of  $\tau_b$  allows to predict the axial load on the bolt, which is an important piece of information required by the design engineer to define the reinforcement pattern. More precisely, the interface behaviour is defined along its tangential and normal directions, yielding a complete constitutive law defined by  $\tau_b(W, p_b)$  and  $\Delta u_{rb}(W, p_b)$ , where  $W$  is the axial displacement,  $p_b$  is the bolt-grout interface normal pressure and  $\Delta u_{rb}$  is the normal opening. Knowledge of this constitutive law is important because it provides access to the reinforcement anchoring capacity and the factors that influence it.

During the loading process, the interface can be described by the relationships  $\tau_b(Z)$  or  $\tau_b(W)$ , that are determinable experimentally:

- if the shear stress distribution along the interface,  $\tau_b(Z)$ , is known, integration of equation (1.1) along the embedded length leads to the axial distribution of the force,  $F(Z)$ ;
- if the local shear stress-slip relationship,  $\tau_b(W)$ , is known, differentiation of equation (1.1) taking Hooke's law into account leads to the calculation of the axial displacement distribution,  $W(Z)$ , the axial strain distribution,  $W'(Z)$  and the shear stress distribution,  $\tau_b(Z) = \frac{E_b R_b}{2} W''(Z)$ , where  $E_b$  is the bolt Young's modulus. Since the strain distribution is known, the axial load distribution,  $F(Z)$ , can be calculated.

The relationship  $\tau_b(W)$  is a material property because it takes part in the interface constitutive law. It can be found experimentally, provided the tests are carried out under accurate conditions. This subject will be discussed in chapters 2 and 3. As it will be explained later, knowledge of  $\tau_b(W)$  will lead to the determination of  $\tau_b(Z)$  and vice versa. Nonetheless, the axial distribution  $\tau_b(Z)$  is subject to change during the loading process, whereas the bond-slip relationship  $\tau_b(W)$  does not change, so that the information required to calculate the axial load throughout the loading process is comprised in a simpler expression.

Li and Stillborg, Moosavi *et al.* and Verderame *et al.* [Li1999, Moosavi2005, Verderame2009a] have proposed three main components to the shear or *bond* strength of an interface: chemical adhesion, mechanical interlock (for rebars) and friction. These components are lost sequentially as the deformation compatibility is lost along the failure interface; that is to say, as decoupling occurs. On the other hand, after the onset of slip between the bar and the grout, friction plays an important role, whence the importance of the normal pressure acting on the failure interface.

### 1.3.1 The pull-out test

To experimentally examine the anchoring capacity of rockbolts and cablebolts, pull-out tests are used, both in the laboratory and *in situ*. In the laboratory, bolts are anchored to a rock sample or alternatively to an artificial sample (made of cement or concrete) whose mechanical properties are comparable to those of a typical rock. The embedment length is the distance along which the bolt is grouted within the sample. Since the aim of a pull-out test is to study the load transfer mechanism between the bar and the surrounding media, the embedment length should be short enough to avoid failure of the bolt material. The test consists in applying a tensile axial load to the bolt at the point where it protrudes from the borehole. The far end of the bar is free; thus, the axial force at this point is equal to zero. The load and the displacement at the loaded end are recorded during the test. The

test results are normally presented as a load-displacement plot. If the bolt is instrumented along the embedment length, the axial strain and the axial stress distributions are also known. Pull-out tests can be conducted under either axial displacement control or axial load control; however, in order to investigate the interface behaviour, axial displacement control conditions are more reliable.

The widespread utilisation of laboratory pull-out tests has led to a standardization in many countries. Concerning the field execution of such tests, the ISRM outlined a suggested method for rockbolt testing, *cf.* [ISRM1973], while for cablebolts, Bawden *et al.* [Bawden1992] developed an innovative procedure to avoid the unscrewing mechanism that may distort the results (the embedment lengths tested were short, of about 250 mm). It is important not to confuse unscrewing with untwisting: under axial loads, unscrewing takes place when the embedment length is short and is due to the helical structure of the cable (similar to what happens to a nut and a screw); on the other hand, untwisting occurs when one extremity of the cable is fixed: due to the axial load, the cable elongation will bring about some straightening out of the wires. Thus in both situations the cable rotates, but in the first case the cable geometry is not modified.

In practice, laboratory tests are preferred to *in situ* tests because they are more compliant (the parameters under study can be changed with ease and more measurements can be made), generally cheaper and easier to control. Besides, the laboratory pull-out tests standardization allows for the comparison of the results obtained for different bars. Since the 1990s, sophisticated experimental benches have been developed to test the influence of a large number of parameters, such as the confining pressure, the quality of the grouting material or the thickness of the grout annulus. Nevertheless, *in situ* tests, although destructive, are very helpful to know whether the bolt and grout in use are compatible with the mechanical properties of the surrounding ground and its degree of damage. They are therefore conducted very often, but with another purpose.

The first laboratory pull-out tests were carried out on bolts cement-grouted into steel pipes; thus, under constant outer radial stiffness boundary conditions. Fuller and Cox [Fuller1975] devised the *split-pipe* test shown in the left-hand side illustration in figure 1.16. The test specimen was allowed to cure in a 50.8 mm schedule 80 steel tube and was afterwards installed in a testing machine. The bolt was pulled at a rate of 0.3 mm/s. This set-up, as shown in the figure, favours an excess of confinement in the vicinity of point A (pulling threads), and hence an uneven confinement along the embedded length. To overcome this limitation, Hyett *et al.* [Hyett1992b] conceived the set-up illustrated in the right-hand side of figure 1.16. The authors used different pipes to study the influence of the radial stiffness: aluminium, PVC and steel pipes. They also used transparent heatshrink sleeves, which provided low radial stiffness and at the same time allowed to visualize the sample during the pull-out test.

The British Standards Institution specified in [BS 7861-1, BS 7861-2] the laboratory *Double Embedment Tensile Test* (DETT), which is shown to the left in figure 1.17. In this test, the rockbolt or cablebolt is grouted into two steel tubes, internally threaded to facilitate failure at the bolt-grout interface. The tubes are butted together and pulled apart in a tensile testing machine. Embedment lengths of 250 mm and 900 mm are respectively recommended for rockbolts and cablebolts. Besides, when testing cables, relative rotation of the tubes is prevented using a pin and hole arrangement at the mating surfaces of these tubes. This test is used to measure the yield bond strength (load at which the slope of the load-displacement curve falls below 20 kN/mm) and the system stiffness (slope of the load-displacement curve over a specified load range, in general between one third and two thirds of the yield bond strength).

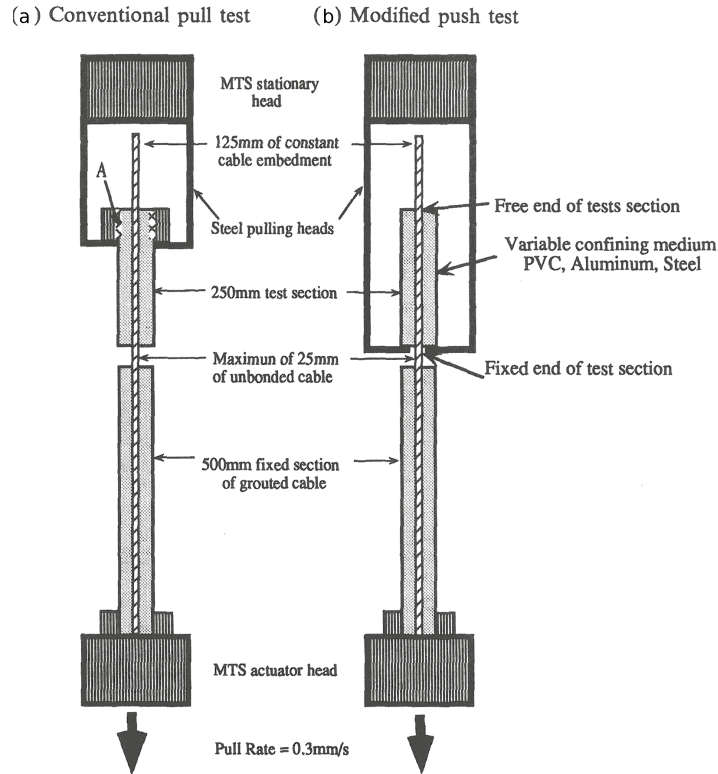


**Figure 1.16:** (a): the split-pipe pull-out test set-up proposed by Fuller and Cox [Fuller1975]; (b): modified set-up proposed by Hyett *et al.* [Hyett1992b]. In this set-up, a force may be applied to both the pipe and the grout next to the *fixed end of test section*. This fact ought to be accounted for when analyzing the initial stiffness of the test results.

The idea of conducting pull-out tests using confining cells was introduced in the 1990s. The use of such cells allows to execute tests under constant radial stiffness conditions and also under constant confining pressure conditions. Moreover, the use of confining cells permits to measure the radial pressure and displacement during the test, that provide valuable information about the bond failure mechanism.

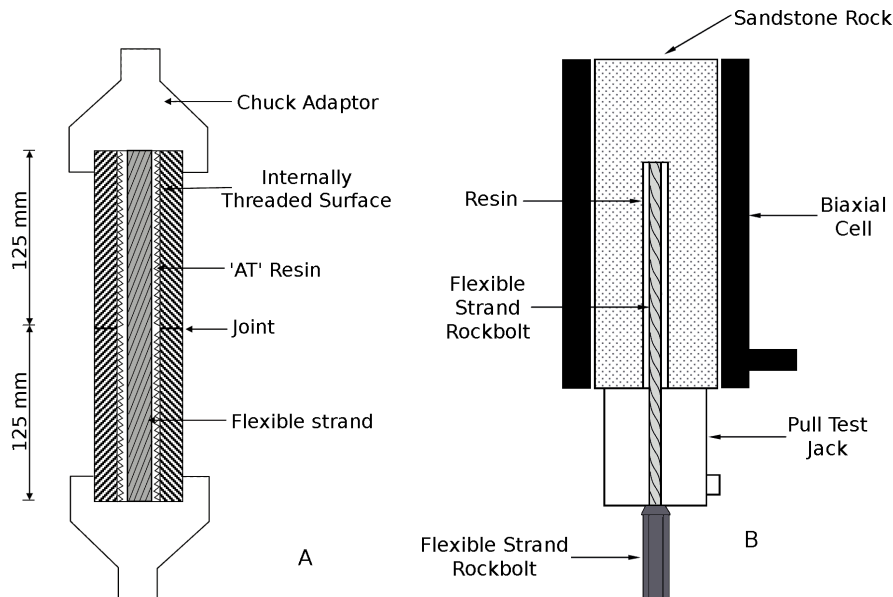


**Figure 1.17:** A: double embedment tensile test; B: short encapsulation pull test (adapted from the British HSE [Reynolds2006]).

In this context, a revision of the British standards [BS 7861-1, BS 7861-2] has considered that the DETT described above is inadequate to study the load transfer mechanism mobilized *in situ*. Instead, the *Laboratory Short Encapsulation Pull Test* (LSEPT) has been introduced. This test simulates the field scenario more accurately because it takes into account not only the grout and the bolt, but also the rock mass. In fact, a test specimen comprises a cylindrical rock sample which is drilled along its axis to grout a rockbolt or cablebolt. Bond failure may take place at the rock-grout interface in this test. To simulate the field conditions, the rock sample is installed inside a biaxial cell during the drilling and the rifling processes and also during the test, so that a confining pressure can be applied at the outside of the rock core sample. A radial pressure of 10 MPa is advised because it is thought to be representative of the stress field in regular coal longwall mining operations in the UK. A schematic diagram is shown in the right-hand side of figure 1.17. In the case of rockbolts, an embedment length of 160 mm is recommended; nevertheless, since for a given diameter the tensile strength of a cablebolt is higher than that of a rockbolt, a greater length is needed to explore the bond capacity of the former: 450 mm for resin-grouted cablebolts and 325 mm for cement-grouted cablebolts.

Similarly, a pull-out test facility in which a biaxial cell is used to provide radial confinement has been designed at the University of New South Wales in Australia. The majority of the tests have been conducted under a confinement of 10 MPa. A 200 mm long and 145 mm diameter cement cylinder has been used to simulate the rock mass. The borehole diameter is 26 mm and the encapsulation length varies between 150 and 175 mm. Different types of rockbolts of same nominal diameter have been tested (helical and ringed profiles) and in some tests strain gauges have been mounted along the bars. Hagan [Hagan2004] has analyzed some of the results. Further details are given in the following subsection.

### 1.3.2 Analytical and experimental studies

According to the literature, the proper design practice of rockbolts and cablebolts became a matter of concern in the late 1960s and especially in the 1970s. At the beginning, the decoupling of the interface was not considered (*i.e.*, the deformation was assumed to be compatible across that interface) and it was also supposed that the shear stress was evenly distributed along the embedment length. Consequently, from equation (1.1) and using data derived from pull-out tests, the bond strength could be determined. Such bond strength, together with the bolt maximum acceptable load, would be later used to define the required bolt length,  $L$ , as well as the bolts spatial distribution. As one could remark, this approach is very conservative, but safe. In the cases where no experimental data were available, the ultimate bond strength was taken as 10 % of the rock mass uniaxial compressive strength,  $UCS_r$ , yielding the design equation

$$F = 2\pi R_b (0.1 \cdot UCS_r) L \quad (1.2)$$

Still today, Standards such as the *BSI* or the *AFNOR* assume for design purposes that the interfacial shear stress  $\tau_b$  is uniformly distributed along the anchored length. Such a safe hypothesis is primarily justified by a lack of complete understanding of the mechanisms of bond failure. However, due to the different research works conducted in the past years and presented below, many limitations have already been overcome.

Farmer [Farmer1975] carried out one of the first investigations concerning the stress distribution along a grouted rock anchor and put especial emphasis on the importance of such distribution in the derivation of design data. In his theoretical approach, he considered an elastic steel rod of radius  $a$

and Young's modulus  $E_a$  grouted into a rigid rock using a resin grout of shear modulus  $G_g$ . The bolt was subjected to a tensile stress  $\sigma_0$ . In order to solve equation (1.1) (combined with Hooke's law), he considered two possible cases:

- the grout annulus is thin, and therefore the shear stress at the steel-resin interface is representative of the shear stress in the annulus:

$$\tau_x = G_g \frac{\xi_x}{R - a} \quad (1.3)$$

where  $\xi_x = W$  is the bar extension and  $R$  the borehole radius;

- the annulus is thicker, and therefore the shear stress at the interface is affected by radial changes in the shear stress within the annulus:

$$\tau_x = G_g \frac{\xi_x}{a \ln(R/a)} \quad (1.4)$$

In both cases, the boundary conditions are:  $\sigma_x = \sigma_0$  at  $x = 0$  and  $\sigma_x = 0$  at  $x = L$ . Under these circumstances, the solution of the second-order differential equation reads

$$\xi_x = \frac{\sigma_0}{E_a \alpha} \frac{\cosh(\alpha[L - x])}{\sinh(\alpha L)} \quad (1.5)$$

and hence

$$\tau_x = \frac{\sigma_0 a \alpha}{2} \frac{\cosh(\alpha[L - x])}{\sinh(\alpha L)} \quad (1.6)$$

where

$$\alpha^2 = \frac{2G_g}{E_a a (R - a)} \quad (1.7)$$

or

$$\alpha^2 = \frac{2G_g}{E_a a^2 \ln(R/a)} \quad (1.8)$$

for the two possible cases defined above, respectively. As stated by Farmer [Farmer1975], for most anchorages  $L$  and  $\alpha$  verify the condition  $L \gg 1/\alpha$ , which leads to an exponential decay of  $\xi_x$  and  $\tau_x$  along the anchored length. This means that the load on the bolt is effectively dissipated over a certain length that extends from the point where the load was applied ( $x = 0$ ). This length, called *transfer length*, is equivalent to the optimum design length for the anchorage. As defined by Farmer [Farmer1975], it corresponds to the length at which  $\xi_x$  and  $\tau_x$  are reduced to 1 % of their magnitude at  $x = 0$ . The exponential decay of  $\tau_x$  is shown in figure 1.18 for  $\alpha = 0.2/a$ .

In order to validate these theoretical predictions, laboratory pull-out tests were carried out on instrumented 20 mm diameter steel bars resin-grouted in different materials (concrete, limestone and chalk). The experimental measurements proved to be in quite good agreement with the analytical predictions for low axial loads; nevertheless, for high axial loads (greater than 60 kN) the exponential decay of  $\xi_x$  and  $\tau_x$  only took place along part of the embedded length due to the decoupling process along the other part, close to the point where the load is applied ( $x = 0$ ). This can be seen in figure 1.19, in which the load-displacement curve and the strain and shear stress distributions obtained for a bar anchored 350 mm in concrete are displayed. The shear stress has been calculated from the strain data using

$$\tau_x \simeq \frac{E_a a (W'(x_i) - W'(x_{i-1}))}{2(x_i - x_{i-1})} \quad (1.9)$$

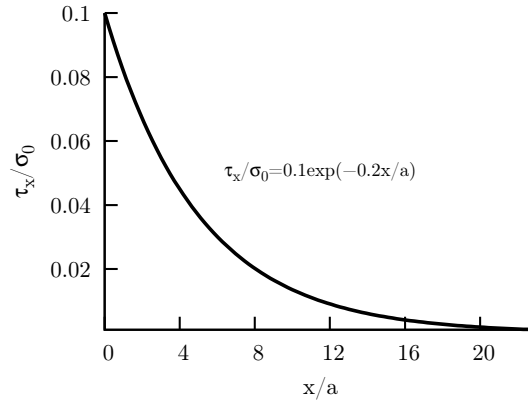


**Figure 1.18:** theoretical stress distribution along a resin grouted anchor in a rigid socket, having a thin resin annulus (after Farmer [Farmer1975]).

As a whole, Farmer's investigation is significant because he contemplated a nonuniform stress distribution along the anchorage length, but he failed to account for the decoupling mechanism because he simplified the behaviour of the interface (equations (1.3) and (1.4) only apply when the interface is coupled). At the same time, he assumed that the rock is very stiff with respect to the grouting material ( $E_r/E_g \geq 10$ ).

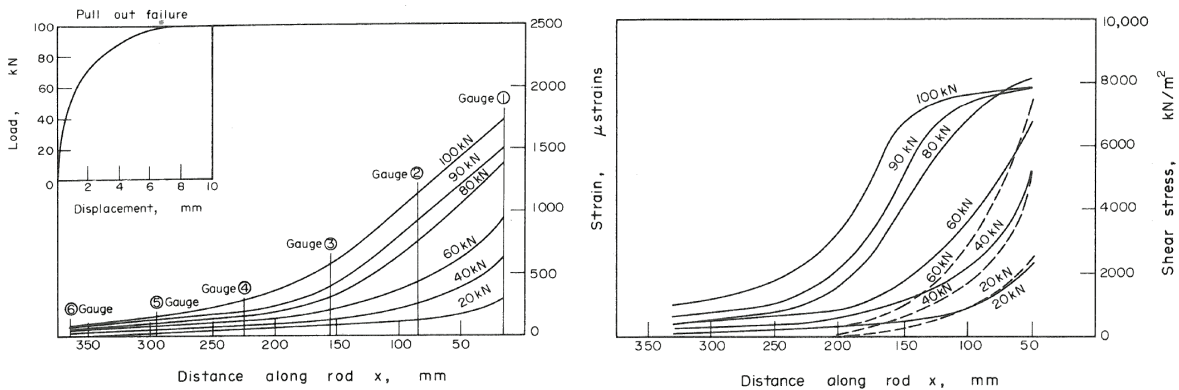


**Figure 1.19:** experimental and predicted strain and stress distributions along a fully grouted steel bar during a pull-out test, after Farmer [Farmer1975]. The load-displacement curve is displayed in the upper left corner. The graphs correspond to a bar anchored 350 mm in a concrete sample. As it can be seen, for loads greater than 60 kN the exponential decay only occurs along part of the embedded length.

Short later, Dunham [Dunham1976] conducted pull-out tests on 25 mm diameter ribbed steel bars resin-grouted in 36 mm diameter holes drilled in a sandstone block. In order to monitor the strain distribution along the bar, he installed *ers* gauges at different points and back-calculated the shear stress from the strain measurements using equation (1.9). He used two embedment lengths: 300 and 750 mm. The results are presented in figures 1.20a ( $L = 750$  mm) and 1.20b ( $L = 300$  mm). It can be seen that, for low loads, the shear stress distribution follows an exponential decay (*i.e.*, the interface is totally coupled), which also confirms Farmer's theoretical approach (the differences between theory and experiments can be explained by the assumption  $E_r/E_g \geq 10$  not being valid [Li and Stillborg [Li1999] improved this limitation by relaxing the hypothesis of a rigid rock mass, see page 38]). However, for high loads decoupling progressively occurs and as a result the shape of the stress distribution varies along  $L$ . This is more obvious for  $L = 300$  mm because decoupling is more likely to occur for short embedment lengths.

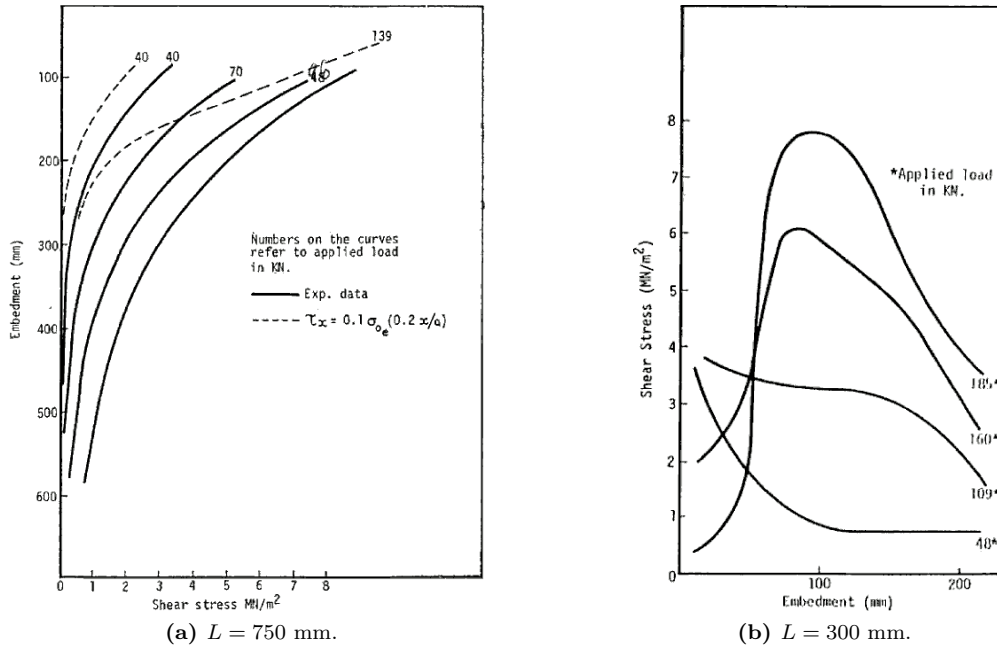


**Figure 1.20:** experimental and predicted shear stress distributions along fully grouted steel rebars during pull-out tests, after Dunham [Dunham1976].

An axisymmetric FEM analysis of a bonded cablebolt subjected to a pull-out test carried out by Fuller and Cox [Fuller1975] also indicated an exponential decay of the load along the tendon. Further experimental evidence of the non-linear distribution of the axial force was provided by Signer [Signer1990].

Benmokrane *et al.* [Benmokrane1995] proposed a tri-linear bond-slip model  $\tau_b(W)$  for the interfacial mechanism between the bolt and the grout. The model consists of three stages:

- I: the ascending branch corresponds to the elastic behaviour of the interface and is characterized by a linear relationship between the shear stress and the shear slip. The peak value represents the interface shear strength;
- II: the descending branch corresponds to the decoupling process of the interface as the shear slip increases. As it can be seen, the interface strength decreases linearly with the shear slip;
- III: the horizontal plateau accounts for the residual resistance that remains due to friction.

This bond slip-model, shown in figure 1.21, can be mathematically expressed

$$\tau_b(W) = \begin{cases} \frac{\tau_1}{\delta_1} W & \text{for } 0 \leq W \leq \delta_1 \\ \frac{\tau_1 - \tau_2}{\delta_1 - \delta_2} W + \frac{\tau_2 \delta_1 - \tau_1 \delta_2}{\delta_1 - \delta_2} & \text{for } \delta_1 \leq W \leq \delta_2 \\ \tau_2 & \text{for } W \geq \delta_2 \end{cases} \quad (1.10)$$

This shape is based upon laboratory pull-out test results on both rockbolts and cablebolts. A short and constant embedment length was used to ensure a uniform distribution of the shear stress along the grout-tendon interface. The value  $L = 8R_b$  was utilized. Under these conditions, the shear stress can be calculated using

$$\tau_b(W) = \frac{F(W)}{2\pi R_b L} \quad (1.11)$$

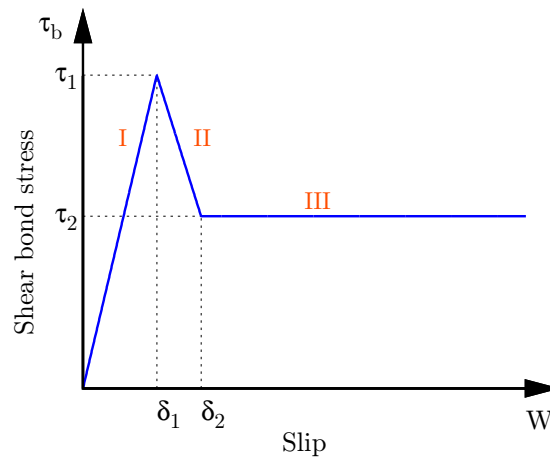


**Figure 1.21:** idealized bond-slip model (after Benmokrane *et al.* [Benmokrane1995]).

The model parameters, namely  $\tau_1$ ,  $\tau_2$ ,  $\delta_1$  and  $\delta_2$  (and the associated slopes  $m_1 = \tau_1/\delta_1$  and  $m_2 = (\tau_1 - \tau_2)/(\delta_1 - \delta_2)$ ) are derived from pull-out test results (in Farmer's approach, only the radii and the bolt and grout elastic properties are taken into account, because the interface is assumed to be coupled). A typical specimen prepared to be tested is indicated as *Model B* in figure 1.22. Concrete cylinders ( $E=30$  GPa and  $UCS=60$  MPa) were used to reproduce the host rock. The bolts were grouted by means of cement-based grouts ( $w : c = \{0.45, 0.6\}$ ). Benmokrane *et al.* [Benmokrane1995] also conducted pull-out tests using the specimen arrangement displayed as *Model A* in figure 1.22, characterized by a decreasing embedment length. The aim was to investigate the pull-out strength as a function of both the grout quality and the ratio anchored length-bar radius (the anchored length verified  $L \in [14R_b, 40R_b]$ ). The results show that the maximum pull-out force increases almost linearly with that ratio and that the pull-out capacity is related positively to the grout compressive strength.

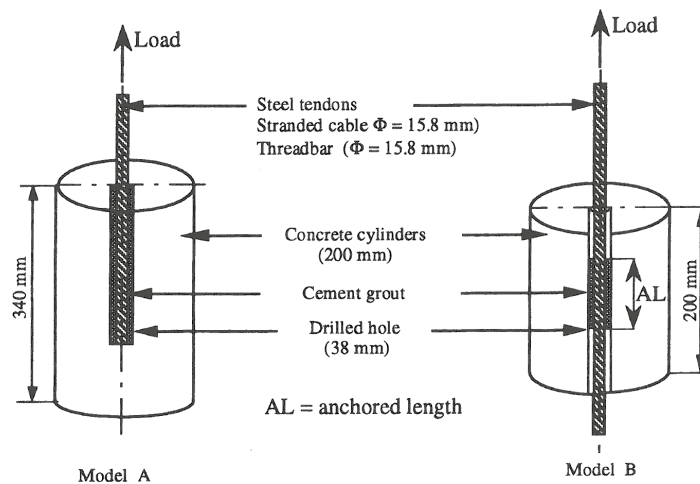


**Figure 1.22:** prepared specimens to carry out pull-out tests (after Benmokrane *et al.* [Benmokrane1995]).

Figure 1.23 shows the results of several pull-out tests conducted on 15.8 mm diameter rockbolts (200 kN Dywidag threadbars) and cablebolts (270 kN standard strands) using the *Model A* set-up displayed in figure 1.22. The load levels attained for cablebolts are due to the unscrewing phenomenon,

previously highlighted by Bawden *et al.* [Bawden1992]: as the cable is pulled, it is energetically easier for it to unscrew itself from the grout column than to slip axially, shearing the grout between the wires in the process. Thus, the two bolt types behave differently in terms of the load transfer mechanism. Moreover, it seems that unscrewing leads to low values of axial load and shear stress; additionally, Benmokrane *et al.* [Benmokrane1995] state that the mechanical interlock is lower for cablebolts than for rebars.

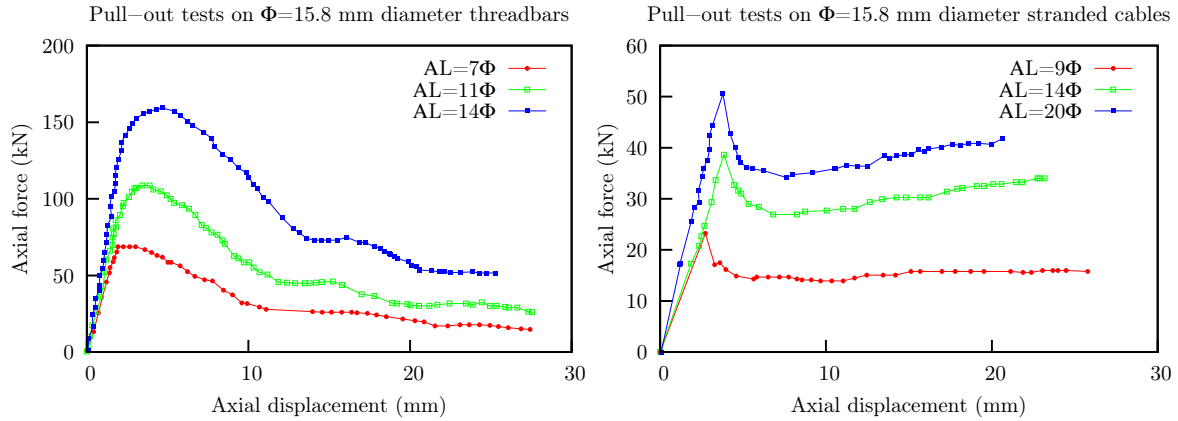


**Figure 1.23:** pull-out test results conducted by Benmokrane *et al.* [Benmokrane1995] on Dywidag threadbars and on seven-wire strands.

Li and Stillborg [Li1999] introduced the term *decoupling front* to designate the boundary between the decoupled and coupled parts of the embedment length. The shear stress is at the level of the shear strength at the decoupling front. Such front moves from the loading point (when the applied force is large enough) towards the bolt far end gradually as the load increases.

These authors also proposed three analytical models for the shear stress distribution along the embedded length,  $\tau_b(Z)$ , that apply for CMC and CFC rockbolts: one for the pull-out test configuration, one for rockbolts installed in uniformly deformed rock masses and one for bolts subjected to rock joint opening. In the first case, the proposed model for CMC bolts was based on pull-out test results conducted on instrumented bars. The experimental data are shown in the left-hand side graph in figure 1.24 and the inferred model is shown in the right-hand side graph in the figure. The integration of equation (1.1) taking into account the shear stress in each length  $x_i - x_{i-1}$  (or equivalently  $Z_i - Z_{i-1}$ ) makes the calculation of the axial force  $F(Z)$  possible.

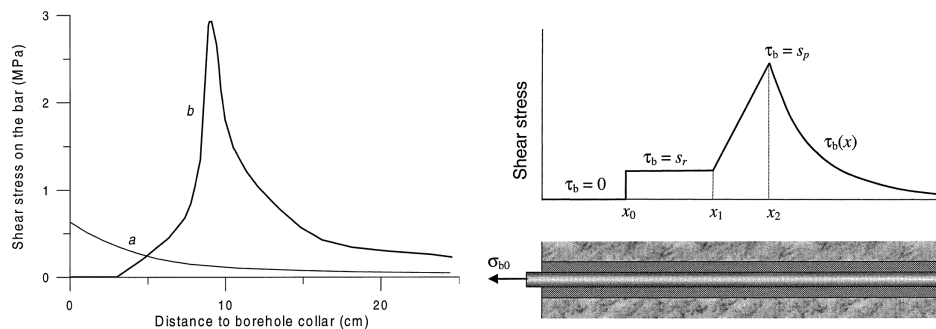


**Figure 1.24:** experimental and theoretical shear stress distribution along a CMC rockbolt in a typical pull-out test configuration (after Li and Stillborg [Li1999]). In the left figure, curve *a* corresponds to a coupled interface and in curve *b* the interface is partially decoupled (the *decoupling front* is approx. at 10 cm). In the right figure,  $x$  stands for  $Z$  in equation (1.1).

With respect to the approach proposed by Farmer [Farmer1975], where the interface behaviour before decoupling occurs was inferred from the grout annulus elastic properties, in this case both the grout and rock mass elastic properties are taken into account; accordingly, when the interface is totally coupled (*i.e.*, when  $x_2 = 0$  in figure 1.24), the shear stress is calculated using

$$\tau_b(x) = \frac{\alpha}{2} \sigma_{b0} \exp^{-2\alpha x/d_b} \quad (1.12)$$

where

$$\alpha^2 = \frac{2G_r G_g}{E_b [G_r \ln(d_g/d_b) + G_g \ln(d_0/d_g)]} \quad (1.13)$$

and  $\sigma_{b0}$  is the axial stress on the bolt at the loading point,  $d_b$  is the bolt diameter,  $d_g$  is that of the borehole,  $d_0 \approx 10d_g$  is the diameter of a circle in the rock mass outside which the influence of the bolt disappears,  $G_r$  is the rock shear modulus and  $G_g$  is that of the grout.

The shear stress in the other sections shown in the right-hand side graph in figure 1.24 can be easily obtained. The major advantage of using an approach based on a model  $\tau_b(Z)$  is that the shear stress distribution along the bolt (thus, the coupled -or *resistant*- and decoupled parts) is known. But, such distribution changes with the axial stress  $\sigma_{b0}$ . On the other hand, an approach based on  $\tau_b(Z)$  cannot be implemented in numerical modelling software and furthermore it does not provide direct access to the interface shear stiffness. As one could remark, an approach based on  $\tau_b(W)$  does provide the interface shear stiffness.

Recently, Ren *et al.* [Ren2010] have proposed a closed-form solution to predict the full-range mechanical behaviour of grouted rockbolts under tensile loads. Analytical expressions for the theoretical load-displacement relationship obtained in a pull-out test, as well as for the distribution along the embedment length of the axial stress, the shear stress and the shear slip are provided. A tri-linear bond-slip model similar to that proposed by Benmokrane *et al.* [Benmokrane1995] (see figure 1.21) has been considered for the rockbolt-grout interface. Assuming that the bolt remains within the elastic range during the whole loading process and that the shear slip at the interface equals the rockbolt axial displacement, the equilibrium equation (1.1) is solved in its differential form. To do so, five different stages are considered for the shear stress distribution as the load is applied to the bolt:

- elastic stage: for low axial loads, the interface remains in the elastic range (*i.e.*, there is no softening or debonding). The whole embedment length behaves according to branch I in figure 1.21;
- elastic-softening stage: as the axial load increases, the shear stress will reach its maximum  $\tau_1$  at the loaded end  $Z = L$  when the shear slip at this point equals  $\delta_1$ . Softening of the interface starts at this point and propagates towards the free end  $Z = 0$  for greater values of slip. The softening part length is denoted by  $a$ . This leads to two zones along the interface: for  $0 \leq Z \leq L - a$  the interface behaves elastically (branch I in figure 1.21) whereas in  $L - a \leq Z \leq L$  the shear stress is in the softening state (branch II);
- elastic-softening-debonding stage: when the shear slip at the loaded end reaches  $\delta_2$ , the shear stress at that point equals  $\tau_2$ . Debonding of the interface starts for  $W > \delta_2$  at the loaded end and the debonded part length is  $d$ . Thus, the interface is now divided in three regions: in  $0 \leq Z \leq L - d - a$  the interface is elastic (branch I); in  $L - d - a \leq Z \leq L - d$  the interface is within the softening state (branch II) and in  $L - d \leq Z \leq L$  the interface is debonded (branch III);
- softening-debonding stage: when the shear slip at the free end reaches  $\delta_1$ , the shear stress verifies

$\tau_b(Z=0) = \tau_1$ . The elastic region disappears. The embedded length is in the softening state for  $0 \leq Z \leq a$  and totally decoupled or debonded in  $a \leq Z \leq L$ ;

- debonding stage: when the shear slip at the free end reaches  $\delta_2$ , the shear stress verifies  $\tau_b(Z=0) = \tau_2$ . The softening region disappears. The interface is totally decoupled or debonded and the axial load on the bolt is due to the non-zero residual shear strength  $\tau_2$ , attributable to friction.

The closed-form solutions are developed assuming that the embedment length is constant during the pulling process. Moreover, it should be noticed that Ren *et al.* [Ren2010] assume that the softening length is constant during the elastic-softening-debonding stage; as it will be seen in chapter 2, this is not necessarily true. The boundary conditions used are related to both extremities of the bolt: at the free end,  $F(Z=0) = 0$  and at the loaded end, the load on the bolt is the applied load,  $F(Z=L) = P$ . Furthermore, in the stages where two or more states co-exist along the interface, continuity of the magnitudes is imposed at the borders. Input data are:  $R_b$ ,  $L$ ,  $E_b$ ,  $\tau_1$ ,  $\tau_2$ ,  $\delta_1$  and  $\delta_2$ . Thus, the bond-slip model parameters should be known in advance. These parameters can be practically obtained from pull-out test results.

The three first stages described above are plotted as solid lines in figure 1.25. Data used are:  $R_b = 16$  mm,  $L = 1$  m,  $E_b = 210$  GPa,  $\tau_1 = 8.10$  MPa,  $\tau_2 = 0.73$  MPa,  $\delta_1 = 0.19$  mm and  $\delta_2 = 0.53$  mm. With respect to the analytical model proposed by Li and Stillborg [Li1999] and displayed in figure 1.24, it can be seen that in this case the shear stress does not decrease linearly in the softening state. The data  $R_b$ ,  $L$  and  $E_b$  above correspond to an *in situ* pull-out test conducted by Rong *et al.* [Rong2004] on an instrumented grouted rockbolt. The comparison between the theoretical shear stress distribution proposed by Ren *et al.* [Ren2010] and the experimental shear stress distribution obtained using equation (1.9) is shown in the figure. As it can be seen, the agreement is quite satisfactory. The bond-slip parameters  $\tau_1$ ,  $\tau_2$ ,  $\delta_1$  and  $\delta_2$  have been calibrated by Ren *et al.* [Ren2010] as explained below.

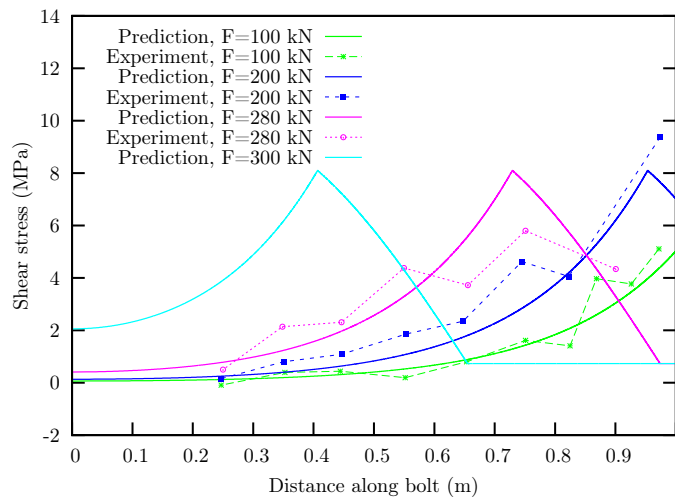


**Figure 1.25:** theoretical and experimental evolution of the interfacial shear stress along the embedment length of a grouted rockbolt (after Ren *et al.* [Ren2010]). The experimental shear stress distribution, deduced using equation (1.9), is represented by the dashed lines (experimental data for F=300 kN is not available).

In order to validate their approach, Ren *et al.* [Ren2010] compared their load-displacement prediction with *in situ* experimental data issued from pull-out tests (conducted by Rong *et al.* and Chen

and Ren [Rong2004, Chen2008]) and the results were in quite good agreement, see figure 1.26. The bond-slip parameters  $\tau_1$  and  $\tau_2$  needed to predict the load-displacement curves were calibrated using their analytical solution; that is to say, only the shear slips  $\delta_1$  and  $\delta_2$  were derived directly from the experimental data.

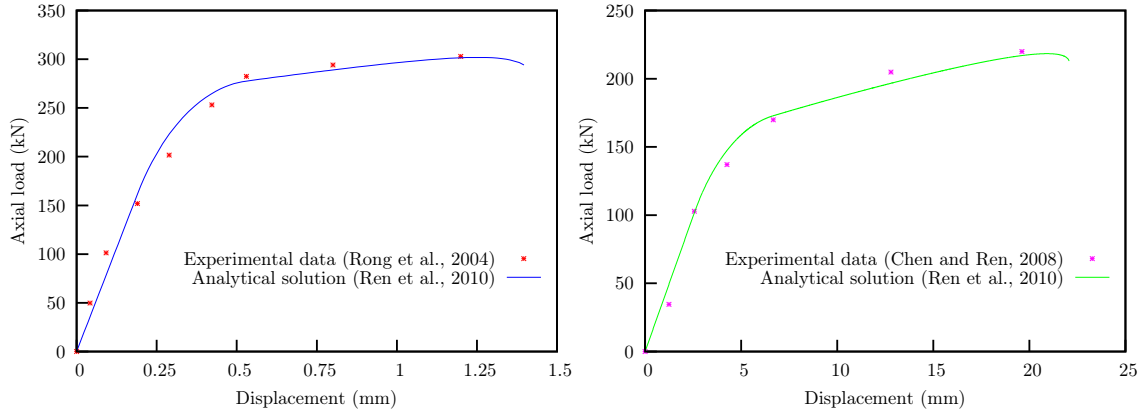


**Figure 1.26:** comparisons between experimental data (Rong *et al.*, Chen and Ren [Rong2004, Chen2008]) and predicted load-displacement curves provided by the approach proposed by Ren *et al.* [Ren2010].

In the 1990s, Yazici and Kaiser [Yazici1992] presented a theory to ascertain the bond strength of fully grouted cablebolts: the Bond Strength Model, hereafter *BSM*. By that time, experience all over the world had confirmed that the mechanisms of slip-based failure of grouted rockbolts and cablebolts are not the same and that as a result the two reinforcement techniques should be studied separately. The experimental results obtained by Benmokrane *et al.* [Benmokrane1995] and shown in figure 1.23 clearly reveal significant differences between the pull-out response of grouted rockbolts and cablebolts. More evidence has been discussed by other authors such as Hyett *et al.* and Moosavi *et al.* [Hyett1995, Moosavi2005] and is presented later in this subsection.

The *BSM* is a conceptual model to explain the bond strength development in grouted cablebolts. It deals only with the ultimate capacity and not with the complete loading process. The model states that the bond strength is mainly frictional; consequently, it depends strongly on the lateral pressure at the bolt-grout interface. Among other factors, such pressure is dependent on the lateral displacement or *dilation* that is created at the bolt-grout interface as the cable is pulled. Dilation is caused by the rough profile of the cable, so that a smooth bar would have no dilation at all.

There are four main components in the *BSM*: the axial and lateral displacements,  $u_{ax}$  and  $u_{lat}$  respectively, the bond strength  $\tau$  and the normal pressure at the bolt-grout interface,  $p_1$ . These interrelated components define four quadrants, as shown in figure 1.27. In the first quadrant, the bond strength is plotted as a function of the axial displacement. This quadrant is derived from the load-displacement curve obtained in a pull-out test, provided a uniform distribution of the shear stress along the embedment length is assumed (in this context, short lengths should be used). In the second quadrant the bond strength is related to the interface normal pressure. Such relationship can be the classic linear criterion in equation (1.14) (since failure is considered to be a fully frictional phenomenon, the cohesion is zero), or, alternatively, it can take into account an increase in the bond strength due to the dilation created in the case of rough bolts, like in equation (1.15). In these equations,  $\varphi$  is the friction angle between the bolt and the grout.

$$\tau = p_1 \tan \varphi \quad (1.14)$$

$$\tau = p_1 \tan (\varphi + i) \quad (1.15)$$

The dilation angle  $i$  is in general thought to decrease from the geometrical angle of the asperities,  $i_0$ , to zero as the interface pressure increases (several relationships are available, inspired from the shear behaviour of rock joints).

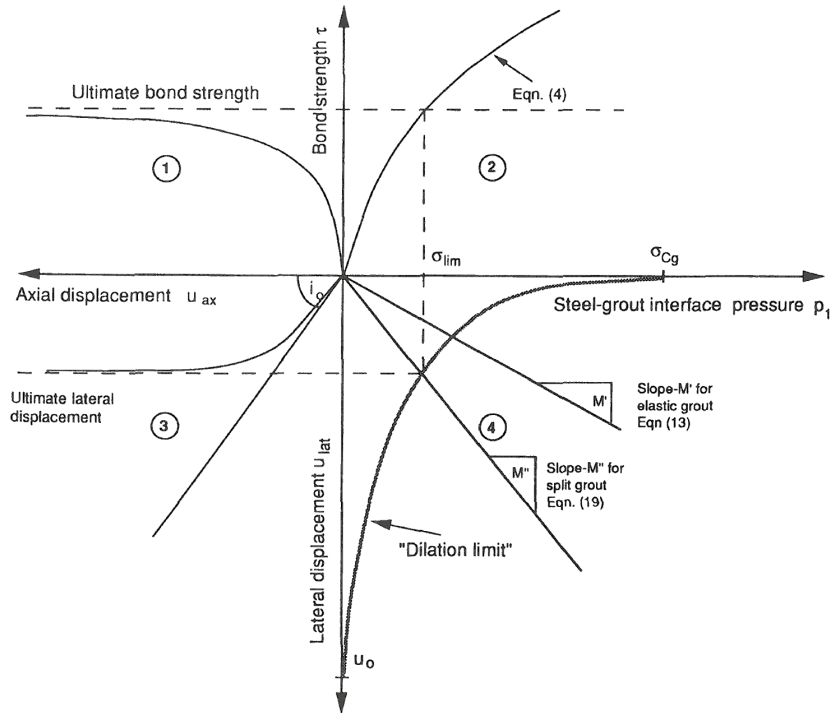


**Figure 1.27:** the Bond Strength Model (after Yazici and Kaiser [Yazici1992]).

In the third quadrant, Yazici and Kaiser [Yazici1992] relate the axial and lateral displacements. The relationship reads

$$u_{lat} = u_{ax} \tan i \quad (1.16)$$

In the fourth quadrant, the pressure and the lateral displacement at the bolt-grout interface are related. The behaviour of the grout annulus is examined first. Three cases are considered depending on its state as observed after pull-out tests held at constant outer radial stiffness conditions: elastic, fully or partially fractured in the radial direction (radial cracks appear at the bolt-grout interface and start propagating towards the borehole wall when the hoop stress at that interface reaches the grout tensile strength). In the first two cases, the relationship between  $p_1$  and  $u_{lat}$  is linear and the slopes  $M'$  and  $M''$  in figure 1.27 only depend on the grout and confining medium elastic properties and on the borehole geometry. While the cracks propagate through the annulus, the relationship between  $p_1$  and  $u_{lat}$ , given by  $M'''$ , is non-linear (this case is not represented in the graph, but the slope  $M'''$  lies between  $M'$  and  $M''$ ).

To relate the behaviour of the grout annulus to that of the interface, the *dilation limit*,  $u_{lim}$ , is introduced. It accounts for the following:

- a decrease in the radial dilation when the pressure  $p_1$  acting on the interface is high (contrary to what happens in the annulus);
- if the interfacial pressure  $p_1$  reaches the grout compressive strength,  $UCS_g$ , the annulus breaks under radial compression and dilation is suppressed;
- when the surrounding rock is soft,  $p_1$  is low and the maximum lateral displacement is equal to the height of the asperities,  $u_0$ .

The empirically-chosen model for the dilation limit of fully grouted seven-wire strands reads

$$u_{lim} = u_0 \left( 1 - \frac{p_1}{UCS_g} \right)^{B/UCS_g} \quad (1.17)$$

The parameters  $u_0$  and  $B$  are calibrated by curve-fitting pull-out test data using quadrants 1, 2 and 4 in figure 1.27.

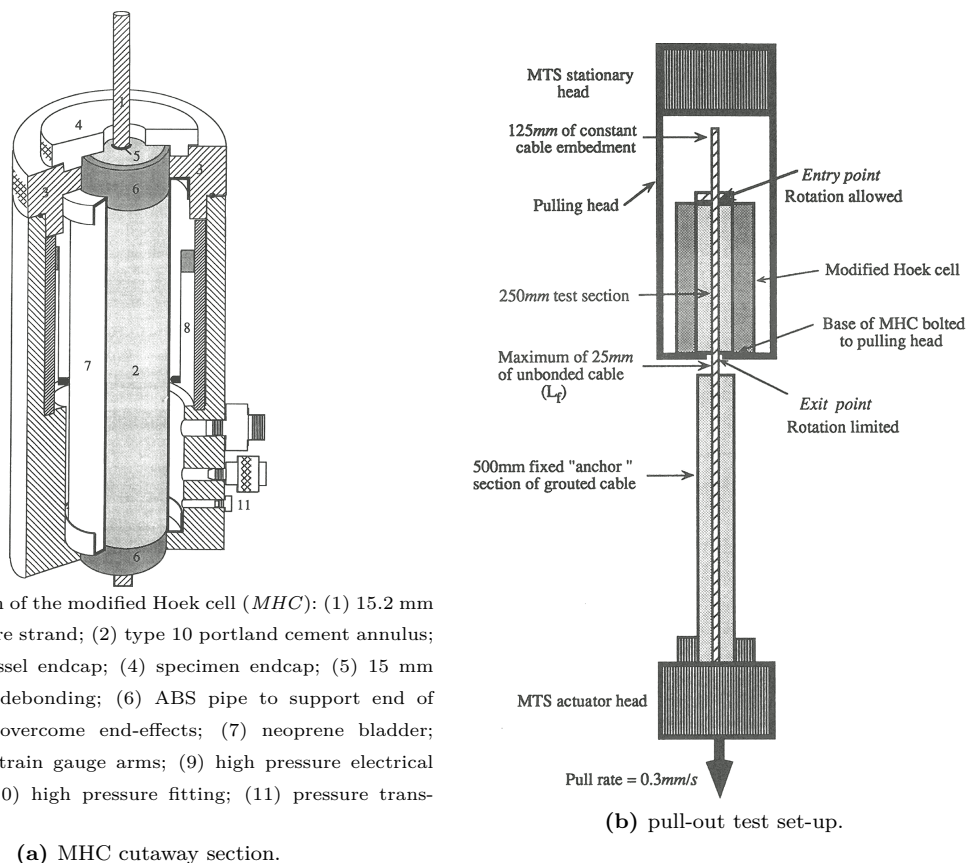
Yazici and Kaiser [Yazici1992] also carried out a parametric study within the *BSM* and concluded that the bond strength increases with the rock-to-grout stiffness ratio, the grout strength and the interface friction coefficient. On the other hand, it decreases with the borehole diameter.

As a whole, the *BSM* is important because it proposes a basis to understand the bond failure of grouted cables (and hence part of the result of a pull-out test) from the problem geometry, the grout and rock mass properties and equations (1.17) and (1.14) (or (1.15)). However, this model is limited to the ultimate bond strength. At the same time, it does not consider the rotation phenomenon and the relationship between the axial and lateral displacements at the interface (quadrant 3 in figure 1.27) is not properly described. Furthermore, the procedure to determine the *dilation limit* is largely empirical.

Some time later, Hyett *et al.* [Hyett1995] proposed a constitutive law for the bond failure of grouted cablebolts. To date, this work is considered as a reference within the related research community. The new law defines the frictional-dilational behaviour of the cable-grout interface. From this law, the authors developed a model to reproduce pull-out tests held using different boundary conditions. The model is able to take into account the rotation of the cable, so that three failure modes coexist along the embedment length: dilational slip, shear of the cement imprints (bolt-grout interface) and rotation. As one may expect, dilational slip and shear are the principal failure mechanisms in the length where rotation is avoided.

To gain more insight into cablebolts bond failure, Hyett *et al.* [Hyett1995] also carried out a series of laboratory pull-out tests. These tests were conducted using a Modified Hoek Cell, *MHC*, which allows to study the effect of the confining pressure on the bond capacity. The *MHC* has become a laboratory standard. A cutaway section is shown in figure 1.28a. Classic 15.2 mm diameter seven-wire strands with a tensile strength of 250 kN and embedded along a constant length of  $L = 250$  mm were tested. This length had been previously used successfully by other researchers, *cf.* [Fuller1975, Stillborg1984] for instance. Each specimen consisted of a cable grouted into two cylindrical pipes using a cement paste: the first pipe, made of PVC, was 250 mm long and served only as a mould during the curing time of the grout. It was removed before the test. The second pipe, made of steel and 500 mm long, was used not only as a mould but also to anchor the test specimen during the pull-out test as shown in figure 1.28b. Hence, the real *test section* is the 250 mm part, to be installed inside the *MHC* as indicated in the figure. The outer radius of the grout cylinder was chosen to represent a borehole in a real situation:  $r_2 \approx 24$  mm. Thus, the rock mass is not represented in these tests. The influence of the grouting material was analyzed using three different qualities:  $w : c = 0.3, 0.4, 0.5$ . Three or four confining pressures were tested for each grout: 1, 2-3, 5, 10 and 15 MPa, which were thought to

be representative of those at the borehole wall *in situ* during regular underground operations. All the tests were repeated four times on average to identify any possible scatter in the results. Accordingly, about 50 pull-out tests were conducted to define the new law. The axial load  $F_{ax}$ , confining pressure  $p_2$ , axial displacement  $u_{ax}$  and radial displacement  $u_{r2}$  were monitored<sup>1</sup>. The tests were carried out in a MTS testing frame under axial displacement control conditions and at a rate of 0.3 mm/s, used earlier by Fuller and Cox [Fuller1975]. The confining pressure was maintained constant during each test. The radial displacement was measured at the outside of the neoprene bladder by means of two sets of diametrically opposed cantilever strain gauge arms placed at the midpoint of the test section, see figure 1.28a. The axial force was measured by the testing machine. For all this, the control or independent variables are the axial displacement and the confining pressure, while the measured or dependent variables are the axial force and the radial displacement. It should be noticed that, within the context of the constitutive law, the radial displacement and radial pressure that are significant are that occurring at the cable-grout interface,  $u_{r1}$  and  $p_1$  respectively; nonetheless, it is not possible to monitor these variables.



Cutaway section of the modified Hoek cell (MHC): (1) 15.2 mm (0.6") seven-wire strand; (2) type 10 portland cement annulus; (3) pressure vessel endcap; (4) specimen endcap; (5) 15 mm PVC tube for debonding; (6) ABS pipe to support end of specimen and overcome end-effects; (7) neoprene bladder; (8) cantilever strain gauge arms; (9) high pressure electrical feedthrough; (10) high pressure fitting; (11) pressure transducer.

(a) MHC cutaway section.

(b) pull-out test set-up.

**Figure 1.28:** Experimental configuration used by Hyett *et al.* [Hyett1995].

At the *exit point* displayed in figure 1.28b, the cell was bolted to the pulling head, so that rotation of the cell and sample was prevented. However, the cable was allowed to rotate at the *entry point* because it was not fixed. Comparing figures 1.15 and 1.28b, the *excavation surface* in the former corresponds to the *entry point* in the latter, and similarly the cable section at the *discontinuity* in figure 1.15 corresponds to the *exit point* in figure 1.28b. At the beginning of the test, a free length

<sup>1</sup>These notations correspond to those used by Hyett *et al.* [Hyett1995]. The equivalent notations used in this manuscript can be found in the preamble [Nomenclature and Acronyms](#).

$L_f = 25.4$  mm existed between the *test* and the *anchor sections*.

According to this set-up, and due to its helical structure and low torsional rigidity, when the cablebolt is subjected to a tensile force it will tend to unscrew itself from the grout in the *test section*. The length anchored in the *anchor section* is longer and the cable will remain totally fixed in this part. As a result, untwisting of the cable wires will occur, especially near the *entry point*. This phenomenon has been considered in the model and represents a real situation where the face plate is absent.

The new constitutive law is a combination of theoretical and experimental considerations. As with the *BSM* proposed by Yazici and Kaiser [Yazici1992], this law is based on a frictional nature of the bond strength. Consequently, the radial pressure at the interface,  $p_1$ , plays an essential role. It should be noted that this law only accounts for bond failure; that is to say, it does not consider the sample behaviour before failure, when all of its components are coupled. From experimental results, it has been concluded that the grout annulus is totally split after approximately 1 mm of axial displacement; therefore, the law defines the theoretical response of the interface (and more generally, of the tested sample through the developed model) between 1 mm and the end of the test (pull-out tests are normally conducted until 50-60 mm of axial displacement). It is also important to note that the new constitutive law has been determined assuming a uniform response of the anchorage along its length, so that the  $Z$  coordinate is not involved (only the  $r$  coordinate is relevant), even if Hyett *et al.* [Hyett1992b] had previously highlighted that for  $L = 250$  mm the variations in the shear stress distribution along the embedment length cannot be ignored. In the model, the rotation phenomenon is accounted for in the form of an axial force developed in the cable free length between the *test section* and the *anchor section* (see figure 1.28b). It represents the force needed to untwist such free length: the longer this length is, the harder it is to untwist the cable. With respect to the *test section*, an average axial force is considered because neither the interplay between rotation, dilation and shear, nor the length over which each one dominates is properly understood. On this matter, SEM (*Scanning Electron Microscope*) micrographs after some tests have suggested that the grout imprints are almost undamaged along 175 mm from the *entry point* of the cell, which could reflect the predominant effect of unscrewing in this part; nevertheless, these results are not concluding. On the other hand, since the authors state that the bond strength is primarily frictional, the axial force at the *exit point* is simply the product  $2\pi r_1 L p_1 \tan \varphi'$ , where  $\varphi'$  is an empirical, average coefficient of friction over the whole *test section*. Therefore, the measured axial force is expressed as follows:

$$F_{ax} = 2\pi r_1 L p_1 \tan \varphi' + \frac{4\pi^2 C u_{ax}}{l^2 (u_{ax} + L_f)} \quad (1.18)$$

where  $C$  is the cablebolt torsional rigidity and  $l$  is its pitch length (*i.e.*, the length, measured along the axis of the cable, of a complete turn of the helical wires).

Using the new constitutive law and the hypotheses above, Hyett *et al.* [Hyett1995] proposed a model to simulate pull-out tests. The model consists of an analytical approach that describes incrementally the mechanism of bond failure, namely from  $u_{ax} = 1$  mm to the end of the pulling process. As in the model proposed by Yazici and Kaiser [Yazici1992], there are four interrelated variables: axial force  $F_{ax}$ , axial displacement  $u_{ax}$ , radial displacement  $u_{r1}$  and radial pressure  $p_1$ . Their interplays lie on the same principles as in the *BSM*:

- shear (or bond) strength-radial pressure relationship: the bond strength is thought to be mainly frictional. The classic linear criterion defined in equation (1.14) (replacing  $\varphi$  with  $\varphi'$ ) is adopted;
- radial displacement-radial pressure: the relationship between these two variables is determined

separately for the bolt-grout interface and for the grout annulus. At every stage,  $u_{r1}$  and  $p_1$  must be equal in both parts (continuity in space). In the framework of the constitutive law, the interface is assumed to behave as a hyperbolic dilatant joint, so that any pressure increase will reduce the radial outward movement  $u_{r1}$  and therefore favour joint closure. The radial rigidity of the cable  $K_{rc}$  is included as well. The expression for  $u_{r1}$  reads

$$u_{r1} = \frac{k_1}{p_1} (u_{ax} - 1) + \nu_0 - \frac{p_1 \nu_0}{K_0 \nu_0 + p_1} - \frac{p_1}{K_{rc}} \quad (1.19)$$

where  $k_1$  is an empirical constant (to relate the axial and radial displacements),  $K_0$  is the joint normal rigidity and  $\nu_0$  is its maximum closure.

As for the grout annulus, even if it is fully split, it is accepted that there are three possible states (elastic, fully or partially fractured) depending on the value of the hoop stress,  $\sigma_{\theta\theta}$ . The idea is the same as that proposed by Yazici and Kaiser [Yazici1992], explained before;

- radial displacement-axial displacement: this is the dilatant response of the interface, corresponding to the first term in equation (1.19). An empirical, linear relationship between both displacements is assumed in the absence of a sound theory (it should be noted that Yazici and Kaiser [Yazici1992] did not use the third quadrant in the application of the *BSM*);
- axial force-axial displacement: these variables are related as indicated in equation (1.18). From the changes in the interface and annulus radial response during each incremental displacement  $du_{ax}$ , the increment of the axial force is calculated.

The parameters of the model are:

- cablebolt: radial rigidity  $K_{rc}$ , torsional rigidity  $C$  and pitch length  $l$ . The radial rigidity is determined empirically<sup>2</sup> (due to the absence of reliable data);
- bolt-grout interface: normal rigidity  $K_0$ , maximum closure  $\nu_0$ , constant  $k_1$  and friction angle  $\varphi'$ . These parameters are all empirical<sup>2</sup>;
- grout annulus: internal and external radii  $r_1$  and  $r_2$  respectively, Young's modulus  $E_g$  and Poisson's ratio  $\nu_g$ . They are all known parameters.

A comparison between experimental data issued from pull-out tests and the prediction offered by the model is exhibited in figure 1.29. The data are represented by dots and the analytical prediction by solid lines. It can be seen that the agreement is satisfactory, particularly for the axial load-axial displacement prediction.

This model has also been used to simulate tests under constant outer radial stiffness and variable confining pressure conditions. The results are quite satisfactory for the former, but since the load path may affect the bond strength and given that the new law assumes that the bond strength does not depend on the load path, the correlation between theory and experiments when the radial pressure is varied is only reasonable. But in any case, the law proposed by Hyett *et al.* [Hyett1995] is suitable for implementation to simulate the interaction between the rock mass and the reinforcement. Their model is also more elaborated than the *BSM* proposed by Yazici and Kaiser [Yazici1992]. However, it simulates only bond failure, and not the whole pulling process (it starts at  $u_{ax} = 1$  mm). Additionally,

<sup>2</sup>Empirically means that the value of the constant has been indirectly obtained based on a best fit to the pull-out test results (*i.e.*, it has not been obtained from specific laboratory investigations).

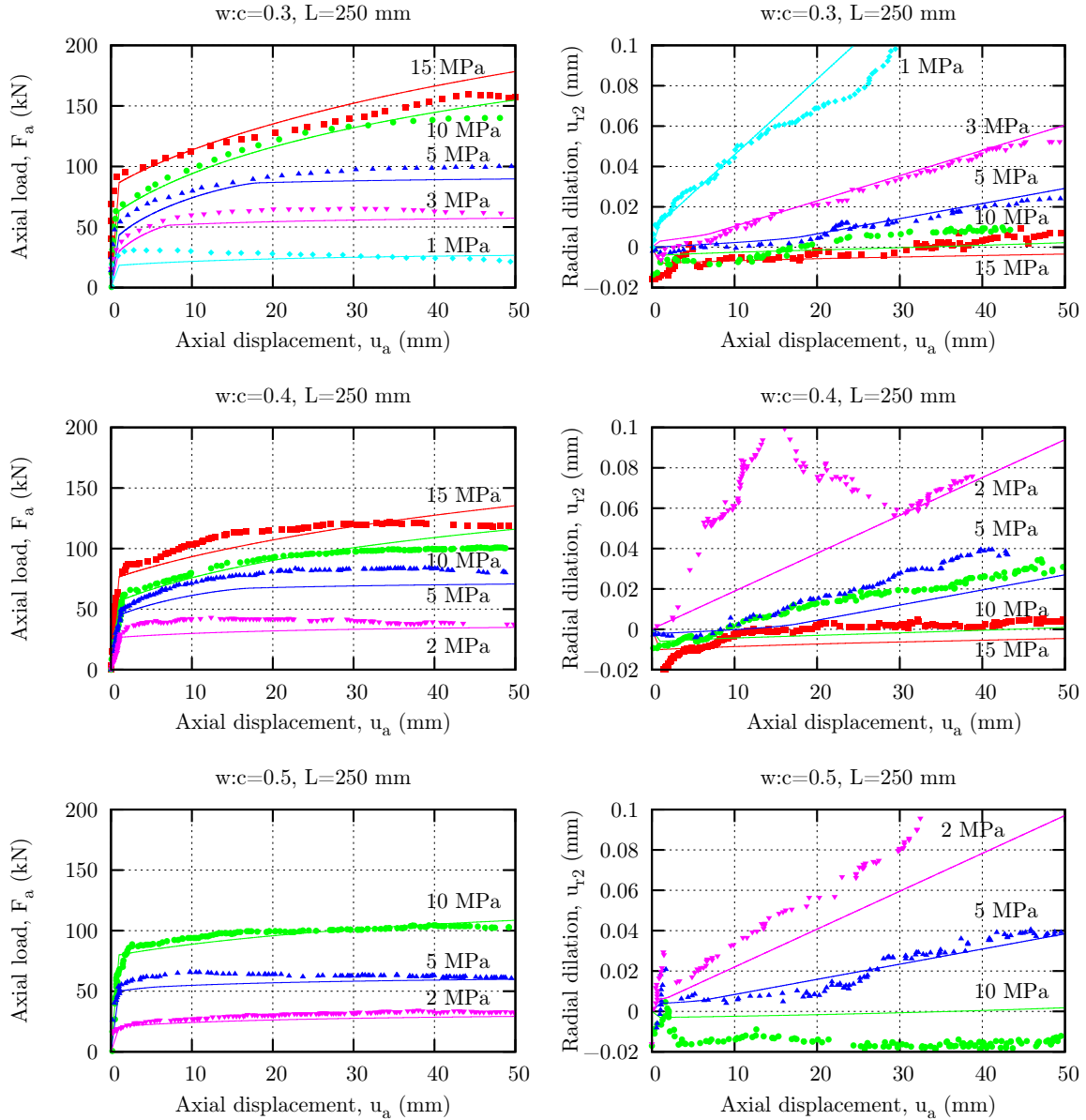


**Figure 1.29:** comparison between experimental data (laboratory pull-out tests under constant confining pressure) and the theoretical prediction proposed by Hyett *et al.* [Hyett1995].

the interface radial behaviour is supposed to be similar to that of a nonlinear rock joint, but no evidence is provided on this. At the same time, to the best of the author's knowledge, an equivalent model for rockbolts is not available.

Using a similar *MHC*, Moosavi *et al.* [Moosavi2005] conducted a series of pull-out tests on three different cement-grouted rockbolts: 22 and 28 mm diameter rebars and 20 mm diameter Dywidag bars. Two embedment lengths were used:  $L = 100$  mm and  $L = 150$  mm, as well as two different grout qualities:  $UCS = 30$  MPa and  $UCS = 42$  MPa. In addition to the diameter, these rockbolts differ in the ribs shape: the ribs are continuous in the rebars, whereas in the Dywidag bolts two flat sides with no ribs exist. Figure 1.30 displays the pull-out test results for a 28 mm diameter rebar and for a 20 mm diameter Dywidag bar. With respect to the load-displacement results obtained by Hyett *et al.* [Hyett1995] on classic cablebolts and shown in figure 1.29, a moderately marked peak-residual behaviour is obtained in the case of rockbolts, that is in agreement with the pull-out

test results obtained by Benmokrane *et al.* [Benmokrane1995] for the Dywidag bars, *cf.* figure 1.23. The dilation curves also show important differences with respect to those displayed in the right-hand side in figure 1.29, particularly in the residual phase, where contraction is observed for confinements beyond 2-3 MPa. Furthermore, when dilation is important (*i.e.*, for low pressures), the spacing of the peaks in the dilation graphs matches the ribs spacing on the bar.

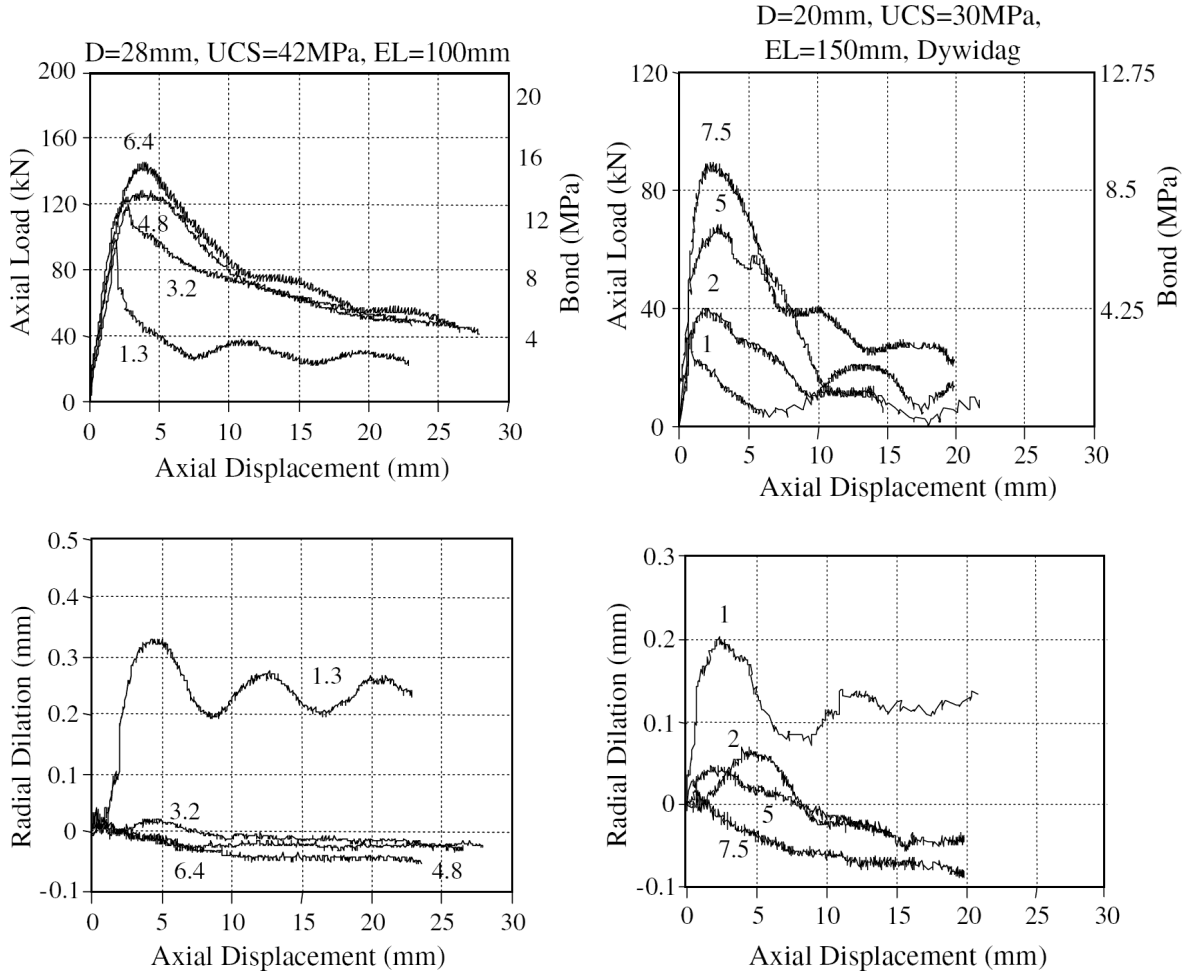


**Figure 1.30:** pull-out test results on 28 mm ribbed bars and 20 mm Dywidag bolts (after Moosavi *et al.* [Moosavi2005]).

According to these results, it seems that rockbolts are less performant than cablebolts in the post-peak phase because the axial load substantially decreases after the peak. Hence, Moosavi *et al.* [Moosavi2005] state that when large rock movements are expected, the use of cablebolts over rockbolts might be more beneficial.

Like Hyett *et al.* [Hyett1995], these authors also reported that the slip between the bolt and the grout is mainly of frictional nature, whence the importance of the radial pressure. From the experimental results, they obtained a non-linear relationship between the confining pressure  $p_2$  and the bond strength (calculated from the peak axial force, assuming a uniform distribution along the embedment length). The results are shown in figure 1.31 for the two different grouts. However, it should be reminded that as far as the cable-grout interface is concerned, the relevant pressure is  $p_1$  and not  $p_2$ . For that interface, Hyett *et al.* [Hyett1995] assumed the linear dependency described in equation (1.14).

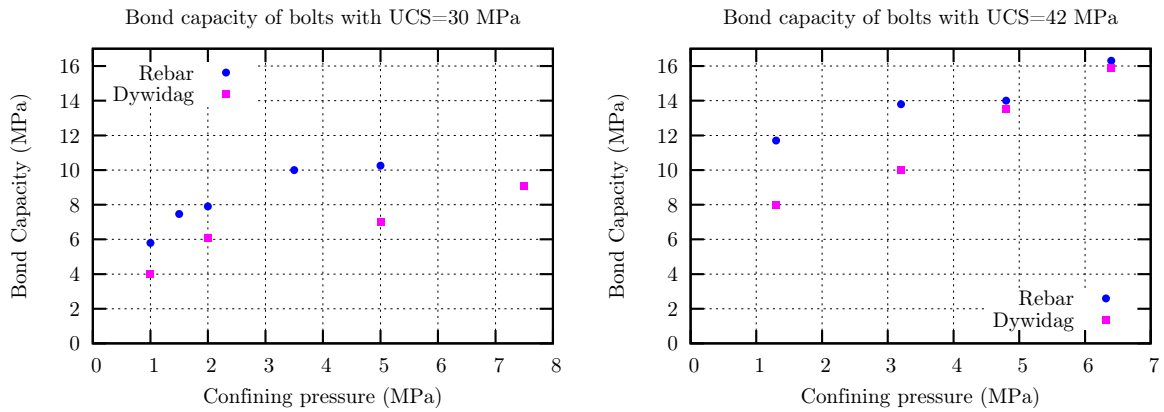


**Figure 1.31:** pressure dependency of the bond capacity (after Moosavi *et al.* [Moosavi2005]).

Almost at that time, Hagan [Hagan2004] conducted pull-out tests on instrumented resin-grouted 21.7 mm diameter rockbolts using two different loading arrangements. Six pairs of strain gauges equally spaced at 30 mm intervals were installed on the bolts with the last pair 10 mm far from the bolt end. The embedment length used was 170 mm, the borehole diameter was 26 mm and a confining pressure of 10 MPa was applied using a biaxial load cell. A supplementary pair of gauges laid outside the cell, on the rockbolt free length (to verify the load applied). A cementitious grout was used to reproduce the rock sample. The first arrangement studied corresponded to the conventional pull-out test configuration and the second represented the loading of a rockbolt due to bed separation. Both configurations are shown on top of figure 1.32. As for the differences between them, in the first set-up the reaction force from the hydraulic cylinder acts against the free surface of the test sample, whilst in the second set-up this reaction force is transferred to the opposite end of the sample, so that the free surface of the test sample is not constrained.

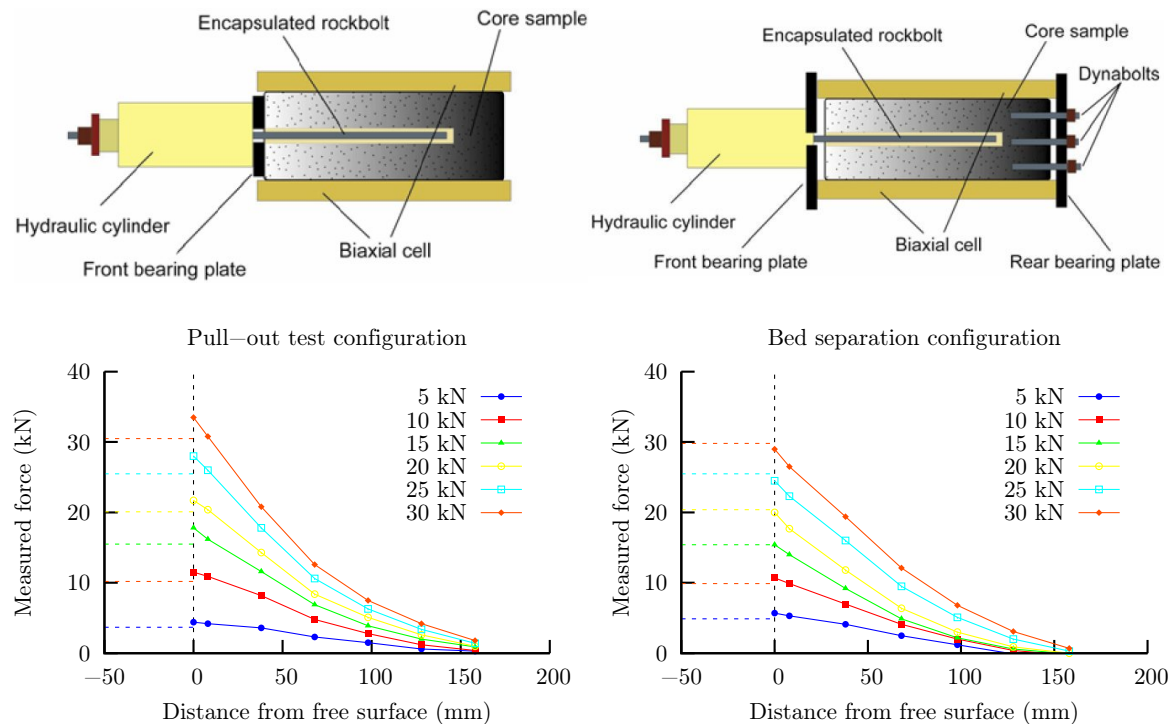


**Figure 1.32:** loading arrangements used and results obtained by Hagan [Hagan2004].

The results are not analyzed in the form of a load-displacement curve, but in terms of axial load distribution, calculated from the strain measurements. The lower graphs in figure 1.32 display the load distribution for six values of applied load. These graphs reveal an interesting fact: in the conventional pull-out test configuration, the axial load on the rockbolt free length (represented by the horizontal dashed lines) is slightly lower than the axial load on the embedded part, close to the *front bearing plate*. On the other hand, in the alternative loading configuration this anomaly does not take place, which suggests that the confinement acting against the free surface of the rock sample (due to the reaction force) may change significantly the stress field around the borehole. Thus, if it is intended to use the pull-out test results to study the interface behaviour, this distortion should be taken into account. Further details on this matter will be provided in chapter 3.

### 1.3.3 Numerical modelling of passive reinforcement elements

Numerical modelling is particularly useful to predict the response of complex excavations, if not exactly, at least in terms of trends of evolution and development of local phenomena. Additionally, numerical modelling proves to be very advantageous to help design bolting patterns; in fact, rockbolts and cablebolts exist as implemented elements in several numerical software for rock and soil mechanics applications. The way these elements and their interaction with the surrounding ground are accounted for in the most popular computer programs is described here, with emphasis on the two-dimensional available versions. It is important to highlight that other approaches to model the passive reinforcement action such as changing the reinforced ground strength parameters (classically, the cohesion and the friction angle) are not considered here, because once the "equivalent" constitutive law of the ground is obtained, no numerical particularity exists (unless the proposed law requires a local discontinuity in the displacement field).

The effect of passive reinforcements has been numerically proved by Laigle [Laigle2004], who modelled the excavation of a drift in a soft rock mass considering two different scenarios. In the first one, the drift was not reinforced, whilst in the second one, a bolting pattern consisting of 20 mm diameter, 4 m long fully grouted rebars spaced 1 m<sup>2</sup> was assumed. This pattern was activated when the deconfinement ratio was  $\lambda = 0.9$ . The comparison of the rock mass response in the two scenarios at further levels of deconfinement shows that the convergence is restrained up to 1 % when the bolts are modelled (the same order of magnitude is obtained analytically). This decrease in the convergence measurements is equivalent to an increase in the confinement ratio, or to a delay in the onset of the rock mass damage. Therefore, even if the bolting pattern might not be sufficient to ensure the stability of the drift, the positive effect of the passive bolts can be reproduced numerically.

In addition, it should be noted that, in order to realistically model the reinforcement-ground interaction, numerical methods such as the finite element, finite difference or distinct element should be used; in fact, methods based on limit equilibrium analysis only consider the reinforcement action in the form of a *point support force*, as it was explained in part 1.2.4. For instance, Unwedge is a 3D limit equilibrium wedge analysis program developed by Rocscience and based on Goodman and Shi's block theory (1985) that allows for evaluation of wedge failure around excavations in hard rock. It calculates the maximum sized wedges which can be formed around the opening and evaluates their stability considering mainly gravitational loadings. Since the stability analysis is a limit equilibrium one, it is assumed that the displacements take place at the discontinuities, so that the wedges move as rigid bodies with no internal deformation or cracking. Therefore, even if reinforcement elements such as bolts and shotcrete can be introduced, the interaction between these elements and the wedges is limited

to a *support force*, which in the case of bolts can be either tensile or shear (they are exclusive). To calculate the *tensile support force* that a bolt can apply to a wedge, three failure modes are considered: pullout, tensile and stripping (*i.e.*, failure of the end plate and sliding of the wedge whilst the bolt remains embedded in the stable rock mass). The maximum force that can be mobilized by each mode is calculated and then the minimum of the three is applied to the wedge in order to calculate the safety factor (ratio of the resisting forces to the driving forces).

Within the finite difference codes, FLAC is a software developed by Itasca and available in 2D (plane strain, plane stress and axisymmetric problems) and 3D. It proposes the *cable element* (*cable-SEL* in 3D, based on the same concept), which is a one-dimensional element that can be point-anchored or grouted to the surrounding material. This element is also available in 3DEC (distinct element code in 3D) through the *STRUCT Cable* command. The *cable element* consists of a series of nodal points that allow to model the bar axial behaviour and the shear resistance along the bar length; thus, this element is useful to model reinforcement systems in which the grout may fail in shear (namely, fully grouted rockbolts and cablebolts). The *cable element* can sustain tensile and compressive loads, but not bending moments. In cases where the bending resistance is important (for instance, to provide resistance to the relative displacement of blocks in jointed rock masses), the *rockbolt element* is available. It consists of a two-dimensional element that can work in axial, shear and bending. It is suitable to represent a reinforcing element in which the non-linear effects of confinement, grout bonding or tensile rupture are important. However, the shear behaviour of the grout annulus is not considered as in the *cable element*.

Back to the *cable element*, the axial behaviour (which depends solely on the cable itself) is described by an elastic-perfectly plastic model. The cable cannot sustain shear forces on its cross-sectional area. The grout annulus behaviour is accounted for in the shear direction; it is also elastic-perfectly plastic, but the maximum shear force depends linearly on the stress normal to the cable element. A conceptual visualization of the cable element and a schematic representation of the behaviour of the cable and the grouting material are shown in figure 1.33.

As a whole, the necessary input data are:

- cable Young's modulus,  $E$ ;
- cable cross-sectional area,  $A$  or *area*;
- cable tensile and compressive yield limits (force), *yield* and *ycomp* respectively;
- shear stiffness, *kbond*;
- cohesion, *sbond*;
- friction angle, *sfraction*;
- cable element exposed perimeter, *perimeter*.

A supplementary parameter, *spacing*, can be introduced to scale these properties in the out-of-plane direction (for the 2D assumption of a continuous reinforcement layer in that direction). Since the cable element nodal points go through the surrounding ground mesh (one nodal point per mesh element), an interpolation scheme is used to compute the displacement of the medium in the cable axial direction at the cable node,  $u_{\text{medium}}$ . In the normal direction, the cable element is slaved to the grid motion and it doesn't exert any normal force on this grid because the cable segments are co-linear. As for the input data, the cable properties are easy to obtain. Ideally, the data *kbond*, *sbond* and *sfraction*



grout annulus in a material data base (for the interface, the parameters  $K_0$ ,  $\nu_0$  and  $k_1$  are supposed to be constant, so that only the friction angle  $\varphi'$  depends on the  $w : c$  ratio. As it was indicated earlier in this chapter, a linear cohesionless criterion is used for the shear strength).

Plaxis is another finite element code for two and three-dimensional analysis in soil geotechnical engineering that was originally developed by the Technical University of Delft. Plaxis can deal with plane strain and axisymmetric problems. In this software (at least in the 2D version), ground anchors can be modelled by a combination of two elements: *node-to-node anchors* and *geogrids*. A node-to-node anchor is a two-node element that can withstand axial tensile and compressive forces (bending is not accounted for, nor is shear). It is characterized by a normal stiffness,  $E_b \pi R_b^2$ , and two yield forces (compressive and tensile), introduced to account for failure of the rod. The geogrid is introduced to simulate the grout. It consists of a one-dimensional element comprising three or five nodes (depending on the triangular elements in use to model the soil) and can bear tensile but not compressive nor shear or bending loadings. As with the node-to-node element, it is characterized by a normal stiffness,  $E_g \pi R_g^2$ . Plasticity may be taken into account by specifying a maximum tensile force. As a whole, the ground anchor element proposed by Plaxis is not appropriate for the simulation of fully grouted bolts because the node-to-node anchor and the geogrid are only linked at one node, not along the anchor length (in other words, both elements are co-linear, but the geogrid starts where the node-to-node anchor ends). Moreover, the grout body is totally linked to the soil and consequently it is assumed that it does not slip relative to the surrounding ground.

VIPLEF is a 2D-3D numerical software based on the finite element method developed at the Geosciences Department of MINES-ParisTech, cf. [Tijani2008]. The 2D version can solve plane strain, plane stress and axisymmetric problems. Fully grouted bolts can be simulated in this version of the program. In this software, the bolt is represented by two series of three nodes each (for 6-node triangular elements [second order interpolation]), so that the bar can stand not only axial but also bending loadings. The parameters needed to model the bolt are: cross-sectional area, Young's modulus, Poisson's ratio and the second moment of inertia with respect to the out-of-plane direction (to simulate bending). In total, the bolt can withstand axial, shear and bending loadings. The interface is represented by a joint element (therefore, two series of three nodes) whose normal behaviour is linear with normal stiffness  $K_n$  (high to restrain the reinforcement displacement in the normal direction) and whose shear response is accounted for in the form of a pressure dependent shear stress-slip relationship,  $\tau_b(W, p_b)$ , defined by

$$\tau_b(W, p_b) = \left( a_1 a(p_b) \sqrt{\frac{W}{W_c}} + b(p_b) \right) \cdot \exp \left[ - \left( \frac{W/W_c}{c(p_b)} \right)^d \right] \quad (1.20)$$

where

$$a(p_b) = \left( 2 - \frac{q(p_b)}{p_c} \right) q(p_b), \quad (1.21)$$

$$q(p_b) = \min(p_b, p_c) \quad (1.22)$$

$$b(p_b) = a_2 p_c + a_3 p_b \quad (1.23)$$

$$c(p_b) = 1 + a_4 \frac{p_b}{p_c} \quad (1.24)$$

In equations (1.20)-(1.24),  $p_b$  is the pressure acting normal to the interface. Besides, the parameters  $a_1$ ,  $a_2$ ,  $a_3$ ,  $a_4$ ,  $d$ ,  $W_c$  and  $p_c$  may change with the grout quality, thereby accounting for the influence of the grouting material.

It is important to emphasize that this particular interface law has been developed and used in previous works (*cf.* [Jomaa2003]); however VIPLEF is a general code in which any other constitutive law can be implemented. The particular model defined in equations (1.20)-(1.24) has been deduced by a best fit to the pull-out test results conducted by Hyett *et al.* [Hyett1995] (*cf.* the load-displacement curves in figure 1.29), assuming that the shear stress is uniformly distributed along the embedment length. A comparison between the experimental data obtained for  $w : c = 0.3$  and the response predicted using equations (1.20)-(1.24) is shown in figure 1.34. The parameters for this grout quality are:  $a_1 = 1.5$ ,  $a_2 = 0.25$ ,  $a_3 = 0.1$ ,  $a_4 = 3.43$ ,  $d = 2/3$ ,  $W_c = 28$  mm and  $p_c = 8$  MPa. However, it should be noted that the fit has been made using the confining pressure applied, *i.e.* pressure  $p_2$  using the notation in Hyett *et al.* [Hyett1995], instead of pressure  $p_b$  ( $p_1$  in those authors' notation).

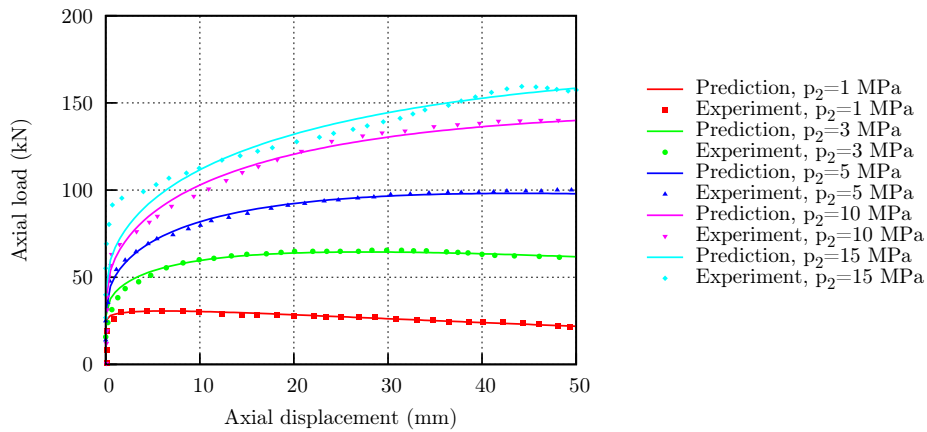


**Figure 1.34:** comparison between experimental data (laboratory pull-out tests conducted by Hyett *et al.* [Hyett1995],  $w : c = 0.3$ ) and the load-displacement curves predicted using the pressure dependent shear stress-slip relationship implemented in VIPLEF.

A schematic representation of a fully grouted rockbolt as implemented in VIPLEF is shown in figure 1.35.

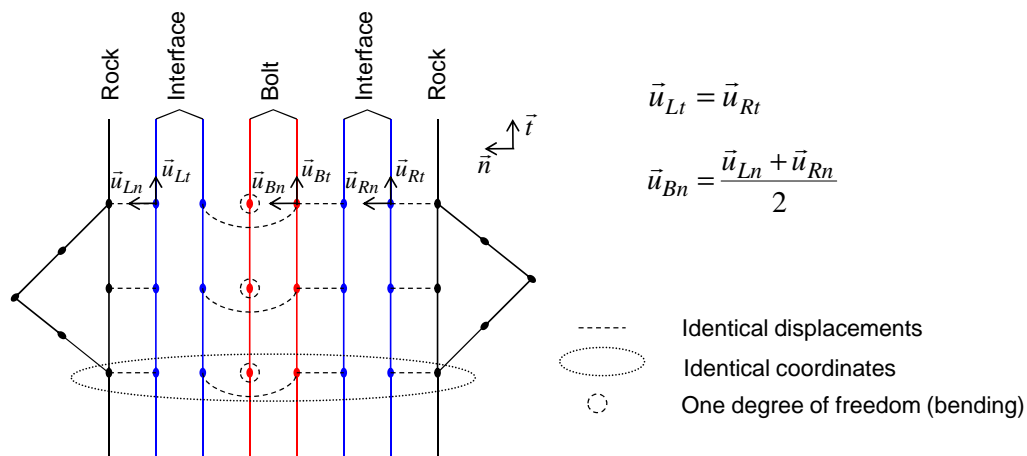


**Figure 1.35:** schematic representation of the fully grouted bolt model implemented in VIPLEF.

The interface is represented at both sides of the bolt element. As it can be seen, one of the series of the interface is linked to the bolt and the other is linked to the rock mass. The tangential displacement of the rock mass is imposed coincident at both sides of the bar,  $\vec{u}_{Lt} = \vec{u}_{Rt}$  (the bolt is a punctual discontinuity in the surrounding ground). Furthermore, the cable is constrained in the normal direction: its normal displacement is the average of the normal displacements in the rock mass at both sides of the reinforcement (the normal pressure acting on the interface is assumed equal around the cable, in  $2\pi R_b$ ).

CESAR-LCPC is a finite element software developed by the French LCPC (*Laboratoire Central des Ponts et Chaussées*) to model civil engineering structures in particular. It is available in 2D and 3D. Three types of reinforcing bars exist in the 2D version of this software; among these elements, one has been especially designed to account for the ground-reinforcement interaction. It consists of a one-dimensional, linear elastic bar element that can only withstand tensile and compressive loads. In the implementation, it is considered that the grout stiffness may be neglected with respect to that of the bar and consequently the borehole radius  $R_g$  is taken into account. The ground-reinforcement interface, which is thought of as a fictitious material, is modelled by contact elements placed at  $R_g$ . These elements are linear in the direction normal to the contact zone and quadratic in the tangential direction. When they are generated, they are coupled to the ground and the reinforcement. They have a small thickness,  $e$ , calculated proportionally to the size of the structure under study. Two types of contact elements are defined around the reinforcement: at the far end, the elements are provided with a low tensile strength (equal in general to the ground cohesion) to model a possible detachment as the bar is axially loaded; on the other hand, the lateral contact elements are provided with a high tensile strength (greater than the stress field close to the excavation), because in this case it is the possible slip between the ground and the reinforcement that is important. Once the tensile strength is reached (thus for the elements at the far end), the contact element contribution to the stiffness matrix vanishes. As for the lateral elements, the onset of slip is determined by the Mohr-Coulomb criterion with a non-associative potential. The expression for the criterion reads

$$f = |\tau_b| - C + p_g \tan \varphi \quad (1.25)$$

and for the plastic potential, the expression reads

$$g = |\tau_b| + p_g \tan \psi \quad (1.26)$$

where  $C$  and  $\varphi$  are respectively the cohesion and the friction angle of the contact interface  $R_g$  and  $\psi$  is its dilation angle. Beyond failure, the behaviour of the contact element is perfectly plastic and its shear stiffness is set equal to zero.

Five parameters are required in total to model contact elements: the stiffness  $E$ , which has no physical sense and is usually determined as  $E = \inf(E_{\text{ground}}, E_{\text{reinforcement}})$ , the tensile strength  $R_t$ ,  $C$ ,  $\varphi$  and  $\psi$ . The interface shear strength,  $q_s$ , is normally obtained through a pull-out test conducted in equivalent conditions to those modelled (in terms of materials used and geometry), and assuming a uniform distribution of the shear stress along the reinforcement. In general,  $q_s$  is totally attributed to either  $C$  or  $\varphi$ , cf. [Al Hallak1999]. Finally, it should be noted that the ground displacement is imposed coincident at both sides of the reinforcement elements. As the model runs, it is also verified that the contact elements do not penetrate in each other.

To summarize, the contact interface between the reinforcement and the ground is only accounted

for in a few programs. Only the interface that is likely to fail is discretized to avoid making the simulations heavier and longer. In some codes, the interface is modelled as a joint element (*i.e.*, as a discontinuity like in VIPLEF), and in other programs it is modelled as a continuous medium (like in CESAR-LCPC). The shear response of this interface is often elastic-perfectly plastic and the characteristic parameters are issued from pull-out tests, making a number of simplifications. The interface normal response is in general linear until a possible failure. While an elastic-perfectly plastic model may suit the pull-out response of a fully grouted cablebolt, it is not appropriate to model the response of a grouted rockbolt. Moreover, in the majority of the programs the bar can only bear axial loadings, but in VIPLEF shear and bending loads are also possible. The bars are implemented as one-dimensional elements not only to reduce the computational requirements but also to avoid mesh size problems, caused by the excavation-reinforcement scale ratio. In some cases, the contact interface is not modelled, so that the grout shear behaviour is utilized to simulate the reinforcement-ground interaction; but in this case, the relative displacement cannot be considered. Finally, as regards the comparison between the 2D and 3D modellings, it should be noticed that, in 2D, the reinforcement elements are converted into continuous layers in the out-of-plane direction (the value of the parameters are adjusted to account for this transformation), except in the case of an axisymmetric simulation in which the bolt axis and the axis of revolution coincide (but in that case only one bolt can be modelled). The 3D approaches overcome this limitation and the results are slightly more accurate than those obtained in a two-dimensional analysis, but the simulations are slower and the memory requirements higher, in particular because the bolt thickness must be accounted for; otherwise, the contact (cylindrical) interface cannot be taken into account. Under these circumstances, the choice of the mesh size remains a delicate matter.

## 1.4 Conclusions

Fully grouted rockbolts and cablebolts have been used as reinforcement elements in mining and civil engineering for almost 50-60 years. Their success has brought about not only technological advances but also a significant amount of scientific investigations that aim at a better understanding of the way these structures interact with the surrounding ground.

This work deals more precisely with the behaviour of continuously mechanically coupled (CMC or fully grouted) rockbolts and cablebolts subjected to tensile axial loads, in static conditions. The literature review is presented in this chapter.

After a general introduction to the bolting technology, that comprises active and passive reinforcement systems, attention is focused on fully grouted rockbolts and cablebolts. The load transfer mechanism between the surrounding ground and the reinforcement is explained. An overview of the most popular tendons and grouting materials is exposed, together with some technical aspects, the different ways these bolts can come into operation and their main roles. The principal tools available at present to design bolting patterns are briefly presented, as well as a review of the different failure modes of this type of reinforcement. It is explained that, when a CMC bolt is subjected to a tensile load, failure is more likely to take place at the bolt-grout interface *via* a decoupling mechanism. Finally, the technological background describes the principal factors that influence the performance of fully grouted rockbolts and cablebolts and proposes a non-exhaustive list of existing methods to assess such performance.

The scientific background focuses on the research carried out to understand the response of CMC bolts under axial loadings. Typically, the situation under study is shown in figure 1.15, where a

grouted bolt intersects a discontinuity close to the excavation surface. While the upper, long length is assumed to remain anchored, the lower anchorage may be damaged and even lost if the axial load on the bolt exceeds a critical value. In such a case, the lower rock block will slip with respect to the bolt. The bolt equilibrium is expressed in equation (1.1), that defines the interface shear stress  $\tau_b$  as the change in the axial force  $dF$  along the length  $dZ$ ; that is to say, the load is transferred between the reinforcement and the surrounding media in the form of a shear stress,  $\tau_b$ . This equation proves the importance of the stress  $\tau_b$ , and more generally of the interface behaviour (that includes the tangential and normal directions), because it provides access to the reinforcement anchoring capacity and the factors that influence it. The behaviour of the bolt-grout interface, that can be expressed in terms of a constitutive law, is the core of the current investigation.

The bolt-grout interface response can be explored through the execution of pull-out tests, both in the laboratory and the field; however, in order to study the bolt-grout interface, laboratory pull-out tests are usually preferred because they allow to study a wide range of parameters and also to make more measurements than field tests, especially in the radial direction. The most popular pull-out arrangements are exposed, and an evaluation of the effect of the loading configuration on the pull-out test results, conducted by Hagan [Hagan2004], is also presented. Moreover, it is explained that the pull-out response of rockbolts and cablebolts is different, due mainly to the different structure of both tendons.

The different analytical approaches to determine the response (in terms of axial load, axial slip and shear stress) of CMC bolts subjected to tensile loads are also described. These approaches are based on either the shear stress distribution along the embedment length,  $\tau_b(Z)$ , or the shear stress-slip relationship,  $\tau_b(W)$ , also referred to as bond-slip model. Nevertheless, the latter is preferred because it can be implemented in numerical modelling programs and it provides access to the interface shear stiffness. The tri-linear bond-slip model displayed in figure 1.21 is the classic  $\tau_b(W)$  relationship accepted to describe the decoupling mechanism along the bolt-grout interface. It has been used by many researchers, such as Benmokrane *et al.* and Ren *et al.* [Benmokrane1995, Ren2010]. With respect to the first analytical study of a fully grouted rockbolt subjected to a tensile load undertaken by Farmer [Farmer1975], in which the decoupling along the interface was not considered, the classic tri-linear relationship does account for the decoupling process.

The global behaviour of the bolt-grout interface has only been studied in a few cases; in fact, the approaches based on either  $\tau_b(Z)$  or  $\tau_b(W)$  focus on the tangential direction. While a global behaviour has not been defined for rockbolts, Hyett *et al.* [Hyett1995] established a constitutive law for the bolt-grout interface of seven-wire cablebolts and developed a model to reproduce pull-out tests (after bond failure) using that law and the radial behaviour of the grout annulus. The rotation of the cables was also considered in the computation of the axial force, that is given in equation (1.18). In the interface law, the normal response, which is defined in equation (1.19), is supposed to be similar to that of nonlinear rock joints, even if there is no evidence on this assumption; as for the shear response, the classic linear criterion defined in equation (1.14) is used.

The review of the numerical programs that propose models to simulate fully grouted bolts proves that the contact interface is only accounted for in a few cases. Besides, only the interface that is likely to fail is discretized (either as a joint element or as a continuous medium) to avoid making the simulations heavier and longer. If the contact interface is not modelled, the grout shear behaviour may be used to reproduce the interface tangential response; however, in this case the relative slip cannot be taken into account. Furthermore, the reinforcement-ground shear interaction is in general considered to be elastic-perfectly plastic. While this may be suitable for cablebolts, it is not for rockbolts because

their pull-out response is different, *cf.* figure 1.23 for instance. Since numerical modelling is useful not only to design bolting patterns but also to predict the response of reinforced excavations, the way the reinforcement is simulated takes a major role. Laigle [Laigle2004] has proved that the effect of passive reinforcement can be captured numerically. As regards the comparison between 2D and 3D modellings, the latter overcome the limitation of the continuous layer in the out-of-plane direction, leading to slightly more accurate results; however, the bolt thickness needs to be discretized in order to be able to model the contact, cylindrical interface. This makes the simulations slow and the memory requirements quite high. In addition, under these circumstances the choice of the mesh size is quite complicated because of the excavation-reinforcement scale ratio; therefore, 3D modellings are in general reserved to complex cases.

As a whole, the state-of-the-art proves that the interface behaviour of fully grouted rockbolts and cablebolts is not fully understood. This work aims at providing some insight into such behaviour. Useful analytical tools that may help understand the response of a fully grouted bolt subjected to a tensile axial load are presented in chapter 2. The laboratory and field experimental campaigns conducted on rockbolts and cablebolts to gain more understanding about the interface behaviour (before and after bond failure) are presented in chapter 3. Finally, the analysis of the results issued from laboratory pull-out tests on rockbolts is offered in chapter 4. Such analysis is directed towards the future definition of the bolt-grout interface constitutive law, which changes for each combination of bolt and grouting material.

Ce chapitre est consacré à l'étude théorique d'un boulon à ancrage réparti soumis à une force axiale de traction, en conditions statiques. La configuration en étude est montrée dans la figure 2.1. Un système de coordonnées cylindriques a été choisi en vue de la géométrie du problème. Comme la réponse du système en étude est supposée symétrique dans la direction orthoradiale, les deux seules directions importantes sont  $r$  et  $Z$ .

La réponse (élastique) du scellement et du terrain est étudiée d'abord, dans les directions radiale et axiale séparément. Le comportement radial est particulièrement important pour évaluer l'effet de la pression de confinement,  $p_r$ , sur la pression normale à l'interface barre-scellement,  $p_b$ . Le comportement axial de ces deux matériaux est utile pour estimer la contrainte de cisaillement dans cette interface,  $\tau_b$ , lorsque l'ancrage n'est pas endommagé.

La dernière partie du chapitre est consacrée à la présentation du nouvel outil développé pour déterminer la distribution axiale de la force  $F$ , de la contrainte de cisaillement  $\tau_b$  et du déplacement axial  $W$  au cours d'un essai d'arrachement. Cet outil s'avère particulièrement pratique pour de grandes longueurs d'ancrage, pour lesquelles le comportement n'est pas uniforme dans la partie ancrée. Les données nécessaires pour utiliser cet outil sont : la longueur d'ancrage  $L$ , le rayon du boulon  $R_b$ , son module de Young  $E_b$  et la relation  $\tau_b(W)$ . Les deux cas de figure possible pendant un essai d'arrachement, à savoir longueur d'ancrage constante ou décroissante, ont été considérés. Par rapport à d'autres solutions analytiques existantes du même problème, l'innovation de la nouvelle approche consiste à utiliser des conditions aux limites ne concernant que l'extrémité libre du boulon. Le développement détaillé de la solution analytique est présenté pour le cas d'une relation  $\tau_b(W)$  tri-linéaire, très couramment utilisée comme indiqué dans le premier chapitre. La détermination de cette relation à partir des résultats d'essais d'arrachement est expliquée, et on montre que l'utilisation de petites longueurs d'ancrage est plus adaptée pour trouver de façon précise  $\tau_b(W)$ . La comparaison entre plusieurs résultats expérimentaux, issus d'essais d'arrachement *in situ* et en laboratoire, et la réponse prédite par le nouvel outil est satisfaisante. Les relations  $\tau_b(W)$  employées ont été dérivées à partir des résultats expérimentaux suivant la méthode décrite.

Finalement, dans le but de mettre en évidence l'influence de la longueur d'ancrage sur le résultat d'un essai d'arrachement, le nouvel outil est appliqué pour prédire le résultat, en termes de force-déplacement axial, de six essais effectués dans les mêmes conditions (*i.e.*, mêmes  $R_b$ ,  $E_b$ ,  $\tau_b(W)$  et longueur d'ancrage constante), mais avec des longueurs très différentes, allant des petites valeurs

utilisées en laboratoire aux grandes longueurs *in situ*. Les résultats montrent clairement que la réponse est très influencée par la longueur d'ancrage,  $L$ . En même temps, l'analyse de la distribution de la contrainte de cisaillement  $\tau_b$  sur la longueur  $L$  confirme que l'emploi de petites longueurs d'ancrage est favorable pour pouvoir supposer une distribution uniforme de  $\tau_b$  sur  $L$  pendant toute la durée de l'essai.

## 2.1 Introduction

This chapter is dedicated to the theoretical study of a fully grouted rockbolt subjected to a tensile axial load. A schematic representation of the problem is shown in figure 2.1, which corresponds to the typical pull-out test set-up used during this research. The topics discussed in this chapter are analytical tools that help understand the response of a CMC bolt subjected to a tensile load, either in a field situation or in a laboratory set-up. In both layouts, there are three materials involved: a **bolt** of nominal radius  $R_b$ , which is grouted to the **surrounding ground** (rock or soil) by means of a **grouting material**. The borehole radius is  $R_g$ . The main difference between the two situations concerns the rock mass outer radius,  $R_r$ , which is smaller in the laboratory. But, in both cases, when an axial load  $F$  acts on the bolt, a shear stress develops in both the grout and the ground. The bolt axial displacement with respect to the rock mass at  $r = R_r$  is denoted by  $W$ .

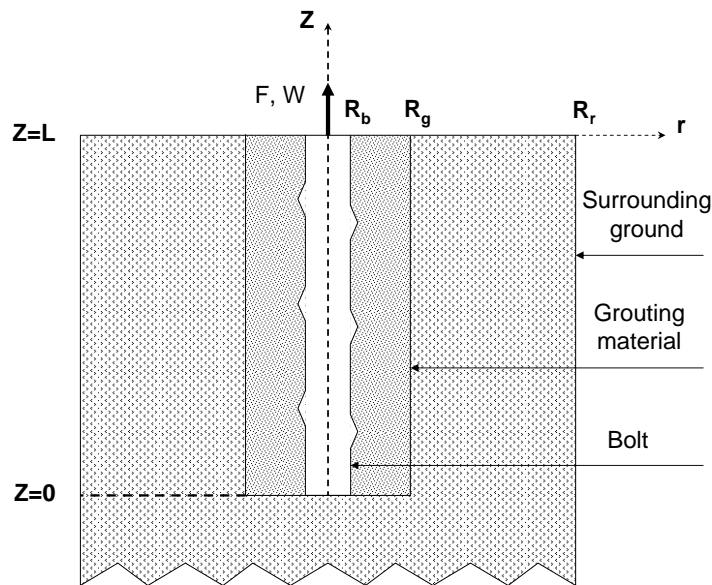


Figure 2.1: definition of the geometry and coordinate system in use.

According to the system geometry, a cylindrical coordinate system is used. The cylindrical axis  $Z$  corresponds to the bolt axis. Since the reinforcement is supposed to behave uniformly in the azimuthal direction, rotational invariance is assumed. Therefore, there are only two relevant coordinates to the problem:  $Z$  and  $r$ . It is important to note that the assumption of rotational invariance is less accurate if the grout or the ground are radially fractured.

As brought forward in chapter 1, the bolt is assumed to work solely under axial loads (beam theory). Its equilibrium is given simply by

$$dF = 2\pi R_b \tau_b dZ \quad (2.1)$$

In other words, the axial load  $dF$  in a rockbolt infinitesimal length  $dZ$  is compensated by a shear stress  $\tau_b$  acting around the bar outer surface,  $2\pi R_b dZ$ . A direct implication of equation (2.1) is that the axial load along the bar is not constant.

Regarding the grout annulus and the rock mass, their equilibrium is defined through the equation of motion,

$$\operatorname{div} \underline{\underline{\sigma}} + \underline{\underline{f}} = \underline{\underline{0}} \quad (2.2)$$

where  $\underline{\underline{\sigma}}$  is the Cauchy stress tensor and  $\underline{\underline{f}}$  represents the body forces per unit volume acting on the grout and the rock mass (they are equal to zero in this problem). For the relevant directions  $r$  and  $Z$ , it comes respectively that

$$\frac{\partial \sigma_{rr}}{\partial r} + \frac{1}{r} \frac{\partial \sigma_{r\theta}}{\partial \theta} + \frac{\partial \sigma_{rZ}}{\partial Z} + \frac{\sigma_{rr} - \sigma_{\theta\theta}}{r} + f_r = 0 \quad (2.3)$$

$$\frac{\partial \sigma_{ZZ}}{\partial Z} + \frac{\partial \sigma_{rZ}}{\partial r} + \frac{1}{r} \frac{\partial \sigma_{Z\theta}}{\partial \theta} + \frac{\sigma_{rZ}}{r} + f_Z = 0 \quad (2.4)$$

Within the context of the present research, these equations are solved assuming a generalized plane stress state; actually, as it can be seen in figure 2.1, the ground and the grout are free to deform axially at  $Z = L$ . For this reason, the plane strain hypothesis is less accurate to analyze the current configuration. Thus, the rotational invariance and the plane stress assumptions let simplify equations (2.3) and (2.4) as indicated in equations (2.5) and (2.6) respectively:

$$\frac{\partial \sigma_{rr}}{\partial r} + \frac{\sigma_{rr} - \sigma_{\theta\theta}}{r} = 0 \quad (2.5)$$

$$\frac{\partial \sigma_{rZ}}{\partial r} + \frac{\sigma_{rZ}}{r} = 0 \quad (2.6)$$

In the previous equations,  $\sigma_{rZ}$  refers to the shear stress,  $\tau$ . Let us clarify that while the shear stress  $\sigma_{rZ} = \tau$  is likely to vary along the  $Z$  coordinate, the term  $\partial \sigma_{rZ} / \partial Z$  in equation (2.3) has been neglected. This classic simplification, that can be found in numerous publications, allows to study the axial and radial directions separately (*i.e.*, it permits to dissociate the  $r$  and  $Z$  axes).

The resolution of equations (2.1), (2.5) and (2.6) taking into account the behaviour of the implicated materials will help understand the reinforcement response under a tensile load. In the current chapter, the radial behaviour of the grout and the ground will be dealt with first and afterwards their axial behaviour will be studied. Since at  $r = R_b$  the shear stress  $\tau_b$  obtained from equations (2.1) and (2.6) (*i.e.*, from the bolt and the annulus respectively) should be equal, it is explained in section 2.3 that the use of equation (2.6) may help obtain the interface shear stress (and hence, the axial load on the bolt) when the interface is coupled. Once decoupling starts, the bond-slip model  $\tau_b(W)$  may be obtained through pull-out test results as discussed in section 1.3 and subsection 2.4.3. Finally, in order to predict the grouted bar axial response (in terms of axial displacement, axial load and shear stress along the embedded length) once the interface bond-slip model is known, a new analytical solution has been developed and is fully explained in section 2.4. The influence of the embedment length on the pull-out response is explored through the use of this analytical solution.

## 2.2 Radial response of the grout and ground annuli

In this section, the radial stress  $\sigma_{rr}$  and displacement  $u_r$  within the grout and the surrounding ground will be evaluated analytically. The radial stress is particularly important because, since the bond has

a frictional component, the confining pressure acting at the bolt-grout interface (which is associated with the radial stress  $\sigma_{rr}(r = R_b)$ ) plays an important role.

Hereafter, compressive stresses are negative and tensile stresses are positive. At the same time, radial outward displacements are positive.

In the current development, it will be assumed that both the grout and the ground are linear elastic materials. Besides, as explained before, a generalized plane stress state is supposed. Hence, the constitutive equations may be expressed

$$\sigma_{ZZ} = (2\mu + \lambda)\varepsilon_{ZZ} + \lambda(\varepsilon_{rr} + \varepsilon_{\theta\theta}) = 0 \quad \Rightarrow \quad \varepsilon_{ZZ} = -\frac{\lambda}{2\mu + \lambda}(\varepsilon_{rr} + \varepsilon_{\theta\theta}) \quad (2.7)$$

$$\sigma_{rr} = (2\mu + \lambda)\varepsilon_{rr} + \lambda(\varepsilon_{\theta\theta} + \varepsilon_{ZZ}) = \frac{4\mu(\mu + \lambda)\varepsilon_{rr} + 2\mu\lambda\varepsilon_{\theta\theta}}{2\mu + \lambda} \quad (2.8)$$

$$\sigma_{\theta\theta} = (2\mu + \lambda)\varepsilon_{\theta\theta} + \lambda(\varepsilon_{rr} + \varepsilon_{ZZ}) = \frac{4\mu(\mu + \lambda)\varepsilon_{\theta\theta} + 2\mu\lambda\varepsilon_{rr}}{2\mu + \lambda} \quad (2.9)$$

where  $\lambda$  and  $\mu$  are the first and second Lamé's parameters, respectively. The latter is equal to the shear modulus of the material, so that

$$\lambda = \frac{\nu E}{(1 + \nu)(1 - 2\nu)} \quad (2.10)$$

$$\mu = \frac{E}{2(1 + \nu)} \quad (2.11)$$

The pertinent strain-displacement equations are

$$\varepsilon_{rr} = \frac{\partial u_r}{\partial r} = u_r' \quad (2.12)$$

$$\varepsilon_{\theta\theta} = \frac{u_r}{r} \quad (2.13)$$

Combining the equilibrium equation (2.5) with equations (2.8), (2.9), (2.12) and (2.13), one finds that

$$u_r'' + \frac{u_r'}{r} - \frac{u_r}{r^2} = 0 \quad \Rightarrow \quad u_r = \frac{1}{2}C_1 r + \frac{C_2}{r} \quad (2.14)$$

Therefore, replacing equations (2.12), (2.13), the expression for  $u_r$  in (2.14) and its first derivative in equations (2.8) and (2.9) gives

$$\sigma_{rr} = \frac{E}{2(1 - \nu)}C_1 - \frac{E}{1 + \nu}\frac{C_2}{r^2} \quad (2.15)$$

$$\sigma_{\theta\theta} = \frac{E}{2(1 - \nu)}C_1 + \frac{E}{1 + \nu}\frac{C_2}{r^2} \quad (2.16)$$

The constants  $C_1$  and  $C_2$  are calculated from the boundary conditions. In the case under study, both the grout and the ground are subjected to compressive stresses at their inner and outer radii. Hence,  $\sigma_{rr}(r = R_r) \equiv -p_r$ ,  $\sigma_{rr}(r = R_g) \equiv -p_g$  and  $\sigma_{rr}(r = R_b) \equiv -p_b$ . This yields

$$\sigma_{rr} = \frac{R_i^2 p_i - R_j^2 p_j}{R_j^2 - R_i^2} - \frac{(p_i - p_j) R_i^2 R_j^2}{R_j^2 - R_i^2} \frac{1}{r^2} \quad (2.17)$$

$$\sigma_{\theta\theta} = \frac{R_i^2 p_i - R_j^2 p_j}{R_j^2 - R_i^2} + \frac{(p_i - p_j) R_i^2 R_j^2}{R_j^2 - R_i^2} \frac{1}{r^2} \quad (2.18)$$

$$u_r = \frac{(1 - \nu_j)}{E_j} \frac{R_i^2 p_i - R_j^2 p_j}{R_j^2 - R_i^2} r + \frac{(1 + \nu_j)}{E_j} \frac{(p_i - p_j) R_i^2 R_j^2}{R_j^2 - R_i^2} \frac{1}{r} \quad (2.19)$$

where  $\{i, j\} = \{b, g\}$  for the grout annulus and  $\{i, j\} = \{g, r\}$  for the ground. The hoop stress  $\sigma_{\theta\theta}$  is important because, if the radial compressive pressure at  $R_b$  in the grout (or at  $R_g$  in the ground) increases in absolute value and exceeds its value at  $R_g$  (or  $R_r$ ), the hoop stress becomes a decreasing function of the radius and it may turn positive and eventually reach the grout (or ground) tensile strength. If the tensile strength of these materials is attained, radial fractures will appear, which are likely to modify the interface behaviour. In the geometry under study, any possible radial fracture will start at  $R_b$  in the grout (or at  $R_g$  in the ground) and propagate towards the outer boundary. The radial pressure at the formation of radial fractures is given by

$$p_{i,crit} = \frac{2p_j R_j^2 + R_{t,j} (R_j^2 - R_i^2)}{R_j^2 + R_i^2} \quad (2.20)$$

where  $R_{t,j}$  is the grout or ground tensile strength. Equation (2.20) indicates that low pressures  $p_j$  make the formation of radial fractures easier.

## 2.3 Axial response of the grout and ground annuli

Solving equation (2.6), it comes that

$$\frac{\partial}{\partial r} (\tau r) = 0 \Rightarrow \tau r = C \Rightarrow \tau = \frac{C}{r} \quad (2.21)$$

The boundary condition is  $\tau(r = R_b) \equiv \tau_b$ . Therefore,

$$\tau = \frac{\tau_b R_b}{r} \quad (2.22)$$

Equation (2.22) is a continuous function of the radius and it applies  $\forall r \in [R_b, R_r]$ . As it can be inferred from this equation, the shear stress in the grout is maximum at  $r = R_b$  and in the rock it is maximum at  $r = R_g$ . Moreover, thicker resin layers offer lower load transfer possibilities. Besides, at  $r = R_b$  the shear stress in the grout and the bolt are equal.

It should be also noted that interfaces are in general weaker than solid bodies and that failure takes place along the surface of minimum strength. Bearing these two facts in mind, and according to equation (2.22), failure is more likely to take place at the bolt-grout interface; however, if the borehole wall is particularly weak, the shear strength of this interface may be attained by the shear stress  $\tau(r = R_g) \equiv \tau_g$  before the bolt-grout interface shear strength is reached by the shear stress,  $\tau_b$ .

The grout and rock shear behaviour is defined below, assuming linear elasticity and that the axial and radial displacements,  $w$  and  $u_r$  respectively, verify  $|\frac{\partial w}{\partial r}| \gg |\frac{\partial u_r}{\partial Z}|$  (this hypothesis has been corroborated by way of a simple numerical simulation of the geometry under study):

$$\tau = \begin{cases} \frac{E_g}{2(1+\nu_g)} \left( \frac{\partial u_r}{\partial Z} + \frac{\partial w}{\partial r} \right) = \frac{E_g}{2(1+\nu_g)} \frac{\partial w}{\partial r}, & \forall r \in ]R_b, R_g[ \\ \frac{E_r}{2(1+\nu_r)} \left( \frac{\partial u_r}{\partial Z} + \frac{\partial w}{\partial r} \right) = \frac{E_r}{2(1+\nu_r)} \frac{\partial w}{\partial r} & \forall r \in ]R_g, R_r[ \end{cases} \quad (2.23)$$

Let  $\mu_i = \frac{E_i}{2(1+\nu_i)}$  be the shear modulus of each material. The combination of the equilibrium equa-

tion (2.22) with the constitutive equation (2.23) yields

$$w(R_g^-) - w(R_b^+) = \frac{\tau_b R_b}{\mu_g} \ln(R_g/R_b) \quad (2.24)$$

$$w(R_r^-) - w(R_g^+) = \frac{\tau_b R_b}{\mu_r} \ln(R_r/R_g) \quad (2.25)$$

The superscripts  $+$  and  $-$  account for both sides of each interface. In fact, the axial displacement  $w$  may be discontinuous at  $r = R_b$  and/or  $r = R_g$ , should a relative slip between each pair of materials occur. Let  $\bar{w}_i = w_i^- - w_i^+$  be the relative slip at the  $i$  interface. The combination of equations (2.24) and (2.25) gives

$$\tau_b R_b \left( \frac{\ln(R_r/R_g)}{\mu_r} + \frac{\ln(R_g/R_b)}{\mu_g} \right) + w_b^- - \bar{w}_b - \bar{w}_g - w_r^- = 0 \quad (2.26)$$

where  $w_b^- \equiv W$ . In practice (in field situations in particular), the radius  $R_r$  is chosen big enough to disregard the ground axial displacement  $w_r^-$ . Therefore, before any relative slip takes place (*i.e.*, when the interfaces are totally coupled), equation (2.26) is useful to derive the shear stress at the bolt-grout interface  $\tau_b$  from the elastic properties of the grout and the ground. This is the approach used by Farmer and Li and Stillborg [Farmer1975, Li1999] exposed in section 1.3. However, when the axial slip starts, the use of equation (2.26) is less obvious.

## 2.4 New analytical solution to the behaviour of grouted bolts under tensile loads

Knowledge of the bond-slip model  $\tau_b(W)$  lets determine analytically the full range behaviour of a CMC rockbolt subjected to a tensile load. In this section, the new approach developed is presented. Through the use of the  $\tau_b(W)$  relationship, this approach allows to predict the distribution of the axial force, the axial displacement and the shear stress along the embedded length of the bar during a pull-out test. Consequently, the load-displacement curve obtained in a test may be reproduced by plotting the axial force as a function of the axial displacement at the point where the load is applied.

In the following discussion, the  $Z$  axis will be set in the bolt-grout interface, so that  $Z = 0$  corresponds to the far end of such interface (*i.e.*, the bolt free end) and  $Z = L$  corresponds to the point where the load is applied. Two different cases, identified by the parameter  $k$ , have been considered with respect to the evolution of the embedment length:

- if at  $Z = 0$  the bolt exceeds the borehole sufficiently, the embedment length does not change throughout the test, so that the contact between the grouting material and the bolt is made along  $Z \in [0, L]$  for the entire duration of the experiment (*i.e.*, the length of the interface between the bolt and the grout does not change). The variable  $T \geq 0$  is then defined as the bolt axial displacement at the position  $Z = 0$ .

In the mathematical model described below, this case has been identified by  $k = 0$ . This situation is often encountered in the laboratory: for instance, Hyett *et al.* and Moosavi *et al.* [Hyett1995, Moosavi2005] conducted their experimental campaign using a constant embedment length;

- if at  $Z = 0$  the bolt does not exceed the borehole, the contact length between the bolt and the

grouting material decreases throughout the test (*i.e.*, the embedment length decreases). This case has been identified by  $k = 1$ , so that at the beginning of the test ( $T = 0$ ) the bolt free end is at point  $Z = kT = 0$  and as the test progresses ( $T > 0$ ), the free end will move towards  $Z = L$  and the contact will be made along  $Z \in [T, L]$ .

In typical field pull-out tests, the embedment length decreases during the test; however, if such length is very long with respect to the bar axial displacement, it may be assumed that the test is carried out under constant embedment length conditions. In the laboratory, several studies (*cf.* [Benmokrane1995, Hagan2004, Ivanovic2009], for example) have also been conducted using a decreasing embedment length.

Let  $W(Z, T)$  be the axial displacement of the bolt cross-section that is in front of point  $Z$  of the interface. The use of the variable  $T$  as a *cinematic time* will be explained below. The axial strain of the rockbolt is  $W' = \frac{\partial W}{\partial Z}$ . Let  $F$  be the axial force on the bolt ( $\sigma_b$  is the axial stress), which decreases along the embedment length from its maximum value at  $Z = L$  to zero at the bolt free end,  $Z = kT$ .

As it has been explained, the bolt equilibrium at any moment is given by equation (2.1). It will be accepted henceforth that the shear slip  $U(Z, T)$  at the interface (*i.e.*, the relative displacement between the rockbolt and the grouting material) equals the axial displacement of the rockbolt,  $W(Z, T)$ . This simplification is true as long as the axial movement of the grout (and the ground) is blocked. It will be assumed as well that the bolt remains within the elastic range during the whole pull-out test. The Young's modulus of the bolt is  $E_b$ . Thus, the rockbolt constitutive equation is

$$F(Z, T) = \pi R_b^2 \sigma_b(Z, T) = \pi R_b^2 E_b W' \quad (2.27)$$

According to equation (2.27), once  $W'$  is known, the axial force  $F$  is also known (at every point  $Z$  of the interface and at every stage  $T$  of the pulling process). The pull-out test is then completely characterized by  $W(L, T)$  and  $W'(L, T)$ , at the extremity  $Z = L$ .

As for the interface, it was explained in section 1.3 that its constitutive law is fully described by the relationships  $\tau_b(W, p_b)$  and  $\Delta u_{rb}(W, p_b)$ ; however, during a pull-out test the interface shear response can be reduced to a relationship  $\tau_b(W)$  if the annuli radial behaviour is accounted for. Moreover, the bond-slip model  $\tau_b(W)$  is only applicable in the case of a monotonic solicitation, which means that  $\forall Z \in [kT, L]$  the axial displacement  $W(Z, T)$  must be an increasing function of time. Given that the variable  $T$  increases with time and that it equals the axial displacement  $W$  at point  $Z = kT$  (the bolt free end), it can be used as a *cinematic time*.

Furthermore, in practice  $\tau_b(W)$  is a continuous function defined as follows:  $\tau_b(W) > 0$  for  $W > 0$  and  $\tau_b(W) = 0$  otherwise. Its derivative  $\tau_b'(W) = \frac{d\tau_b}{dW}$  is a piecewise-defined function that must verify

$$\tau_b' \leq 0 \text{ when } \tau_b'' > 0 \quad (2.28)$$

The explanation to this condition is given in subsection 2.4.2. Hence, combining equations (2.1) and (2.27) with the bond-slip model  $\tau_b(W)$ , the governing equation of the pull-out test problem is

$$W'' = \frac{2}{E_b R_b} \tau_b(W) \quad (2.29)$$

For a given value of  $T$ , the problem is thereby reduced to finding the axial displacement  $W$  (as a

function of  $Z$ ) that solves the differential equation (2.29). Boundary conditions are

$$\begin{aligned} W(kT, T) &= T \\ W'(kT, T) &= 0 \end{aligned} \quad (2.30)$$

Since the aforementioned boundary conditions do not depend on point  $Z = L$  (they are both related to the free end of the rockbolt), it is possible to solve equation (2.29) for  $Z \in [kT, +\infty[$ . Actually, the innovation of this new approach proposed to solve the pull-out test problem lies in not using boundary conditions related to  $Z = L$  (classically, the pull-out test problem is solved using the following boundary conditions:  $W'(0) = 0$  and  $W'(L) = \frac{\sigma_b(L)}{E_b}$ ).

On the other hand, the condition  $W(kT, T) = T$  together with  $T > 0$  allows the use of the variable  $T$  as the only control parameter during the pull-out test. This is particularly useful for tests conducted under axial displacement control conditions. The experimental campaign presented in chapter 3 has been executed under these conditions, because they are very useful to fully study the bolt-grout interface response under tensile axial loads.

To sum up, the data required to solve the problem given by equation (2.29) with the boundary conditions (2.30) are:  $k$ ,  $R_b$ ,  $E_b$ ,  $L$  and the interface bond-slip model,  $\tau_b(W)$ . A complementary condition is  $\frac{\partial W}{\partial T} \geq 0 \forall Z \in [kT, L]$ .

It should be noted that the approach to the problem presented above is also valid when failure takes place at the grout-rock interface; in such a case, an appropriate bond-slip model, the borehole radius and an equivalent material Young's modulus should be used. Anyway, the mathematical problem remains the same.

### 2.4.1 Resolution method

The problem is solved using reduced variables because this leads to a generalized solution. The new variables are therefore

$$z = \frac{Z}{R_b} \quad (2.31)$$

$$t = \frac{T}{R_b} \quad (2.32)$$

$$w(z, t) = \frac{W(Z, T)}{R_b} \quad (2.33)$$

$$f(w) = \frac{2\tau_b(W)}{E_b} \quad (2.34)$$

Thus, the new differential equation is

$$w'' = f(w) \quad (2.35)$$

with the following boundary conditions pertaining to  $z = kt$ :

$$\begin{aligned} w(kt, t) &= t \\ w'(kt, t) &= 0 \end{aligned} \quad (2.36)$$

and the complementary condition  $\frac{\partial w}{\partial t} \geq 0 \forall z \in [kt, L/R_b]$ . The pull-out test is now characterized by  $w(L/R_b, t)$  and  $w'(L/R_b, t)$ .

Inasmuch as  $w'' \geq 0$ ,  $w'$  is an increasing function  $\forall z \in [kt, +\infty[$ . Moreover  $w'(kt, t) = 0$ ;

therefore  $w' \geq 0 \forall z \in [kt, +\infty[$ . This means that  $w$  is an increasing function too, and given that  $w(kt, t) = t \geq 0$ , it follows that  $w \geq 0 \forall z \in [kt, +\infty[$ .

In order to solve the problem easily, equation (2.35) may be multiplied by  $w'$ . Let  $g(w)$  be the increasing positive function defined by

$$g(w) = 2 \int_0^w f(u) du \quad (2.37)$$

Therefore, the function  $g(w)$  is known as long as the interface bond-slip model is known. Equation (2.35) may now be written

$$\frac{\partial (w')^2}{\partial z} - \frac{\partial g(w)}{\partial z} = 0 \Rightarrow \frac{\partial}{\partial z} \left( (w')^2 - g(w) \right) = 0 \Rightarrow (w')^2 - g(w) = C \quad (2.38)$$

where  $C$  is a constant. Considering the boundary conditions (2.36) and the fact that  $w' \geq 0$ , it comes that

$$C = -g(t)$$

and consequently

$$w' = \sqrt{g(w) - g(t)} \quad (2.39)$$

The problem has been reduced to solving the first order differential equation (2.39) with the boundary condition  $w(kt, t) = t$ .

As long as  $z > kt$ ,  $w' > 0$  and as a result  $w$  is a strictly increasing function of  $z$ . This makes it possible to inverse the problem, and so to calculate  $z$  as a function of  $w$ . It comes that

$$\int_{kt}^z dz = \int_t^w \frac{du}{\sqrt{g(u) - g(t)}} \Rightarrow z - kt = \int_t^w [g(u) - g(t)]^{-1/2} du = \zeta(w) \quad (2.40)$$

In short, from the known function  $f(w)$ , the functions  $g(w)$  and  $\zeta(w)$  are calculated, and then, the inversion of  $\zeta(w)$  permits the determination of the axial displacement  $w$  and the axial strain  $w'$  as a solely function of  $t$  for a given  $z$ . A detailed explanation of this new solution is presented in the next subsection. A tri-linear bond-slip model has been considered for the tendon-grout interface because the literature review in chapter 1 has indicated that this model has often been used with quite satisfactory results. However, it is important to notice that the new tool is able to deal with any other form of bond-slip model, which, as explained before, can be obtained from experimental data.

### 2.4.2 Analytical solution using a tri-linear bond-slip model

The bond-slip model considered is shown in figure 2.2. It is characterized by four pairs in reduced variables:  $(w_0, f_0) \equiv (0, 0)$ ,  $(w_1, f_1)$ ,  $(w_2, f_2)$  and  $(w_3, f_3)$ . These pairs divide the function  $f(w)$  into three intervals that correspond to  $]w_{i-1}, w_i[$  for  $i \in \{1, 2, 3\}$ . Inside each interval  $f'_i$  is constant, so that

$$f(w) = f_i + f'_i(w - w_i) \quad (2.41)$$

with

$$f'(w) = f'_i = \frac{f_i - f_{i-1}}{w_i - w_{i-1}} \quad (2.42)$$

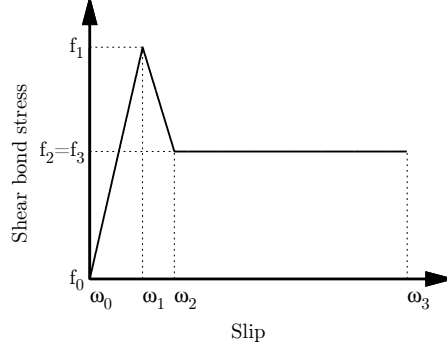


**Figure 2.2:** bond-slip model considered and characteristic parameters.

The values for function  $g(w)$  are  $g_i = g(w_i)$  with  $g_0 = 0$ . For  $i \in \{1, 2, 3\}$ , the  $g_i$  are calculated by integration:

$$g_i = g_{i-1} + (f_i + f_{i-1})(w_i - w_{i-1}) \quad (2.43)$$

Similarly, inside each interval  $]w_{i-1}, w_i[$ ,

$$g(w) = g_i + [f(w) + f_i](w - w_i) \quad (2.44)$$

In order to determine the integral  $\int [g(w) - g(t)]^{-1/2} dw$ , function  $h(w)$  is defined as follows:

$$h(w) = f(w)^2 - f'(w)[g(w) - g(t)] \quad (2.45)$$

with

$$h'(w) = -f''(w)[g(w) - g(t)] \quad (2.46)$$

Equation (2.45) indicates that for  $t > 0$ ,  $h(t) = f^2(t) > 0$ . Thus, as long as the derivative  $h'(w) \geq 0$ , the function  $h(w)$  will be positive,  $h(w) > 0$ . In case  $f''(w) > 0$ , the derivative verifies  $h'(w) < 0$ . However, the condition in equation (2.28) guarantees that  $f' \leq 0$  when  $f'' > 0$ . So, in case  $f'' > 0$ , using equation (2.45) one obtains  $h(w) > 0$ . Consequently,  $h(w) > 0$  in every possible case.

In the particular case of a tri-linear bond-slip model, it comes that

$$h'(w) = -f''(w)[g(w) - g(t)] = 0 \quad (2.47)$$

Hence, inside each interval  $]w_{i-1}, w_i[$ ,

$$h(w) = h_i(t) = f_i^2 - f'_i[g_i - g(t)] > 0 \quad (2.48)$$

And so, for  $]w_{i-1}, w_i[$ ,  $i \in \{1, 2, 3\}$ :

- if  $f'_i \neq 0$ ,

$$g(w) - g(t) = \frac{f(w)^2 - h_i(t)}{f'_i} \quad (2.49)$$

and  $dw = df/f'_i$  ;

- if  $f'_i = 0$ ,

$$g(w) - g(t) = g_i + 2f_i(w - w_i) - g(t) \quad (2.50)$$

In the same way, the evolution of the bolt free end reduced axial displacement, which is represented

by the control parameter  $t > 0$ , is described by  $w_{j-1} \leq t \leq w_j$ ,  $j \in \{1, 2, 3\}$ . Thus for  $]w_{j-1}, w_j[$ ,

$$f(t) = f_j + f'_j(t - w_j) \quad (2.51)$$

$$f'(t) = f'_j = \frac{f_j - f_{j-1}}{w_j - w_{j-1}} \quad (2.52)$$

$$g(t) = g_j + [f(t) + f_j](t - w_j) \quad (2.53)$$

Let us now focus on function  $\zeta(w) = \int_t^w [g(u) - g(t)]^{-1/2} du$ , which varies with  $t$ . Given that for  $w' > 0$  the reduced axial displacement  $w$  is a strictly increasing function of  $z$ , it comes that  $w(z, t) > t$  for  $z > kt$ . As for the two indices that characterize the bond-slip model discretization,  $]w_{m-1}, w_m[$  where  $m = \{i, j\}$ , this implies that  $i \geq j$ , meaning that the displacement of any point  $z \in ]kt, L/R_b[$  is larger than the displacement of the bolt free end,  $t$ , even if they are both in the same interval  $]w_{m-1}, w_m[$ . The function  $\zeta(w)$  is then defined by  $\zeta_0 = 0 < \zeta_1 < \zeta_2 < \zeta_3$ , where:

- for  $i < j$ ,

$$\zeta_i = 0 \quad (2.54)$$

- for  $i = j$ ,

$$\zeta_j = \int_t^{w_j} [g(u) - g(t)]^{-1/2} du \quad (2.55)$$

- for  $i > j$ ,

$$\zeta_i = \zeta_{i-1} + \int_{w_{i-1}}^{w_i} [g(u) - g(t)]^{-1/2} du \quad (2.56)$$

Thus  $\zeta_i$ ,  $i \in \{1, 2, 3\}$  are only function of  $t$ . From a physical point of view, they represent the evolution during the pull-out test of the boundary position of each characteristic state of the bond-slip model (*i.e.*, elastic, softening or residual behaviour, represented by  $]w_{i-1}, w_i[$ ) with respect to the bolt free end,  $z = kt$ . Since the maximum axial force occurs at  $z = L/R_b$ , every possible state of the interface will start at this point and move towards  $z = kt$ . Thereby,  $\zeta_1$  represents the spatial evolution of the elastic domain boundary: as the test goes on (*i.e.*, as  $t$  increases), this boundary will move from  $z = L/R_b$  to  $z = kt$  and arrive at the free end when  $t = w_1$ . As  $\zeta_1$  moves towards  $z = kt$ ,  $\zeta_2$  and  $\zeta_3$  will progressively appear at  $z = L/R_b$  and move in turn towards the bolt free end.

Three scenarios are possible to determine  $\int [g(w) - g(t)]^{-1/2} dw$  in either  $[w_{i-1}, w_i]$  or  $[t, w_j]$ . Let  $[w_a, w_b]$  be a generic interval:

- if  $f'_b > 0$ ,

$$\int_{w_a}^{w_b} [g(u) - g(t)]^{-1/2} du = \frac{\operatorname{arccosh}(f_b/\gamma) - \operatorname{arccosh}(f_a/\gamma)}{\beta} \quad (2.57)$$

- if  $f'_b < 0$ ,

$$\int_{w_a}^{w_b} [g(u) - g(t)]^{-1/2} du = \frac{\arccos(f_b/\gamma) - \arccos(f_a/\gamma)}{\beta} \quad (2.58)$$

- if  $f'_b = 0$ ,

$$\int_{w_a}^{w_b} [g(u) - g(t)]^{-1/2} du = \frac{\sqrt{g_a + 2f_a(w_b - w_a) - g(t)} - \sqrt{g_a - g(t)}}{f_a} \quad (2.59)$$

where the constants  $\beta$  and  $\gamma$  are defined by:  $\beta = \sqrt{|f'_b|}$  and  $\gamma = \sqrt{h_b(t)}$ .

The development of the analytical solution for a given  $z$  (*i.e.*, the position where the axial force and the axial displacement are to be determined) involves consequently the following steps:

1. Calculating  $\zeta_i$ ,  $i \in \{1, 2, 3\}$  for  $i \geq j$  ( $j \in \{1, 2, 3\}$ ) according to equations (2.54), (2.55) and (2.56). The analytical development of such functions is helped by equations (2.57), (2.58) and (2.59) as appropriate. All the values required can be obtained using equations (2.42), (2.43), (2.48), (2.51), (2.52) and (2.53);
2. Finding  $\zeta_i$  such that  $\zeta_{i-1} < z - kt < \zeta_i$ . The axial displacement  $w(z, t)$  will be therefore inside  $[w_{i-1}, w_i]$ ;
3. Calculating  $z - kt - \zeta_i = \int_{w_i}^w [g(u) - g(t)]^{-1/2} du$ . Again, equations (2.57), (2.58) and (2.59) are used as appropriate;
4. Inversing the last expression leads to the determination of  $f(w)$  if  $f' \neq 0$  and to the determination of  $w$  if  $f' = 0$ . In the former case, integration of  $f(w)$  gives  $w'$  and  $w$  can be determined by

$$w = w_i + \frac{f(w) - f_i}{f'_i} \quad (2.60)$$

In the latter case, derivation of  $w$  with respect to  $z$  gives  $w'$ .

A new analytical solution to the pull-out test problem is henceforth available. A prediction of the load-displacement curve is supplied by the last equations applied to point  $z = L/R_b$ . In addition, the application of steps 1-4 when the whole interface is within the elastic stage (that is, when  $z - kt < \zeta_1$ ), yields the following load-displacement relation:

$$w' = w \sqrt{f'_1} \tanh\left(\sqrt{f'_1}(z - kt)\right) \quad (2.61)$$

Bearing in mind the function  $\tanh(x)$ , it is deduced from equation (2.61) that there exists a critical length beyond which the axial force at the end of the elastic stage remains essentially the same; in other words, when the interface is longer than a critical length  $L_c$ , only part of the bonded length of the bolt will carry most of the load when the interface behaves elastically. Since  $\tanh(2.6) \approx 0.99$ , such length can be approximated by

$$L_c \approx \frac{2.6R_b}{\sqrt{f'_1}} \quad (2.62)$$

### 2.4.3 Determination of the bond-slip model

The load-displacement curve obtained in a pull-out test may help derive a bond-slip model,  $\tau_b(W)$ . The requirements to be able to deduce a full constitutive law (including the normal and tangential directions) from pull-out test results are not described here, but in chapter 4. The bond-slip model determination, and more generally the definition of an interface behaviour model is a crucial step in the design of fully grouted rockbolts. Through the execution of pull-out tests in the correct conditions, matter that will be discussed in chapters 3 and 4, the influence of various parameters such as the grout quality, the borehole-to-rockbolt-diameter ratio, the confining pressure and the borehole roughness can be studied, and the most influencing ones can then be determined. Since the constitutive law of the tendon-grout interface (or the grout-rock interface if failure takes place at  $r = R_g$ ) is an intrinsic property, it does not depend on the embedment length, nor does the bond-slip model. Therefore, the validation of such model can be carried out by conducting two pull-out tests under identical conditions

but with different anchoring lengths. The monitoring of a pull-out test provides the following data:  $w'(L/R_b, t)$  and  $w(L/R_b, t)$ . Equation (2.39) can then be written

$$w'(L/R_b, t) = \sqrt{g(w(L/R_b, t)) - g(t)} \quad (2.63)$$

The relationship between  $f(w)$  and  $g(w)$  would yield to the determination of the bond-slip model:

$$g(w) = 2 \int_0^w f(u) du \Rightarrow f(w) = \frac{g'(w)}{2} \quad (2.64)$$

However, even if  $t$  (bolt free end displacement) were monitored, it would be in general not possible to deduce a single expression for  $g(w)$ . There are two extreme cases where  $f(w)$  can be unequivocally determined:

- the embedment length is long enough, so that  $t \ll w(L/R_b, t)$ . In this case,

$$[w'(L/R_b, t)]^2 \approx g(w(L/R_b, t)) \quad (2.65)$$

Equation (2.65) is accurate for small values of axial displacement. Once debonding (*i.e.*, full decoupling) has occurred along the interface, the difference between the displacements of both bolt ends becomes

$$w(L/R_b, t) - t = 0.5f_3(L/R_b - kt)^2 \quad (2.66)$$

- the embedment length is short enough to ensure a uniform distribution of  $f(w)$  in  $[kt, L/R_b]$ . This is the typical case in laboratory set-ups. It comes that

$$f(w(L/R_b, t)) \approx \frac{w'(L/R_b, t)}{L/R_b - kw(L/R_b, t)} \quad (2.67)$$

As it can be seen, neither of the two situations require the bolt free end displacement. Besides, it is important to note that, in general, *in situ* pull-out tests do not allow the determination of an accurate bond-slip model for the rockbolt-grout interface, because the embedment lengths tested are too long.

#### 2.4.4 Comparison of analytical predictions with experimental results

In order to evaluate the analytical approach presented in this section, experimental data issued from both field and laboratory pull-out tests have been compared to the predicted load-displacement curves. The comparisons are presented here, together with the way the bond-slip model has been determined.

##### Field pull-out test

Chen and Ren [Chen2008] carried out a pull-out test on a novel steel strand rockbolt whose properties were:  $R_b = 7.63$  mm,  $E_b = 200$  GPa and  $L = 5$  m. The load-displacement result obtained during the test is shown as points in figure 2.3b. This test has also been analyzed by Ren *et al.* [Ren2010], *cf.* figure 1.26.

From these data, a tri-linear set of parameters has been derived. Considering the embedment length announced, the first case in subsection 2.4.3 has been accounted for; hence, from the experimental force data, the strain  $w'$  has been calculated (the bolt remained within the elastic range during the test) and the values of function  $g(w)$  have been estimated using equation (2.65). The reduced shear stresses

$f_i$  have been obtained using equation (2.64). Then, the best set of parameters  $(w_i, f_i)$ ,  $i \in \{1, 2, 3\}$  has been computed by a good fit to the experimental data using the new analytical solution applied to  $z = L/R_b \approx 655$ . Since the third interval of the bond-slip model is a horizontal plateau, the value of  $w_3$  is only dependent on the amount of axial displacement that takes place during the pull-out test. The relevant parameters are:  $w_1 = \frac{1.45}{R_b} = 0.19$ ,  $w_2 = \frac{12.60}{R_b} = 1.65$ ,  $f_1 = \frac{2 \cdot 1.62}{E_b} = 1.62 \cdot 10^{-5}$  and  $f_2 = f_3 = \frac{2 \cdot 0.34}{E_b} = 3.40 \cdot 10^{-6}$ . This bond-slip model is plotted in figure 2.3a.

Once all the input data are known, the steps 1-4 in part 2.4.2 have been performed. The axial displacement  $w$  and the axial strain  $w'$  at  $z = L/R_b$  have been sequentially obtained as a function of the bolt free end displacement,  $t$ . The predicted load-displacement curve is represented by the solid line in figure 2.3b. The accuracy of the prediction is quite satisfactory.

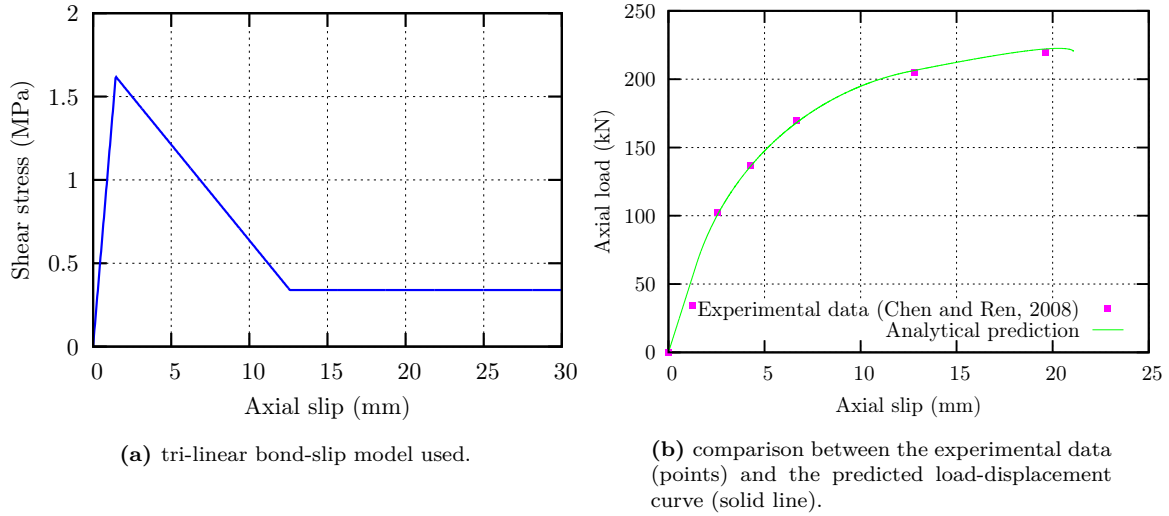


**Figure 2.3:** comparison between predicted solution and experimental results. The bond-slip model used has been derived from the experimental data obtained in a field pull-out test conducted by Chen and Ren [Chen2008].

It is important to highlight that other sets of parameters close to the one selected could have been used to reproduce the experimental data fairly well. This is due to the large embedment length in use; as announced, short embedment lengths are more reliable to deduce a bond-slip model from experimental data.

### Laboratory pull-out test

The pull-out tests conducted by Benmokrane *et al.* [Benmokrane1995] on rockbolts and presented in the left-hand side graph in figure 1.23 have been analyzed here. These results are shown as points in figure 2.4b. The relevant characteristics of the tested rockbolts are:  $R_b = 7.9$  mm,  $E_b = 205$  GPa,  $L_1 = 14R_b = 110$  mm,  $L_2 = 22R_b = 174$  mm and  $L_3 = 28R_b = 221$  mm.

The tri-linear bond-slip model proposed by Benmokrane *et al.* [Benmokrane1995] for the cement grout named *CG6 grout* will be used first to validate the new analytical approach. Since the embedment length decreased during these pull-out tests (see the *Model A* set-up in figure 1.22), the case  $k = 1$  has been considered. The parameters of the bond-slip model are:  $w_1 = \frac{2 \cdot 90}{R_b} = 0.37$ ,  $w_2 = \frac{10.60}{R_b} = 1.34$ ,  $f_1 = \frac{2 \cdot 12.80}{E_b} = 1.25 \cdot 10^{-4}$  and  $f_2 = f_3 = \frac{2 \cdot 3.70}{E_b} = 3.61 \cdot 10^{-5}$ . This model is plotted in figure 2.4a. The comparison between the experimental data and the predicted load-displacement curves offered by the new analytical tool is shown in figure 2.4b.

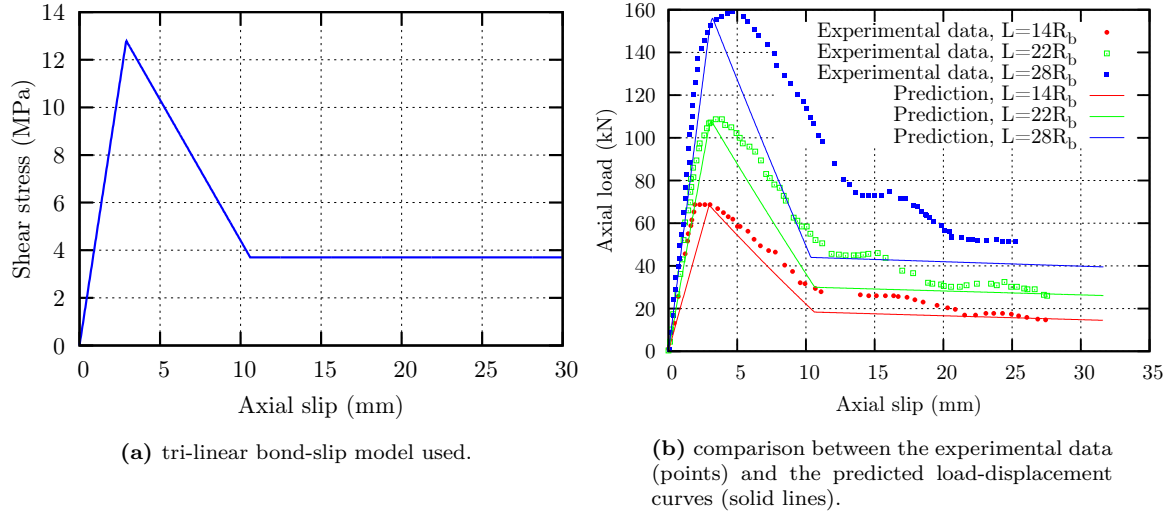


**Figure 2.4:** comparison between predicted solution and experimental results. The bond-slip model used has been proposed by Benmokrane *et al.* [Benmokrane1995] and is derived from laboratory pull-out test results.

It can be seen that the use of the tri-linear bond-slip model defined above does not allow a totally accurate prediction of the experimental results (the peak and residual loads are quite well reproduced, but not the general trend of the load-displacement curves). The following set of parameters has been tried:  $w_1 = \frac{3.00}{R_b} = 0.38$ ,  $w_2 = \frac{13.00}{R_b} = 1.65$ ,  $f_1 = \frac{2 \cdot 12.80}{E_b} = 1.25 \cdot 10^{-4}$  and  $f_2 = f_3 = \frac{2 \cdot 4.80}{E_b} = 4.68 \cdot 10^{-5}$ . This bond-slip model and the comparison between the experimental data and the analytical predictions are displayed in figure 2.5.

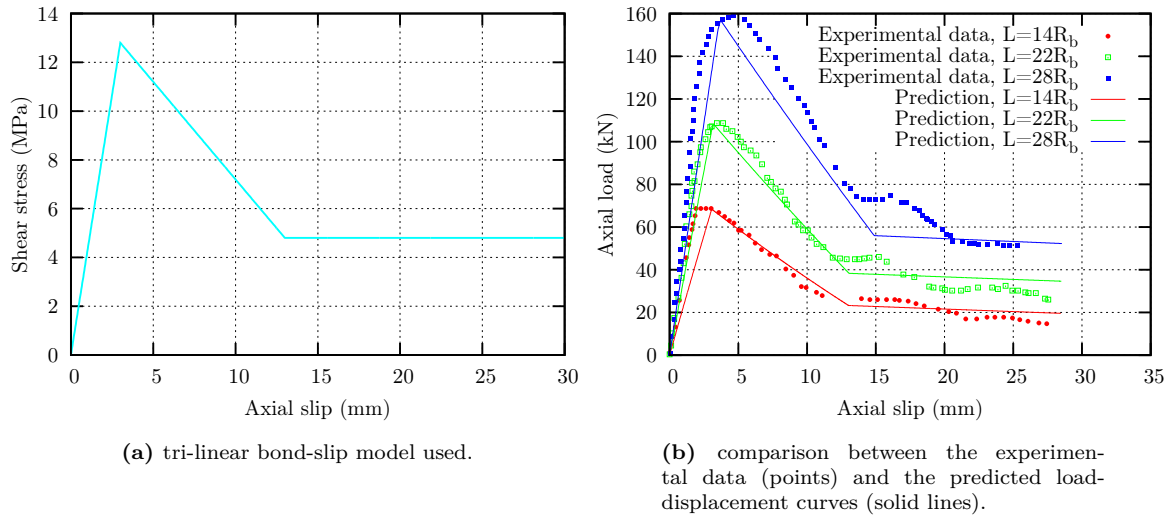


**Figure 2.5:** comparison between predicted solution and experimental results. A different bond-slip model, derived from the same laboratory pull-out test results, has been used.

In order to check the feasibility of a better prediction, the same experimental data have been used to infer a bond-slip model. Given that the embedment lengths in use are short, the second case in subsection 2.4.3 has been taken into account with  $k = 1$ , so that the reduced shear stress has been calculated from the experimental data using equation (2.67). The results (in non-reduced variables) are shown as points in figure 2.6a.

It can be noticed that, as expected, the shear stress hardly depends on the embedment length

(the small differences may be explained by the scatter in the results). Moreover, with a view to these results, the non-linear bond-slip model defined in equation (2.68) has been considered:

$$f(w) = (a \cdot w - c) \cdot \exp(-b \cdot w^d) + c \quad (2.68)$$

with  $a = 7.06 \cdot 10^{-4}$ ,  $c = 4.31 \cdot 10^{-5}$ ,  $b = 2.85$  and  $d = 1.08$ . This model is represented in figure 2.6a. The experimental data and the predicted load-displacement curves for the three embedment lengths announced are shown in figure 2.6b. As it can be seen, the use of a non-linear bond-slip model provides more satisfactory results than a tri-linear model. Likewise, these results prove that the use of equation (2.67) is accurate for the typical embedment lengths used in the laboratory.

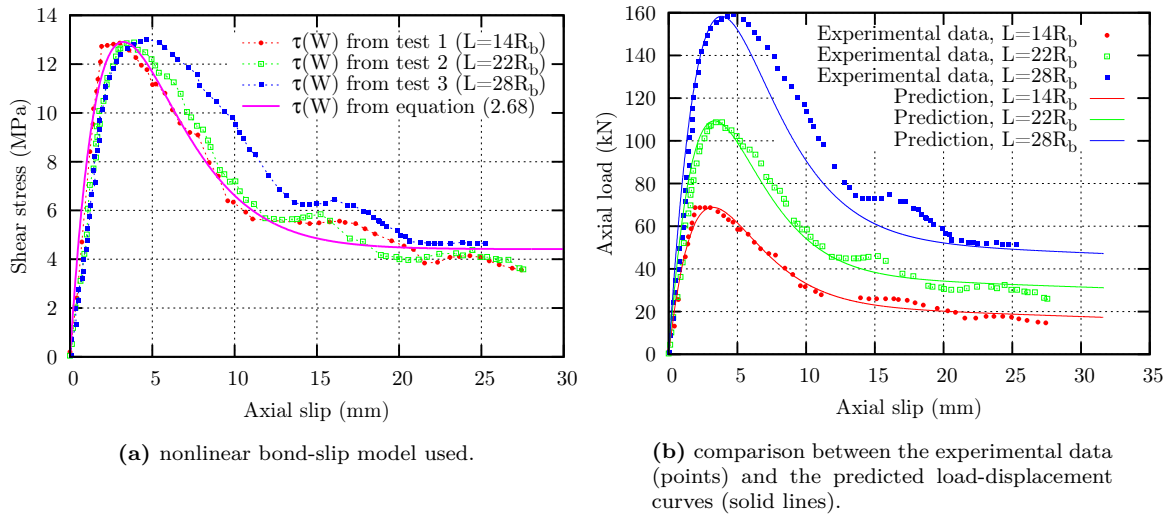


**Figure 2.6:** comparison between predicted solution and experimental results. The nonlinear bond-slip model as derived from laboratory experimental data (*cf.* [Benmokrane1995]) using equation (2.67) has been used.

Finally, it is important to notice that, even if a non-linear bond-slip model predicts more accurately the total pull-out response, a tri-linear bond-slip model has been initially used in the analysis presented in chapter 4. The two main reasons for this choice are the fact that the differences between the predictions provided by the two models do not concern the peak and residual values (which are after all the most important information) and the ease of handling a tri-linear curve over a non-linear curve in mathematical analysis.

### 2.4.5 Influence of the embedment length

The experimental results in the field and the laboratory discussed in the last subsection (figures 2.3b and 2.4b respectively) show important differences. In particular, the maximum axial load in the laboratory is reached for short values of axial slip, whereas in the field, the peak force is reached for much higher slips. It should be highlighted that these tests are considered to be satisfactory tests and that many other analyzed tests show comparable results. Even if the tests were not conducted under the same conditions (for instance, the bond-slip model is not the same, nor is the geometry or the bolt mechanical properties), it will be seen in this subsection that the embedment length plays an important role on the pull-out response. To do so, the new analytical tool will be used to predict the load-displacement curves of several tests conducted using a constant embedment length (case  $k = 0$ ). The only difference between these tests will be the length used.

Let us consider a rockbolt with  $R_b = 12.5$  mm,  $E_b = 160$  GPa and elastic limit  $\sigma_e = 1000$  MPa. The following hypothetical tri-linear bond-slip model is applied:  $w_1 = \frac{1.00}{R_b} = 0.08$ ,  $w_2 = \frac{2.00}{R_b} = 0.16$ ,  $f_1 = \frac{2 \cdot 5.00}{E_b} = 6.25 \cdot 10^{-5}$  and  $f_2 = f_3 = \frac{2 \cdot 0.50}{E_b} = 6.25 \cdot 10^{-6}$ . Six embedment lengths have been considered:  $L_1 = 75$  mm,  $L_2 = 150$  mm,  $L_3 = 250$  mm,  $L_4 = 500$  mm,  $L_5 = 1000$  mm and  $L_6 = 3000$  mm. With respect to the critical length  $L_c$  at the end of the elastic stage defined by equation (2.62), in this case  $L_c \approx 1160$  mm. The predicted load-displacement curves are represented in figure 2.7.

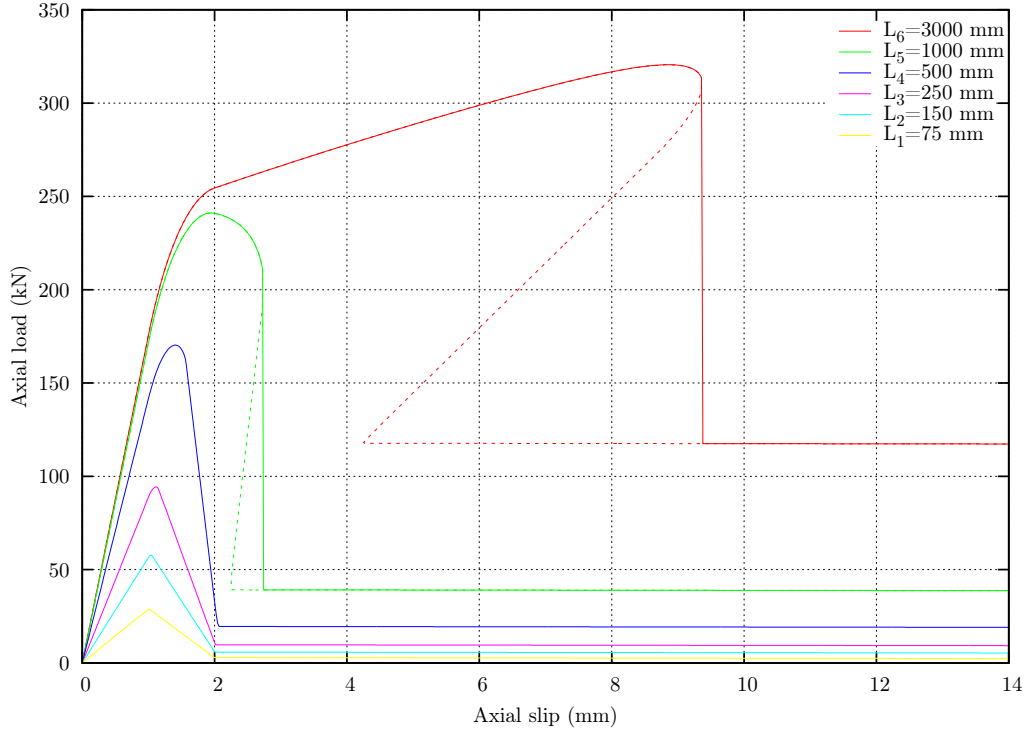


**Figure 2.7:** effect of the embedment length on the pull-out response.

It can be seen that the embedment length has an important effect on the pull-out response: when this length is short, the shear stress is uniform (*i.e.*, the local and global scales are equivalent) and therefore the shape of the bond-slip model and that of the load-displacement curve is similar. On the other hand, for high values of  $L$  the shear stress is not uniform (*i.e.*, the local and global scales are not comparable), which explains the different shape of the load-displacement curve. The slip at the peak load increases with  $L$ . Moreover, for short embedment lengths the maximum force increases linearly with such length (this observation has been reported by Benmokrane *et al.* [Benmokrane1995]), whereas for high values of  $L$  the relationship is not linear. The figure shows also clearly the existence of the critical length,  $L_c$ . Additionally, the decoupling of the interface requires lower axial loads for short lengths than for long lengths. Furthermore, for long embedment lengths the predicted load-displacement response exhibits a phase characterized by a sudden drop of the axial load. This is due to the fact that the new analytical model is only valid for monotonic loadings. In fact, as discussed in Ren *et al.* [Ren2010], a phase characterized by a decrease of both the axial slip and the axial force cannot be captured in real pull-out tests, neither force nor displacement controlled and hence such phenomenon has not been taken into account in the new approach. The dashed lines in the figure represent the load-displacement response when the evolution of the axial displacement is not restricted,

while the solid lines correspond to the physically admissible solution under axial displacement control conditions.

Figure 2.8 plots the distribution of the shear stress along the embedment length at several values of free end displacement,  $t$ , for the six cases described above. The graphs show clearly that short embedment lengths favour a uniform distribution of the bond stress throughout the entire test. Consequently, short embedment length pull-out tests should be used to derive a bond-slip model,  $\tau_b(W)$ . Nonetheless, for short lengths the scatter in the results requires that several tests be made, as remarked by Hyett *et al.* [Hyett1992b].

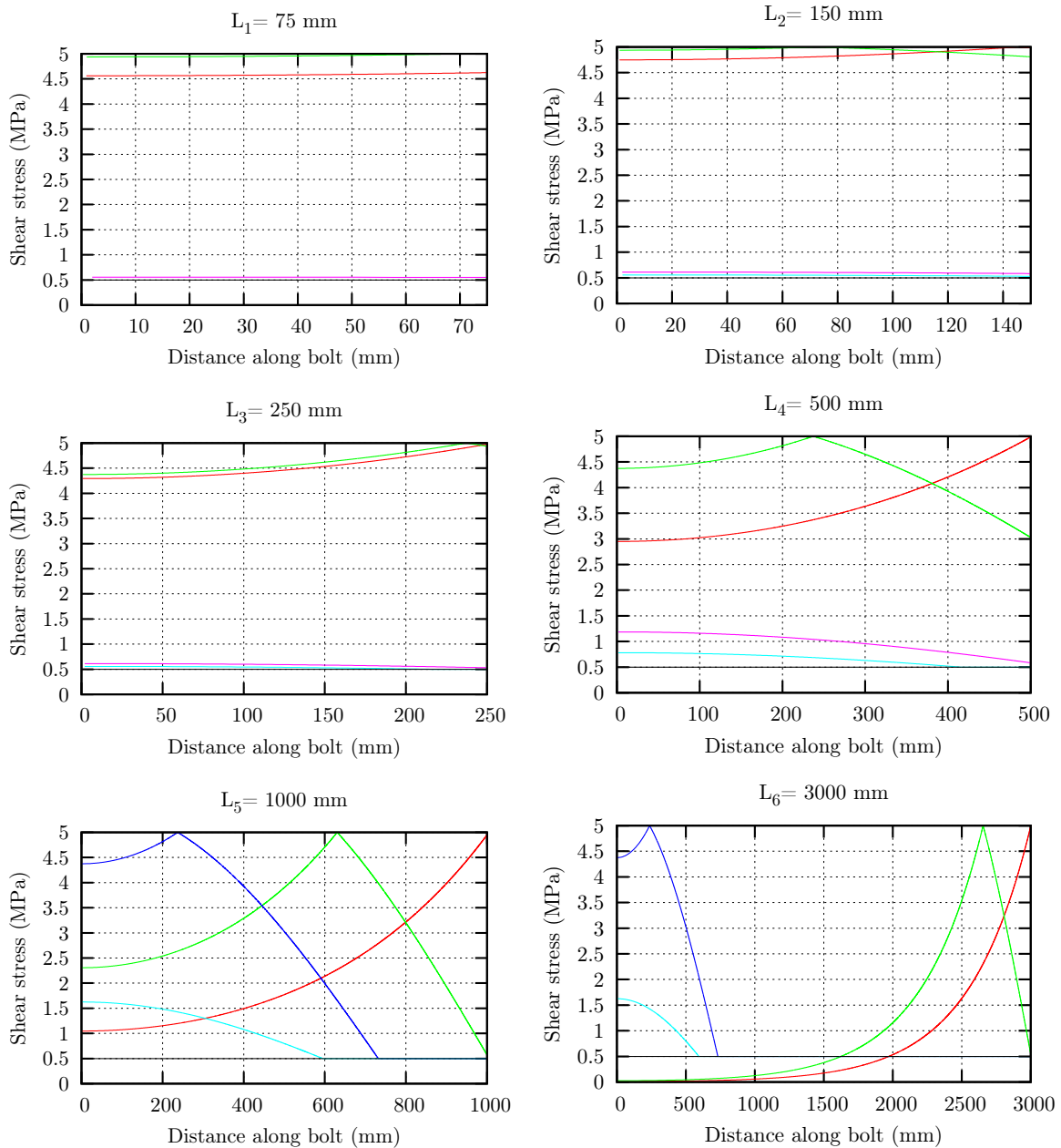


**Figure 2.8:** shear stress distribution at several values of  $t$  for six pull-out tests conducted using a different  $L$ . Red: elastic stage; green: elastic-softening stage; dark blue: elastic-softening-debonding stage; magenta: softening stage; cyan: softening-debonding stage; grey: debonding stage.

Additionally, the evolution during these pull-out tests of the shear stress distribution along the embedded length proves that not only the five stages proposed by Ren *et al.* [Ren2010] for long lengths exist (these stages are elastic, elastic-softening, elastic-softening-debonding, softening-debonding and debonding, see pages 39 through 41); as a matter of fact, the embedment length determines the possible stages that are developed during the pulling process. For instance, in the case of short lengths, a totally softening stage may occur. In the current example, lengths  $L_1$  to  $L_4$  show a pure softening stage and don't exhibit the elastic-softening-debonding stage. On the other hand, for  $L_1$  the softening-debonding stage does not take place. Finally, it can be seen that for  $L_5$  and  $L_6$  the elastic-softening-debonding stage occurs.

## 2.5 Conclusions

This chapter deals with analytical tools that may help understand the response of a fully grouted rockbolt subjected to a tensile axial load.

The elastic response of the grout and ground annuli is explored first, in the radial and axial directions separately. The radial response is useful to examine the pressure transmission from the annuli outside to the bolt-grout interface. This study is interesting because the interface shear stress,  $\tau_b$ , has a frictional component, whence the importance of the normal pressure acting on the interface. The axial response is in turn helpful to estimate  $\tau_b$  from the annuli shear behaviour, but only before decoupling occurs; that is to say, when the bolt-grout interface is coupled.

The last part of the chapter describes the new tool developed to predict the full range response of a fully grouted rockbolt subjected to a tensile axial load. This tool provides the distribution of the axial displacement  $W$ , the axial load  $F$  and the shear stress  $\tau_b$  during a pull-out test. It proves to be particularly advantageous for long embedment lengths, along which the shear stress  $\tau_b$  is not uniformly distributed. The new approach is limited to monotonic loadings and to cases where the bolt remains within the elastic range during the whole loading process. On the other hand, it is applicable to pull-out tests conducted using a constant or a variable embedment length. The data required to use this tool are the embedment length, the bolt radius and Young's modulus and the interface bond-slip model,  $\tau_b(W)$ . With respect to the previous approaches to the same problem exposed in part 1.3, the innovation of the new tool consists in using boundary conditions that are solely related to the bolt free end. The complete development of the solution is explained in the case of a classic tri-linear bond-slip model. This model is part of the interface constitutive law (that includes not only the tangential direction but also the normal direction) and can be determined through pull-out test results as described in part 2.4.3, in which it is also explained that short lengths are more accurate to derive the  $\tau_b(W)$  relationship. Then, the load-displacement response predicted by the new tool is compared with experimental data issued from field and laboratory pull-out tests, which were carried out using long and short embedment lengths, respectively. The comparisons are quite satisfactory, not only in the case of the classic tri-linear bond-slip model, but also when a nonlinear  $\tau_b(W)$  relationship is considered.

Finally, the influence of the embedment length on the pull-out response is explored through the use of the new analytical tool to predict the load-displacement curves of six pull-out tests conducted under identical conditions except for the embedment length. The results, shown in figure 2.7, clearly prove that the embedment length has an important effect on the pull-out response. What is more, the axial distribution of the shear stress during these tests, displayed in figure 2.8, affirms that short embedment lengths favour a uniform distribution of the stress  $\tau_b$  throughout the entire test. This,

combined with the fact that short lengths are more accurate to derive the  $\tau_b(W)$  relationship, leads to the execution of pull-out tests using short embedment lengths when the interface behaviour is investigated. The laboratory campaign presented in chapter 3 observes to this condition.

## CHAPTER 3

# EXPERIMENTAL METHODS AND RESULTS

*Ce chapitre est consacré à l'étude expérimentale du comportement sous sollicitation axiale d'un boulon ou d'un câble à ancrage réparti. Des essais d'arrachement ont été effectués en laboratoire et in situ.*

*A l'échelle du laboratoire, les essais ont été effectués dans un nouveau banc expérimental mis en opération pendant la thèse. Ce banc a été conçu pour représenter la situation in situ décrite dans la figure 1.15. Par conséquent, la barre est ancrée sur deux longueurs très différentes, de façon à ce que le glissement relatif barre-scellement se produise dans la petite longueur, pendant que la grande longueur assure l'ancrage. Les échantillons testés se composent d'une éprouvette de roche pourvue d'un trou borgne dans lequel on scelle la barre à arracher, et d'un tube métallique creux scellé sur la longueur de la barre qui sort du trou. Ce tube représente la grande longueur qui assure l'ancrage pendant la sollicitation axiale. Toute la préparation des échantillons est effectuée dans notre laboratoire, à l'exception du filetage externe et du rainurage interne du tube. Des procédures de préparation des échantillons et de réalisation de l'essai ont été établies, et ce pour chaque type de tige testée. D'autre part, au fur et à mesure que les essais ont été réalisés, on a introduit des améliorations afin de s'approcher au plus possible des conditions optimales permettant d'étudier l'interface tige-scellement. En particulier, ces améliorations concernent l'utilisation d'une faible longueur d'ancrage, la restriction de la rupture au contact barre-scellement, le contrôle de la pression de confinement et celui de la vitesse de déplacement de la barre. En même temps, une analyse exhaustive du nouveau banc a été effectuée pour évaluer la représentativité des mesures prises vis-à-vis du phénomène à étudier. Cette analyse nous a amenés à étalonner le banc et à entreprendre les corrections nécessaires du déplacement brut, de façon à avoir des données permettant d'étudier de façon plus précise l'interface tige-scellement. Suite à l'étalonnage, l'ancrage tube-barre a été reconsidéré.*

*Au total, environ une soixantaine d'essais a été effectuée sur des boulons en acier (HA25), en fibres de verre (Powerthread) et sur des tiges lisses. Des câbles classiques à sept torons ont également été testés. Dans le but d'empêcher le phénomène de rotation qui pourrait fausser les résultats (dévissage du câble par rapport à l'anneau de scellement), de nouvelles pièces complémentaires ont été conçues et leur efficacité a été vérifiée. Les essais effectués sur les câbles ont été destinés à évaluer la performance de ces dernières et à comparer qualitativement la réponse des boulons et des câbles.*

*Les paramètres étudiés plus en détail sont la longueur d'ancrage, la pression de confinement et le type et profil du boulon. Dans la plupart des cas, on a utilisé de la résine pour sceller les barres. Quant aux conditions opératoires, les essais ont été faits soit à rigidité radiale extérieure constante,*

soit à pression de confinement extérieure constante. Les résultats montrent que le comportement de l'interface est très influencé non seulement par la pression de confinement et par le profil des tiges, mais aussi par la réponse de l'anneau de scellement et de la roche sous le régime de sollicitations imposé.

Les essais d'arrachement *in situ* ont été réalisés au laboratoire de recherche souterrain de l'ANDRA en Meuse/Haute-Marne. Plusieurs types de boulons (HA25, Dywidag, CT-bolt et Swellex) ont été testés. Les scellements utilisés sont de la résine et du coulis de ciment, et les longueurs d'ancrage sont de 2,4 et 3 m. À cause de ces grandes longueurs de scellement, les essais n'ont pas permis de provoquer un glissement relatif important entre la barre et le milieu environnant. Les essais *in situ* ont été effectués avant les essais à l'échelle du laboratoire et leur but principal a été de comparer la performance dans le terrain des différents types de boulons testés. Étant donné que parmi ces boulons, on n'a testé en laboratoire que les barres HA25, seules ces dernières ont été exploitées pendant la thèse. Cependant, il est nécessaire de remarquer que les essais en laboratoire et *in situ* n'ont pas été effectués dans le même but. En effet, du point de vue de la recherche en cours, l'idéal aurait été de commencer par les essais à petite échelle, puis définir un modèle préliminaire pour l'interface de rupture et ensuite modéliser les longs essais *in situ*, afin de les dimensionner correctement pour étudier le même phénomène qu'à l'échelle du laboratoire. La comparaison entre les résultats de terrain et ceux issus de la modélisation aurait alors aidé à la validation de l'étude à petite échelle.

À la fin du chapitre, on explique que pour pouvoir comparer les résultats obtenus à l'échelle du laboratoire et *in situ*, il faut prendre en compte non seulement l'écart entre les longueurs d'ancrage utilisées, déjà expliqué dans le chapitre 2, mais aussi les différentes conditions opératoires : en effet, les essais *in situ* sont effectués à rigidité radiale constante en paroi du trou borgne, tandis que le banc expérimental permet d'effectuer les essais soit à pression de confinement constante, soit à rigidité radiale extérieure constante (i.e., rigidité à l'extérieur de la roche si elle se casse pendant l'essai ou bien en paroi du trou borgne lorsqu'elle ne se casse pas). De ce fait, la comparaison des résultats n'est pas immédiate, mais elle peut se faire via la modélisation, une fois la loi d'interface connue grâce aux essais en laboratoire.

### 3.1 Introduction

In order to gain some insight into the behaviour of the bolt-grout interface before and after bond failure, pull-out tests have been carried out on rockbolts and cablebolts. Part of these tests have been conducted in the laboratory, using a new experimental bench. Field pull-out tests conducted on the same rockbolts as those tested at laboratory-scale have also been analyzed. These field tests have been carried out before the laboratory pull-out tests and their principal aim has been to evaluate the bolts performance with regard to the surrounding ground.

In the laboratory, both rockbolts and cablebolts have been tested. The principal objective of the laboratory campaign has been to get useful information to understand the behaviour of the bolt-grout interface. The influence of different parameters, in particular the confining pressure, the embedment length and the bolt type and profile, has been studied. The majority of the tests have been carried out on rockbolts; the main target of the pull-out tests conducted on cablebolts has been to validate the set-up designed to prevent these tendons from unscrewing.

The full pull-out test campaign is presented in this chapter. First, the research carried out in the laboratory is fully explained and the pull-out test results are discussed. The experimental relationships  $\tau_b(W)$  of some tests are also presented. Then, the field pull-out test campaign is exposed and the

results are commented. The  $\tau_b(W)$  relationships derived from field data are also shown, but only partially because the tests were stopped at low values of axial displacement. Finally, the aspects that should be considered to compare laboratory and field results are explained.

## 3.2 Laboratory pull-out test campaign

### 3.2.1 Equipment: new experimental bench

The tests have been carried out using a new laboratory pull-out bench. The bench principle was defined before the beginning of this thesis; however, the bench was first used and tuned during the current doctorate.

#### General description

The new bench has been designed to match the field situation displayed in figure 1.15; accordingly, it is based on the *double embedment* principle. An overall view and a cutaway section of this bench are shown in figure 3.1. On the other hand, a picture of the experimental facility during a pull-out test is displayed in figure 3.2.

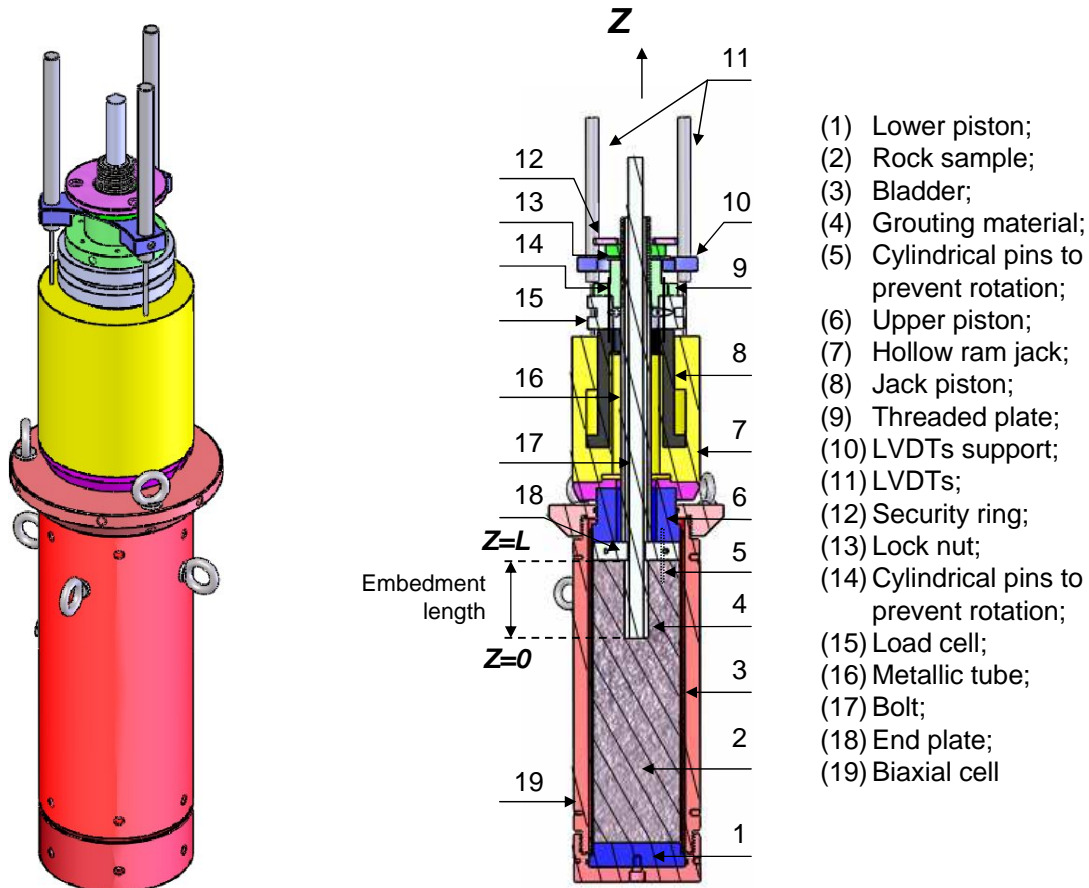


Figure 3.1: overall view and cutaway section of the pull-out bench used in the laboratory.

The bench can be divided into two main parts: in the lower part, the *bolt* is grouted by means of a *grouting material* to a cylindrical *rock sample* over a variable length, namely the *embedment length*. This part corresponds to the *embedment length* zone in figure 1.15 (it should be noted that the face

plate is absent in this figure). An *end plate* is placed on the rock sample to constrain the rock and grout annuli vertically at point  $Z = L$ . In the upper part, a steel *metallic tube* is grouted along the bolt length that protrudes from the rock borehole. This part represents the *rock mass* zone in figure 1.15. Part of the outer surface of this tube is threaded. The metallic tube is considerably longer than the embedment length; therefore, any axial slip is more likely to occur in the rock borehole, while the bolt remains anchored to the metallic tube. As it can be seen in the cutaway section, the bolt links together the upper and the lower parts of the bench.



**Figure 3.2:** view of the experimental installation during a pull-out test.

The *biaxial cell* is used to apply a lateral confining pressure to the rock sample. Hydraulic oil is used as confining fluid. The confining pressure may be varied or held constant during the test, so that the tests may be conducted under constant outer radial pressure ( $p_r$ ) or constant outer radial stiffness ( $K_{R_r^+} = \partial p_r / \partial u_{r,r^+}$ ) conditions. The maximum confinement the new bench can withstand is 25 MPa. To prevent the formation of pore pressures and to ensure a proper distribution of the confinement, a cylindrical *bladder* is placed around the rock core sample. The bladder is a bit longer than the rock sample-end plate assembly because it is used as an alignment tool for the *upper piston* of the cell, see the detailed view in figure 3.3a (the bladder is the green part). Moreover, as it can be seen in this enlarged view, the lateral surface of this piston inside the biaxial cell is slightly conical (with the vertex oriented downwards). This design choice has been made to create a supplementary horizontal base to the piston: this way, such piston will remain in contact with the end plate under the effect of the confining pressure (as it can be seen in the view, the space between the cell top cover and the piston horizontal base is filled with confining fluid).

To apply the axial force, a *hollow ram jack* is used. The jack is placed above the confining cell, on the upper piston. Two notches have been machined on the upper face of the piston to make the fixed body of the jack and this piston interdependent, see the enlarged view in figure 3.3a. The force is transmitted to the metallic tube (thus, to the bolt) *via a threaded plate* that is screwed on the tube. A customized *load cell* provided with a load bearing/distribution plate is placed between the *jack*

*piston* and the threaded plate. The axial displacement is measured by three *LVDT* (*Linear Variable Differential Transformer*) sensors. The *LVDTs* support is installed on the threaded plate and is fixed by the *lock nut*. A security ring is placed on the lock nut and is linked to the biaxial cell using two metallic chains. All the details of the upper part of the bench are displayed in figure 3.3b.

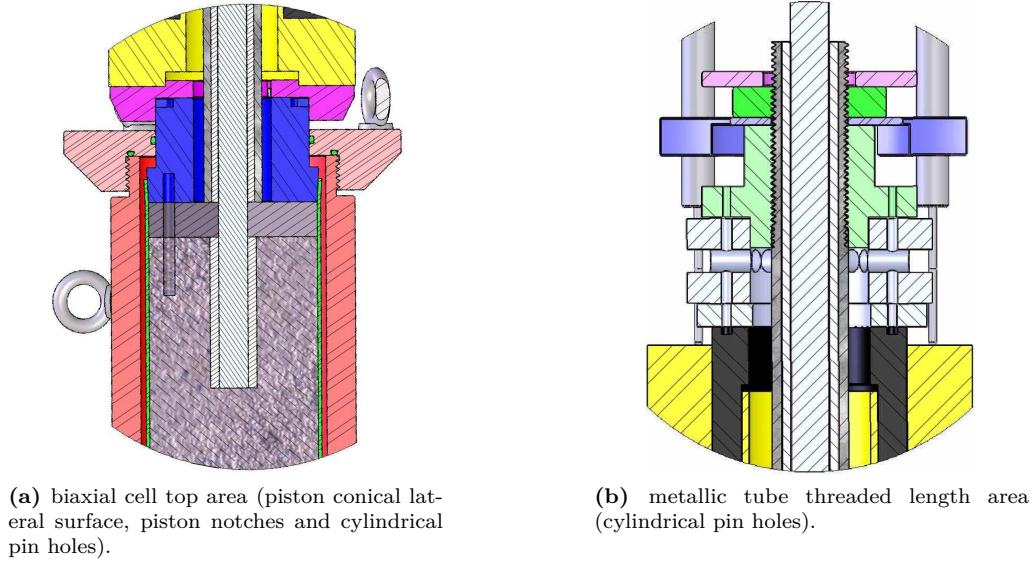


**Figure 3.3:** enlarged views of the pull-out bench.

Table 3.1 shows the most important dimensions of the bench, as well as the operating ranges of the devices utilized.

**Table 3.1:** main dimensions and operating ranges of the new experimental bench used in the laboratory.

|                  |                   |                         |
|------------------|-------------------|-------------------------|
| Rock sample      | Length            | $470 \pm 1$ mm          |
|                  | Outer diameter    | $144 \pm 1$ mm          |
|                  | Borehole diameter | Variable                |
|                  | Borehole length   | Variable                |
| Bladder          | Height            | $560 \pm 1$ mm          |
|                  | Inner diameter    | $145 \pm 1$ mm          |
|                  | Thickness         | $4 \pm 0.1$ mm          |
| Biaxial cell     | Height            | $617 \pm 1$ mm          |
|                  | Inner diameter    | $160 \pm 1$ mm          |
|                  | Outer diameter    | $210 \pm 1$ mm          |
|                  | Maximum pressure  | 25 MPa                  |
| Hollow ram jack  | Maximum stroke    | 76 mm                   |
|                  | Maximum capacity  | 931 kN                  |
|                  | Oil capacity      | 1011 cm <sup>3</sup>    |
|                  | Weight            | 63 kg                   |
| Metallic tube    | Length            | $540 \pm 5$ mm          |
|                  | Outer diameter    | $50 \pm 1$ mm           |
|                  | Inner diameter    | Variable                |
|                  | External thread   | 4 mm pitch along 180 mm |
| Load cell        | Maximum load      | 350 kN                  |
|                  | Height            | 55 mm                   |
| LVDTs sensors    | Maximum stroke    | 100 mm                  |
| Pressure sensors | Maximum pressure  | 35 MPa                  |

The non-reusable parts of a test are the rock sample, the bolt, the metallic tube and the grouting materials used. All the permanent parts have been manufactured in high strength steel (type 40CrMnNiMo8-6-4 complying with standard NF-EN-ISO-4957, yield strength  $\sigma_e \in [980, 1130]$  MPa). The metallic tubes are also made in steel (types S470M [NF A 49-312] and E235 [NF A 49-330], yield strength  $\sigma_e \in [440, 700]$  MPa).

The parameters that can be studied with this bench are:

- the embedment length;
- the confining pressure;
- the bolt type and profile;
- the grout annulus thickness;
- the type and mechanical properties of the grouting material;
- the mechanical properties of the rock mass;
- the borehole wall roughness.

It is important to note that, during a pull-out test, the embedment length does not remain constant, but decreases (this situation corresponds to the case  $k = 1$  in section 2.4). With respect to pull-out tests carried out under constant embedment length conditions, the advantage of using a decreasing embedment length is that no portion of bare, ungrouted bolt, comes into contact with the grouting material at  $Z = 0$ , which could cause an increase of the shear stress as the bar slips. This matter has been previously discussed by Verderame *et al.* [Verderame2009a].

Finally, it should be noticed that, as shown in figure 3.1, the reaction force of the hydraulic jack is exerted against the rock core sample. This configuration corresponds to Hagan's [Hagan2004] pull-out test arrangement, displayed in the upper left-hand side illustration in figure 1.32. The influence of this set-up will be investigated in parts 3.2.3 and 3.3.

### Bench operation

Once the bench is assembled, the desired confining pressure is applied using a 655 cm<sup>3</sup> hydraulic hand pump. When the tests are conducted under constant outer radial pressure conditions, a hydraulic accumulator is connected to the biaxial cell. On the other hand, when the tests are carried out at constant outer radial stiffness conditions, the cell is closed and consequently the confining fluid mass is constant throughout the test. It should be noted that, as far as the grout and rock annuli behave elastically, the tests are conducted at constant stiffness at the grout inner surface, *i.e.*  $K_{R_b^+} = \partial p_b / \partial u_{rb}^+$ ; however, if the annuli split radially, it is the outer (confining fluid) stiffness that remains constant, *i.e.*  $K_{R_r^+} = \partial p_r / \partial u_{rr}^+$ . In general, the last case will be referred to as constant outer stiffness,  $K_{R_r^+}$ .

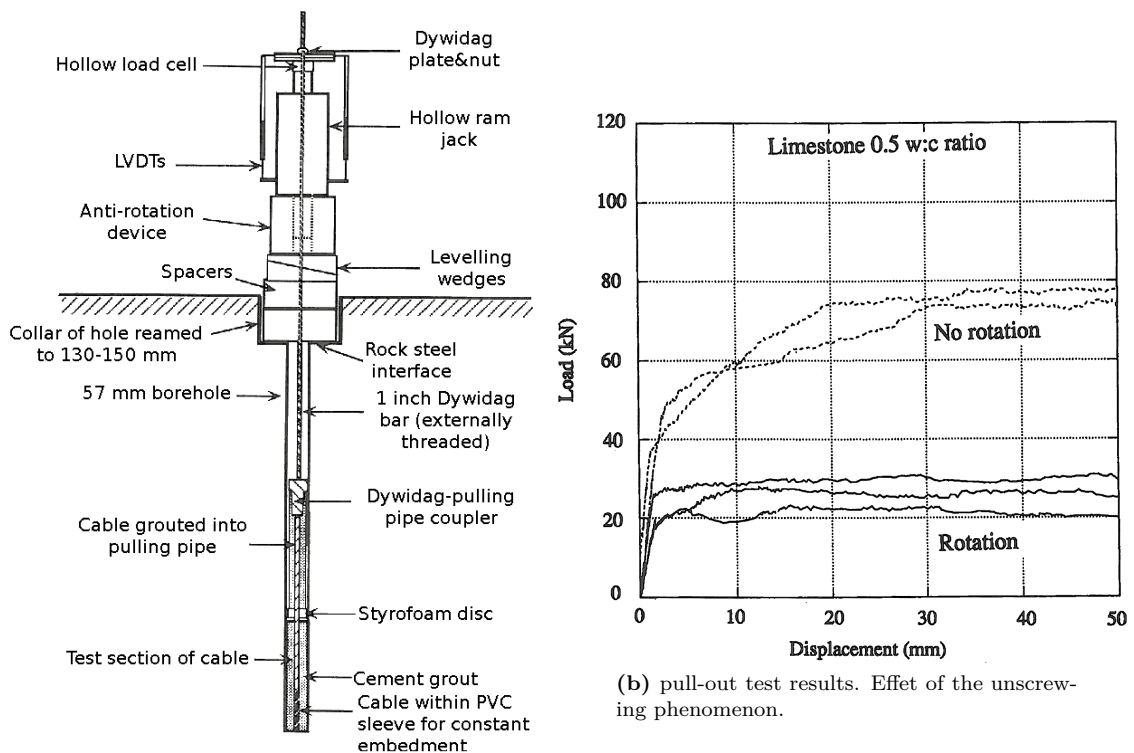
The hollow ram jack is then brought into operation. To do so, a second hydraulic hand pump is used (see the vertical pump in figure 3.2). The volume capacity of this pump is enough to displace the jack piston to its maximum stroke, which allows for a thorough study of the post-peak phase of the tests. As the jack piston moves upwards, a load is applied to the bolt *via* the threaded plate. This force equals the axial force on the bolt at point  $Z = L$  in figure 3.1. As for the displacement measured, it corresponds to the relative vertical displacement between the fixed body of the jack and the LVDTs support. Assuming that the bench is not deformable (*i.e.*, the rock sample is incompressible and the metallic tube-bolt assembly is totally rigid), such displacement is equal to the bolt displacement at

point  $Z = L$ , plus the strain over the bolt free length, between the upper and lower parts of the bench. The appropriateness of this assumption will be discussed in section 3.3.

During the test, data are recorded and visualized using LabVIEW. The acquisition frequency is 5 Hz. The variables monitored are: axial displacement, axial force, confining pressure and jack pressure. The tests are carried out in static conditions and under displacement control, using a constant displacement rate of 0.02 mm/s. Moreover, the embedment lengths tested are calculated so that the bolt remains in the elastic phase throughout the entire duration of the test.

### Tools to prevent cablebolts from unscrewing

It has been explained in chapter 1 that, as a consequence of their helical structure and low torsional rigidity, cablebolts may unscrew from the grout annulus during a pull-out test, particularly if the embedment length is short. Many researchers have faced this problem, *cf.* 1.3. In particular, Bawden *et al.* [Bawden1992] studied the influence of unscrewing on field pull-out test results, with the aim to define an ISRM Suggested Method. The authors compared results from pull-out tests in which the unscrewing mechanism was allowed or restricted. The set-up used is displayed in figure 3.4a and some results are shown in figure 3.4b. This figure clearly indicates that unscrewing distorts the results, leading to an almost perfectly plastic response. But, most importantly, it is an unrealistic phenomenon because cablebolts cannot unscrew in real field situations: as shown in figure 1.15, it is the rock which may slide along the cable, and this rock will not rotate due to the tendon geometry. Therefore, unscrewing has little relevance to any mining or civil engineering application.



(a) field set-up. Unscrewing is avoided using a hexagonal nut (clamped onto the Dywidag bar) that rides within a hexagonal sleeve.

**Figure 3.4:** pull-out test results on 15.2 mm diameter 7-wire strands when unscrewing is allowed and restricted (adapted from Bawden *et al.* [Bawden1992]).

In order to avoid the unscrewing phenomenon when testing cablebolts with the new experimental bench described above, some additional parts have been designed. As shown in figure 3.3a, the rock mass and the biaxial cell upper piston are linked together by three *cylindrical* steel *pins* that are placed in the three purposely drilled holes in the rock sample (upper face), the end plate and the upper piston (lower face). These boreholes are evenly spaced at  $120^\circ$  apart. This way, the rock and the fixed part of the hydraulic jack are interdependent and hence no relative rotation is allowed between them. In addition, two pins are inserted between the jack piston and the threaded plate (see the detailed view in figure 3.3b), so that any possible relative rotation between that piston and the metallic tube (thus, the cablebolt) is blocked.

At this stage, the only possible relative rotation would take place between the fixed part of the jack and its piston. In order to prevent such relative movement, a metallic ring is screwed around the fixed body of the jack and blocked in rotation using three cone-point screws. The threaded plate is linked to this ring by two 20 mm diameter steel rods that are fixed to the ring and go across the plate (*i.e.*, the plate can slide along the two rods). Figure 3.5 shows the set-up designed to prevent the relative rotation between the two parts of the jack.

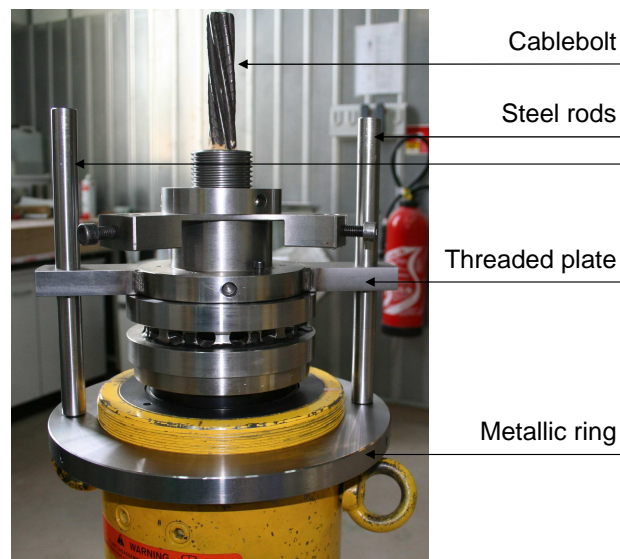


**Figure 3.5:** designed set-up to avoid the unscrewing phenomenon (cablebolts).

Under these circumstances, as the jack piston moves upwards during the test, all the parts of the bench will rotate together, should any rotation take place. Furthermore, the cable will *untwist* itself (rather than *unscrew* from the borehole) during the pull-out process, thereby simulating the field conditions of a rock block sliding off an unplated cable.

As a concluding remark, it is important to notice that the influence of unscrewing on the test results may depend on the operating conditions (type of cablebolt, grouting material in use, confining pressure, *etc.*). The importance of unscrewing within this research is explored in part 3.3.2.

### Bench modifications

The tests execution and the analysis of the results have led to some modifications and improvements, which aim at a more accurate study of the bolt-grout interface. These modifications were introduced

during the main campaign on rockbolts, *cf.* part 3.2.3. The most important are:

- change of the boundary conditions: some tests have been carried out at constant outer radial stiffness conditions,  $K_{R_r^+} = \partial p_r / \partial u_{r,r^+}$  (the quantity of confining oil was maintained constant throughout the test), whereas the others have been conducted at constant confining pressure conditions,  $dp_r = 0$ . Both tests let study the bolt-grout interface; however, the tests at constant  $p_r$  require an additional measurement (such as the radial displacement at the outside of the rock sample or the confining fluid volume variation) in order to get useful information about the bolt-grout interface radial behaviour. Given that within the context of the current thesis the only radial measurement available is the pressure  $p_r$ , more tests have been conducted at constant radial stiffness;
- introduction of an end plate between the rock sample and the biaxial cell upper piston: due to design considerations, the reaction force is made directly on the rock mass. In the initial design of the bench, the rock sample, which was 500 mm high, abutted against the biaxial cell upper piston. Owing to the stress regime in the rock sample (high compressive stresses around the upper face beneath the piston and high tensile stresses around the borehole), a crater depression was likely to be created around the point  $Z = L$  during the pull-out test, which caused a reduction in the embedment length. The angle of this crater was always around  $45^\circ$  (the vertex was oriented towards the borehole far end), which confirms that it was caused by an excess of tensile stress. Nonetheless, the main drawback of the crater formation was not the reduction in the embedment length, but the disruption of the decoupling process along such length, particularly when it was short. The pictures in the left-hand side of figure 3.6 show the open views of two samples after the tests. The two tests were carried out under similar conditions except for the prevention of the crater depression (lower picture). The upper photo clearly illustrates the irregular rupture that takes place when the crater depression occurs. The right-hand side graph in the figure shows the load-displacement curve of both tests; as it can be seen, the results are quite different.

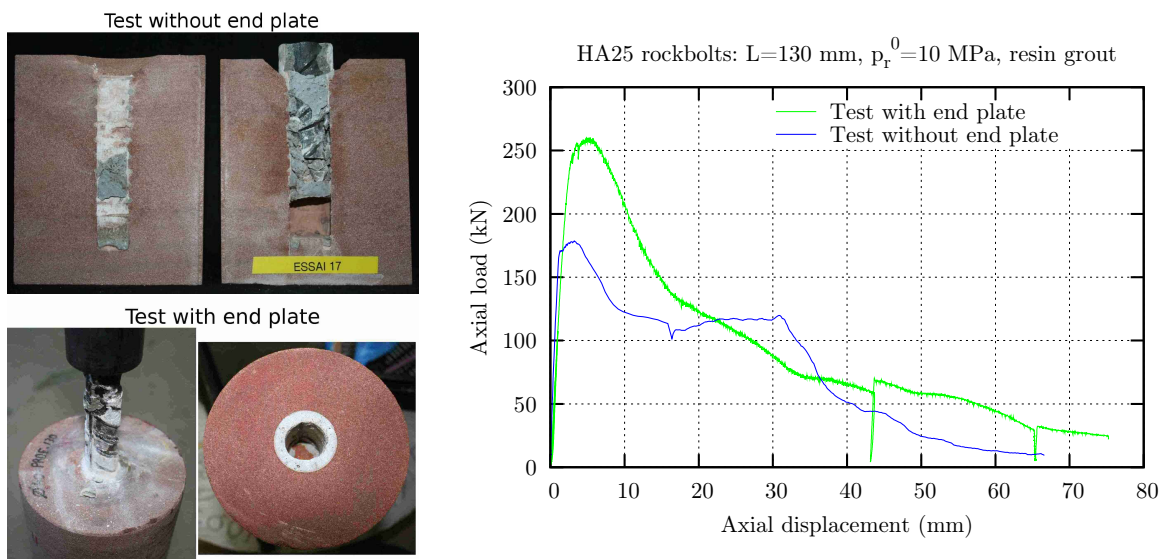


**Figure 3.6:** importance of the end effect (on top of the rock sample) on the pull-out test results. Both tests have been conducted under similar conditions except for such end effect.

The crater depression has been prevented by the introduction of a metallic end plate between the rock sample and the biaxial cell upper piston. Its internal diameter matches the maximum diameter of the tested bolt and its height is  $h_{pl} = 30$  mm. The stress regime in the rock mass in the two configurations (*i.e.*, with or without end plate) has been analyzed numerically using a FEM software. The situation where both the bolt-grout and the grout-rock interfaces are coupled has been simulated because the crater is created when the axial slip starts (evidence on this statement is provided by the fact that the crater base is stuck to the metallic tube end). Therefore, a relative displacement of only 0.25 mm has been applied between the upper and lower parts of the bench. The results for the maximum (tensile) principal stress are shown in figure 3.7. As it can be seen, the introduction of the plate reduces the tensile stresses around the borehole collar by 2.2. In addition, the compressive stresses in the vicinity of the rock sample upper face decrease too as a result of the increase in the reaction surface caused by the introduction of the plate. These results agree with those presented by Hagan [Hagan2004]. In the simulations, all the materials have been supposed elastic;

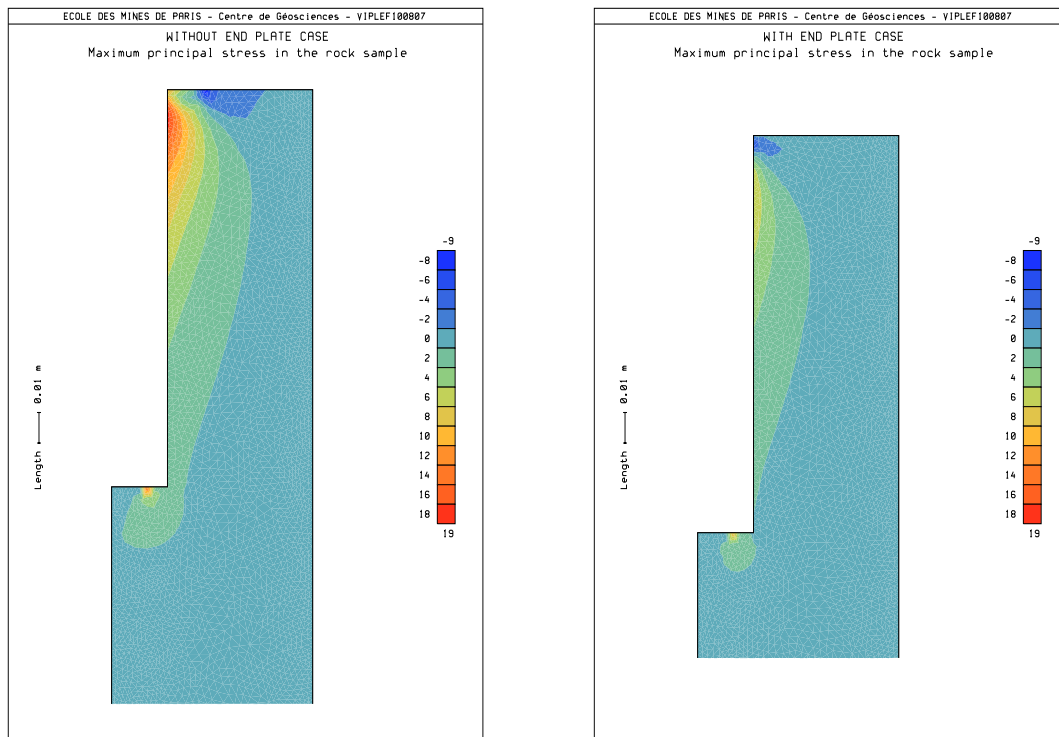


**Figure 3.7:** FEM results. Maximum (tensile) principal stress distribution in the rock mass after 0.25 mm of relative displacement between the upper and lower parts of the bench. Left: without end plate; right: with end plate.

- move from an electric to a hand pump to drive the hydraulic ram jack. This decision was made to control the displacement rate; in fact, the electric pump output flow rate was 0.55 l/min, which corresponds to a displacement rate of about 0.84 mm/s. This rate was too high and hindered any intervention during the tests (execution of loading-unloading cycles in particular).

### 3.2.2 Samples preparation

A laboratory pull-out test sample consists of the rockbolt, the rock core sample, the metallic tube and the materials used to grout the bolt to the rock and to the tube. The proper preparation of the

samples and in particular the precise co-axiality of all elements is very important to ensure the correct assemblage of the experimental bench. The main steps in the preparation of a laboratory sample are described below. Detailed procedures have been defined for each step.

### Rock drilling

The rock samples are drilled from a rock block. The typical dimensions of the blocks used are  $1000 \times 400 \times 470 \text{ mm}^3$ , which allow to prepare 10-12 samples. First, the sample is drilled to a depth of 20-30 mm using a 145 mm inner diameter core drill. This lets create an initiation to ensure the co-axiality between the borehole and the rock core sample axes. The borehole is then drilled to the predefined depth (the embedment length) using a smaller core drill, whose diameter depends on the tendon tested. Finally, the rock sample is drilled to 470 mm using the initial core drill. A water flush is used during all these drilling operations. The pictures in figure 3.8 show the rock block drilling system and a detailed view of a drilling operation.



(a) overview of the installation.



(b) drilling of a borehole.

**Figure 3.8:** rock block drilling.

If at the end of the drilling operations any minor irregularities or depressions are found in the outer surface of the rock sample, they are filled with a self-hardening filler to avoid any localized deformation.

### Rifling of the borehole walls

In order to favour decoupling at the bolt-grout interface, the borehole wall is rifled to improve the bond between the rock sample and the grouting material. This operation is carried out using a vertical lathe and a customary steel instrument equipped with a diamond-based tool head, see figure 3.9a. Circular grooves  $3.5 \pm 1 \text{ mm}$  deep and spaced  $10 \pm 1 \text{ mm}$  are machined along the embedment length. Figure 3.9b shows a rifled borehole.



(a) overview of the vertical lathe during the rifling of a borehole.



(b) rifled borehole.

**Figure 3.9:** rifling of the borehole wall.

### Preparation of the metallic tube

The metallic tube used to pull the bolt out of the rock sample is prepared from 5-6 m long steel pipes. First, the pipe is cut to  $540 \pm 5$  mm long parts. Then, the external surface of each tube is threaded along 180 mm from one extremity. The tube internal surface is rifled to difficult decoupling inside this tube. Circular grooves  $2 \pm 1$  mm deep and spaced  $10 \pm 5$  mm are made. The external threading and internal rifling of the tubes are carried out by a subcontractor. The picture in figure 3.10 shows a metallic tube ready to use.



**Figure 3.10:** metallic tube with internal rifling and external threading.

### Grouting the bolt to the rock mass

Once the rock core sample is ready, the bolt is anchored using either a cement mortar or a resin-based grout. This operation is made with the rock sample in a vertical position. The procedure is slightly different depending on the grouting material in use:

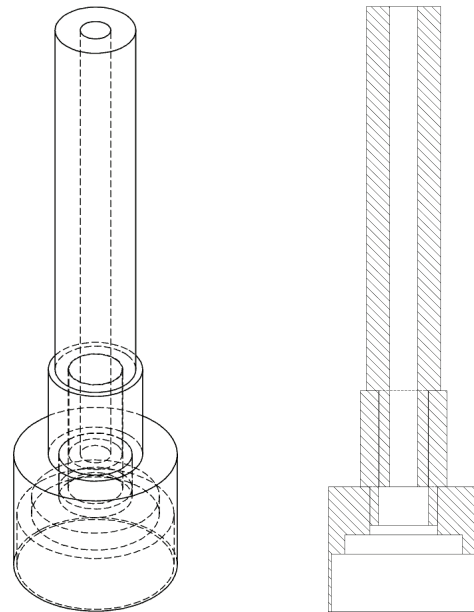
- in the case of cement, the desired  $w : c$  ratio is prepared separately. For high ratios, a fluidifier is added to the mixture to facilitate pouring. Then, the mortar is poured into the borehole and the bolt is pushed in;

- in the case of resin, the required volume of resin&hardener is squeezed from the cartridge into the borehole. The plastic cartridge does not remain in the borehole to better study the grout-bolt or grout-rock bond. Then, the resin and the hardener are mixed using a power drill provided with a blade. In order to carry out these operations, a slow setting resin is used. Once the grout is properly mixed, the bolt is pushed in.

In both cases, the volume of grout needed is calculated in advance (with a 40 % excess to account for losses and the rough profile of the bolt). A centring pattern has been manufactured in Plexiglas and is installed on the rock sample and around the bolt during the setting time of the grouting material to ensure that the bar is correctly centred in the borehole. This pattern consists of three parts that fit together as shown in figure 3.11.



(a) test sample during the setting time of the grouting material (with centring pattern installed).



(b) centring pattern layout and plan.

**Figure 3.11:** grouting inside the borehole.

Once the grout has set, any excess of material is wiped away from the rock sample surface. It should be noted that, in the case of cementitious grouts, the samples are left to cure for 28 days.

### Grouting the bolt to the metallic tube

The next stage consists in grouting the metallic tube along the protruding length of the bolt. At least 30 mm of free length should be left above the rock core sample in order to place the end plate. The grouting is made using a fast cure adhesive. The tube is installed on the end plate with the threaded end upwards. It is centred using the two lower centring parts shown in figure 3.11. To ensure that the adhesive is properly poured along the tube, a flexible plastic sheath is connected to the adhesive injector and pushed to the bottom of the tube. As the annular space between the tube and the bolt is filled, the plastic sheath is slowly removed.

Once the adhesive has set, the sample is ready to conduct a pull-out test. Figure 3.12 shows a laboratory sample. It should be noted that, with respect to the samples preparation procedure used

by Offner *et al.*, Hagan and the British HSE [Offner2000, Hagan2004, Reynolds2006], in the current research the confining pressure is only applied during the test, and not during the preparation as well (these authors left the samples to cure in free air, but the bolt installation was made under confinement). The influence of preparing the samples under confinement is explored in the next paragraph.

### Effect of preparing the laboratory samples under confinement

In a real field situation, boreholes are drilled under the confinement provided by the *in situ* stress field. As with tunnel drilling, this will bring about some radial convergence and hence the borehole radius will be reduced. Assuming the surrounding ground to be an elastic linear material and the stress field to be isotropic, the expected convergence can be calculated by setting  $R_r \rightarrow \infty$ ,  $p_g = 0$  and  $\sigma_{rr}(R_r \rightarrow \infty) = -p_r$  in equation (2.19). The final borehole radius will be

$$R_g^{\text{field}} = R_g^{\text{field}_0} - \frac{2R_g}{E_r} p_r \quad (3.1)$$

where  $R_g^{\text{field}_0}$  is the drilled borehole radius. Once the bolt and the grout are installed, the radial pressures  $p_b$  and  $p_g$  will be equal to zero if the grout is not poured under pressure. Under these circumstances, before the bolt is activated by the surrounding ground, the radial pressures  $p_b$  and  $p_g$  will only be modified if the stress field changes (for instance, if the rock mass is viscoelastic or if drilling or mining operations are occurring nearby).

In the laboratory, if the rock borehole is drilled under a confining pressure  $p_r$ , the final borehole radius will be

$$R_g^{\text{lab}} = R_g^{\text{lab}_0} - \frac{2R_r^2 R_g}{E_r (R_r^2 - R_g^2)} p_r \quad (3.2)$$

where  $R_g^{\text{lab}_0}$  is the drilled borehole radius. The comparison between equations (3.1) and (3.2) indicates that, other parameters being equal, the final borehole radius will be greater in the field; however, the difference is not significant. What is really important in the laboratory is to keep the pressure  $p_r$  until the test. In fact, in the laboratory configuration, the radial pressures  $p_b$  and  $p_g$  will be equal to zero once the bolt and grout are installed, as far as the grout is not poured under pressure. This sample preparation procedure matches the field situation if the confining pressure  $p_r$  is held until the pull-out test is conducted. However, if such pressure is removed at the end of the sample preparation stage (for instance, if the confining cell is required to prepare other samples or to conduct a test), radial tensile stresses will inevitably be induced, which could damage in particular the bolt-grout and the grout-rock interfaces, before the beginning of the test.

As with the current laboratory set-up, the confining pressure  $p_r$  is applied just before the beginning of the pull-out test. In this situation, the confinement range to apply is determined by the expected



**Figure 3.12:** laboratory sample ready for a pull-out test.

stress change *in situ*. As reported by many researchers such as Hyett *et al.* [Hyett1995], stress changes up to about 10-15 MPa may occur during regular bolt operational conditions. Thus, confining pressures comprised between 0 and 15 MPa have been used in this study.

### 3.2.3 Experimental campaign conducted

Within the present thesis, 63 pull-out tests have been conducted on both rockbolts and cablebolts. Most of the tests have been conducted on rockbolts; the tests carried out on cablebolts have been mainly intended to evaluate the new set-up designed to avoid the unscrewing phenomenon (five tests).

Before starting the main pull-out test campaign, eight tests were conducted on rockbolts to tune and make the new bench correctly operational. The preliminary samples preparation procedures were also defined at that time. During this phase of the research, it was verified that the three most common failure modes of fully grouted bolts could be reproduced in the laboratory: failure at the bolt-grout and grout-rock interfaces and failure of the bolt itself (ultimate tensile strength attained). Thereafter, the research focused on failure at the bolt-grout interface, which was one of the reasons that led to the introduction of the end plate displayed in figure 3.1. All the improvements that have been progressively introduced are described in this subsection.

The main pull-out test campaign on rockbolts has focused on the study of the influence of the following parameters:

- embedment length;
- bolt profile and elastic properties;
- confining pressure.

These parameters will help define an interface behaviour model for the bolt-grout interface.

#### Materials used

All the pull-out tests have been conducted using sandstone rock samples ("grès des Vosges" or Vosges sandstone). This is because sandstone is homogeneous, has good mechanical properties and it is a rock often present in coal mining environments (rockbolts and cablebolts are important reinforcement elements in gateroads for coal longwall mining). Moreover, sandstone has been previously used by other researchers with satisfactory results, *cf.* [Reynolds2006]. To fully characterize the sandstone rock in use, uniaxial and triaxial compressive tests and also indirect tensile tests have been carried out in the laboratory. Table 3.2 shows the relevant mechanical properties of the rock used.

**Table 3.2:** relevant mechanical properties of the sandstone used to prepare the samples.

| Property (unit)                        | Value |
|--|-------|
| Density, $\rho_r$ (kg/m <sup>3</sup> ) | 2130  |
| Young's modulus, $E_r$ (MPa)           | 25600 |
| Poisson's ratio, $\nu_r$               | 0.26  |
| $UCS_r$ (MPa)                          | 62.4  |
| Tensile strength, $R_{t,r}$ (MPa)      | 3.1   |
| Cohesion, $C_r$ (MPa)                  | 12.4  |
| Friction angle, $\varphi_r$ (°)        | 46    |

Three different rockbolts have been tested:

- 25 mm diameter steel rebars (HA25 bars conforming to NF EN 10080 and NF A 35080-1, cf. [NF EN 10080, NF A 35 080 1], manufactured by Riva Acier S.A. in steel grade B500B), hereafter referred to as HA25 rockbolts;
- 25 mm diameter Fiberglass Reinforced Polymer (FRP) threaded rockbolts (*Powerthread* manufactured by Minova-FiReP), hereafter referred to as FRP rockbolts;
- 25 mm diameter smooth bars (type SS 316L, manufactured by Acieries de la Seine). These bars have been tested to study the influence of the bolt profile.

As for cablebolts, 23 mm diameter Reflex Flexible bolts (manufactured by Osborn Strata Products and referred to as Flexible cablebolts) have been used. The relevant mechanical properties of the tested bolts are compiled in table 3.3. The profile of the HA25 and FRP rockbolts and that of the Flexible cablebolt are described in figure 3.13.

**Table 3.3:** relevant mechanical properties of the tested bolts.

| Property (unit)  | HA25 | FRP    | Smooth bars | Flexible |
|--|------|--------|-------------|----------|
| Nominal diameter, $d_n$ (mm)                             | 25   | 25     | 25          | 23       |
| Maximum (minimum) diameter, $d_{max}$ ( $d_{min}$ ) (mm) | 29   | (23.2) | 25          | 22       |
| Young's modulus, $E_b$ (GPa)                             | 160  | 40     | 193         | 188      |
| Yield strength, $\sigma_{e,b}$ (MPa)                     | 500  | 1060   | 200         | 970      |
| Tensile strength, $R_{t,b}$ (MPa)                        | 620  | 1060   | 600         | 1200     |

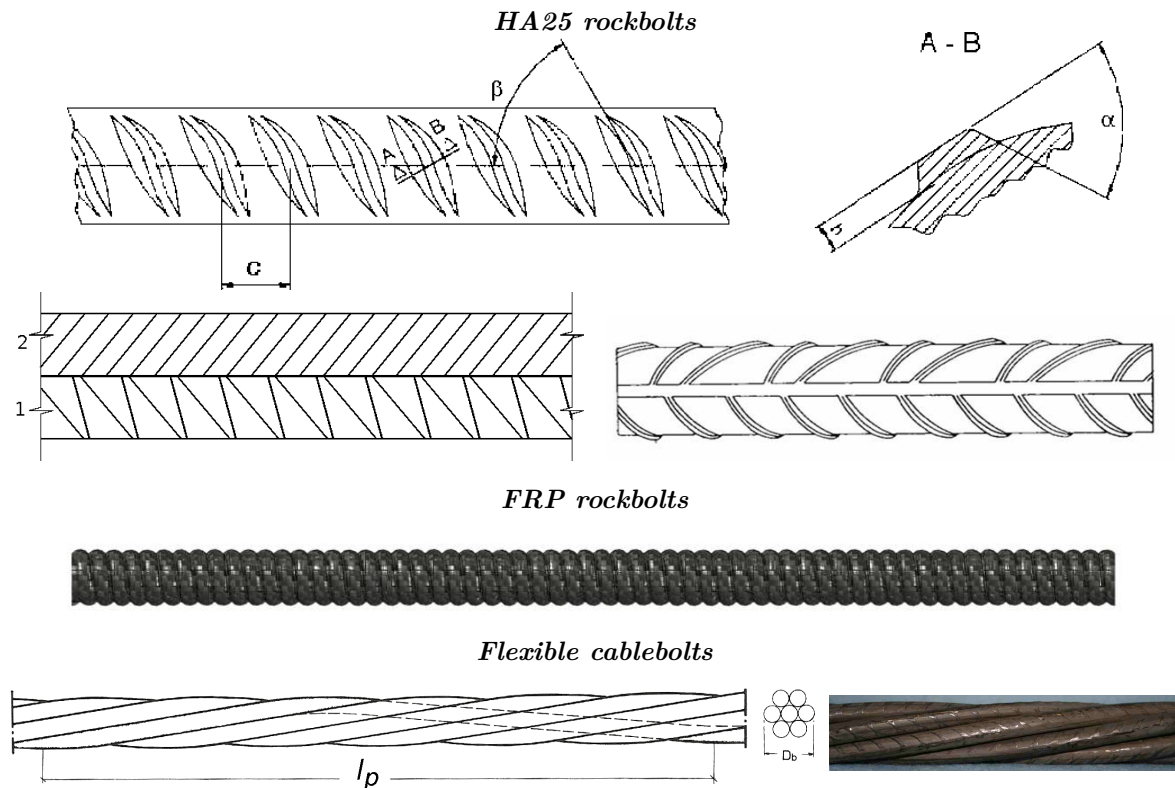


**Figure 3.13:** bolt profiles. Top: HA25 rockbolts (after NF EN 10080 and NF A 35080-1, cf. [NF EN 10080, NF A 35 080 1]); middle: FRP rockbolts; bottom: Flexible cablebolts (plan adapted from Stillborg [Stillborg1984], and detailed view of the indentations).

It is important to notice that the indentations in FRP rockbolts are smoother and shallower than those in HA25 rockbolts. In fact, HA rebars are characterized by two series of sharp indentations uniformly distributed along the bar perimeter and separated by two longitudinal ribs. In each series, the indentations are evenly spaced as shown in the sketches on top of the figure. On the other hand, FRP rockbolts show a smooth threaded profile as indicated in the middle drawing in the figure. As for the Flexible cablebolts, their outer surface is provided with a regular pattern of small indents to increase the bond strength. The geometric data for these three bolts are compiled in table 3.4.

**Table 3.4:** bolts profile geometric characteristics.

|                                   |                |                      |
|-----------------------------------|----------------|----------------------|
| Ribs height, $h_r$                | 1.04 - 0.35 mm |                      |
| Ribs thickness, $t_r$             | 2.7 mm         |                      |
| Indentations thickness (top), $t$ | Series 1       | 2.6 mm               |
|                                   | Series 2       | 2.4 mm               |
| Indentations height, $h$          | Series 1       | 2.4 mm               |
|                                   | Series 2       | 2.1 mm               |
| Indentations angle, $\alpha$      | Series 1       | 45 °                 |
|                                   | Series 2       | 46 °                 |
| Indentations orientation, $\beta$ | Series 1       | 69 ° - 53 °          |
|                                   | Series 2       | 62 °                 |
| Indentations spacing, $c$         | Series 1       | 32.6 (7.8 - 24.8) mm |
|                                   | Series 2       | 16.3 mm              |

(a) HA25 (series 1 stands for the double profile in figure 3.13).

|          |         |
|----------|---------|
| $R_b$    | 12.5 mm |
| $h$      | 1.6 mm  |
| $\alpha$ | 25 °    |
| $c$      | 8 mm    |

(b) FRP.

|                            |              |
|----------------------------|--------------|
| $R_b$                      | 12 ± 0.15 mm |
| $R_{wire}(R_{king\ wire})$ | 7.8 (8.9) mm |
| Pitch length, $l_p$        | 300 mm       |
| $t$                        | 1.65 mm      |
| $h$                        | 0.28 mm      |
| $\beta$                    | 50 °         |
| $c$                        | 7.5 mm       |

(c) Flexible.

In the case of smooth bolts, a barrel and wedge system is installed on the metallic tube to prevent this tube from sliding off the bolt. In fact, in the case of rough bolts, the bolt profile (plus the grooves made along the metallic tube inner surface) difficulties the slip between the tube and the bar. However, a smooth rod makes such slip easier, especially if the confining pressure applied to the rock mass is high.

The borehole radius depends on the bolt type:  $R_g = 20$  mm for the metallic rockbolts samples and  $R_g = 17.5$  mm for the FRP rockbolts and the Flexible cablebolts samples. This way, the ratio  $R_g/R_b$  remains practically constant. Concerning the metallic tubes, two different inner diameters have been used to keep the ratio tube inner diameter/bolt maximum diameter constant:

- 37 mm inner diameter tubes for HA25 rockbolts;
- 32 mm inner diameter tubes for FRP rockbolts, smooth bars and Flexible cablebolts.

The resin grout used is Minova Lokset SiS SF-L 32/500. This resin has a setting time of 3 minutes and is provided in cartridges. Some samples have been prepared in the laboratory to conduct unconfined and triaxial compressive tests and also indirect tensile tests. The relevant mechanical characteristics of the resin used are summarized in table 3.5. To prepare the cementitious grouts, Portland cement has been used. For grouts with ratios  $w : c \geq 0.35$ , Chryso's Fluid Optima 175 fluidifier has been added to improve the workability of the mixture. The dosage used is 1 % in mass of the weight of cement. As with resin, some samples have been prepared to characterize the cementitious grouts in use (only ratio  $w : c = 0.35$  because it has been used more times). The results are also shown in table 3.5.

**Table 3.5:** relevant mechanical properties of the two grouts most commonly used to anchor the bolts to the rock samples.

|  | Resin | Cement ( $w : c = 0.35$ ) |
|--|-------|---------------------------|
| Density, $\rho_g$ (kg/m <sup>3</sup> ) | 1987  | 1958                      |
| Young's modulus, $E_g$ (MPa)           | 11450 | 17500                     |
| Poisson's ratio, $\nu_g$               | 0.31  | 0.27                      |
| $UCS_g$ (MPa)                          | 67.1  | 44.1                      |
| Tensile strength, $R_{t,g}$ (MPa)      | 12.1  | 3.2                       |
| Cohesion, $C_g$ (MPa)                  | 20.2  | UV                        |
| Friction angle, $\varphi_g$ (°)        | 28    | UV                        |

UV: undertermined value

### Pull-out test campaign on cablebolts

Table 3.6 compiles the characteristics of the pull-out tests conducted on Flexible cablebolts. All the results are presented in appendix B. As mentioned before, the main target of these tests was to evaluate the effectiveness of the set-up designed to prevent the cables from unscrewing and to compare the results issued from tests in which unscrewing was permitted or restricted. All the pull-out tests on cablebolts have been conducted at constant outer radial pressure, at a displacement rate of 0.02 mm/s and using the end plate. Two different embedment lengths have been used. These lengths are longer than those used for rockbolts according to the recommendations made by Hyett *et al.* [Hyett1992b]: cablebolts embedment lengths should be chosen to correspond to typical fracture spacings observed underground. Under these circumstances the scatter within the results is reduced, but the shear stress is less uniform along the embedded length, see figure 2.8. Furthermore, since these embedment lengths are only slightly shorter than the metallic tube length, a barrel and wedge system has been installed on top of such tube to block any possible relative slip between the bolt and the tube.

**Table 3.6:** pull-out tests conducted on cablebolts.

| Cablebolt | $p_r$ (MPa) | L (mm) | Grout | Unscrewing |
|-----------|-------------|--------|-------|------------|
| Flexible  | 2.7         | 325    | Resin | Yes (1)    |
|           |             |        |       | No (2)     |
|           |             | 250    | Resin | Yes (1)    |
|           |             |        |       | No (1)     |

### Pull-out test campaign on rockbolts

The main pull-out test campaign on rockbolts comprises 47 tests. All the pull-out tests conducted on HA25, FRP and smooth bars are compiled in table 3.7. Two short embedment lengths, 90 and 130 mm, were used in most tests. These lengths are comprised within the range  $L \in [6R_b, 10R_b]$ , recommended previously for rockbolts, *cf.* [Benmokrane1995, Verderame2009b] for instance. Some tests have been conducted two or more times to validate the results and to identify any scatter (the number of tests held at each combination of parameters should be still increased); but in fact, as stated by Hyett *et al.* [Hyett1992b], it is important to emphasize that the scatter within the results may be regarded as an inherent property (of failure) rather than due to experimental error. The asterisk \* indicates that the test was conducted at constant outer radial stiffness. Within these, some correspond to the tests in which the crater depression took place, *i.e.*, all the tests executed at constant outer radial pressure were carried out using the end plate. The most altered tests, due to the crater formation, have not been taken into consideration in the analysis described in chapter 4. All the test

results are compiled in appendix A.

**Table 3.7:** pull-out tests conducted on rockbolts.

| Rockbolt   | $p_r$ (MPa) | L (mm)     | Grout                              |
|------------|-------------|------------|------------------------------------|
| HA25       | 15          | 150        | Resin (1*)                         |
|            | 10          | 130        | Resin (3*, 2), $w : c = 0.35$ (1*) |
|            |             | 90         | Resin (1*)                         |
|            | 5           | 130        | Resin (1*,1), $w : c = 0.40$ (1*)  |
|            |             | 90         | Resin(1*, 1)                       |
|            | 2           | 130        | Resin (1*), $w : c = 0.35$ (1*)    |
|            |             | 90         | Resin (1*)                         |
|            | 1.2         | 130        | Resin (3)                          |
|            |             | 90         | Resin (1)                          |
|            | 0           | 130        | Resin (1*,1)                       |
| 90         |             | Resin (1*) |                                    |
| FRP        | 10          | 130        | Resin (1*)                         |
|            |             | 90         | Resin (1*)                         |
|            | 6           | 90         | Resin (1)                          |
|            | 5           | 130        | Resin (2*), $w : c = 0.35$ (1*)    |
|            |             | 90         | Resin (1*,1)                       |
|            | 2           | 130        | Resin (1*), $w : c = 0.35$ (1*)    |
|            |             | 90         | Resin (1*,1)                       |
|            | 0.6         | 90         | Resin (1)                          |
|            | 0           | 130        | Resin (1*), $w : c = 0.35$ (1*)    |
|            |             | 90         | Resin (1*,1), $w : c = 0.35$ (1*)  |
| Smooth bar | 5           | 130        | Resin (1)                          |
|            |             | 100        | Resin (1*)                         |
|            | 2           | 130        | Resin (1)                          |
|            |             | 100        | Resin (1)                          |
|            | 1.2         | 130        | Resin (1)                          |
|            | 0           | 130        | Resin (1)                          |

### 3.3 Analysis of the laboratory pull-out test results

#### 3.3.1 Pull-out tests on rockbolts

The following graphs show typical load-displacement curves issued from laboratory pull-out tests. Figure 3.14 corresponds to HA25 rockbolts, figure 3.15 corresponds to FRP rockbolts and finally figure 3.16 compiles the results obtained for the smooth bars. In addition to the load-displacement curves (as measured), the results are also shown in terms of the experimental bond-slip relationship,  $\tau_b(W)$ . The equation used to compute the shear stress reads

$$\tau_b(W) = \frac{F(W)}{2\pi R_b(L-W)} \quad (3.3)$$

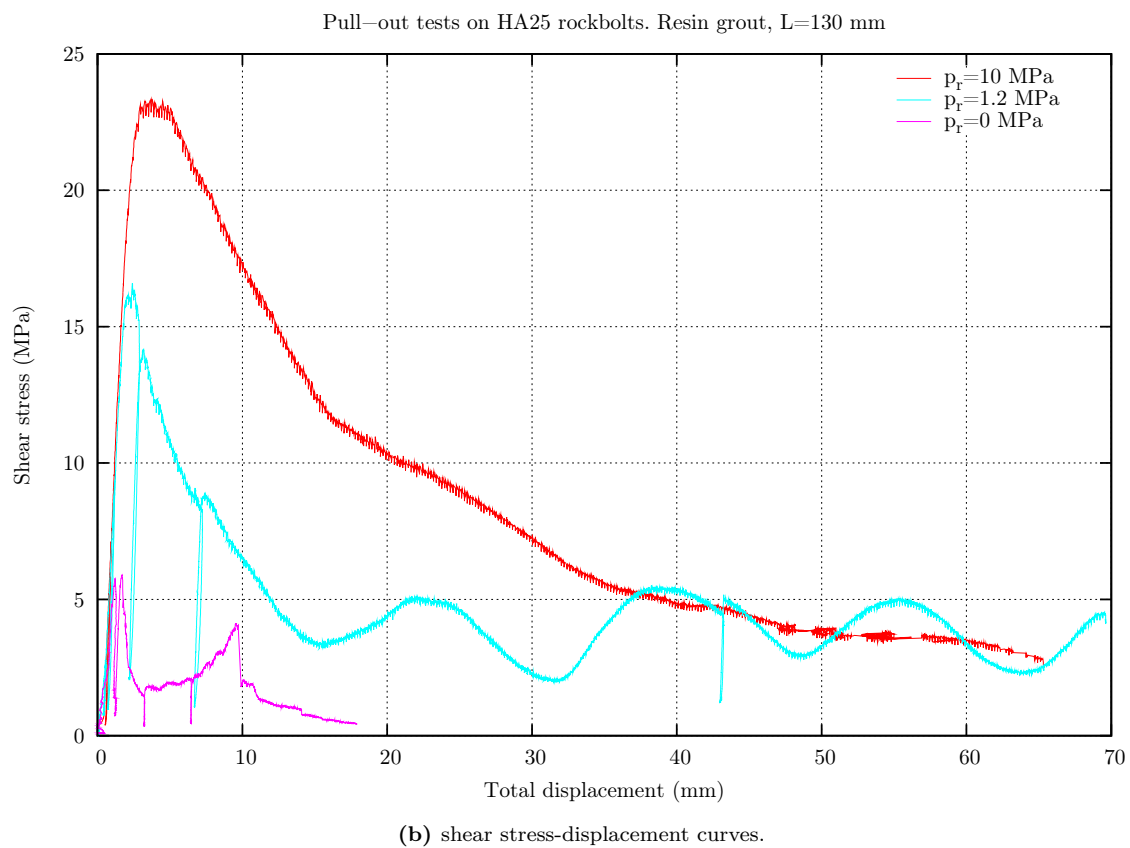
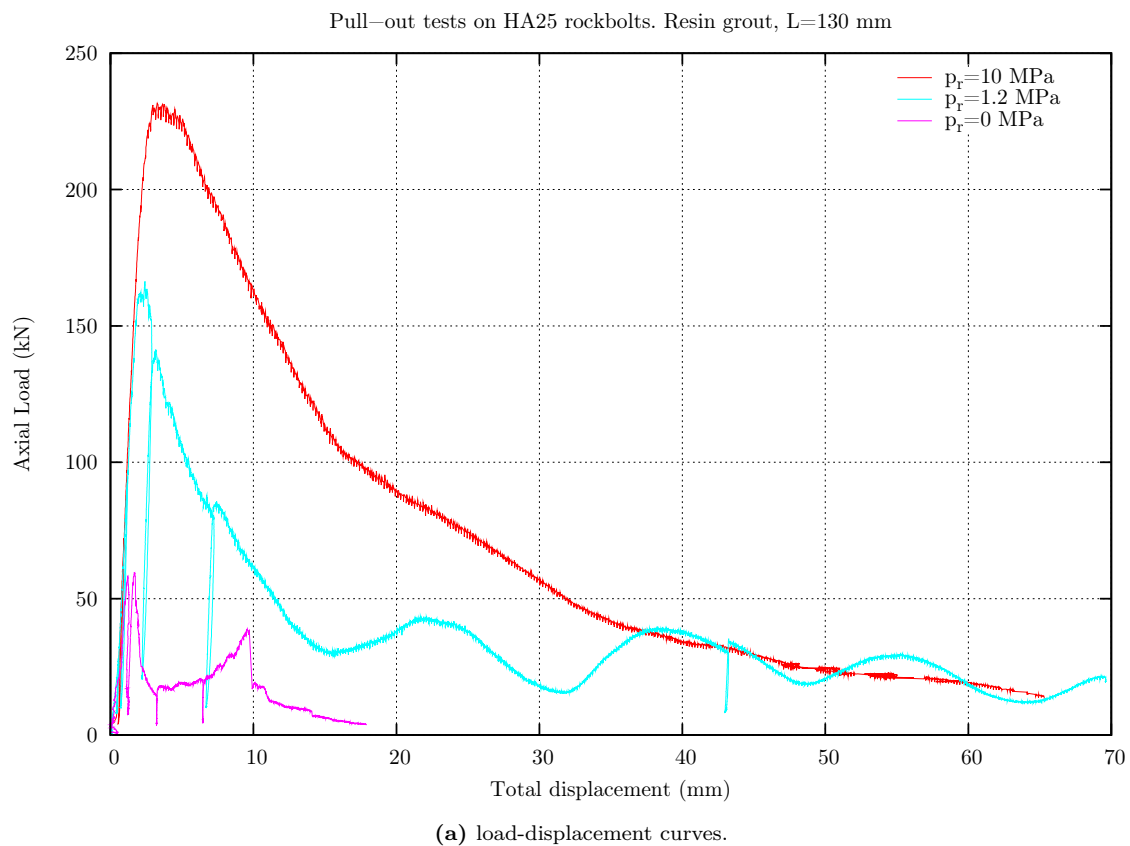


**Figure 3.14:** typical pull-out test results on HA25 rockbolts. The test at  $p_r = 0$  MPa is only shown partially because part of the test was purposely driven under different conditions (the whole test is displayed in appendix A.1, figure A.13).

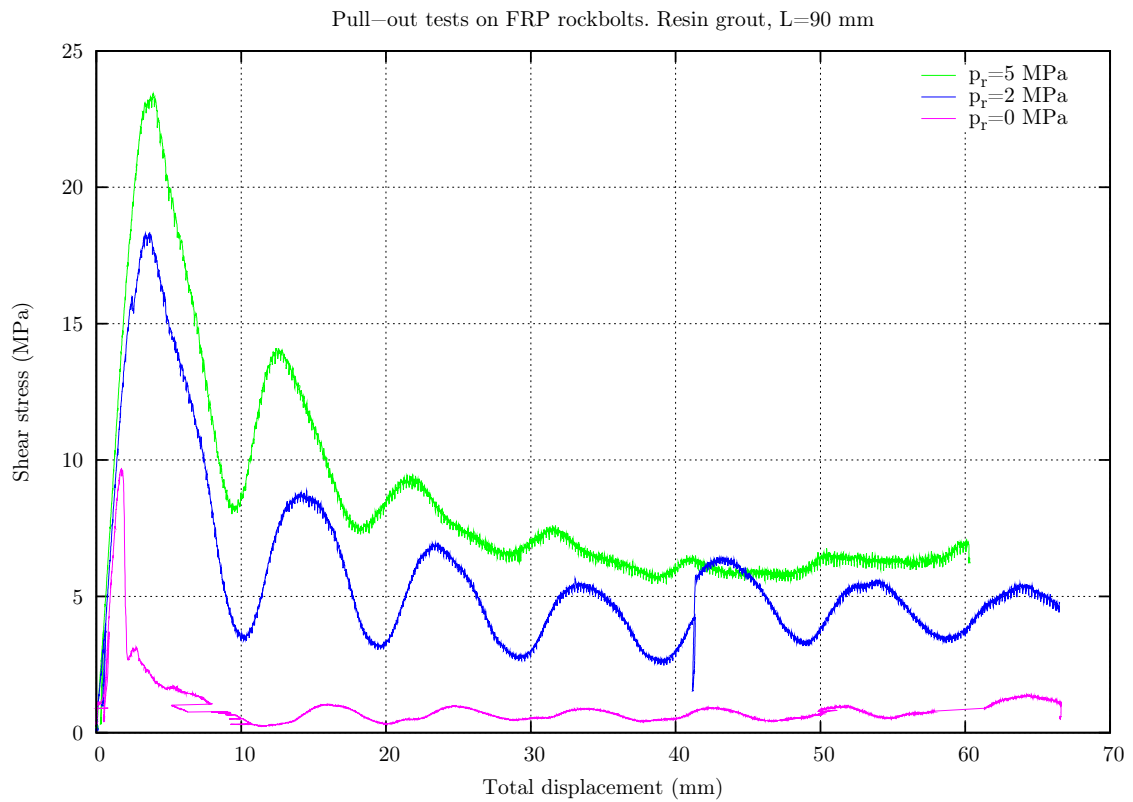
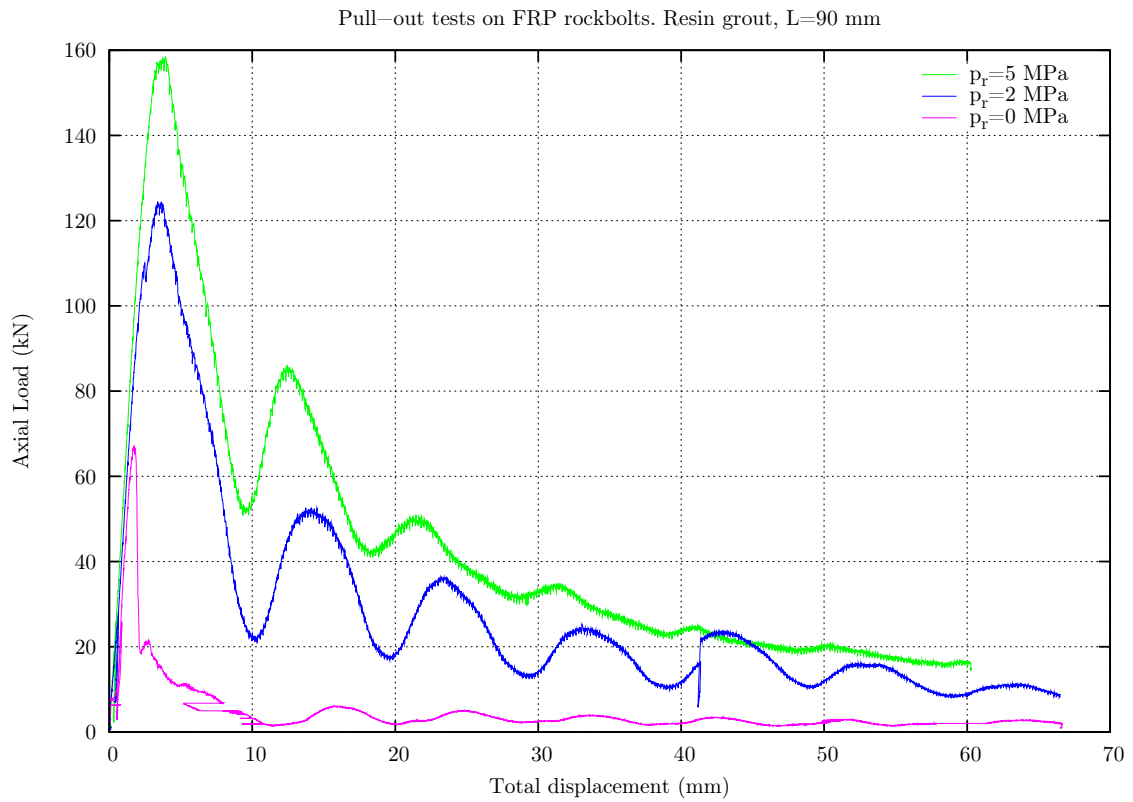


**Figure 3.15:** typical pull-out test results on FRP rockbolts.

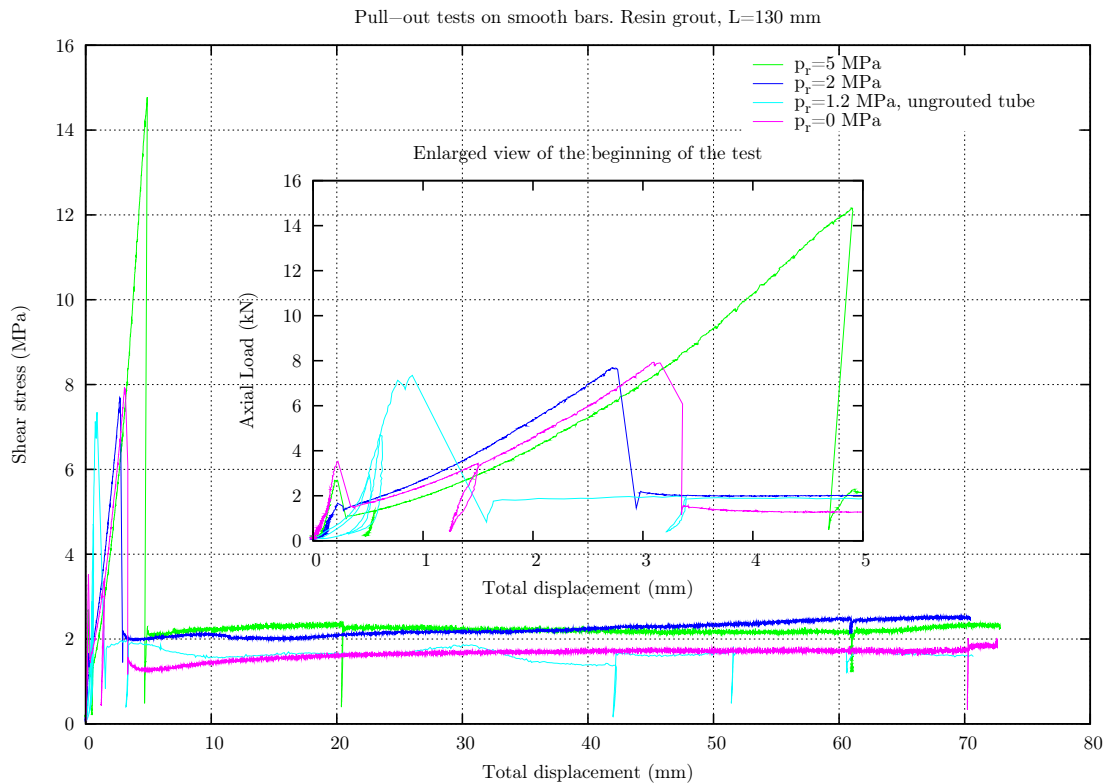
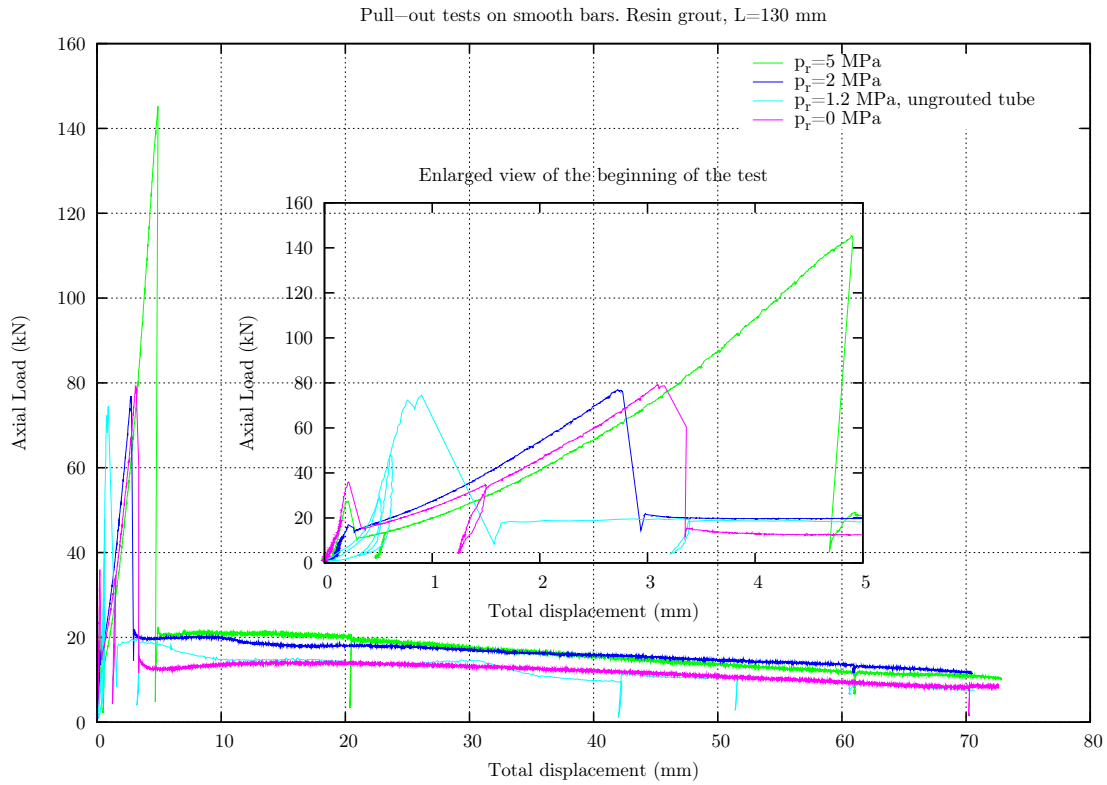


**Figure 3.16:** typical pull-out test results on smooth bars.

All these results correspond to pull-out tests carried out at constant outer radial pressure, at a displacement rate of 0.02 mm/s and using the end plate. In each figure, the only difference between the test results shown is the confining pressure applied. It should be noted that, globally, these results are consistent with those found in the literature and issued from tests carried out in similar conditions: for instance, the pull-out test results conducted by Benmokrane *et al.* and Moosavi *et al.* [Benmokrane1995, Moosavi2005] are akin to the results shown here. Furthermore, in this research loading-unloading cycles have been made during most of the pull-out tests, in particular in the pre-peak phase. The aim of these cycles has been to investigate the irreversibilities that may arise as the axial displacement increases, in order to gain more insight into the decoupling mechanism at the bolt-grout interface.

Overall, the load-displacement response of HA25 and FRP rockbolts can be divided into four stages. Each stage is associated with a particular mechanism. The general characteristics of each stage are given here, while the full analysis of the results is discussed in chapter 4:

1. for small values of axial displacement ( $< 1.5$  mm for HA25 rockbolts and  $< 2.5$  mm for FRP rods), the pull-out plot is characterized by a quasi-linear response that verifies  $dF/dW > 0$ . The axial stiffness  $dF/dW$  in the range 50-80 kN lies within 100-140 kN/mm for HA25 rockbolts and within 60-100 kN/mm for FRP rockbolts. In this stage, interface adhesion, mechanical interlock and friction contribute to the bolt-grout bond;
2. before the peak force is reached, the axial stiffness drops and the load-displacement response becomes non-linear, but the inequality  $dF/dW > 0$  still holds. In some of the tests, at low confining pressures in particular, this stage is accompanied by an audible sound. The results show that the load at which this phase starts increases with the confining pressure. This stage is associated with the joint development, that damages the bolt-grout bond gradually, thereby decreasing the reinforcement bearing capacity. However, since the axial force continues to increase, the damaging of the interface bond is thought to be stable during this stage;
3. at the peak force, the maximum capacity is attained. The peak load is reached within 1-4 mm. The higher the confining pressure, the higher the peak displacement. Moreover, the range of axial displacements for which the maximum load persists is pressure dependent: for high confinements, the maximum capacity can be maintained about 2-3 mm, whereas for the tests conducted without confinement, this capacity is lost after a short axial slip ( $< 1$  mm). The maximum load increases with the confining pressure, but not necessarily in a linear fashion;
4. post-peak stage: after the peak load, the pull-out response is characterized by an initial load drop ( $dF/dW < 0$ ) followed by a residual phase. The damaging of the interface is believed to occur in an unstable manner in this stage. The two different phases within the post-peak stage are distinguished as follows:
  - (a) the load decreases linearly until a displacement of approximately 15 mm for HA25 bolts and 10 mm for FRP bars (but in fact as it will be explained in the following chapter, this amount of displacement depends on the bolt profile). The slope of this part,  $k_p$ , increases (in absolute value) with the decrease of the confining pressure. This fact is related to the physical phenomenon that takes place during the test: for low confinements, both the grout and the rock sample are radially fractured (in the axial direction of the rock mass, the length of the fractured zone roughly coincides with the embedment length), and the

fractures are open. The sound detected during stage 2 may be due to the onset of the annuli splitting. The resulting wedges may be pushed apart as the bolt is axially pulled (in particular for the tests conducted at constant  $p_r$ ), thereby reducing the confinement provided at the bolt-grout interface by the grout and the ground. As a result, the axial load decreases steadily for a given increase in the axial displacement (this failure mechanism is quite brittle). However, for high confining pressures, the grout and the rock are not radially fractured (or at least, the fractures are not visible): instead, failure occurs within the grout itself, in shear. Hence, the decrease in the axial load is less steep for a given displacement increase (*i.e.*, this failure mode is less unstable than the radial splitting of the annuli). Figure 3.17 shows the final state of the grout and rock annuli for confining pressures of 10, 5 and 1.2 MPa (pull-out tests on HA25 rockbolts held at constant  $p_r$ ). As it can be seen, no fractures are visible for 10 MPa while for 5 MPa, the radial fractures are closed. Finally, for 1.2 MPa the radial fractures are fully open,



**Figure 3.17:** aspect of the grout and rock annuli after three pull-out tests conducted on HA25 rockbolts at constant  $p_r$ . From left to right:  $p_r = 10$  MPa,  $p_r = 5$  MPa and  $p_r = 1.2$  MPa.

- (b) for values of axial displacement greater than 10-15 mm, the residual phase is reached. The average axial load decreases at a lower rate with respect to the axial displacement. The residual load depends on both the confining pressure (friction) and the mechanical interlock (due to the bolt profile), as indicated by the load fluctuations observed in this phase in some tests. As for the oscillations, they are clearer for FRP rebars than for HA25 bolts at every pressure tested. The main reason for this difference is the bolt profile, which is smoother (in terms of angle of the indentations) for the FRP bars: if the bolt profile is rougher, it is more likely that the grout between the indentations is damaged as the bolt slips (and even sheared, so that the bolt imprints are deleted). On the other hand, in the case of FRP bars the failure interface is not smooth, but reproduces the bolt profile quite well, even at the end of the test (this has been proved by the visual observation of the samples after the tests). In this case, the bolt-grout contact surface varies as the bolt slips.

It can be seen that the pull-out test results on the smooth bars are very different to the results on HA25 and FRP rockbolts. The differences are due mainly to the fact that, in the case of the smooth bars, failure takes place first inside the metallic tube, at the bar-adhesive interface. Failure of the bar-adhesive bond corresponds to the first peak in the curves in figure 3.16. Thereafter, the barrel and wedge system starts to act, gripping itself to the smooth bar, thereby blocking the relative displacement between the tube and the bar. This process corresponds to the second ascending branch

in the curves, see the enlarged view in the plots. The second peak load corresponds to the failure of the bolt-resin bond inside the rock core sample. The load decreases sharply due to the loss of the interface adhesion and the absence of mechanical interlock. The residual phase is then attained which, according to the results displayed in the figure, does not depend significantly on the confining pressure. In order to verify these results, a pull-out test has been conducted without grouting the bar to the metallic tube; instead, the relative movement between the bar and the tube has been directly blocked on top of the tube. The results are also displayed in figure 3.16. As it can be seen, there is only one peak, which corresponds to the bar-resin bond failure inside the rock core sample. The peak and the residual phase are comparable to those obtained when the bar is grouted to the metallic tube.

As regards the pull-out tests in which the crater depression occurred, the cone height  $h_{\text{cone}}$  must be subtracted from the nominal embedment length  $L$  after the cone creation, that is thought to take place at the onset of the axial slip according to the samples visual observation. Therefore, the effective length of the test sample decreases from  $L$  to  $L_{\text{eff}} = L - h_{\text{cone}}$ . This length correction has only been made for the tests in which failure clearly occurred at the bolt-grout interface (again, the other tests have been disregarded in the analysis presented in chapter 4).

Finally, the effect of the boundary conditions is shown in figures 3.18 and 3.19. All the results shown correspond to pull-out tests on resin-grouted HA25 rockbolts.

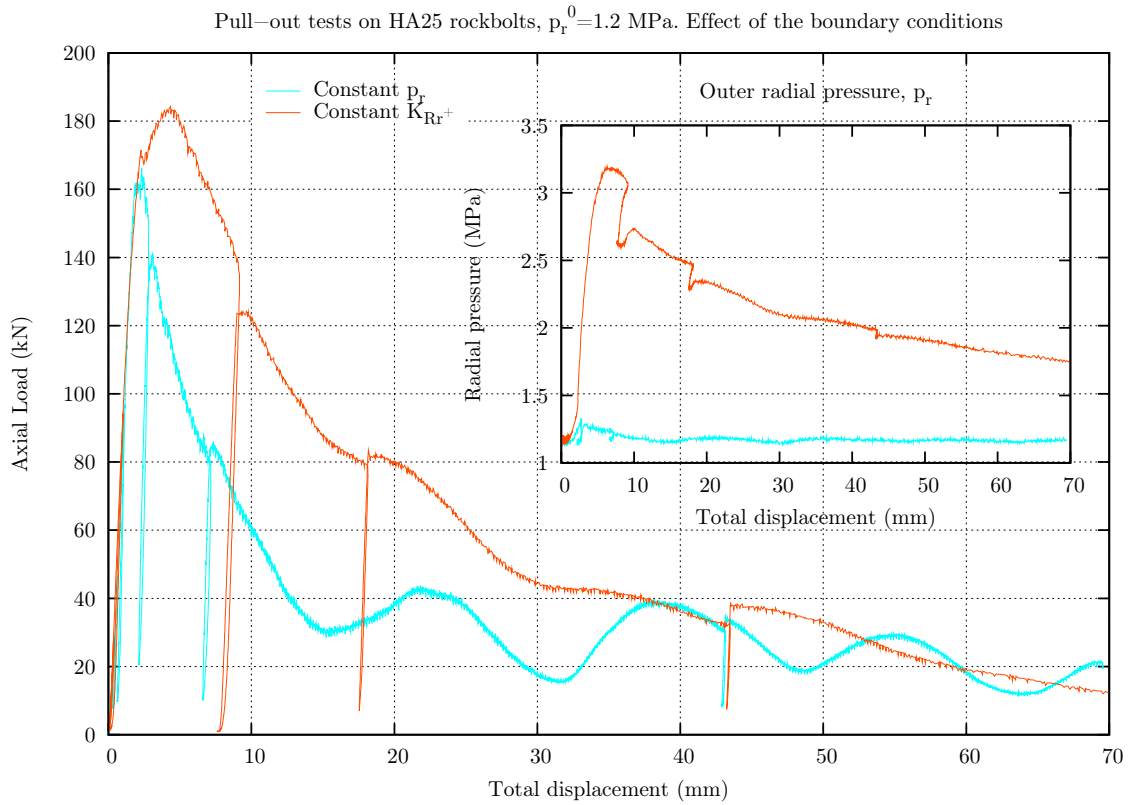


**Figure 3.18:** pull-out test results on HA25 rockbolts. Effect of the boundary conditions.

The tests were held at a displacement rate of 0.02 mm/s, using the end plate and with an embedment length  $L = 130 \text{ mm}$ . Owing to the pressure increase that takes place in the tests conducted at constant outer radial stiffness, the axial load required to pull the bolts is higher than in the tests held at constant outer radial pressure. Furthermore, the pressure increase brings about more friction

and consequently the interface damage is high. This explains the results in figure 3.18, where the oscillations due to the bolt profile are clearer for the test held at constant  $p_r$ . In figure 3.19, the pressure variation is much lower and as a result the interface damage is similar for the two tests.

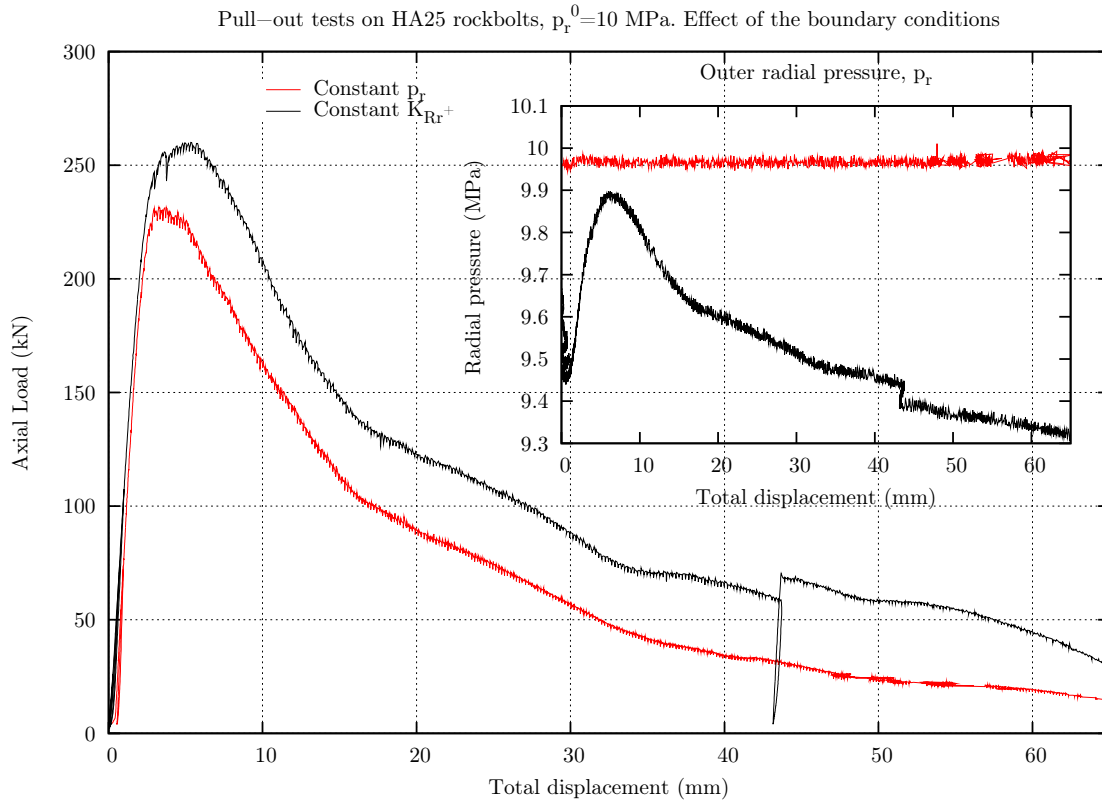


**Figure 3.19:** pull-out test results on HA25 rockbolts. Effect of the boundary conditions.

### Analysis of the loading-unloading cycles

Figure 3.20 shows the loading-unloading cycles made around the peak load of a pull-out test on a HA25 rockbolt embedded along 130 mm. The confining pressure applied is  $p_r = 1.2$  MPa (this test is fully represented in figure 3.14a, cyan curve).

As it can be seen, since an early stage of the test some irreversibilities appear, which are thought to be due to the progressive damaging of the interface until the peak force, when the joint fully develops. The fact that these irreversibilities occur even when neither the grout nor the rock sample split radially (*i.e.*, when they behave elastically) confirms that they are due to the interface behaviour. Thus, before the peak load, the response is non-reversible. The slopes of the ascending branches of the four cycles shown are 130, 167, 181 and 148 kN/mm, respectively (the slope of a fifth cycle made at  $W \approx 43$  mm is 125 kN/mm). The tangent slope of the load-displacement curve within the range 40-120 kN is about 110 kN/mm.

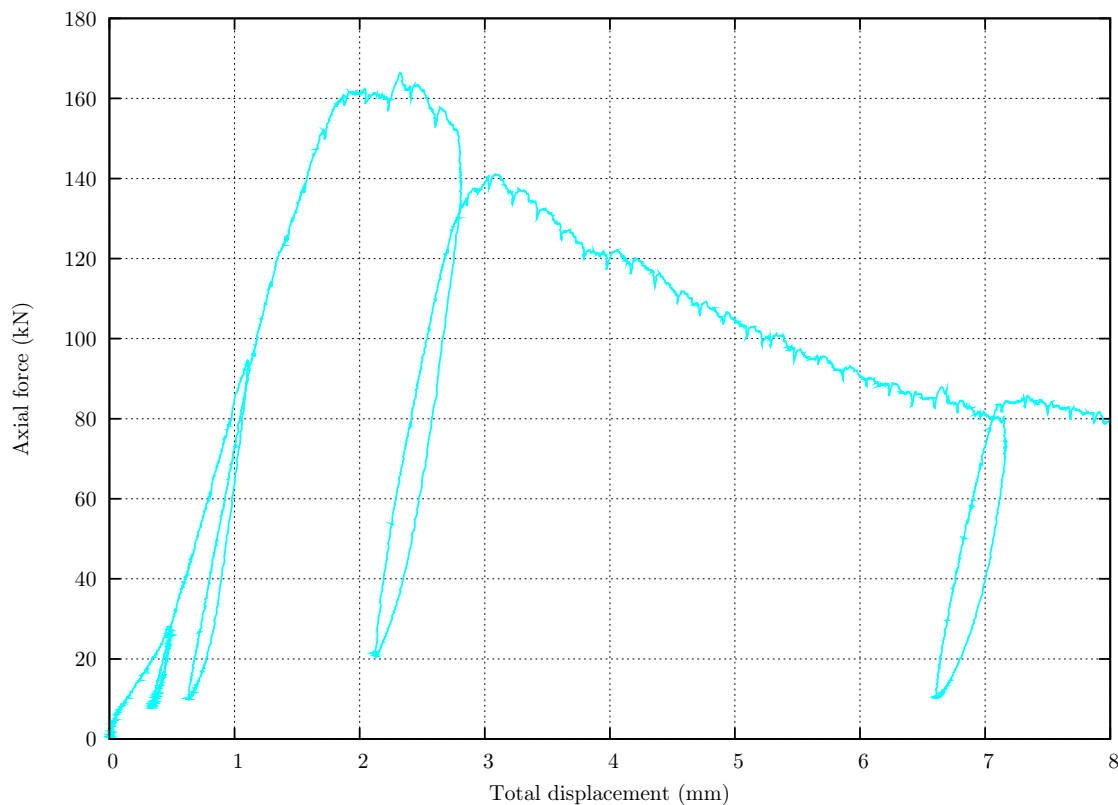


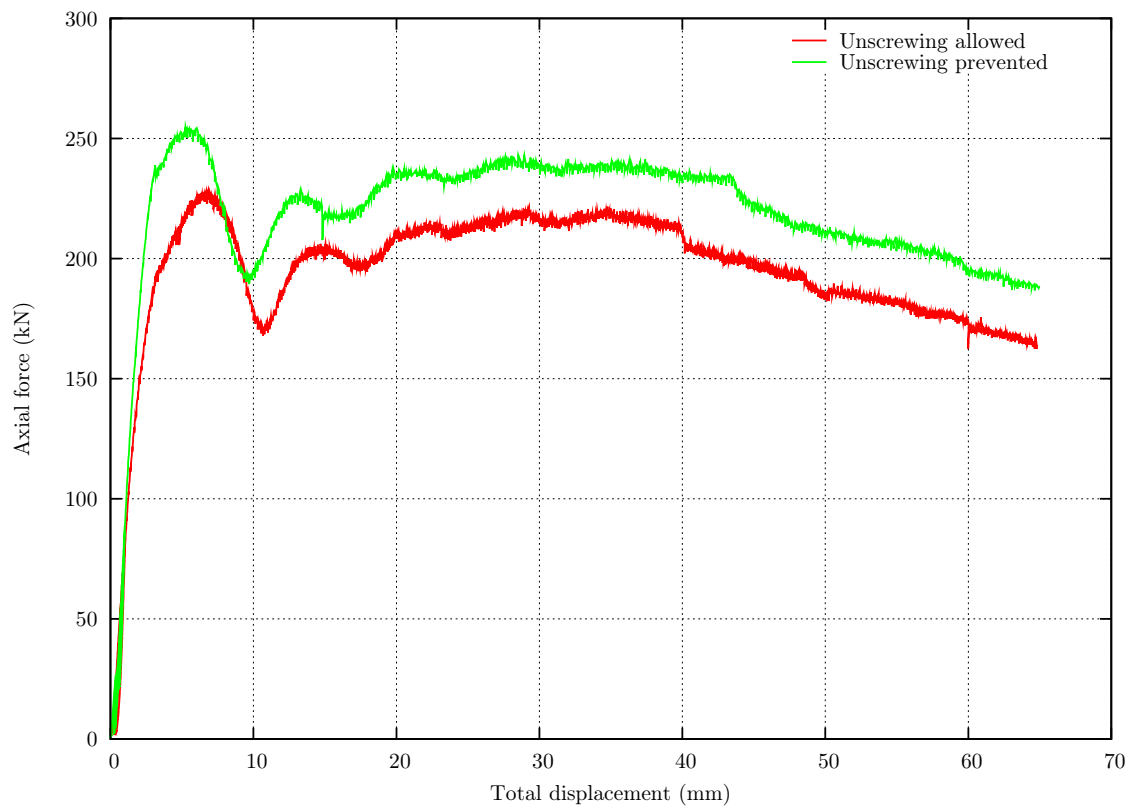
**Figure 3.20:** loading-unloading cycles made during the pull-out tests.

### 3.3.2 Pull-out tests on cablebolts

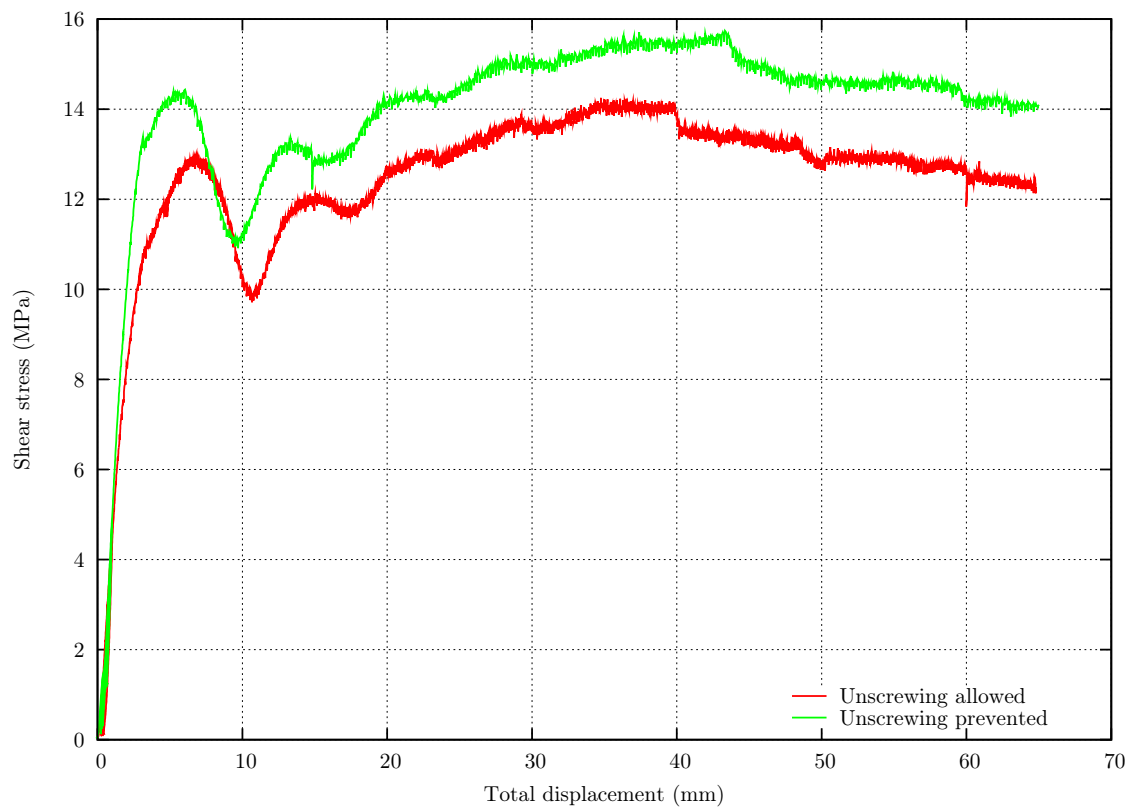
Figure 3.21a shows the load-displacement results of two pull-out tests carried out on Flexible cablebolts using an embedment length  $L = 250$  mm (see table 3.6 for a full description of the tests). Regarding the operating conditions, the only difference between these two tests is that the new tools designed to prevent the unscrewing phenomenon (*cf.* part 3.2.1) were used in one of the tests. The results, in terms of shear stress-axial displacement are plotted in figure 3.21b; in fact, according to figure 2.8, the shear stress distribution in the case  $L = 250$  mm is almost uniform throughout the pulling process.

In the case where unscrewing was allowed, at the end of the test an angle of  $60^\circ$  was measured between the fixed part of the jack and its piston (clockwise because the wires are wound left-handed). The geometric angle is  $78^\circ$ , but as explained by Hyett *et al.* [Hyett1995], the measured angle is normally  $10\text{--}20^\circ$  lower than the geometric one because at the beginning of the test, it is more difficult for the cable to unscrew from the grout. When the new tools were installed, there was no relative rotation between the parts of the experimental bench. Figure 3.21a shows that the load was approximately 25 kN higher in the post-peak phase when unscrewing was restricted than when it was allowed. However, these results do not look like those displayed in figure 3.4b. In fact, the visual observation of the samples after the tests reveals that the failure mode was quite similar in both cases, *i.e.*, the resin grout was damaged even when unscrewing took place, see figure 3.22.

In their research, Bawden *et al.*, [Bawden1992] used a non-indented cablebolt grouted using a cementitious grout. Thus, the differences in the results are likely to arise from the strand profile and the grout properties. To verify this point, pull-out tests should be conducted on smooth cablebolts



(a) load-displacement curves.



(b) shear stress-displacement curves.

**Figure 3.21:** pull-out test results on Flexible cablebolts. Influence of the unscrewing phenomenon in the current set-up.

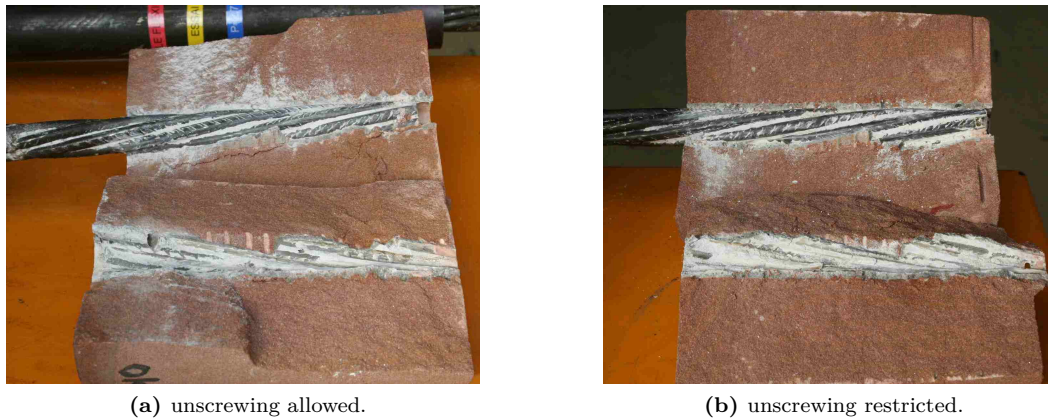


**Figure 3.22:** overview of two cablebolt samples after the tests.

grouted in a cementitious grout similar to that used by Bawden *et al.* But anyway, it is important to recall that, in order to reproduce the field situation, cablebolts should be prevented from unscrewing at laboratory-scale, even if the results are not significantly different from those obtained using the unscrewing-prevented set-up. This justifies the use of the new designed tools.

### 3.3.3 Comparison of pull-out test results on rockbolts and cablebolts

The contrast of figures 3.14a, 3.15a, 3.16a and 3.21a shows important differences, mainly in the post-peak phase: in the case of rockbolts, the load decreases quite sharply towards a lower residual load; however, in the case of cablebolts the load increases again after a short decrease of about 60 kN. The oscillations of the load-displacement curve within this phase are due to the wires indentations. After 40-50 mm of axial displacement, the load starts to decrease almost linearly.

The principal reason to this difference is to be found in the bar profiles: Flexible cablebolts are provided with very small asperities (in terms of height and angle of the indentations), while the rockbolt indentations are more marked. Rougher profiles favour the damaging of the grouting material, which will be progressively crushed and sheared as the axial displacement increases, thereby reducing the necessary force to pull the bolt out of the borehole.

### 3.3.4 Application of analytical and numerical tools to interpret and understand the results

Before starting using the pull-out test results to define a constitutive law for the bolt-grout interface, the bench has been analyzed both analytically and numerically. The main reason for this analysis is that, when the current thesis began, the bench had just started to be used and therefore some insight was needed to understand the way it works.

Let us first try to reproduce the initial slope observed in most of the laboratory pull-out tests. As for the analytical tools, the axial analysis described in section 2.3 has been applied to the lower part of the bench (*i.e.*, to the grout annulus and the rock sample). Actually, the metallic tube-adhesive assembly cannot be analyzed in the same way due to two main reasons:

- the boundary conditions along the metallic tube outer surface are not uniform: as a matter of fact, the load is transmitted only along part of the metallic tube threaded length (in the form of a shear force), while the rest of the tube outer surface is not constrained;

- with a view to the embedment length inside the tube ( $L_{\text{tube}} = 540$  mm), the shear stress is not likely to be uniformly distributed along the  $Z$  coordinate, *cf.* figure 2.8. Therefore, equations (2.6) and (2.22) are not totally accurate.

Equation (2.26) has then been applied to the rock and grout annuli under the assumption that both the bolt-grout and the grout-rock interfaces are coupled. This yields

$$\tau_b R_b \sum \frac{\ln(R_m/R_i)}{\mu_m} = w_b^- - w_m^- \quad (3.4)$$

where the indices  $m$  and  $i$  depend on the boundary conditions on top of the rock sample: before the end plate was used,  $w_m^- = w_{\text{pist}}^-$  and  $\sum \frac{\ln(R_m/R_i)}{\mu_m} = \ln(R_{\text{pist}}/R_g)/\mu_r + \ln(R_g/R_b)/\mu_g$ , where pist stands for the piston inner radius; after the introduction of the end plate,  $w_m^- = w_{\text{pl}}^-$  and  $\sum \frac{\ln(R_m/R_i)}{\mu_m} = \ln(R_{\text{pl}}/R_b)/\mu_g$ , where pl represents the end plate inner radius. As explained in section 2.4, the combination of the bolt equilibrium equation (2.1) with equation (3.4) lets determine the axial load, axial displacement and shear stress along the bolt, when the interfaces are coupled. But, in order to do this correctly, the axial movement of the grout and the rock should be bound, so that the displacement at the interface equals the axial displacement of the rockbolt. It can be easily realized that the use of the end plate is favorable in this sense. Thus, the combination of the mentioned equations gives equation (3.5), in which  $w_b^- \equiv W$  and  $w_{\text{pl}}^- = 0$ :

$$\pi R_b^2 E_b W'' = 2\pi R_b \frac{\mu_g W}{R_b \ln(R_{\text{pl}}/R_b)} \quad (3.5)$$

The differential equation (3.5) may be written

$$W'' = \frac{2\mu_g}{R_b^2 E_b \ln(R_{\text{pl}}/R_b)} W \quad (3.6)$$

The resolution of equation (3.6) allows to determine the slope of the load-displacement relationship when the bolt-grout interface is totally coupled:

$$F(Z=L) = E_b \pi R_b \beta \tanh(\beta L/R_b) W(Z=L) \Rightarrow k = E_b \pi R_b \beta \tanh(\beta L/R_b) \quad (3.7)$$

where

$$\beta^2 = \frac{2\mu_g}{E_b \ln(R_{\text{pl}}/R_b)} \quad (3.8)$$

The application of equation (3.7) to the pull-out tests conducted on HA25 rockbolts ( $R_{\text{pl}} = 14.5$  mm,  $L = 130$  mm, resin grout) gives an estimate of the slope:  $k_{\text{analy}} \approx 3730$  kN/mm. This slope is steep because when the interface is coupled, the axial displacement is small. In order to verify this analytical approach, a FEM simulation of the bench has been carried out in 2D (axisymmetric conditions). The geometry and mesh used are illustrated in figure 3.23. Like in the analytical case, all the materials have been supposed to behave elastically and the interfaces to be coupled because only the beginning of the test is modelled. In order to simulate the test, a relative displacement between the threaded plate and the biaxial cell upper piston has been applied. The result gives a slope in the lower part  $k_{\text{low,num}} \approx 3420$  kN/mm, which is in quite good agreement with the theoretical prediction. To calculate this slope, the grout axial displacement at  $R = R_{\text{pl}}$  has been taken into account; otherwise the slope would be  $k'_{\text{low,num}} \approx 2950$  kN/mm. In other words, the assumption

$w_{pl}^- = 0$  leads to an underestimation of the initial stiffness of approximately 14 % (but, without the end plate,  $k'_{low, num} \approx 2200$  kN/mm [initial stiffness underestimation of 36 %]). However, neither the analytical nor the numerical slope are close to the initial slope of a typical pull-out test result on a HA25 rockbolt,  $k_{test, exp} \approx 100 - 140$  kN/mm.

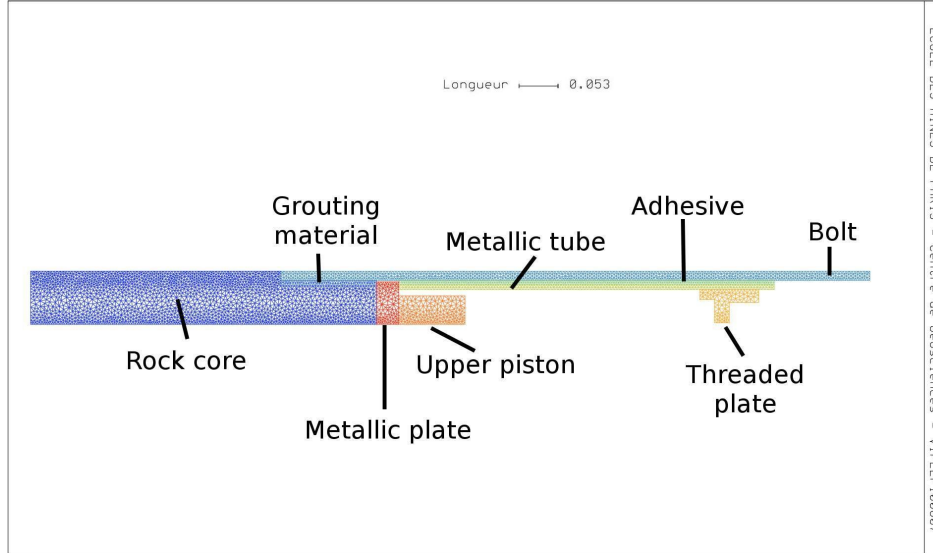


**Figure 3.23:** finite element mesh and geometry used in the numerical simulations.

This analysis shows that the initial phase of the tests possibly does not correspond to the elastic behaviour of the grout and the rock. As a second possibility, the initial slope of the test could be due to the upper assembly elasticity. Thus, such slope has been calculated from the numerical results (taking this time into account the total displacement as measured during the test and not only the displacement in the lower part of the bench). The numerical slope is  $k_{test, num} \approx 280$  kN/mm. Consequently, although the upper part elasticity is not negligible, the experimental slope is much lower than the predicted one. The difference between the two is believed to be beyond a reasonable theory-experience gap. At this stage, it was decided to test the metallic tube-rockbolt anchorage: any displacement occurring in the bench upper part, whatever its origin (that is to say, the behaviour of the components or the decoupling along the interfaces), is not involved in the determination of the constitutive law of the bolt-grout interface, so it should be subtracted from the measured displacement. Hence, in order to evaluate the bench "stiffness", namely the rigidity of the bolt-tube assembly (the other parts of the bench are made of steel and are supposed to be indeformable with respect to the bolt-tube assemblage), three samples composed of a HA25 rockbolt grouted to a metallic tube (*i.e.*, without the rock sample) were prepared and tested. A similar procedure was undertaken with FRP rockbolts. The results are discussed in the next subsection.

### 3.3.5 Bench calibration

The samples were tested with the rockbolt being completely blocked instead of being grouted to the rock sample. An axial force was applied to the metallic tube like in a regular pull-out test. In the case of HA25 rockbolts, a maximum force of 240 kN was applied (the yield strength of these bars is  $\sigma_{e,b} = 500$  MPa, which corresponds to 245 kN for a 25 mm diameter rod). Loading-unloading cycles were executed. The results of the three calibration tests are consistent. The colored curve in figure 3.24 shows the load-displacement response of one of these tests (each color represents a loading-unloading

cycle). As it can be seen, the response seems to be reversible until an axial load of about 100-120 kN.

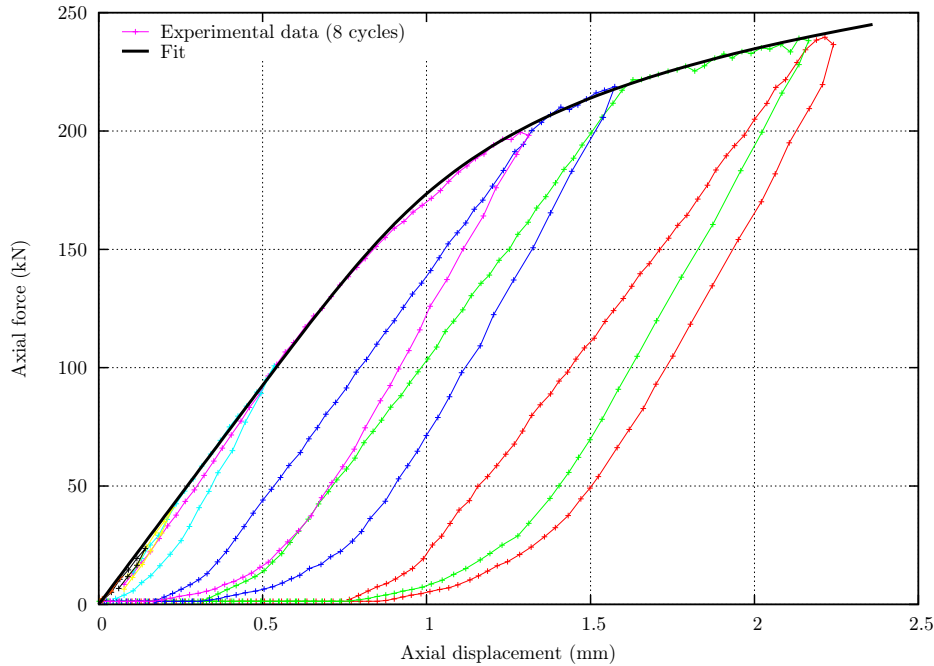


**Figure 3.24:** bench calibration for HA25 rockbolts: load-displacement response of the upper part obtained in a calibration test and fit function used to correct the experimental displacement data (equation (3.9)).

The initial slope of the envelope is about 190 kN/mm. This value is barely higher than the initial experimental slope; consequently, the initial phase of the pull-out test is quite influenced by the response of the upper part of the bench. This phase of the test is especially important if the results are used to derive the bond stiffness, which, as emphasized by Stillborg [Stillborg1983], is a valuable element in the definition of the interface behaviour. Hyett *et al.* [Hyett1992b] also stressed the difficulty of properly ascertaining the initial stiffness of the pull-out test results.

With a view to this finding, the displacement corresponding to the upper part of the bench,  $W_{\text{up}}$ , has been subtracted from the measured displacement,  $W_{\text{raw}}$ , according to equation (3.9), in which  $W_{\text{up}}$  is expressed in [mm] and  $F$  in [kN]. This equation corresponds to a good fit to the data envelope shown in figure 3.24.

$$W_{\text{up}} = 0.0054F + (0.0041F)^{8.1} \quad (3.9)$$

The displacement of the lower part of the bench  $W^*$ , which is the relevant displacement, is then calculated as

$$W^* = W_{\text{raw}} - W_{\text{up}} \quad (3.10)$$

This displacement includes the rock and grout annuli elasticity (it has been proven that it is negligible) plus the displacement occurring at the bolt-grout interface, which is the meaningful one. The comparison between the raw and corrected results is shown in figure 3.25. As expected, this correction is of particular importance at the beginning of the test, for small values of axial displacement. The slope of the initial part is now  $k_{\text{test}}^* \approx 500$  kN/mm.

Finally, the compressibility of the rock mass could also influence the raw displacement measurements (as explained in subsection 3.2.1, the LVDTs sensors measure the relative displacement between the fixed part of the hydraulic jack and the sensors support). The numerical simulations announce a

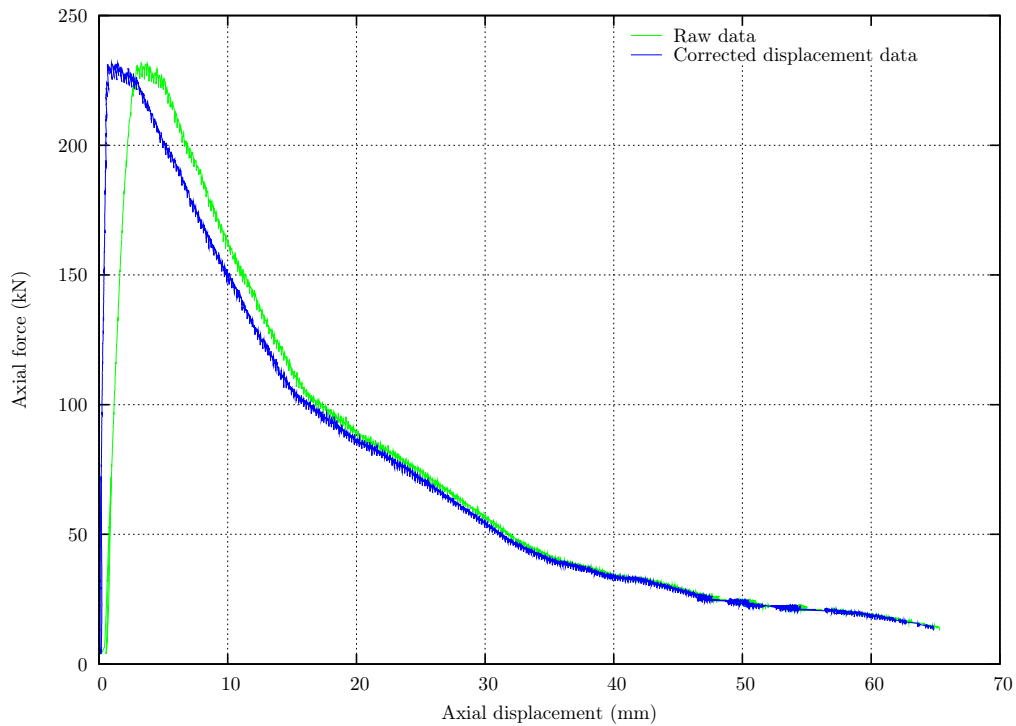
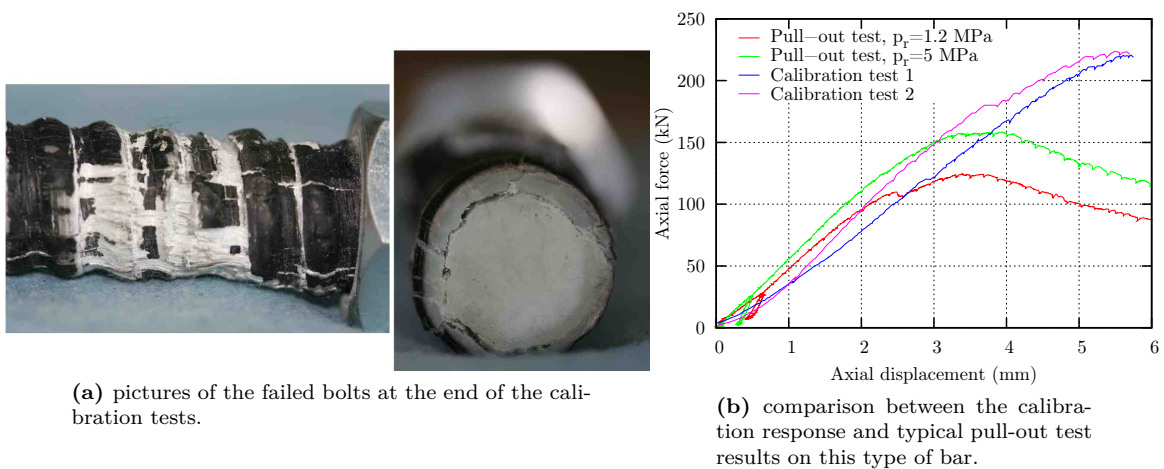


**Figure 3.25:** displacement correction of the pull-out test results: comparison between raw and corrected data.

maximum rock compression  $|W_{\text{rock}}| < 0.1$  mm for a maximum load of 245 kN. This amount is negligible compared to the displacement in the upper part of the bench at the same load,  $W_{\text{up}} \approx 2.25$  mm.

A similar procedure has been followed to test the rigidity of the FRP rockbolt-tube assembly. Two calibration tests have been performed and the results are consistent. In order to block the FRP rockbolts, *Powerthread* 100 mm long steel nuts have been used. In both tests, the bolt itself failed at 220 kN. The visual observation of the samples after the tests reveals that it is the external fibre&coat layer (3-4 mm thick) that failed, while the bolt core resisted. As it can be seen in the pictures in figure 3.26a, the external layer slipped with respect to the bolt core. The comparison between the calibration results and the typical initial pull-out response of FRP rockbolts is shown in figure 3.26b.



(a) pictures of the failed bolts at the end of the calibration tests.

(b) comparison between the calibration response and typical pull-out test results on this type of bar.

**Figure 3.26:** bench calibration for FRP rockbolts.

The graph points out that the pull-out curve of a regular test is stiffer than the calibration curve; consequently, the displacement issued from the calibration test has not been subtracted from the raw displacement data. However, the extension in the bolt free length between the metallic tube and the rock sample has been taken away from the displacement measurements.

Finally, as for the pull-out tests on smooth bars, only the force measurements have been used in the understanding of the bolt-grout interface behaviour. On the other hand, the rigidity of the Flexible cablebolt-tube assembly has not yet been tested at this stage of the research (attention has been focused on rockbolts).

### 3.3.6 Effect of the grout and rock annuli boundary conditions on the radial pressure along the embedment length

With a view to the analysis of the pull-out test results (*cf.* chapter 4), it is important to know whether the interface response is uniform along the embedment length. The uniformity of the shear stress  $\tau_b$  has already been proven due to the use of short lengths. As for the uniformity of the interface pressure  $p_b$ , the simplified analysis described in section 2.2 assumes that the response of the grout-ground assembly is uniform along the  $Z$  axis. However, the bench is a complex structure and it is necessary to verify the uniformity of  $p_b$ . To do so, some numerical simulations have been made. The results show that the distribution of  $p_b$  is uniform, except in the vicinity of both extremities of the borehole, but in particular in the vicinity of the borehole collar. In these simulations, a constant confining pressure of  $p_r = 5$  MPa has been applied and the interfaces have been supposed to be coupled. A relative displacement between the upper and lower parts of the bench of only 0.25 mm has been modelled. The length affected by the uneven radial pressure distribution is about 25 % of the total embedment length. Moreover, the introduction of the end plate reduces the influence of the end effects, see figure 3.27.

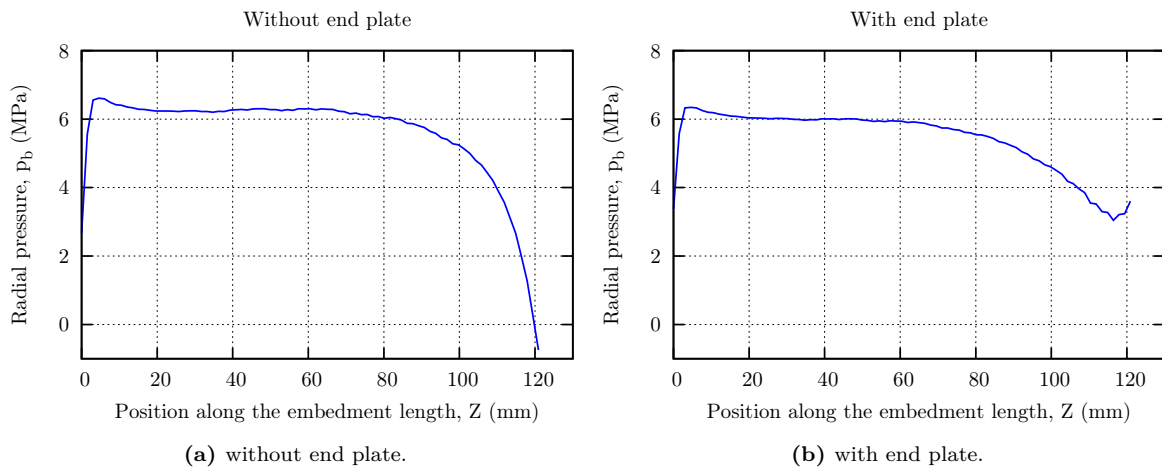


**Figure 3.27:** FEM simulations of the experimental bench. Distribution of the radial pressure  $p_b$  along the bolt-grout interface when  $p_r = 5$  MPa.

In order to understand the reason of this uneven distribution, several simulations of the lower part of the bench (*i.e.*, rockbolt, grout annulus and rock sample) have been made. Again, all the materials involved have been supposed to behave elastically. An axial displacement of 0.09 mm has been applied to the rockbolt at  $Z = L = 130$  mm in all cases. Such displacement corresponds to the average bolt axial displacement at  $Z = L$  extracted from the simulations shown in figure 3.27. The boundary

conditions on the upper surface of the rock sample and the grout annulus have been changed in each modelling. In particular, the rock and the grout were left free at  $Z = L$  in one of the simulations. The aim of such simulation was to evaluate the effect of the reaction force of the hydraulic jack (Hagan [Hagan2004] highlighted that the reaction force has the potential to modify significantly the stress field around the borehole, *cf.* page 88, but didn't evaluate its effect on the radial pressure along the bolt-grout interface). The distribution of the radial pressure  $p_b$  at the bolt-grout interface when both the rock and the grout are free at  $Z = L$  is displayed in figure 3.28. From this figure, it is concluded that the uneven distribution of  $p_b$  is not due to the reaction force, but rather to the other boundary conditions of the problem (vertical displacement not blocked at  $Z = 0$  and  $Z = L$  and application of the axial displacement to the rockbolt).

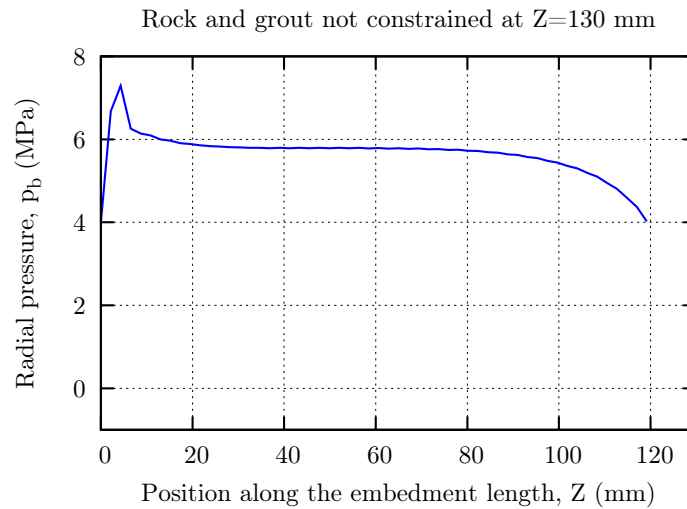


**Figure 3.28:** FEM simulation of the experimental bench. Distribution of the radial pressure  $p_b$  along the bolt-grout interface when  $p_r = 5$  MPa. Case where the grout and the rock at  $Z = L$  are not constrained

The distribution of the radial pressure  $p_b$  throughout the test (*i.e.*, as the embedment length decreases) will be explored in chapter 4.

## 3.4 *In situ* pull-out test campaign

### 3.4.1 General context

The field pull-out tests have been conducted in ANDRA's Underground Research Laboratory (URL) in North-Eastern France. ANDRA is the French public agency in charge of the management of radioactive waste. Given that in the URL rockbolts are used as part of the reinforcement pattern, a collaboration project between ANDRA and the Geosciences Department of MINES-ParisTech has been established within the context of the current research. The main target of this project is to complete the field investigation by an extended study at laboratory-scale to analyze the influence of several parameters on the pull-out response of fully grouted rockbolts.

In autumn 2009, sixty-six pull-out tests were carried out in ANDRA's URL within the framework of the excavation phase 2008-2012. They were carried out in two technical drifts, GT8 and GAT, oriented in the direction of the maximum horizontal principal stress as illustrated in the plan in figure 3.29a.

These galleries were excavated between March–June 2009 and the rockbolts to be studied were installed in July 2009. Four types of rockbolts were tested: Swellex, CT-Bolts, HA25 and Dywidag 26WR. They were placed in the cross-sections between steel arches, with a radial layout (see figure 3.29b). Since HA25 rockbolts have also been tested at laboratory-scale, the comparison between laboratory and field results is limited to this type of bar.

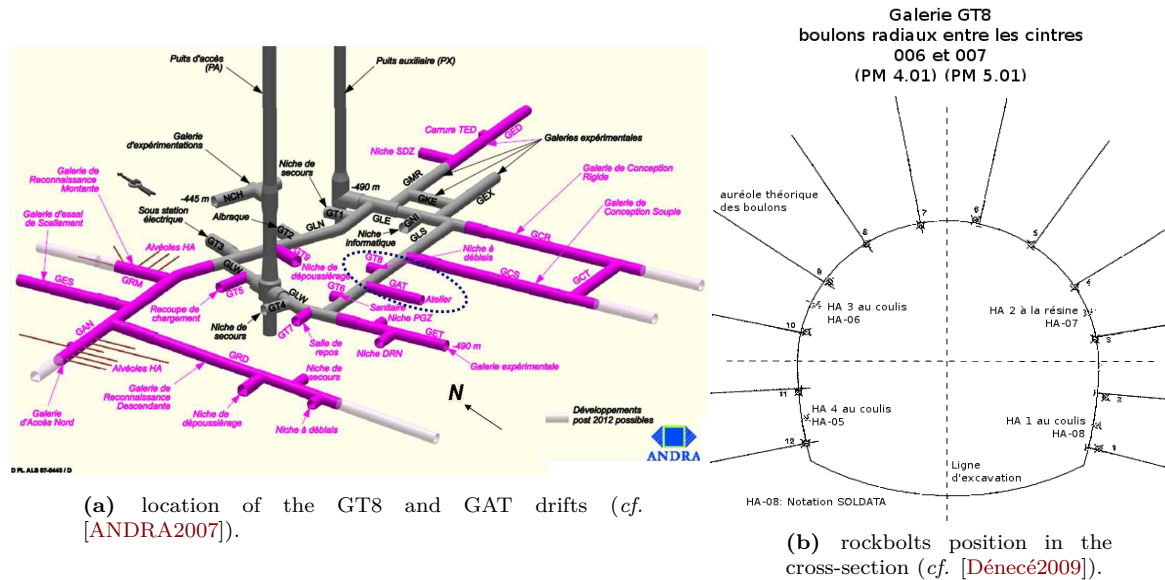
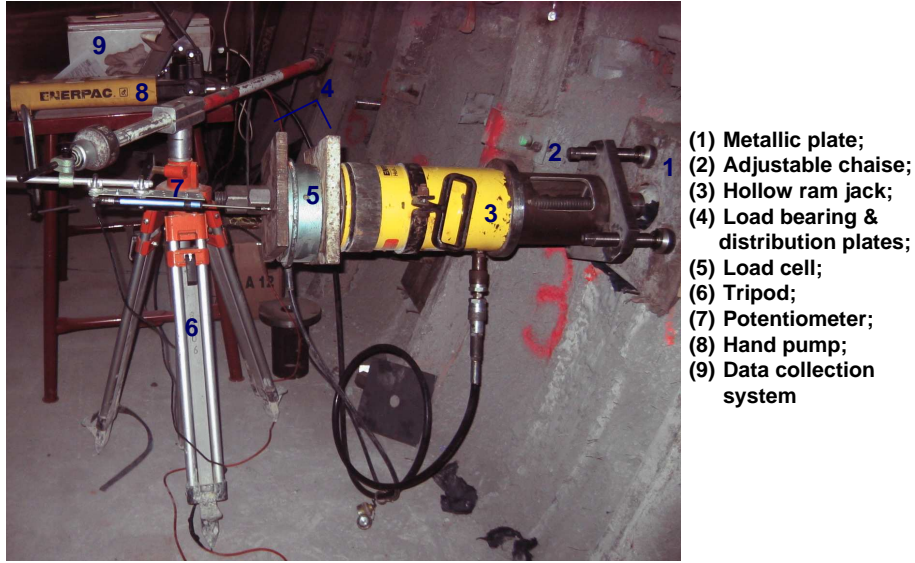


Figure 3.29: ANDRA's URL in Bure (France).

It should be noticed at this stage that the main target of the field pull-out test campaign was to evaluate and to compare the performance of the tested rockbolts. However, within the framework of the current thesis, the principal aim of conducting pull-out tests is to study the behaviour of the bolt-grout interface. On the other hand, and due to external reasons, the field pull-out tests were carried out before the main laboratory campaign. As regards the current research, the laboratory tests should have been conducted first and then the field pull-out tests would have been designed according to the laboratory-scale findings (*i.e.*, the interface behaviour model), in order to study the same phenomenon at both scales. This way, the comparison between the field results and the modelled results for great lengths would have helped evaluate the laboratory-scale research. In the future, field pull-out tests might be carried out once the constitutive law of the failure interface is defined in the laboratory.

The field set-up was slightly different from that used in the laboratory, described in subsection 3.2.1. In fact, in order to be able to pull the bolt out of the borehole, an extension bar 800 mm long was coaxially connected to the threaded part of the bolt. The excavation surface around the borehole collar was prepared and an adjustable chaise was installed to ensure that the reaction surface was orthogonal to the extension bar. Then, a hollow ram jack was installed. A load cell positioned between two load bearing/distribution plates was placed onto the jack piston and the system was blocked by a lock nut. Finally, a potentiometer held by an independent tripod was installed at the end of the extension bar, against the second load bearing plate; hence, the displacement measurements include the deformation of the pull-out tools. The jack was driven using a hydraulic hand pump. During the tests, the axial load and the axial displacement were measured. Figure 3.30 shows the field set-up used.



**Figure 3.30:** field set-up used in ANDRA's URL to conduct pull-out tests on rockbolts. Picture adapted from Dénécé *et al.* [Dénécé2009].

Two types of tests were conducted according to the French Standards NF P 94-242-1 and NF P 94-153 ([NF P 94-242-1, NF P 94-153]):

- constant rate pull-out tests: the pull rate was comprised between 1 and 1.5 mm/min (0.02 mm/s on average);
- creep tests: ten constant load levels were applied ( $\Delta F = 0.09 T_e$ , where  $T_e$  is the yield strength of the bar threaded part). The duration of each level increased with the applied load. The former levels lasted 15 minutes and the latter up to 1 hour.

It was decided that the tests would be carried out until either the axial load reached  $T_{\max} = 0.9 T_e$ , or the axial displacement reached 30 mm. Furthermore, before the beginning of each test, an axial load  $T \approx 0.1 T_e$  was applied to straighten the set-up out.

In total, twenty-three pull-out tests were performed on HA25 rockbolts. The detailed pull-out test campaign on HA25 bars is presented in appendix C. Table 3.8 compiles the main characteristics of all these tests. In general, the applied loads were lower than 173 kN ( $T_e = 192$  kN).

**Table 3.8:** Field pull-out test campaign on HA25 rockbolts.

| Drift | $L$ (m) | Grouting material        | $R_g$ (mm) | Test type (number of tests)   |
|-------|---------|--------------------------|------------|-------------------------------|
| GT8   | 3       | Resin (Minova Lokset SF) | 17.5       | Constant rate (2) & Creep (3) |
|       |         | Cement ( $w : c = 0.5$ ) | 38         | Constant rate (2) & Creep (3) |
| GAT   | 2.4     | Resin (Minova Lokset SF) | 17.5       | Constant rate (2) & Creep (3) |
|       |         | Cement ( $w : c = 0.5$ ) | 38         | Constant rate (4) & Creep (4) |

### 3.4.2 Analysis of the results

Before using the results issued from the tests, the deformation of the extension bar has been subtracted from the displacement measurements. The expression used reads

$$W^* = W_{\text{raw}} - \frac{FL_{\text{bar}}}{E_{\text{bar}}\pi R_{\text{bar}}^2} \quad (3.11)$$

where  $W^*$  is the corrected displacement,  $W_{\text{raw}}$  is the measured displacement,  $F$  is the applied force (it is constant along the extension bar),  $L_{\text{bar}}$  is the length of the extension bar,  $E_{\text{bar}}$  is its Young's modulus and  $R_{\text{bar}}$  is its radius.

The graphs in figure 3.31 show typical field load-displacement curves. Most of the bolts tested were installed in the eastern sidewall of the galleries. The results corresponding to resin-grouted and cement-grouted rockbolts are displayed separately, in different rows. The graphs in the first column correspond to the experimental data as obtained during the tests.

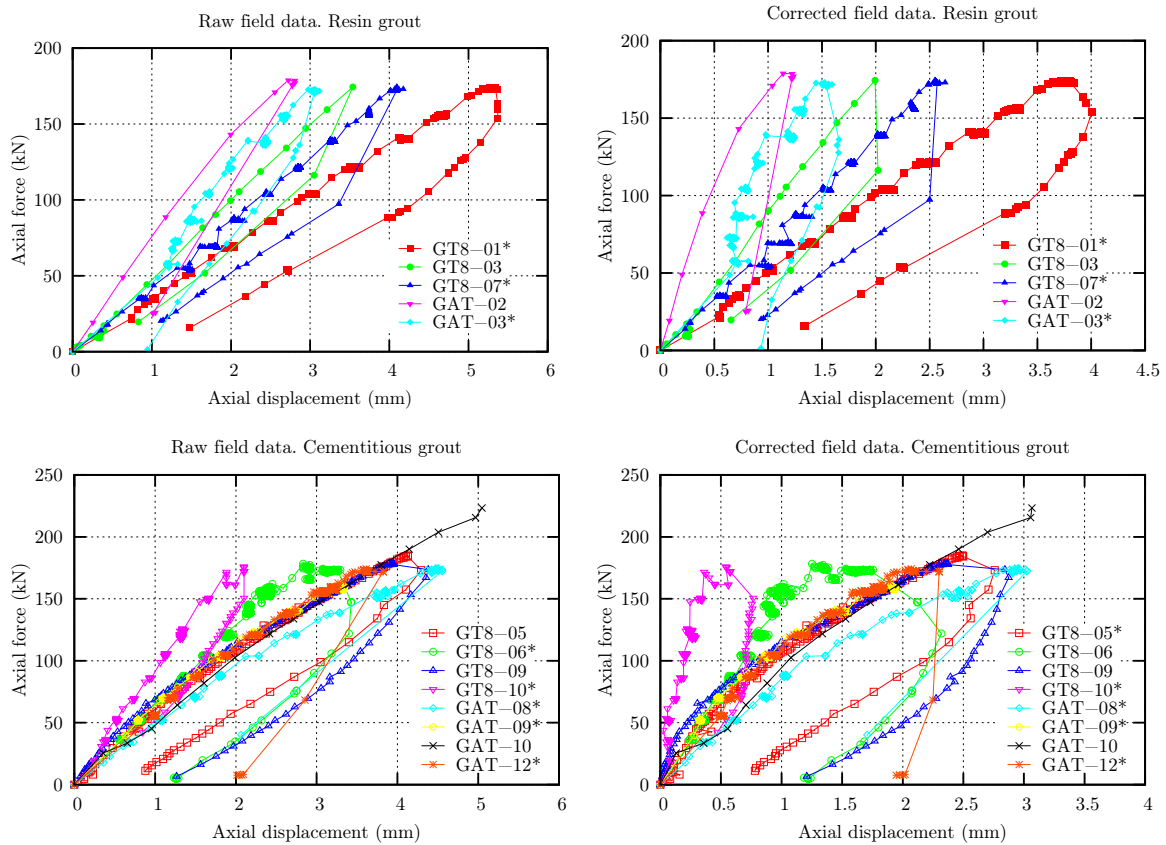


**Figure 3.31:** field pull-out test results on HA25 rockbolts. The asterisks \* indicate the creep pull-out tests.

As a whole, these results are consistent, in spite of the differences that they present with respect to the laboratory pull-out tests displayed in section 3.3. In this context, it is reminded that the embedment length has an important effect on the pull-out response, *cf.* figure 2.7. On the other hand, it can be noticed that the data issued from resin-grouted bolts show more scatter than the data issued from cement-grouted bars. The position of the bolt (upper or lower part of the sidewall) does not seem to have a major impact on the results, nor do the different embedment lengths tested (they are quite similar in fact). Furthermore, since the embedment lengths used are very long, the axial load during the tests reached  $T_{\text{max}}$  before any significant displacement occurred. Finally, in some of the tests the final unloading phase was monitored, but there were no loading-unloading cycles.

In order to ascertain where failure would be more likely to take place in the field configuration, an initial analysis of the structure rock-grout-bolt-interfaces has been carried out. The bolt remains within the elastic range during the test and the rock mass, which is constrained by the metallic plate installed around the borehole collar, has little effect. Therefore, the weakest elements are the grout and

the interfaces. As for the grout, the shear stress is maximum at  $r = R_b$  according to equation (2.22); hence, as long as the grout shear strength,  $\tau_{\max}$ , verifies

$$\tau_b < \tau_{\max} \quad (3.12)$$

the grout will remain within the elastic domain. The maximum average shear stress at  $r = R_b$  can be calculated as follows, admitting a uniform distribution along the embedment length:

$$\bar{\tau}_b = \frac{T_{\max}}{2\pi R_b L_b} = 0.92 \text{ MPa} \quad (3.13)$$

For the Lokset SF resin, the shear strength is  $\tau_{\max} \approx 25 \text{ MPa}$  (laboratory punched shear strength), as reported in the product data information catalogue [Minova2009b]. On the other hand, the shear strength of a  $w : c = 0.5$  grout can be calculated using equation (3.14) (stresses are expressed in [MPa]) as stated by Moosavi and Bawden [Moosavi2003]:

$$\tau_{\max} = 0.65 + 4.33\sqrt{\sigma_n} \quad (3.14)$$

where  $\sigma_n$  is the pressure acting normal to the failure plane ( $p_b$  in the current notation). Assuming that some radial pressure is acting on the interface (if for instance the bolts have been activated by the surrounding rock mass or if the stress field has been modified by close excavation operations), these values are considerably higher than the average shear stress that could be reached during the pull-out tests,  $\bar{\tau}_b$ ; hence, failure will probably take place at the bolt-grout and/or the grout-rock interface rather than in the grout itself.

Let us focus on the bolt-grout interface now. In terms of shear behaviour, it was explained in chapter 2 that the shear stress is not uniform along the embedded length of a long rockbolt, and that in that case equations (2.65) and (2.64) should be used to compute the shear stress as a function of the axial displacement. Figure 3.32 displays the shear stresses derived from the experimental field corrected data; that is to say, the experimental bond-slip relationships  $\tau_b(W)$ . The reduced shear stresses obtained using the equations mentioned above have been approximated by a three degree polynomial and then the coefficients have been calculated by best fitting the experimental data using the analytical solution described in chapter 2.

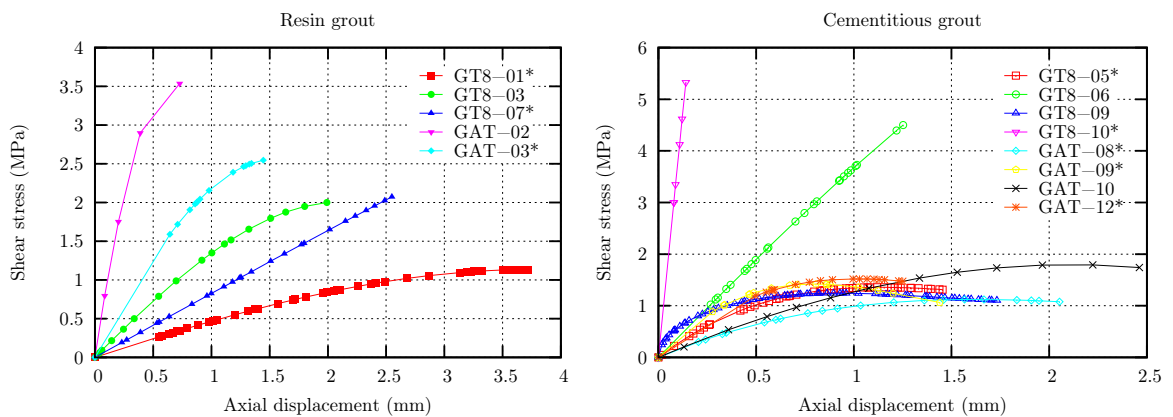


**Figure 3.32:** shear stress-displacement curves derived from the corrected data in figure 3.31.

However, in order to derive a bond-slip model accurately, it should be noticed that short embed-

ment lengths are more suitable. One supplementary reason is that the radial pressure along a field rockbolt may not be distributed uniformly, thereby hindering a correct determination of such model. A particular reason in the current situation is that the field tests were stopped at very low values of displacement. Consequently, it has been decided not to go further in the analysis of the field pull-out test results; let us rather conclude this chapter by explaining how the field test results can be compared with the laboratory-scale results.

### 3.5 Comparison of pull-out test results in the laboratory and the field

In order to compare pull-out test results issued from laboratory and field tests, it is important to understand the differences between the two configurations. First of all, in case the same bolt and the same grout are used, the interface is the same, so that the investigated interface behaviour model applies for the two configurations. Such model is then converted into different pull-out responses according to several aspects. The first aspect is the embedment length, the effect of which has already been discussed, *cf.* part 2.4.5. The second aspect concerns the radial pressure  $p_b$  and the radial opening  $\Delta u_{rb}$ . As explained before, the behaviour of the bolt-grout interface is governed by the stresses and displacements acting in the directions normal ( $p_b$  and  $\Delta u_{rb}$ ) and tangential ( $\tau_b$  and  $W$ ) to it. Since the bolt-grout bond has a frictional component, the importance of the radial response, and in particular of the pressure generation, is not negligible.

The radial pressure build up at the interface is different in the two set-ups described above because, even if the same bolt and the same grout are used, the rock mass and most importantly the boundary conditions are different:

- in the field, the pull-out tests are conducted at constant radial stiffness at the borehole wall, defined as  $K_{R_g^+} = \partial p_g / \partial u_{r,g^+}$ . This stiffness can be calculated by setting  $R_r \rightarrow \infty$  in equation (2.19):

$$K_{R_g^+}^{\text{field}} = \frac{E_r}{(1 + \nu_r) R_g} \quad (3.15)$$

- in the laboratory, the pull-out tests have been conducted under constant outer pressure  $p_r$  conditions, and constant outer radial stiffness conditions,  $K_{R_r^+} = \partial p_r / \partial u_{r,r^+}$  (*i.e.*, it is the hydraulic fluid stiffness that remains constant, while the rock sample stiffness is only constant if radial fractures are not developed).

Consequently, the comparison between the results is not straightforward. Such a comparison can be made through the modelling of the tests using different boundary conditions, dimensions and rock properties, once the interface constitutive law has been determined.

### 3.6 Conclusions

Pull-out tests have been conducted both in the laboratory and the field. In total, around one hundred and thirty tests have been carried out. At laboratory-scale, a new bench has been tuned and put into operation during the current thesis. This bench is shown in figures 3.1 and 3.2. It is based on the double embedment length principle, which accounts for the field situation displayed in figure 1.15,

where the unplated bolt will slip with respect to the surrounding media along the lower, shorter length if the axial load on the bolt exceeds a critical value.

The tested samples are composed of a bolt, a grout annulus, a rock sample provided with a borehole and a metallic tube that represents the longer part that remains anchored while the bolt slips along the rock borehole. During a test, the axial displacement  $W$ , the axial force  $F$  and the confining pressure  $p_r$  are captured. The tests have been carried out using two boundary conditions: constant outer confinement,  $p_r$ , and constant outer radial stiffness,  $K_{R^+}$ . Additionally, the execution of the tests and the analysis of the results have led to some improvements, in particular the introduction of the end plate displayed in figure 3.1.

Several rockbolts have been tested: HA25 rebars, FRP rockbolts and smooth steel bars. Pull-out tests have also been carried out on Flexible cablebolts. The main purpose of the latter has been to validate the new set-up designed to prevent the unscrewing phenomenon that may distort the pull-out results. The campaign on rockbolts has focused on the influence of the embedment length, the confining pressure and the bolt type and profile. A resin-based grout has been used in most tests, while two cementitious grouts have been tested ( $w : c = 0.35$  and  $w : c = 0.40$ ) in a few cases. The results of some tests are shown in figures 3.14-3.16 and 3.21. They are displayed as load-displacement curves and also in terms of the experimental  $\tau_b(W)$  relationships, obtained using equation (3.3). In the case of HA25 and FRP rockbolts, the load-displacement curves are divided into four stages that account for the phenomena involved in the decoupling of the interface. The results clearly illustrate that not only the pull-out response but also the bolt-grout interface response are highly influenced by the grout and ground annuli radial splitting during the test. Moreover, it is stressed that the results depend on the boundary conditions applied. Furthermore, in order to gain more understanding about the interface behaviour and the joint development, loading-unloading cycles have been made in several tests, especially in the pre-peak stage.

The analysis of the results presented in chapter 4 has been preceded by an exhaustive examination of the bench to completely understand the way it works and to determine how to get the data required, in terms of axial displacement in particular, to study the bolt-grout interface as accurately as possible. This examination has proven that the bolt-tube assembly distorts the initial displacement values quite significantly.

The field pull-out tests have been conducted in ANDRA's URL. Several bolt types have been tested, but only HA25 rockbolts have been taken into account in this thesis, because these bolts have also been studied at laboratory-scale. However, since the embedment lengths used are very long, and in order to preserve the bolts elastic response, the tests have been stopped before the advent of any significant slip. From the data available, the experimental  $\tau_b(W)$  relationships have been derived using the analytical tool described in chapter 2. In the future, once the bolt-grout interface behaviour has been defined from short embedment length pull-out tests, field tests designed according to the small-scale findings might be carried out. The comparison of the experimental results with the modelled results for great lengths would then let evaluate the laboratory, small-scale research.

Finally, the aspects that should be taken into account before comparing laboratory and field data are exposed. It is explained that even if the interface under study is the same (*i.e.*, the bolt and the grouting material are identical), the recorded pull-out response is different due to the influence of not only the embedment length, but also the surrounding ground properties and the boundary conditions, in particular in the radial direction. Under these circumstances, the comparison between the two scales can be made through the modelling of the tests, once the interface constitutive law is deduced from the tests held at short embedment lengths.



## CHAPTER 4

### ANALYSIS OF THE RESULTS AND MODELLING

Dans ce chapitre, on présente l'analyse des résultats des essais d'arrachement effectués sur les boulons (HA25, FRP et tiges lisses). L'objectif est d'établir les bases pour l'élaboration d'une loi de comportement relative à l'interface boulon-scellement, ce pour chaque type de boulon employé (le matériau de scellement ne change pas). Cette loi relie les variables contrainte de cisaillement  $\tau_b$ , déplacement axial  $W$ , pression normale à l'interface  $p_b$  et ouverture de l'interface  $\Delta u_{rb}$ , via les relations  $\tau_b(W, p_b)$  et  $\Delta u_{rb}(W, p_b)$ .

Dans l'analyse, on a utilisé la force axiale  $F$  et le confinement  $p_r$  (ou plus précisément la pression sur la jaquette  $p_{bl}$  comme expliqué dans la partie 4.4) tels que mesurés pendant les essais. Quant à  $W$ , on a employé les valeurs corrigées moyennant l'étalonnage décrit dans la partie 3.3.5. Ensuite, à partir de ces données, le cisaillement  $\tau_b$  a été calculé grâce à l'équation (3.3), car les petites longueurs d'ancrage utilisées permettent de supposer que  $\tau_b$  est uniforme.

Les résultats correspondant à chaque type de boulon sont d'abord analysés en termes des paramètres caractéristiques de la relation expérimentale  $\tau_b(W) : \tau_{peak}, W_{peak}, \tau_{res}$  et  $W_{res}$ . Ces paramètres sont étudiés en fonction de  $p_r$  et les tendances générales sont décrites et interprétées vis-à-vis des phénomènes observés après les essais.

Etant donné que la pression impliquée dans le comportement de l'interface boulon-scellement n'est pas la pression extérieure, mais la pression  $p_b$ , il est nécessaire de calculer cette dernière. Le calcul dépend de la rigidité radiale de l'anneau scellement-roche : cette rigidité peut être calculée analytiquement lorsque l'anneau est intact (donc, élastique) ou lorsqu'il est complètement fracturé ; cependant, la rigidité est variable au fur et à mesure que les fractures se propagent, rendant le calcul analytique plus compliqué. En conséquence, on a commencé par analyser les essais dans lesquels on n'a pas observé de fracturation radiale. Afin de calculer la pression à l'interface, une donnée complémentaire au confinement mesuré est nécessaire : on peut utiliser soit le déplacement radial extérieur de l'échantillon, soit la variation volumique du fluide confinant. Dans le cadre de cette thèse, la seule option disponible est la deuxième, en particulier via l'équation d'état de l'huile hydraulique employée. Du fait de cette restriction, seulement les essais menés à rigidité radiale constante (masse d'huile fixée) ont pu être analysés dans un premier temps.

Un modèle analytique pour calculer  $p_b$  en fonction de  $p_{bl}$  et  $W$  est ainsi présenté. Ensuite, la ressemblance des relations  $\tau_b(W)$  et  $p_b(W)$  pousse à décomposer  $\tau_b$  en deux parties : une composante frictionnelle,  $\tau_v$ , et une composante définie à pression constante,  $\tau_c$ , qui prend en compte les autres

contributions au cisaillement, telles que l'adhésion. En vue de ces constats, le modèle semi-empirique défini dans les équations (4.28), (4.29) et (4.30) est proposé.

L'ouverture du joint  $\Delta u_{rb}$  est calculée à partir du comportement de l'anneau et du boulon comme indiqué dans l'équation (4.31). Reflétant le lien entre l'ouverture et le profil de la tige, les expressions empiriques (4.32) et (4.33) ont été retenues pour les boulons HA25 et FRP respectivement.

Dans la dernière partie du chapitre, on applique le modèle semi-empirique  $\tau_b(W, p_b)$ ,  $\Delta u_{rb}(W, p_b)$  (obtenu grâce aux essais menés à rigidité radiale constante) pour reproduire la réponse d'un essai effectué à confinement constant, pour lequel on ne dispose pas d'information dans la direction radiale. La comparaison des cisaillements expérimental et modélisé, montrée dans la figure 4.16, suggère que l'ouverture du joint peut être similaire dans les deux cas, ce qui est encourageant du point de vue de la construction d'une loi de comportement pour l'interface. Cependant, les données disponibles à ce stade sont insuffisantes pour tirer des conclusions. L'instrumentation des essais pour étudier la réponse radiale permettra de mieux comprendre le comportement du contact boulon-scellement.

En résumé, on propose dans ce chapitre une méthode pour déduire le modèle d'interface d'une série d'essais, qui doit être encore complété.

## 4.1 Introduction

This chapter is devoted to the analysis of the laboratory pull-out test results on rockbolts presented in chapter 3. Such analysis is directed towards the definition of a constitutive law for the bolt-grout interface, which is defined by four variables,  $\tau_b$  (interface shear stress),  $W$  (axial displacement),  $p_b$  (interface radial pressure) and  $\Delta u_{rb}$  (radial opening), related by the expressions  $\tau_b(W, p_b)$  and  $\Delta u_{rb}(W, p_b)$ . The bolt-grout interface is defined as the contact surface between the tendon and the grouting material. It is important not to confuse the interface with the joint: the interface is only the boundary between the two materials, bolt and grout, and it exists since the reinforcement is set; the joint, in turn, is formed during the pulling process as decoupling occurs along the interface, leading eventually to a complete debonding. The decoupling of the interface is a local process except for short embedment lengths, along which the response may be assumed to be uniform (this matter has already been discussed in chapter 2).

In general terms, the behaviour of any interface includes two directions:

- the normal or radial direction, in which the relevant variables are  $p_b$  and  $\Delta u_{rb}$ , and
- the tangential or axial direction, in which the relevant variables are  $\tau_b$  and  $W$ .

However, as shown in figure 4.1, some of these variables, in particular the radial pressure and the radial displacement at the interface, cannot be measured directly; at best, they can be measured at the outer surface,  $R_r$ . To measure the radial displacement  $u_{rr}$ , cantilever strain gauge arms or an equivalent equipment is needed. On the other hand, the measurement of the confining pressure is much easier. Finally, in order to relate the radial pressure and the radial displacement acting at  $R_b$  and  $R_r$ , a continuity condition for the radial displacement is assumed at  $R_g$ .

The figure also illustrates the geometry under study during a laboratory pull-out test: at the beginning, the bolt is in full contact with the grouting material and, as the bolt is pulled out and slips with respect to the grout, the contact length decreases significantly. This fact has made it not possible to analyze the results numerically: as a matter of fact, the Geosciences Department FEM code VIPLEF (cf. section 1.3.3 for details) cannot deal with major discontinuity slippages and is

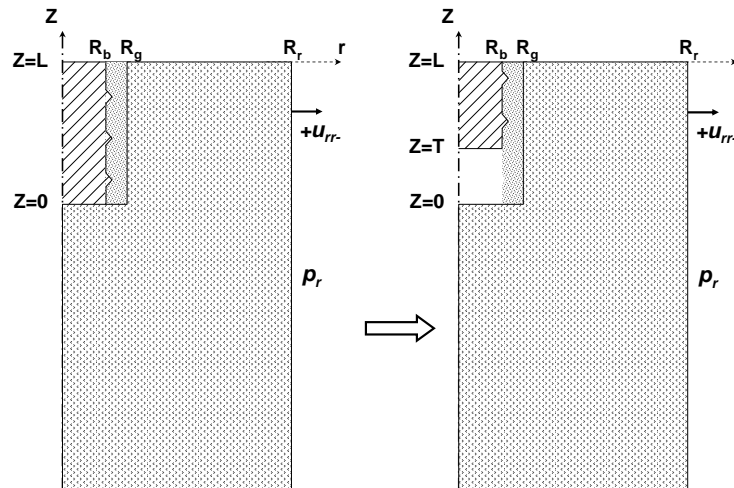


**Figure 4.1:** nomenclature and geometry under study during a laboratory pull-out test. As it can be seen, the geometry (embedment length) changes during the test.

consequently not capable of modelling a laboratory pull-out test as described in chapter 3. Indeed, although VIPLEF allows large displacement and strain computations, the mesh remains the same at every stage; therefore, if large slippages occur, the nodes at the two sides of the joint interface will not longer be in front of each other. For this reason, the analysis presented in this chapter has been conducted analytically in the radial and axial directions, separately (*i.e.*, a one-dimensional formulation has been adopted for each direction).

In the first part of the chapter, the pull-out test results are analyzed as a function of the outer radial pressure. Then, the procedure to convert the external confinement into the interface pressure is described. The state of the rock and grout annuli observed after the pull-out tests (*i.e.*, radially split or not) has been taken into account in the pressure conversion. The tests in which the grout and the rock are believed to remain elastic throughout the pulling process are dealt with first and it is explained why, in the context of the current thesis, the tests conducted under constant radial stiffness conditions provide more information about the interface behaviour than the tests conducted at constant radial confinement. A semi-empirical model for the relationships  $\tau_b(W, p_b)$  and  $\Delta u_{rb}(W, p_b)$  is proposed and its uses and limitations are commented. Finally, the tests conducted under constant confinement are discussed.

## 4.2 Preliminary analysis

In order to study the pull-out test results, the axial load-displacement relationships,  $F(W)$ , have been converted into shear stress-displacement relationships,  $\tau_b(W)$ . Bearing in mind that the embedment lengths used are short, and according to part 2.4.5 and in particular to figure 2.8, it can be assumed that the shear stress is uniformly distributed; hence, equation (3.3) has been used.

The  $\tau_b(W)$  relationships as derived from the experimental data of some tests are shown in figures 3.14b, 3.15b and 3.16b. It should be noticed that in the analysis presented hereafter, the corrected displacement data are used instead of the raw displacement data. This is especially true for HA25 and FRP rockbolts; in the case of the smooth bars, the displacement data have not been considered when the metallic tube is grouted to the bar because, as it can be clearly seen in the enlarged views in figure 3.16, these measurements are distorted. Consequently, the only displacement data used here

correspond to the tests in which the tube was not grouted to the bar (the displacement due to the bar free length elongation has been taken away). Finally, it is important to highlight that, in the case of HA25 rockbolts, the precision of the correction introduced *via* the bench calibration is subjected to the proper grouting of the metallic tube. In addition, and according to chapter 3, in all cases the axial displacement  $W$  is considered to be equal to the relative slip at the bolt-grout interface.

The most important parameters of the  $\tau_b(W)$  relationship are:

- the peak shear strength and displacement,  $\tau_{\text{peak}}$  and  $W_{\text{peak}}$  respectively, and
- the residual shear strength and displacement,  $\tau_{\text{res}}$  and  $W_{\text{res}}$  respectively.

These parameters are presented separately for each bolt type in the three following subsections. They are studied as a function of the outer pressure,  $p_r$ . Only the most reliable tests have been considered. Furthermore, the tests conducted under constant outer radial stiffness conditions are differentiated from the tests carried out at constant outer radial confinement. Moreover, since in the majority of the tests resin has been used as grouting material, only this grout has been taken into account.

### Comparison of the grout shear strength with the parameter $\tau_{\text{peak}}$

Before moving to subsections 4.2.1, 4.2.2 and 4.2.3, it is important to notice that in the graphs corresponding to the experimental peak shear strength,  $\tau_{\text{peak}}$ , the resin grout shear strength has also been plotted for comparison. As indicated in table 3.5, the resin grout shear strength (in [MPa]) is given by

$$\tau_{\text{grout}} = 20.17 + p_b \tan(28^\circ) \quad (4.1)$$

As one could remark, the experimental peak shear strength data are function of  $p_r$ , whereas the grout shear strength is expressed as a function of  $p_b$ . Thus, in order to be able to compare both, the interface pressure  $p_b$  should be converted into  $p_r$ . To do this, the following scenarios have been considered:

- the grout and ground annuli behave elastically;
- the grout and ground annuli are radially fractured.

In both cases, it is assumed that the grout-ground interface is coupled:

$$u_{rg^+} = u_{rg^-} \quad (4.2)$$

Moreover, in the context of a preliminary analysis, it may be assumed that the bolt-grout interface is also coupled at the peak:

$$u_{rb^+} = u_{rb^-} \quad (4.3)$$

In the case where the grout and the ground behave elastically (the bolt material is assumed to be always within the elastic range in this research), the use of equation (2.19) for the three materials (in the case of the bolt,  $R_i = 0$ ) in combination with equations (4.2) and (4.3) leads to the determination of  $p_b$  and  $p_g$  as a function of  $p_r$ . Moreover,  $p_b > p_g$  as long as  $R_g > R_b$ ; however, the ratio  $p_g/p_r$  depends on the elastic properties of the grout and the ground. On the other hand, when both the grout and ground annuli show radial fractures, the hoop stress is equal to zero; in such a case, the resolution of equation (2.5) gives

$$\sigma_{rr} = -\frac{R_i}{r} p_i = -\frac{R_j}{r} p_j \quad (4.4)$$

where  $\{i, j\} = \{b, g\}$  for the grout annulus and  $\{i, j\} = \{g, r\}$  for the ground. As a result, the radial pressure at the grout-ground and the bolt-grout interfaces can be respectively written

$$p_g = \frac{R_r}{R_g} p_r \quad (4.5)$$

and

$$p_b = \frac{R_g}{R_b} p_g = \frac{R_r}{R_b} p_r \quad (4.6)$$

Equations (4.5) and (4.6) reveal that  $p_b > p_g > p_r$  when the annuli are fully split.

### 4.2.1 HA25 rockbolts

The parameters  $\tau_{\text{peak}}$ ,  $W_{\text{peak}}$ ,  $\tau_{\text{res}}$  and  $W_{\text{res}}$  are displayed in figures 4.2 and 4.3. In the case of the peak values, the uncertainty is also given. On the other hand, the comparison of the left-hand side plot in figure 4.2 with the trends announced by Moosavi *et al.* [Bawden1997] and displayed in figure 1.31 reveals important similarities.

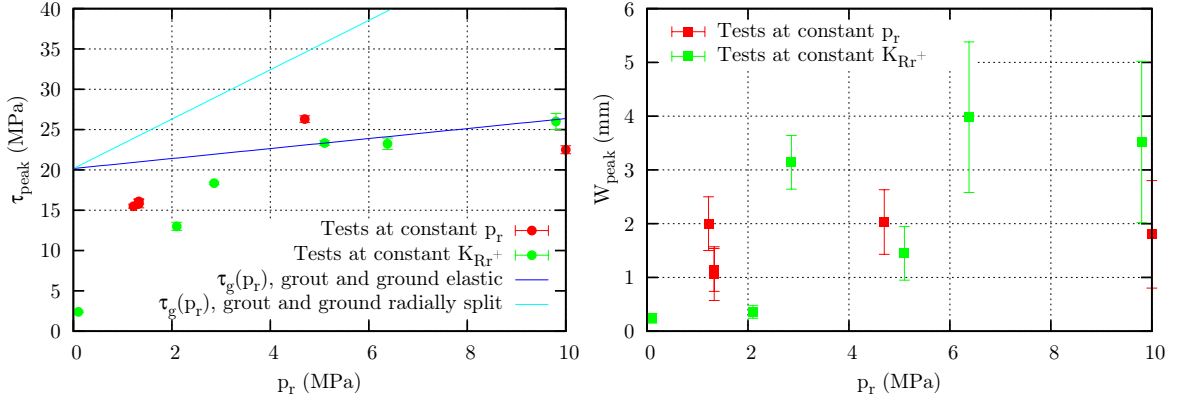


**Figure 4.2:** peak shear strength and displacement for HA25 rockbolts.

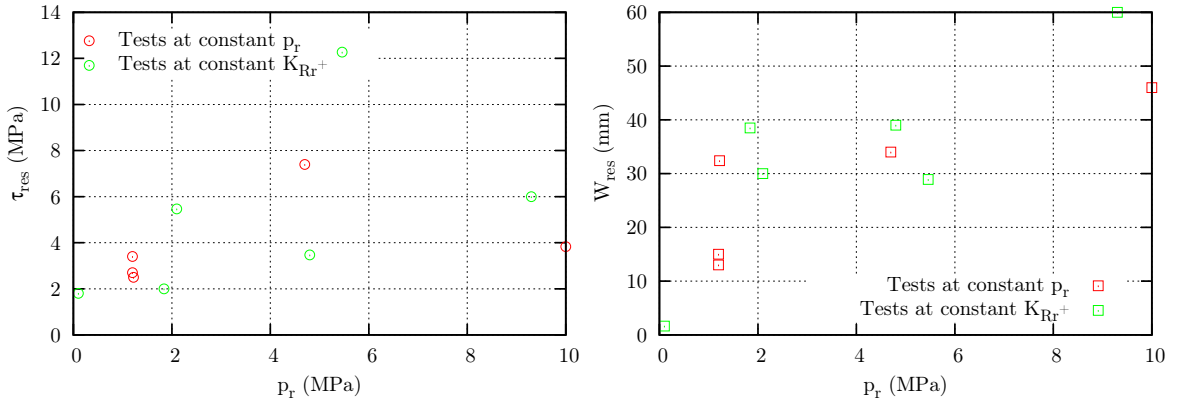


**Figure 4.3:** residual shear strength and displacement for HA25 rockbolts.

As it can be seen in the left-hand side graph in figure 4.2, for  $p_r > 2$  MPa the peak shear strength increases almost linearly with the radial pressure. Moreover, the experimental shear strength within this range is close to the resin grout shear strength when both the grout and the ground behave elastically (at the peak, the possible fractures are probably closed). These facts suggest that it is the grout itself that fails in shear for high confinements. The failure interface is then a cylinder of

radius  $R_{b,\max}$ , created within the grout annulus. The visual observation of the samples after the tests corroborates this statement: the grout within the bolt indentations is sheared off and a lot of gouge material (white resin powder) has been formed as a result of the shearing process. Additionally, the post-peak phase of the experimental curves issued from the tests conducted at high radial pressures does not show the oscillations corresponding to the bolt profile, *cf.* figure 3.14b, which provides support for the resin shearing off argument. Conversely, for low confining pressures, it seems that it may not be the grout that fails in shear; in fact, for small pressures, both the grout and ground annuli split radially (as explained in section 2.2, when the confining pressure is low it is more likely that radial fractures appear). After splitting, the annuli wedges are pushed apart to some extent depending on the boundary conditions, and as result, the grout at  $r = R_b$  is less sheared, so that it may partially preserve the bolt imprints. Accordingly, the post-peak response exhibits the oscillations due to the bolt profile. The post-peak slopes shown in figure 4.4 (*cf.* the post-peak stage in the loading process description in page 101) and the curves in figure 3.14b qualitatively illustrate that when radial fractures occur, and in particular when they are open (see figure 3.17), the move to the residual phase is steeper (*i.e.*, the absolute value of the post-peak slopes increases as the confinement decreases). This move corresponds to a significant damage of the grout and ground annuli, rather than to the damage of the interface itself.

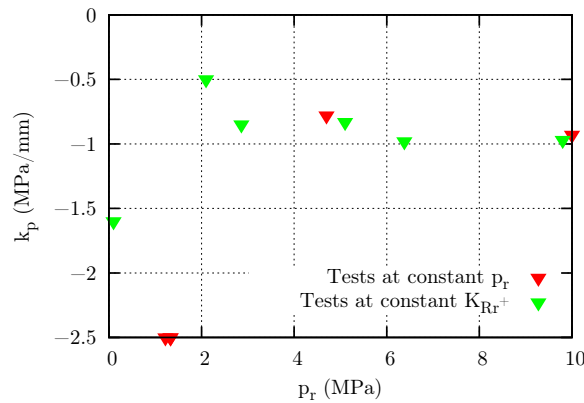


Figure 4.4: post-peak slope for HA25 rockbolts.

As for the peak displacement, the general trend indicates an increase with the radial pressure  $p_r$ , although the scatter is not negligible (more tests are required, but the scatter may be partially due to the bench need for a precise co-axiality). The residual shear strength increases with  $p_r$  and the average residual displacement is about 35 mm (but again, due to the low statistics, more tests should be conducted).

#### 4.2.2 FRP rockbolts

Figures 4.5 to 4.7 illustrate the general trends obtained for FRP rockbolts. Once again, for high values of radial pressure, the peak shear strength matches relatively well the grouting material shear strength, calculated assuming that the annuli remain elastic.

The same reasoning made for high and low confinements in the previous subsection applies for FRP rebars; however, since the profile of FRP bolts is smoother than that of HA25 rebars, the grout damage is much smaller in identical conditions, even if it increases with  $p_r$  as observed after the tests. From the data available, it seems that the axial displacement at the peak increases slightly with the

confinement. The residual displacement is approximately constant, but there is a lot of scatter at  $p_r = 5$  MPa. The residual shear strength increases with the outer radial pressure and the post-peak slopes qualitatively reflect the same trends than in the case of HA25 rockbolts.

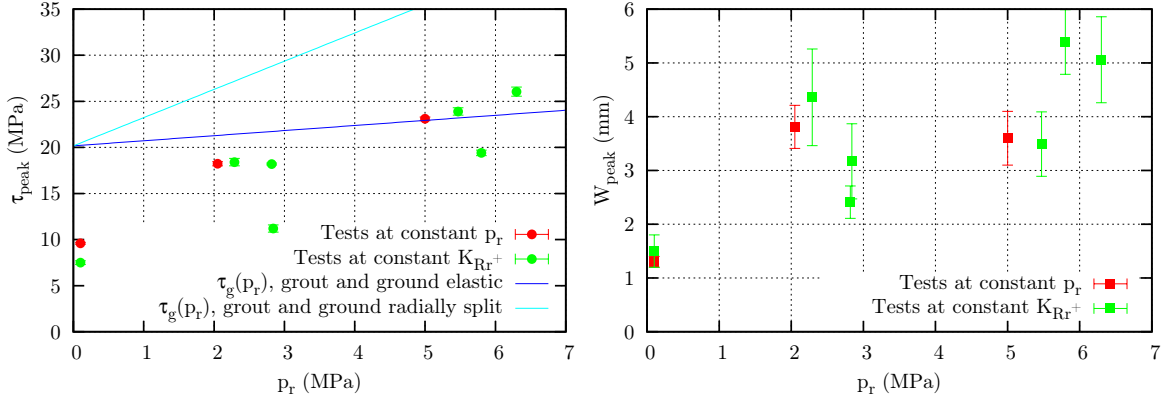


Figure 4.5: peak shear strength and displacement for FRP rockbolts.

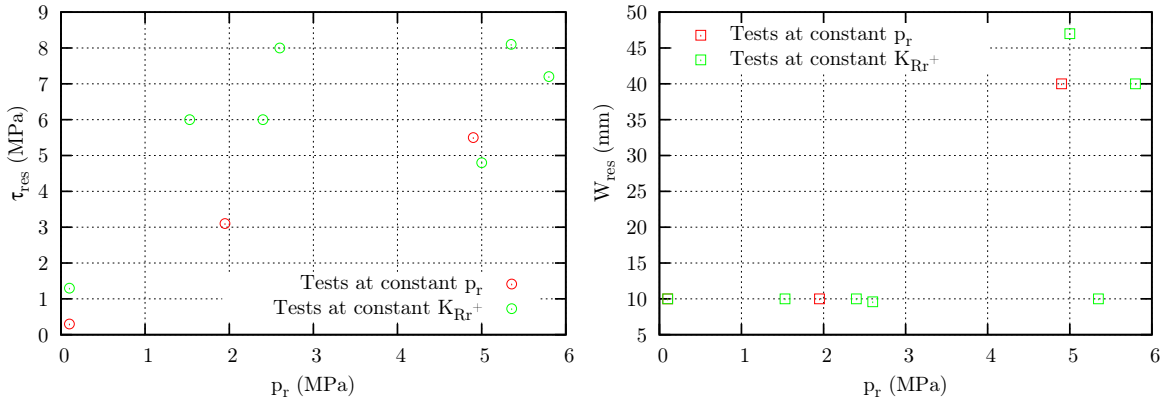


Figure 4.6: residual shear strength and displacement for FRP rockbolts.

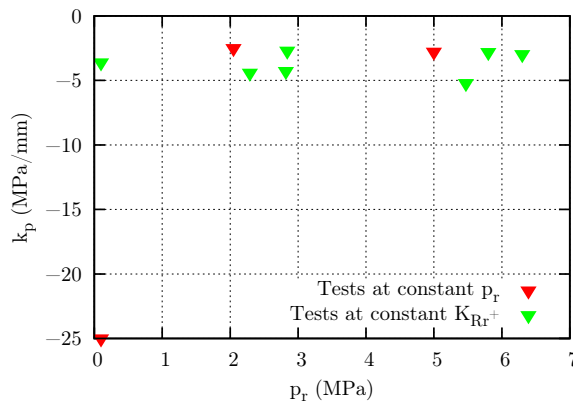
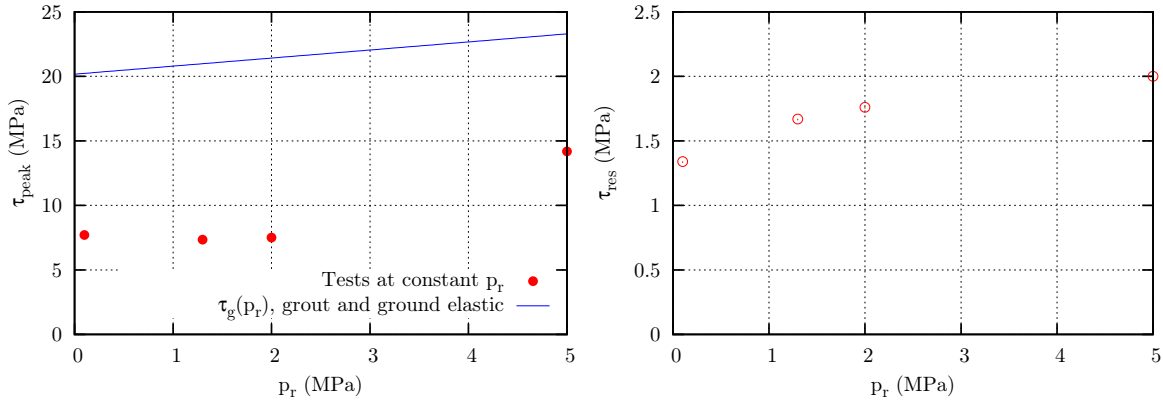


Figure 4.7: post-peak slope for FRP rockbolts.

### 4.2.3 Smooth bars

As announced before, the displacement measurements of the tests in which the bolt was grouted to the metallic tube (4 out of 5 tests) are distorted. Consequently, only the peak and residual shear

strengths (calculated assuming a constant embedment length) are presented here, see figure 4.8. It is important to notice that these results are only presented by way of guidance, due to the low statistics and the uncertainty in the displacement data.



**Figure 4.8:** peak and residual shear strengths for smooth bars.

The peak strength is lower than the grouting material shear strength. This finding is consistent with the observations made after the tests: the resin at  $r = R_b$  is not damaged and there is not gouge material. The residual shear strength does not seem to vary significantly with the confinement (the mechanical interlock contribution is absent here and only friction remains). The visual examination of the samples after the tests shows that the annuli are intact, without radial fractures (see figure A.46). Moreover, both the peak and residual strengths obtained for the smooth bars are considerably smaller than those obtained for HA25 and FRP rockbolts, due mainly to the lack of mechanical interlock.

#### 4.2.4 Conclusions

Figures 4.2, 4.3, 4.5, 4.6 and 4.8 inform about the general trends of the parameters  $\tau_{\text{peak}}$ ,  $W_{\text{peak}}$ ,  $\tau_{\text{res}}$  and  $W_{\text{res}}$ , involved in the  $\tau_b(W)$  relationship. Within the purposes of a preliminary analysis, they have been displayed as a function of the outer radial pressure,  $p_r$ , because this is the only pressure that can be measured during a pull-out test. However, the relevant pressure in relation to the bolt-grout interface is  $p_b$ ; hence, the measured pressure  $p_r$  should be converted into the interface pressure,  $p_b$ . As with the ratio  $p_b/p_r$ , it varies significantly depending on the state of the grout and ground annuli, being minimum when the annuli are elastic and maximum when they are both radially split. Moreover, when radial fractures appear and propagate, it is quite difficult to deal with the problem analytically (in these conditions, the annuli stiffness is not constant throughout the pulling process), in particular if the behaviour of the bolt-grout interface is not known. In this respect, it should be noted that in their model to reproduce pull-out tests, Hyett *et al.* [Hyett1995] assumed the interface radial behaviour to be known, adapted from the nonlinear behaviour of rock joints proposed by Saeb and Amadei [Saeb1992]. Consequently, the annuli have been supposed to behave elastically at first in this study. Therefore, the tests in which no fractures were observed have been selected. These tests are those conducted at high radial outer pressures ( $p_r > 5$  MPa) within the tests at constant outer radial confinement, and most of the tests conducted at constant outer radial stiffness.

The determination of the interface pressure  $p_b$  is discussed in the next section.

## 4.3 Interface radial pressure determination

### 4.3.1 Framework

As said before, the interface pressure  $p_b$  determination starts with the assumption that both the grout and ground annuli behave elastically. This assumption allows to deal with the problem analytically. In fact, even if the numerical code in use could take major discontinuity slippages into account, the pull-out tests could not be modelled because the behaviour of the interface is not known (actually, it is such behaviour that is investigated). On the other hand, it is extremely difficult to study the annuli radial splitting theoretically, and again, the numerical tools are not useful as long as the behaviour of the interface is not known. Thus, the tests in which no fractures were identified at the end of the pulling process have been analyzed first, analytically and within the frame of the linear theory of elasticity. The study has been conducted in the radial direction (hence, it is a one-dimensional analysis) and a generalized plane stress state has been supposed. Finally, with respect to the initial pull-out tests characterized by the formation of the crater depression, only the tests without radial fractures and in which failure took properly place at the bolt-grout interface have been considered.

Within the framework described above, the structure under study is composed of the grout and ground annuli, coupled at  $r = R_g$  and subjected to the following loads:

- the reaction force from the hydraulic jack at  $Z = L$ . Such force acts in  $S_{\text{pist}} = \pi (R_r^2 - R_{\text{pist}}^2)$  before the introduction of the end plate and in  $S_{\text{pl}} = \pi (R_r^2 - R_{\text{pl}}^2)$  after the introduction of that plate, *cf.* part 3.2.1;
- the radial outer pressure  $p_r$ ;
- the interface pressure  $p_b$ .

With the aim of undertaking a simplified one-dimensional analysis, it should be verified that the two radial pressures  $p_r$  and  $p_b$  are uniformly distributed and that the axial stress  $\sigma_{ZZ} = -F/S_i$ ,  $i = \{\text{pist}, \text{pl}\}$  can be neglected. As with the pressure  $p_r$ , it is uniformly distributed along the  $Z$  axis because it is provided by a fluid. Concerning the interface pressure  $p_b$ , several FEM simulations have been conducted to evaluate the effect of the decreasing embedment length on the pressure  $p_b$  distribution. Four geometries have been considered, identified by the ratio free length/embedment length,  $fl/L = 0, 0.5, 0.75, 0.9$ . A pressure  $p_r = 1$  MPa has been applied. To simulate these geometries, the radial displacement  $u_{r,b+}$  has been blocked along the embedded length,  $(1 - fl/L)L$ . From the results plotted in figure 4.9, it has been supposed that, apart from the end effects, the interface pressure  $p_b$  is uniformly distributed along the decreasing embedded length.

Finally, in order to evaluate the axial stress  $\sigma_{ZZ}$ , the maximum force that could be reached in a pull-out test (*i.e.*, the yield strength of HA25 rockbolts) has been taken into account. Such force leads to a maximum stress  $\sigma_{ZZ} \approx 16$  MPa, which is negligible with respect to the sandstone and resin uniaxial compressive strength, see tables 3.2 and 3.5 respectively. Moreover, the numerical simulations show that the effect of the reaction force is localized around the sample upper surface. Hence, due to the last two reasons, the reaction force effect has been neglected in this analysis (the true quantification of this force with respect to the embedment length can be found in appendix A.1, pages 181 through 183).

After the verification of the main hypothesis of the simplified analysis, it can be concluded that the structure under study is composed of two annuli coupled at their contact interface and solely

subjected to two radial pressures,  $p_r$  and  $p_b$ . The confinement pressure  $p_r$  is provided by the hydraulic oil. The calculation of the interface pressure  $p_b$  is explained in the next part.

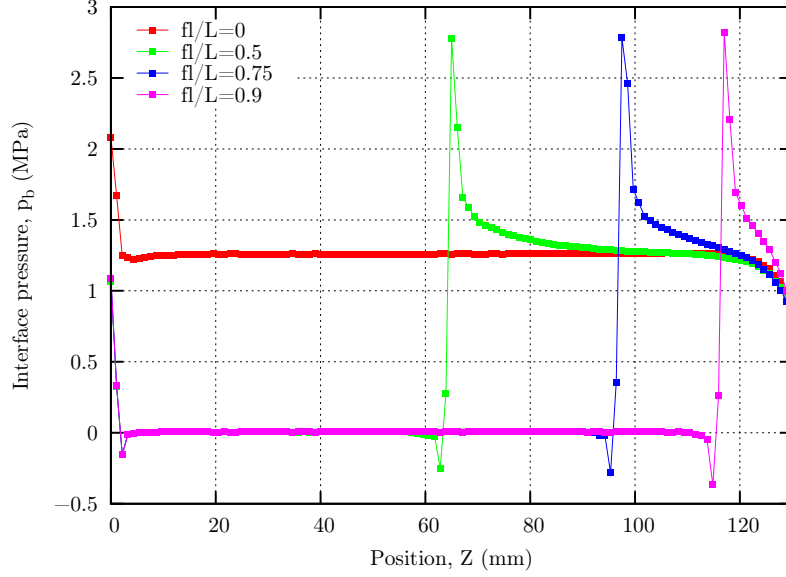


**Figure 4.9:** influence of the decreasing embedment length on the interface pressure distribution.

### 4.3.2 Pressure $p_b$ determination: general principle

Let us consider two coupled elastic annuli. The radial displacement at  $r = R_b$ ,  $u_{rb^+}$ , can be written

$$u_{rb^+} = f(p_b, p_r) \quad (4.7)$$

where function  $f$  is adapted from equation (2.19) and accounts for the grout and ground annuli elastic properties. Let us consider the confining fluid as well, comprised in  $r \in [R_r, R_c]$ , where  $R_c$  is the biaxial cell inner radius. Its relative volume variation,  $\Delta V/V_0$ , may be expressed

$$\frac{\Delta V}{V_0} = \frac{V - V_0}{V_0} = g(p_b, p_r) \quad (4.8)$$

Functions  $f$  and  $g$  are known functions and depend on the geometry and elastic properties of the materials involved. Once  $p_b$  is known, function  $f$  lets calculate  $u_{rb^+}$ . Function  $g$  is used to calculate  $p_b$ :

- in tests at constant outer radial pressure, if the volume variation is measured (by means of a pressure injector or a flow meter for instance),  $p_b$  can be calculated using equation (4.8). Alternatively, if the radial displacement  $u_{rr^-}$  is measured (strain gauges), the volume variation can be estimated and then  $p_b$  can be calculated using the same equation;
- in tests at constant outer radial stiffness, the biaxial cell is a closed system and hence the quantity of confining fluid remains constant. Under these circumstances, if the volume variation is not measured directly, the fluid equation of state can be used. At constant temperature, such equation reads

$$\frac{\Delta V}{V_0} = h(p_r) \quad (4.9)$$

The combination of equations (4.8) and (4.9) allows to compute  $p_b$  as a function of  $p_r$ .

In the particular case of this thesis, only the second case is useful because the tests conducted at constant radial pressure  $p_r$  used neither strain gauges nor flow meters nor injectors. Therefore, the tests conducted at constant outer radial stiffness will be examined first. It should be noticed that the outer pressure increase during pull-out tests has been recorded and highlighted previously, *cf.* [Offner2000] for instance; however, these authors did not calculate the interface pressure from the measured data.

Finally, once the interface pressure  $p_b$  is known, the radial displacements of the grout,  $u_{rb^+}$ , and the bolt,  $u_{rb^-}$ , are also known. The joint radial opening is then given by

$$\Delta u_{rb} = u_{rb^+} - u_{rb^-} \quad (4.10)$$

## 4.4 Analysis of the tests conducted at constant radial stiffness

### 4.4.1 Pressure $p_b$ determination: procedure

Due to the test samples geometry (*i.e.*, decreasing embedment length and presence of a massive rock sample part), function  $g$  depends on the bolt axial displacement  $W$  too. As a consequence, the combination of equations (4.8) and (4.9) lets determine the interface pressure  $p_b$  as a function of both  $p_r$  and  $W$ .

As for the hydraulic fluid, its equation of state is written

$$\frac{\Delta V}{V_0} = -k \Delta p_r \quad (4.11)$$

where  $k$  is the oil compressibility, that is supposed to be constant below 35 MPa:  $k \simeq 4 \cdot 10^{-4} \text{ MPa}^{-1}$ . On the other hand, in order to calculate the hydraulic oil volume variation by means of function  $g$ , the test sample is divided into three parts that behave differently. From bottom to top, these parts are:

- a. massive rock zone: the length of this part is  $H - L$ ;
- b. zone comprised in  $Z \in [0, W]$ : since the resin is no longer in contact with the bolt in this zone,  $p_b = 0$ ;
- c. zone comprised in  $Z \in [W, L]$ : the bolt is in contact with the resin along this zone, so that  $p_b \neq 0$ .

The bladder, the biaxial cell and the end plate (when used) are also taken into account to compute the fluid volume variation. Hence, the relative volume variation reads

$$\frac{\Delta V}{V_0} = \frac{2\pi}{V_0} \left( R_c \Delta u_{rc} H - R_{bl} \sum_{i=a,b,c} (\Delta u_{rbl})_i h_i \right) \quad (4.12)$$

where  $R_{bl}$  is the bladder outer radius and  $i = \{a, b, c\}$  represent the three zones defined above, to which a fourth zone to account for the end plate can be added if necessary. Function  $g$  in equation (4.12) is expressed  $g(p_b, p_r, W)$  as follows.

Within the framework of the linear theory of elasticity, let us consider a cylindrical tube of elastic properties  $E_m$  and  $\nu_m$ , subjected to two compressive pressures  $p_m$  and  $p_n$  at its lateral surfaces,  $R_m$

and  $R_n$  respectively. From work considerations and equation (2.19), it comes that

$$\begin{bmatrix} R_m p_m \\ -R_n p_n \end{bmatrix} = \begin{bmatrix} A_m & -B_m \\ -B_m & C_m \end{bmatrix} \begin{bmatrix} u_m \\ u_n \end{bmatrix} \quad (4.13)$$

where

$$A_m = \frac{E_m [(1 + \nu_m) R_m^2 + (1 - \nu_m) R_n^2]}{(1 - \nu_m^2) (R_n^2 - R_m^2)} \quad (4.14)$$

$$B_m = \frac{2E_m R_m R_n}{(1 - \nu_m^2) (R_n^2 - R_m^2)} \quad (4.15)$$

$$C_m = \frac{E_m [(1 - \nu_m) R_m^2 + (1 + \nu_m) R_n^2]}{(1 - \nu_m^2) (R_n^2 - R_m^2)} \quad (4.16)$$

In the current case, a maximum of three tubes are to be coupled (resin annulus, rock annulus and bladder), for instance from  $R_m$  to  $R_p$ . Taking the continuity condition at the contact interfaces into account, it comes that

$$\begin{bmatrix} R_m p_m \\ -R_p p_p \end{bmatrix} = \begin{bmatrix} \bar{A} & -\bar{B} \\ -\bar{B} & \bar{C} \end{bmatrix} \begin{bmatrix} u_m \\ u_p \end{bmatrix} \quad (4.17)$$

where

$$\bar{A} = A_m - \frac{B_m^2}{C_m + A_n} - \frac{(B_m B_n)^2}{(C_m + A_n)^2 (C_n + A_o) - B_n^2 (C_m + A_n)} \quad (4.18)$$

$$\bar{B} = \frac{B_m B_n B_o}{(C_m + A_n) (C_n + A_o) - B_n^2} \quad (4.19)$$

$$\bar{C} = C_o - \frac{B_o^2 (C_m + A_n)}{(C_m + A_n) (C_n + A_o) - B_n^2} \quad (4.20)$$

Inversing equation (4.17), one finds that

$$\begin{bmatrix} u_m \\ u_p \end{bmatrix} = \begin{bmatrix} \alpha & \beta \\ \beta & \gamma \end{bmatrix} \begin{bmatrix} R_m p_m \\ -R_p p_p \end{bmatrix} \quad (4.21)$$

where

$$\alpha = \frac{\bar{C}}{\bar{A}\bar{C} - \bar{B}^2} \quad (4.22)$$

$$\beta = \frac{\bar{B}}{\bar{A}\bar{C} - \bar{B}^2} \quad (4.23)$$

$$\gamma = \frac{\bar{A}}{\bar{A}\bar{C} - \bar{B}^2} \quad (4.24)$$

On the other hand, since the cell external radial pressure is equal to zero, it comes that

$$u_{rc} = \alpha_c R_c p_{bl} \quad (4.25)$$

where

$$\alpha_c = \frac{C_c}{A_c C_c - B_c^2} \quad (4.26)$$

The displacement and pressure increments are calculated with respect to those at the initial volume,  $V_0$ . Additionally, for  $\Delta V = 0$ , it is supposed that the bolt-grout interface is coupled too.

Using this procedure, the expression to calculate the interface pressure variation,  $\Delta p_b = p_b - p_b^0$ ,

as a function of the radial pressure variation,  $\Delta p_{bl} = p_{bl} - p_{bl}^0$ , and the axial displacement,  $W$ , reads

$$\Delta p_b \left(1 - \frac{W}{L}\right) = \frac{R_{bl} \Delta p_{bl}}{L \beta_T R_b} \left[ \left( k + \frac{2\pi R_c^2 H \alpha_c}{V_0} \right) \frac{V_0}{2\pi R_{bl}^2} + \gamma_T L + \gamma_B (H - L) \right] + p_b^0 \frac{W}{L} \quad (4.27)$$

It should be noticed that the confinement is normally denoted by  $p_r$ , but in this procedure, it is important to make the difference between  $p_r$  and  $p_{bl}$ . In equation (4.27), subscript  $B$  stands for the massive rock zone (where two tubes are coupled: the massive rock and the bladder), subscript  $T$  refers to zones  $i = \{b, c\}$  defined above (three coupled tubes: the grout, the rock and the bladder) and subscript  $C$  refers to the biaxial cell.

With the aim of validating this analytical approach to calculate  $p_b$ , and in particular the ratio  $\Delta p_b / \Delta p_{bl}$  ( $W = 0$ ), three FEM simulations have been made. In each simulation, a single loading ( $-F/S_i$ ,  $p_b$  and  $p_{bl}$ ) has been applied. The loadings have been chosen so that the sum of their corresponding relative volume variations is equal to the relative variation given by equations (4.11) or (4.12). The results show two important facts:

- the influence of the axial loading  $-F/S_i$  on the volume variation is negligible;
- the numerical ratio  $\Delta p_b / \Delta p_{bl}$  ( $W = 0$ ) is slightly higher than the analytical one (but very close, 126 against 119 in the current application). The difference is due to the fact that, in the numerical simulations, the total structure is analyzed as a whole, while in the analytical procedure each zone described above is studied independently.

Finally, a fourth simulation has been undertaken to verify that the ratio  $\Delta p_b / \Delta p_{bl}$  increases as  $W$  increases. The results are satisfactory.

#### 4.4.2 Pressure $p_b$ determination: examples

The approach developed above is applied here to calculate the interface pressure  $p_b$  of four tests conducted at constant radial stiffness. The first two tests correspond to HA25 rockbolts and the last two to FRP rockbolts. Figures 4.10 and 4.11 show the shear stress  $\tau_b$  and the radial pressure  $p_r$  ( $p_{bl}$  strictly) as a function of the axial displacement  $W$  for the four tests.

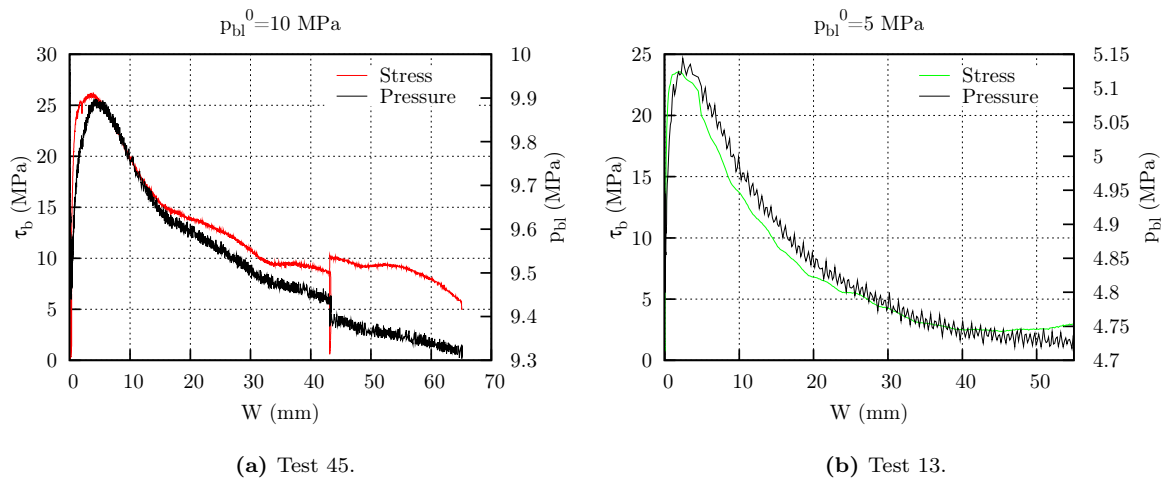
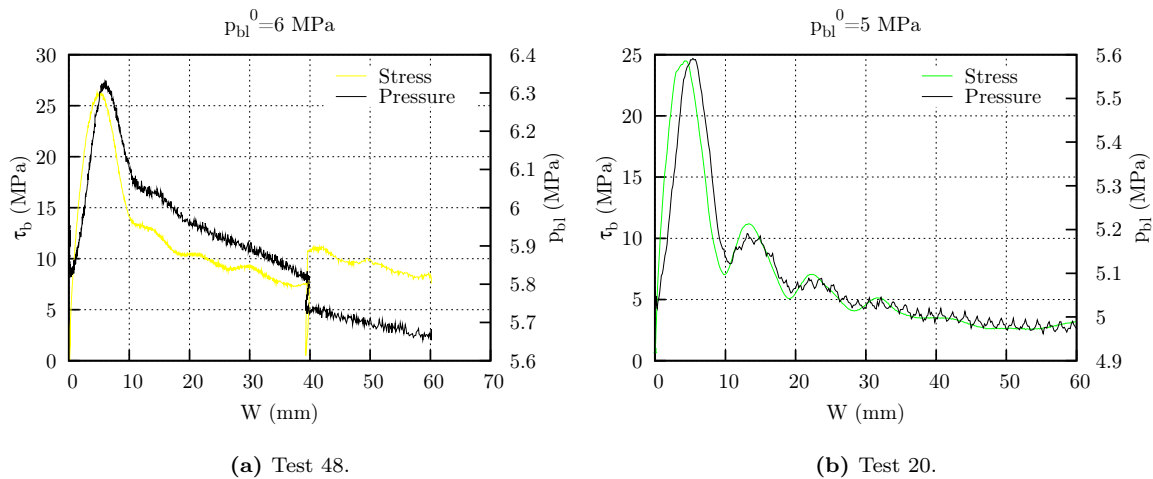


Figure 4.10: experimental results for HA25 rockbolts.



**Figure 4.11:** experimental results for FRP rockbolts.

These figures reveal a few important facts:

- the shape of the  $\tau_b(W)$  and  $p_{bl}(W)$  relationships is quite similar;
- the radial pressure starts to increase at a value of axial displacement that verifies  $W \in ]0, W_{\text{peak}}[$ . Actually, the pressure increase starts for  $W \simeq 0$ . In addition, the first stress and pressure peaks are not in phase;
- the bolt profile is reflected in the shape of these curves through the oscillations. The amplitude of these oscillations decreases as the interface pressure increases, suggesting that the interface damage is pressure dependent. Furthermore, since the FRP rockbolts profile is smoother than that of HA25 rockbolts, the grout between the indentations of FRP bolts is less weathered (for every tested pressure) and consequently the influence of the bolt profile is more obvious;
- the radial pressure at the end of the tests is lower than at the beginning. This is typical of the tests in which no radial fractures occurred; as it can be seen in figure 4.12, the pressure increase is much higher when the annuli split radially (because the hydraulic oil volume decrease is more important as the annuli wedges are pushed apart), leading to a positive (but decreasing) pressure variation in the post-peak phase. The two graphs in the figure also prove that the bolt profile is clearer for low confinements (for both rebars, but in particular for FRP bolts): the radial outward displacement generated at the interface as the bolt is pulled is greater when the annuli break and the wedges are forced apart. This way, the interface damage is less important and the grout is likely to preserve the bolt imprints.

The last fact, namely the negative pressure variation  $\Delta p_{bl}$  for high values of axial displacement, may lead to negative values of  $\Delta p_b$  if equation (4.27) is applied. This radial pressure decrease can be due to the progressive bolt-grout interface deterioration, accompanied by the formation of gouge material, as the bolt is pulled out. Such damage is not taken into account in the analytical development explained above. Notwithstanding, since at the beginning of some tests the measured pressure also decreases, it is suspected that such decrease may be distorted by some more technical reasons (for instance, some lost play between the bench parts or a slight change in the hydraulic fluid temperature after the confining phase). In other words, it is acknowledged that the interface pressure measurement is not

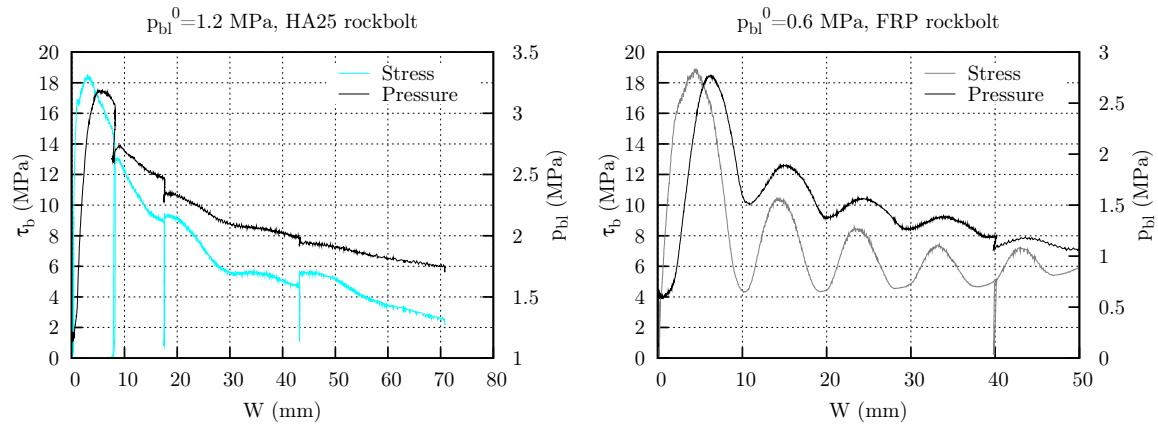


**Figure 4.12:** pressure increase when the annuli split radially.

totally accurate, but it is the only available information of the interface radial behaviour at this stage of the research. Hence, in order to avoid any negative values of  $\Delta p_b$ , equation (4.27) has been used setting  $p_{bl}^0 = \min(p_{bl})$ . Moreover, the pressure variation  $\Delta p_{bl}$  caused by the loading-unloading cycles has not been taken into account. Figure 4.13 shows the calculated interface pressure variation  $\Delta p_b$  for the four cases in figures 4.10 and 4.11.

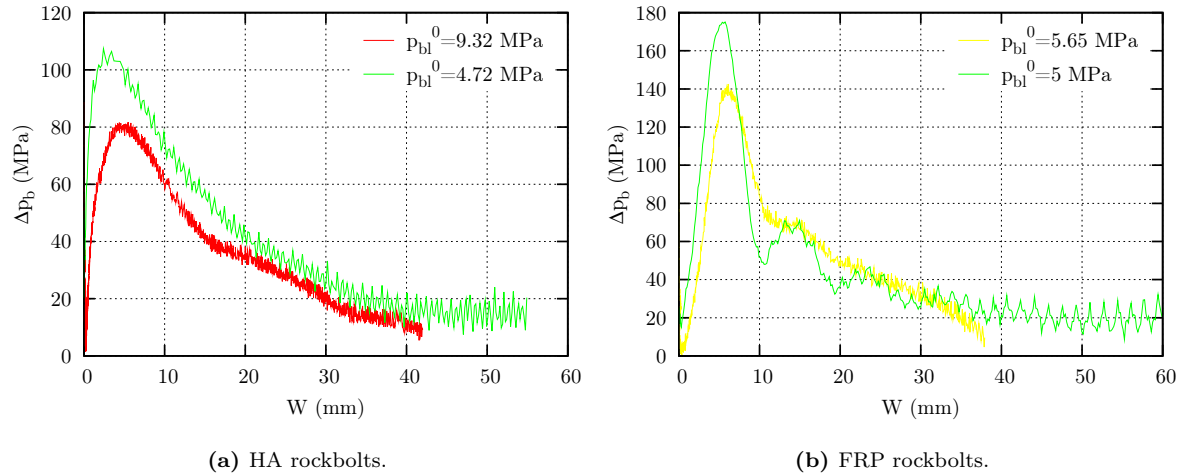


**Figure 4.13:** calculated interface pressure variation,  $\Delta p_b$ .

It is admitted that these values are high, in particular with respect to the material mechanical properties announced in tables 3.2 and 3.5. On the other hand, the FEM simulations are consistent with the analytical formulation. No explanation to these high values has been found so far. For this reason, the remaining of this chapter presents a method to determine the interface shear stress and radial opening, while the displayed values may not be correct.

#### 4.4.3 A model for the shear stress

The computed interface pressures  $\Delta p_b$  displayed in figure 4.13 and the shear stresses shown in figures 4.10 and 4.11 reveal a similar shape. As announced before, it should be noticed that the first shear stress peak and the first pressure peak are out of phase with each other (*i.e.*, the pressure peak

takes place at a higher value of axial displacement than the stress peak). According to the plots, the second and following peaks are in phase. On the other hand, the radial pressure increase starts in the pre-peak phase, for a low value of axial displacement. It is believed that this pressure increase and the initial phase difference are related to the joint formation and development (thus,  $u_{rb^+} \neq u_{rb^-}$ ), and that before the first pressure peak, the interface is still somewhat attached (although not totally coupled), so that not only friction but also chemical adhesion and mechanical interlock contribute to the shear stress. At the first pressure peak, the interface is decoupled and the joint fully developed. Beyond this point, friction becomes the main component of the shear stress; as a result, the interface pressure and the shear stress are proportional.

The hypothesis of the joint development before the peak pressure is reinforced by the aspect of the loading-unloading cycles made in the pre-peak phase: such cycles are not totally reversible, which means that the interface, yet partially coupled, has been altered to some extent.

Bearing these facts in mind, and in order to fill the gap between the experimental shear stress and the experimental interface pressure, it has been assumed that the shear stress is composed of two components:

- a component proportional to the interface pressure variation, that accounts essentially for friction, and
- a component defined at constant interface pressure. This component accounts mainly for the interface mechanical interlock and chemical adhesion. According to the literature review in section 1.3, these factors reach a maximum and then decrease towards a residual value; therefore, a modified tri-linear function has been considered.

This way, the shear stress reads

$$\tau_b(W, \Delta p_b, p_b^0) = \tau_v(\Delta p_b, p_b^0) + \tau_c(W, p_b^0) \quad (4.28)$$

where

$$\tau_v(\Delta p_b, p_b^0) = \Delta p_b \tan \varphi(p_b^0) \quad (4.29)$$

is the component that accounts for friction, and

$$\tau_c(W, p_b^0) = \begin{cases} \frac{\tau_p}{W_p} W & \text{for } 0 \leq W \leq W_p \\ \tau_r + (\tau_p - \tau_r) \left( \frac{W_r - W}{W_r - W_p} \right)^2 & \text{for } W_p \leq W \leq W_r \\ \tau_r & \text{for } W \geq W_r \end{cases} \quad (4.30)$$

is the component that accounts for the other contributions to the shear stress.

Given that the term  $\tau_v$  depends on  $\Delta p_b$ , it accounts for the influence of the bolt profile. The coefficient of proportionality has been defined  $\tan \varphi(p_b^0)$  because the term  $\tau_v$  is inspired from the basic friction concept. Regarding the term  $\tau_c$ , even if the classic tri-linear relationship could have been used, it has been decided to move to the expression described in equation (4.30) to better reproduce the experimental results. Moreover, it should be noted that the parameters  $\tau_p$ ,  $W_p$ ,  $\tau_r$  and  $W_r$  may depend on  $p_b^0$ .

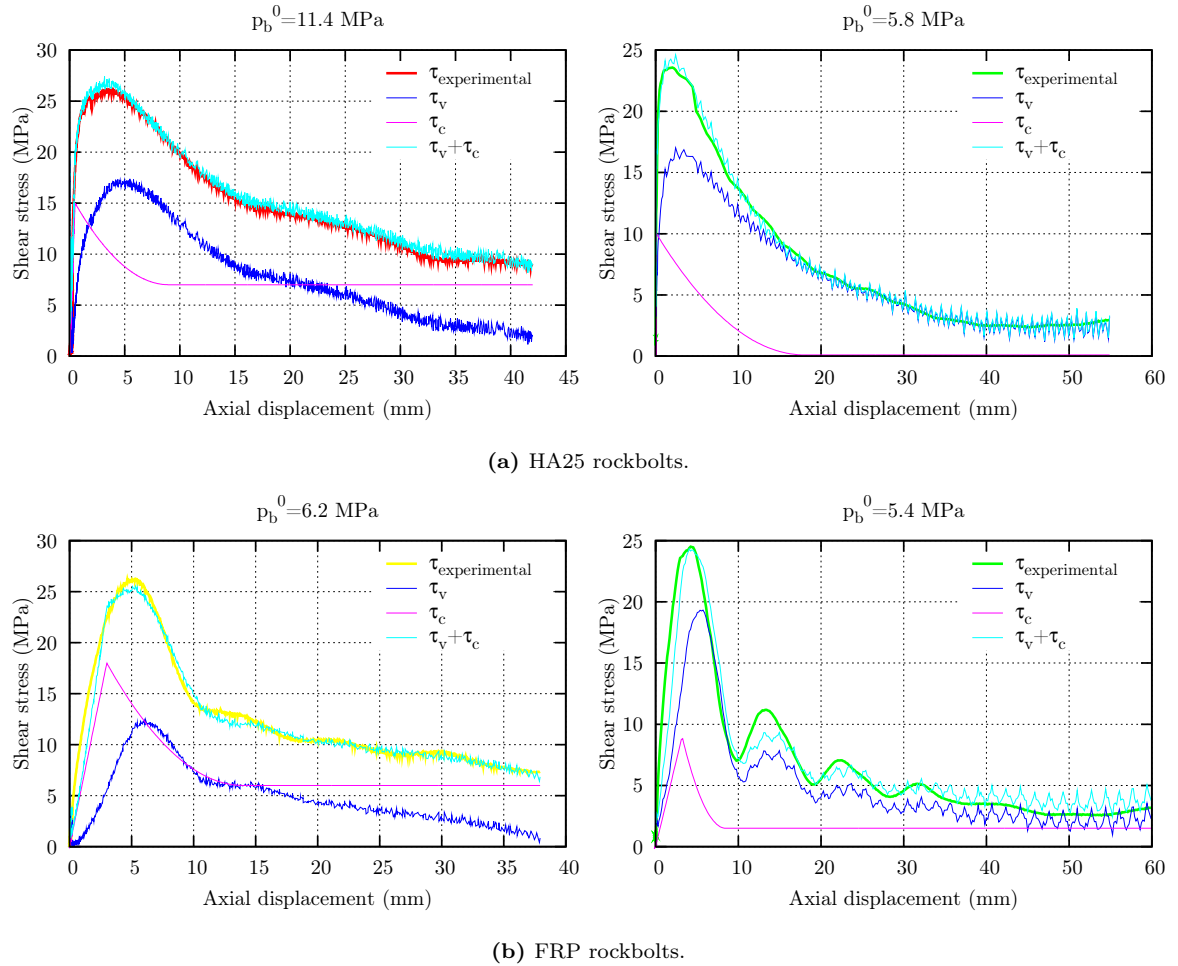
As a whole, the parameters involved in the shear stress model defined in equations (4.28)-(4.30) are  $\tau_p$ ,  $W_p$ ,  $\tau_r$ ,  $W_r$  and the interface friction angle,  $\varphi$ . The values obtained for the analyzed results (issued from tests conducted at constant outer radial stiffness and without radial fractures) are displayed in table 4.1.

**Table 4.1:** Computed values for the shear stress parameters.

| (a) HA25 rockbolts. |               |                   |               |                   |                  | (b) FRP rockbolts. |               |                   |               |                   |                  |
|---------------------|---------------|-------------------|---------------|-------------------|------------------|--------------------|---------------|-------------------|---------------|-------------------|------------------|
| $p_b^0$<br>[MPa]    | $W_p$<br>[mm] | $\tau_p$<br>[MPa] | $W_r$<br>[mm] | $\tau_r$<br>[MPa] | $\varphi$<br>[°] | $p_b^0$<br>[MPa]   | $W_p$<br>[mm] | $\tau_p$<br>[MPa] | $W_r$<br>[mm] | $\tau_r$<br>[MPa] | $\varphi$<br>[°] |
| 11.4                | 0.5           | 15                | 9             | 7                 | 12               | 10.7               | 2             | 7.3               | 8             | 1                 | 10               |
| 5.8                 | 0.1           | 10                | 18            | 0.1               | 9                | 6.2                | 3             | 18                | 14            | 6                 | 5                |
| 2.2                 | 0.1           | 10                | 9             | 1.3               | 4                | 5.4                | 2.6           | 9.5               | 9             | 1.5               | 6.5              |
|                     |               |                   |               |                   |                  | 2.1                | 1.5           | 8                 | 9             | 1                 | 2                |

Due to the low statistics, it is difficult to define a global tendency for  $\tau_p$ ,  $W_p$ ,  $\tau_r$  and  $W_r$  (more tests are required). As for the friction angle, it seems to increase proportionally with  $p_b^0$ , which agrees with the observed phenomena.

Figure 4.14 compares the experimental shear stress in figures 4.10 and 4.11 with the shear stress,  $\tau_b(W, \Delta p_b, p_b^0)$ , defined in equation (4.28). The two components  $\tau_c(W, p_b^0)$  and  $\tau_v(\Delta p_b, p_b^0)$ , are also plotted to illustrate their respective contribution.

**Figure 4.14:** comparison between experimental and modelled shear stresses.

From this figure, it seems that the semi-empirical model defined for  $\tau_b$  is well adapted to the experimental results.

#### 4.4.4 A model for the joint opening

The joint opening, defined in equation (4.10), can now be calculated from the annuli and bolt behaviour. The expression reads

$$\Delta u_{rb} = u_{rb^+} - u_{rb^-} = (\alpha_T + \beta_b) R_b \Delta p_b - \beta_T R_{bl} \Delta p_{bl} \quad (4.31)$$

where  $\beta_b = (1 - \nu_b)/E_b$ . Within the context of the future definition of a constitutive law for the bolt-grout interface, it has been decided to model the interface radial opening,  $\Delta u_{rb}$ , instead of the interface pressure variation,  $\Delta p_b$ . On the other hand, since the bolt profile is different for HA25 and FRP rockbolts, and given that the radial opening accounts for such profile, a different function has been selected for each rebar; in fact, a different model would exist for each combination of bolt and grouting material. The interface radial opening for resin-grouted HA25 and FRP bolts reads respectively

$$\Delta u_{rb}(W, p_b^0) = b \sqrt{\frac{W}{c}} \exp\left(1 - \frac{W}{c}\right) + \frac{d_f}{1 + \frac{a}{5W}} \quad (4.32)$$

$$\Delta u_{rb}(W, p_b^0) = b \exp\left(-\frac{W}{c}\right) \left(1 - \cos\left(2\pi \frac{W}{a}\right)\right) + \frac{d_f}{1 + \frac{a}{5W}} \quad (4.33)$$

These functions are totally empirical and have been selected because they fit accurately the available data. It should be noticed that equations (4.32) and (4.33) are incomplete because they are expressed only as a function of  $W$ ; in fact, the data available do not allow to distinguish between the contributions to the joint opening of the interface pressure and the axial displacement. Consequently, it has been supposed initially that only the axial displacement  $W$  takes part in  $\Delta u_{rb}$ . If more tests were carried out, the influence of the axial displacement and the interface pressure could be better understood.

The parameters are compiled in table 4.2. The wavelength  $a$  is not a fit parameter, but a bolt geometrical characteristic (*i.e.*, the average indentations spacing). In both cases, the initial amplitude  $b$  increases as the interface pressure decreases. As for the inverse of the exponential decay constant  $c$ , it is almost constant for HA25 rebars because only the first oscillation is significant, due to the rough indentations; however, in the case of FRP bolts,  $c$  tends to increase as the pressure decreases, which is consistent with the observations: the lower the pressure, the clearer the profile. With respect to the residual opening  $d_f$ , no clear trend is observed.

**Table 4.2:** Computed values for the radial opening parameters.

| (a) HA25 rockbolts. |             |             |               |             | (b) FRP rockbolts. |             |             |               |             |
|---------------------|-------------|-------------|---------------|-------------|--------------------|-------------|-------------|---------------|-------------|
| $p_b^0$<br>[MPa]    | $b$<br>[mm] | $c$<br>[mm] | $d_f$<br>[mm] | $a$<br>[mm] | $p_b^0$<br>[MPa]   | $b$<br>[mm] | $c$<br>[mm] | $d_f$<br>[mm] | $a$<br>[mm] |
| 11.4                | 0.075       | 7.5         | 0.01          | 15.5        | 10.7               | 0.084       | 6           | 0.012         | 9.6         |
| 5.8                 | 0.095       | 8           | 0.016         | 15.5        | 6.2                | 0.14        | 4.5         | 0.09          | 9.6         |
| 2.2                 | 0.105       | 7.5         | 0.006         | 15.5        | 5.4                | 0.17        | 8           | 0.025         | 9.6         |
|                     |             |             |               |             | 2.1                | 0.19        | 7           | 0.12          | 9.6         |

The comparison of the experimental opening, calculated using equation (4.31), with the semi-empirical joint opening defined in equations (4.32) and (4.33) is displayed in figure 4.15. It should be noted that, even if in some cases the agreement is not completely satisfactory, equations (4.32) and (4.33) have been selected to suit the majority of the accessible results.

Finally, it is important to highlight that the combination of equations (4.32) (for HA25 rockbolts)

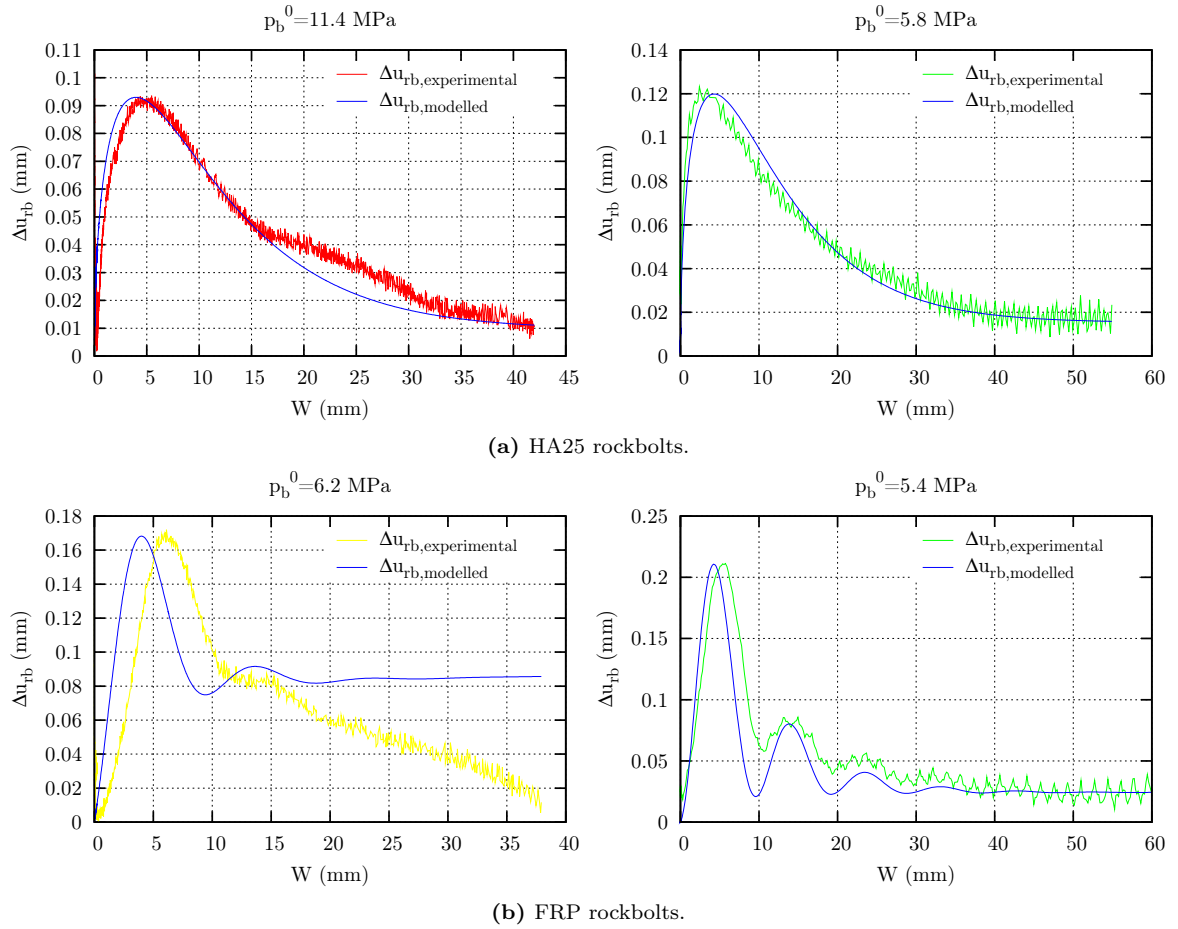


**Figure 4.15:** comparison between experimental and modelled interface openings.

or (4.33) (for FRP rebars), (4.31), (4.29), (4.30) and (4.28) allows to predict the result of a pull-out test conducted under constant outer radial stiffness conditions and without radial fractures. The ability of this method to reproduce a test held at constant confinement (for which no information is available at this stage for the radial direction) is explored in the next section. Ideally, if the developed model revealed to be close to a constitutive law, it would be valid for any boundary condition and path; on the other hand, several works conducted in the field of rock joints (*cf.* [Saeb1990] for instance) suggest that the joint response depends strongly not only on the joint surface properties but also on the boundary conditions.

## 4.5 Analysis of the tests conducted at constant radial pressure

The results obtained at constant radial stiffness have been used to back-analyze the tests conducted at constant confinement. In the future, a radial measurement is necessary to examine the interface radial behaviour accurately, not only in these tests but also in those held at constant outer radial stiffness (due to the lack of precision in the calculation of  $\Delta p_b$  using equation (4.11)).

As explained, the approach described in section 4.4 is only valid when the grout and rock annuli remain within the elastic stage throughout the pulling process; in fact, if the annuli split, the radial stiffness is not constant and coefficients  $\alpha_i$ ,  $\beta_i$  and  $\gamma_i$  change, requiring an incremental resolution of the problem. For the sake of simplicity, a test conducted at constant confinement in which the annuli

behaved elastically has been selected here. This test was carried out on a HA25 rockbolt (this is actually the only available test at constant confinement without radial fractures) and is plotted in figure 3.19, together with an equivalent test held at constant  $K_{R_r^+}$ . The figure shows that the response in terms of  $F(W)$  (or  $\tau_b(W)$ ) is different for the two tests.

The interface pressure variation has been calculated through equations (4.32) and (4.31) setting  $\Delta p_{bl} = 0$  and using the parameters compiled in table 4.2a. Then, the shear stress has been computed using equations (4.28) through (4.30) and the parameters in table 4.1a. The comparison of the experimental shear stress with the calculated one is displayed in figure 4.16. The peak strength is overestimated by about 15 %, but the general trend is reproduced fairly well (it should be noted that equation (4.32) does not account for the periodic bolt profile due to the lack of sufficient information). This suggests that the joint opening obtained from the tests at constant radial stiffness may be similar to the joint opening when the test is conducted at constant confinement; however, more tests need to be analyzed before any conclusion is made. The samples instrumentation in the radial direction will provide a deep understanding of the joint opening under different boundary conditions. Furthermore, in order to analyze the tests in which radial fractures occur, a model to account for the radial stiffness variation as the cracks propagate should be constructed.

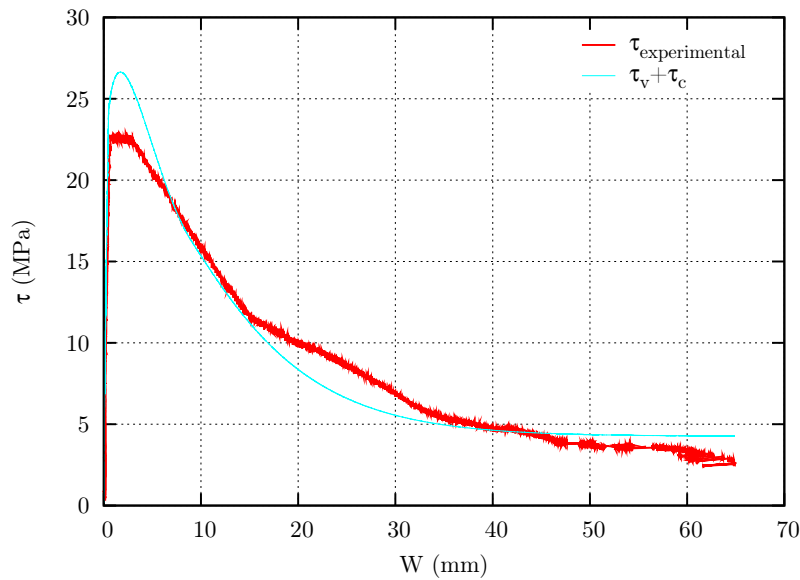


**Figure 4.16:** comparison of the experimental shear stress of a test held at constant confinement with the shear stress obtained using the method developed for the tests conducted at constant radial stiffness.

## 4.6 Conclusions

The analysis of the laboratory pull-out test results on rockbolts has been presented in this chapter. This analysis is directed towards the future definition of a constitutive law for the bolt-grout interface. Such a law involves four variables: the shear stress  $\tau_b$ , the axial displacement  $W$ , the radial pressure  $p_b$  and the radial opening  $\Delta u_{rb}$ . The relationships investigated are  $\tau_b(W, p_b)$  and  $\Delta u_{rb}(W, p_b)$ .

To conduct the analysis, the raw axial force  $F$ , the raw radial pressure  $p_r$  and the corrected displacement data  $W$  (*cf.* part 3.3.5) have been used. The shear stress has been calculated from the

experimental data assuming a uniform distribution along the embedment length  $L$ , which is accurate with a view to the short lengths in use and figure 2.8.

The analysis starts with an initial examination of the results, in terms of the characteristic parameters of the experimental relationship  $\tau_b(W)$ . This way, the values of the parameters  $\tau_{\text{peak}}$ ,  $W_{\text{peak}}$ ,  $\tau_{\text{res}}$  and  $W_{\text{res}}$  are displayed as a function of the measured radial pressure,  $p_r$  (or strictly  $p_{bl}$ , which is the pressure acting on the bladder). The post-peak slope  $k_p$  is also plotted to qualitatively illustrate the importance of the annuli radial splitting during the pulling process. The general trends for each type of rockbolt (HA25, FRP and smooth bars) are identified and interpreted with respect to the observations made after the tests. However, as far as the bolt-grout interface is concerned, the relevant pressure is not the outer, measured pressure  $p_{bl}$ , but the bolt-grout interface pressure,  $p_b$ . The calculation of  $p_b$  depends on the grout and rock annuli stiffness. Such stiffness is constant and calculable analytically when the annuli behave elastically or when they are fully fractured; nonetheless, during the splitting process the stiffness is not constant and its determination is less obvious. Consequently, the tests at the end of which no radial fractures were visible have been examined first. Among these results, only those corresponding to the tests conducted at constant radial stiffness (*i.e.*, the hydraulic fluid mass was kept constant throughout the test) have been considered in the first place because in the particular framework of this thesis, the only available information about the interface radial behaviour is provided by the confining pressure,  $p_{bl}$ . At this point, the smooth bar results have been put aside.

The analytical procedure to calculate  $p_b$  is then exposed: as far as the biaxial cell is a closed system, the hydraulic fluid equation of state lets determine the fluid relative volume variation. This relative volume variation is directly linked to the sample and cell deformation, calculable in turn as a function of  $\Delta p_{bl}$ ,  $\Delta p_b$  and  $W$ . The interface pressure obtained through this procedure is known to be very high. The causes to these values might be mainly technical, but have not been understood so far. For this reason, and in the lack of any other reliable data, the last part of the chapter describes only a method to derive the investigated relationships  $\tau_b(W, p_b)$  and  $\Delta u_{rb}(W, p_b)$ , while the displayed values may not be correct.

The comparison between the experimental  $\tau_b(W)$  and  $p_b(W)$  relationships clearly shows that both magnitudes are proportional. On the one hand, this finding proves the (expected) importance of friction on the interface behaviour; on the other hand, it proves that friction is not the only component to the shear stress, in particular before and short after the peak strength, as illustrated in figure 4.14. For this reason, it has been assumed that the shear stress has two contributions: one proportional to the interface pressure and one non-proportional to it (a modified tri-linear function, similar to the classic tri-linear relationship).

Next, the joint opening  $\Delta u_{rb}$  has been derived from the experimental pressure data using equation (4.31). Since the radial opening accounts for the bolt profile, two different functions have been chosen, one for HA25 rockbolts and one for FRP rebars. The agreement between the experimental and the modelled radial opening is quite satisfactory, as shown in figure 4.15.

At this point, a semi-empirical method to determine the interface behaviour, defined by  $\tau_b(W, p_b)$  and  $\Delta u_{rb}(W, p_b)$ , is available. Finally, a test conducted at constant radial pressure in which no radial fractures were detected has been back-analyzed using the new interface model. Ideally, this model should apply to any boundary condition. The comparison of the experimental shear stress with the predicted one shows a maximum error of 15 %, which suggests that the joint opening may be similar under the two boundary conditions; however, insufficient data are available so far to draw any conclusion. In the future, the samples instrumentation in the radial direction will provide a deep understanding of the joint opening and the interface behaviour.

As a final remark, it should be highlighted that the developed interface model  $\tau_b(W, p_b)$  and  $\Delta u_{rb}(W, p_b)$  accounts for the bolt profile or geometry, that is an intrinsic (sometimes three-dimensional) property of each bar. The effect of the bolt profile gains importance for high values of axial displacement; that is to say, for great amounts of relative slip between the two sides of the joint. To the best of the author's knowledge, the bolt profile has not been considered in previous models. Such a contribution is useful in the context of the finite strain theory, while its relevance within the framework of the infinitesimal strain theory is limited. Nevertheless, the proposed method to calculate  $p_b$  and to compare it to  $\tau_b$  remains valid in both theories.

## CONCLUSIONS AND PERSPECTIVES

*Cette étude est axée sur le comportement des boulons et des câbles à ancrage réparti, soumis à des forces axiales de traction. L'expérience montre que dans ces conditions, la rupture se produit le plus fréquemment à l'interface boulon-scellement via un processus de décohésion. Le comportement de l'interface, avant et après rupture, est le sujet principal de cette thèse. La recherche effectuée comporte deux volets principaux : une étude théorique et une étude expérimentale.*

*L'étude théorique comprend d'une part une analyse unidimensionnelle des réponses radiale et axiale de l'anneau de scellement et du terrain environnant. La réponse radiale est utile pour comprendre l'effet de la pression de confinement externe sur la pression normale à l'interface barre-scellement. La réponse axiale permet d'évaluer le cisaillement à l'interface avant que l'ancrage ne soit endommagé. D'autre part, l'étude théorique présente un nouvel outil analytique capable de déterminer la réponse complète (en termes de déplacement axial, force axiale et contrainte de cisaillement le long de la partie ancrée) d'un boulon à ancrage réparti soumis à une force axiale de traction. Cet outil s'avère particulièrement avantageux dans le cas des grandes longueurs d'ancrage, pour lesquelles la contrainte de cisaillement n'est pas uniforme. Les données nécessaires pour utiliser cet outil sont le rayon de la barre, son module de Young, la longueur d'ancrage et la relation contrainte de cisaillement-glissement,  $\tau_b(W)$ , de l'interface boulon-scellement. Cette relation est expérimentale et peut être déterminée grâce à des essais d'arrachement, ce qui justifie l'étude expérimentale menée. Enfin, on démontre dans cette partie théorique que les courtes longueurs d'ancrage sont mieux adaptées pour établir la relation  $\tau_b(W)$ .*

*L'étude expérimentale a principalement été menée en laboratoire, en conditions statiques. Des essais d'arrachement ont été effectués en utilisant un nouveau banc expérimental, conçu au préalable et mis en opération pendant la thèse. Trois types de boulons (haute adhérence HA25, fibres de verre et des tiges lisses en acier) et des câbles de type Flexible ont été testés. La plupart des essais a été effectuée sur les boulons, les essais sur les câbles ayant pour objectif principal de vérifier l'efficacité des nouvelles pièces conçues afin d'empêcher le phénomène de dévissage du câble par rapport à l'anneau de scellement qui pourrait fausser les résultats.*

*Le banc expérimental est basé sur le principe de la double longueur d'ancrage. Ce principe tient compte de la situation réaliste dans laquelle un boulon sans plaque est ancré sur deux longueurs différentes séparées par une discontinuité proche de la paroi de l'excavation. Cette discontinuité définit un bloc susceptible de glisser sous l'effet de la force axiale. La longueur scellée au-delà de la discontinuité est supposée suffisamment importante pour que l'ancrage soit assuré dans cette partie-là.*

Ainsi, un processus de décohésion ou détérioration du contact scellement-tige aura lieu dans la courte longueur proche de l'excavation si la force dans la barre dépasse une valeur limite. L'équilibre de la barre dans cette partie relie la force axiale avec la contrainte de cisaillement qui se développe sur la surface extérieure de la tige. La connaissance de la contrainte de cisaillement, et plus généralement, la connaissance du comportement de l'interface barre-scellement (qui comporte les directions tangentielle et normale) permet de déterminer la capacité de l'ancrage. Dans ce contexte, les essais d'arrachement ont été effectués pour mieux comprendre quels sont les paramètres qui influencent de façon significative cette capacité. Les échantillons utilisés se composent d'une carotte de roche, d'un matériau de scellement, d'un boulon ou d'un câble et d'un tube métallique creux. Ce tube est ancré à la barre et représente la grande longueur qui assure l'ancrage pendant la sollicitation. La conception du banc expérimental est suffisamment flexible pour tester un grand nombre de paramètres. Dans cette étude, la longueur d'ancrage (petite pour assurer une distribution uniforme du cisaillement), la pression de confinement et le type et profil de la tige ont été étudiés plus en détail. Dans l'avenir, l'influence des propriétés mécaniques de la roche et du matériau de scellement, de l'épaisseur de celui-ci et de la rugosité du trou borgne peut être également étudiée. Une évaluation préliminaire de l'effet des propriétés mécaniques de la roche a été réalisée à la fin de cette thèse. Pour ce faire, deux essais d'arrachement ont été effectués dans les mêmes conditions, mais en utilisant deux roches différentes : du grès et du granite<sup>1</sup>. Même si les résultats obtenus sont préliminaires, ils montrent clairement que la capacité de l'ancrage dépend fortement de la rigidité de la roche, ce qui a été constaté dans la littérature.

Les résultats expérimentaux révèlent l'influence prédominante de la pression de confinement, notamment au pic. Dans la phase post-pic, l'endommagement de l'interface réduit la capacité de l'ancrage à une valeur résiduelle. Les résultats suggèrent également que cet endommagement a deux contributions principales : la pression de confinement (frottement) et le profil de la barre. Plus le confinement est fort et/ou plus le profil est rugueux, plus important sera l'endommagement. Par ailleurs, étant donné que le profil des câbles est moins marqué que celui des boulons, la résistance résiduelle associée aux câbles est plus élevée que celle associée aux boulons. En conséquence, dans les situations où de grands glissements sont susceptibles d'avoir lieu, et si la stabilité de l'ouvrage repose en partie sur l'utilisation des boulons et des câbles à ancrage réparti, l'emploi de câbles semble être plus bénéfique. En revanche, au pic, les deux barres montrent des performances similaires dans les mêmes conditions.

L'analyse des résultats des essais effectués sur les boulons a été orientée vers la définition d'un modèle de comportement pour l'interface barre-scellement. Un tel modèle est défini par les relations  $\tau_b(W, p_b)$  et  $\Delta u_{r,b}(W, p_b)$ , où  $\tau_b$  est la contrainte de cisaillement à l'interface,  $W$  est le déplacement axial,  $p_b$  est la pression normale à l'interface et  $\Delta u_{r,b}$  est l'ouverture radiale. L'analyse s'est concentrée sur les essais menés à rigidité radiale constante (boulons HA25 et en fibres de verre) parce que, tels que conduits dans le cadre de cette thèse, ils fournissent plus d'information que les essais effectués à pression de confinement constante. D'abord, la pression à l'interface  $p_b$  a été calculée analytiquement en fonction de la pression de confinement  $p_{bl}$  et du déplacement axial  $W$ . Les essais dans lesquels on n'a pas observé de fracturation radiale ont été sélectionnés parce que leur analyse est plus directe et simple que celle des essais dans lesquels des fractures se créent et se propagent. La ressemblance entre les relations  $\tau_b(W)$  et  $p_b(W)$  montre l'influence du frottement, en particulier en phase post-pic. Mais étant donné que le frottement n'est pas le seul composant du cisaillement, on a décomposé  $\tau_b$  en deux parties : une composante proportionnelle à la pression à l'interface et une composante non proportionnelle à cette pression (une loi tri-linéaire modifiée, similaire à la relation tri-linéaire

<sup>1</sup> L'essai d'arrachement sur l'échantillon en granite n'a pas été décrit dans les chapitres précédents parce qu'il s'agit d'un essai exploratoire.

classique). Un modèle pour le cisaillement a été ainsi défini. L'ouverture radiale  $\Delta_{u_{r,b}}$  a été déduite des données de pression. Du fait que l'ouverture radiale tient compte du profil du boulon, deux expressions empiriques, une pour les boulons HA25 et une autre pour les boulons en fibres de verre, ont été retenues pour modéliser  $\Delta_{u_{r,b}}$ . Une méthode semi-empirique pour déterminer les relations  $\tau_b(W, p_b)$  et  $\Delta_{u_{r,b}}(W, p_b)$  recherchées est ainsi proposée. La réponse axiale d'un long boulon à ancrage réparti peut être déterminée en combinant cette méthode avec l'outil analytique décrit ci-dessus. D'autre part, en vue de la définition d'une loi de comportement intrinsèque, la capacité du nouveau modèle d'interface à prédire la réponse sous différentes conditions aux limites doit être évaluée. Pour ce faire, des essais d'arrachement menés à pression de confinement constante et instrumentés pour mesurer soit la variation volumique du fluide confinant, soit le déplacement radial de l'échantillon, sont nécessaires. Enfin, une procédure similaire doit être accomplie pour les câbles.

In situ, les essais ont été réalisés au laboratoire de recherche souterrain de l'ANDRA en Meuse/Haute-Marne. En raison des grandes longueurs de scellement utilisées, et dans le but de ne pas plastifier les tiges, les essais ont été arrêtés avant l'obtention d'un déplacement important. Les relations  $\tau_b(W)$  ont donc été déduites partiellement à partir des données disponibles, moyennant le nouvel outil analytique. Dans l'avenir, une fois le modèle d'interface déterminé grâce aux résultats obtenus à petite échelle, on pourra dimensionner les essais in situ à partir de ce modèle. La comparaison entre les résultats expérimentaux et ceux issus de la modélisation pour de grandes longueurs pourrait alors aider à évaluer la recherche menée à échelle réduite en laboratoire.

Globalement, les conclusions et perspectives d'évolution suivantes peuvent être déduites de la réalisation et de l'analyse des essais d'arrachement.

- Dans le cas des boulons HA25 et des tiges lisses, il serait mieux de ne pas sceller le tube métallique. Il a été démontré que l'ancrage boulon-tube fausse les résultats de déplacement, faisant l'étalonnage du banc nécessaire. Cet étalonnage est notamment important en phase pré-pic. D'autre part, la réalisation du scellement boulon-tube est assez compliquée et de plus il est très difficile d'assurer que le matériau de scellement soit correctement distribué dans l'espace annulaire. Une alternative relativement simple serait de fixer le tube à la barre moyennant un système bague-clavette ou similaire, placé en haut du tube. Ainsi, ce tube ne serait pas scellé au boulon, et le déplacement correspondant à la partie libre de la tige pourrait être calculée facilement, car la barre reste dans le domaine élastique et la force dans la longueur libre est constante et égale à la force appliquée. En même temps, la précision de la correction introduite moyennant l'étalonnage du banc est assujettie à la qualité du scellement tube-boulon. Pour toutes ces raisons, une configuration dans laquelle le tube n'est pas scellé au boulon serait non seulement plus pratique, mais aussi plus fiable. Dans le long terme, la meilleure solution pour les boulons HA25 et les tiges lisses serait de tirer directement sur la barre, sans avoir besoin du tube métallique. Cependant, concernant les boulons en fibres de verre, le tube doit être scellé à la tige. Pour ce qui est des câbles, afin d'éviter le détordement des torons dans la longueur libre, on pense qu'il serait mieux qu'ils soient scellés. Dans les cas où l'ancrage scellement tube-barre s'avère nécessaire, il doit être plus rigide que dans cette recherche et bien caractérisé, via un étalonnage similaire à celui décrit dans ce mémoire.
- Quant à la prise de mesures pendant les essais, la pression de confinement ne suffit pas à elle seule pour étudier le comportement normal à l'interface barre-scellement. Dans l'idéal, on devrait mesurer la pression à l'interface  $p_b$  et l'ouverture radiale  $\Delta_{u_{r,b}}$ . Cela n'étant pas possible, on peut utiliser la pression externe  $p_{bl}$  en combinaison avec, soit la variation volumique du fluide

confinant,  $\Delta V$ , soit le déplacement radial de l'échantillon,  $u_{rbl-}$ . Dans cette thèse, seulement la première option était disponible, à travers l'équation d'état de l'huile hydraulique. Néanmoins, elle s'est révélée moins précise que nécessaire, parce que la mesure de la pression de confinement est soumise à des problèmes techniques tels que la perméabilité de la jaquette à haute pression, la variation de la température du fluide confinant ou encore une éventuelle perte de jeu entre les pièces du banc. En conséquence, si l'on retient la variation volumique pour étudier la réponse normale à l'interface, il est préférable de la mesurer directement, moyennant un injecteur ou un débitmètre. Alternativement, le déplacement radial  $u_{rbl-}$  peut être mesuré à plusieurs points le long de la partie ancrée ; dans ce cas, la combinaison de  $p_{bl}$  et  $u_{rbl-}$  permettrait le calcul de  $p_b$  et  $\Delta u_{rb}$ . Le déplacement  $u_{rbl-}$  peut être mesuré grâce à l'utilisation de capteurs cantilever installés sur la surface intérieure de la cellule de confinement. Si cette solution était adoptée, il serait nécessaire d'élargir la cellule afin d'abriter les instruments de mesure. En conséquence, la quantité d'huile requise serait plus grande, ce qui diminuerait sa rigidité. Mais en tout cas, la mesure serait plus précise qu'à l'heure actuelle.

- Pour des raisons de conception, la réaction du vérin se fait directement sur la facette supérieure de l'échantillon de roche, lequel est donc comprimé. La plupart des bancs expérimentaux parcourus dans la revue bibliographique sont basés sur le même principe. Idéalement, un essai d'arrachement consisterait en un vrai essai de traction, durant lequel la roche serait tenue par le bas (i.e., loin du trou borgne) pendant que l'on tire sur le boulon. Durant le processus d'arrachement, la force de réaction du vérin serait transmise soit au bas de l'éprouvette, soit à une surface externe, mais jamais à la surface supérieure de la roche. Concernant les éprouvettes de grès employées dans cette thèse, il serait techniquement compliqué de bien les tenir, en particulier à l'intérieur de la cellule de confinement. Davantage de réflexions est nécessaire pour éclaircir ce problème. Toutefois, l'effet local causé par la réaction du vérin a pu être quantifié. Afin d'éliminer cet effet, on pourrait envisager d'utiliser des longueurs d'ancrage plus grandes ; cependant, il a été souligné que, dans le but de bien étudier la réponse de l'interface et de garantir que le cisaillement soit uniforme, les petites longueurs sont mieux adaptées. En tenant compte de toutes ces observations, une solution faisable serait de garder la conception actuelle du banc, mais de forer des trous borgnes plus longs. Le boulon serait alors ancré en fond du trou, sur une petite longueur. De cette façon, on s'affranchirait de la réaction du vérin, et en même temps, l'interface pourrait être correctement étudiée.

Enfin, ces conclusions et perspectives peuvent mener à un banc et à des mesures bien compris et maîtrisés, à partir desquels on peut déduire des modèles d'interface, comme expliqué. Le but final serait alors d'implémenter ces modèles dans un code de calcul ; la comparaison entre les prédictions numériques et les données de terrain (des mesures de convergence et d'extensométrie provenant d'un ouvrage renforcé par des boulons et des câbles à ancrage réparti) permettrait d'examiner la capacité des ces modèles à reproduire l'action du soutènement. En outre, les simulations numériques sont des outils très pratiques pour concevoir des schémas de boulonnage/câblage, d'où l'importance de bien modéliser ces éléments et leur interaction avec le terrain.

This study focuses on the behaviour of fully grouted rockbolts and cablebolts subjected to tensile axial loads. Experience throughout the world has proven that, in these conditions, failure is more likely to take place by a decoupling mechanism at the bolt-grout interface. The interface behaviour of fully grouted rockbolts, before and after the peak strength, is the core of this thesis. The research comprises two principal parts: a theoretical study and an experimental investigation.

The theoretical study consists of a one-dimensional analysis of the radial and axial responses of the grout and surrounding ground annuli. The radial response is useful to understand the pressure transmission from the annuli outside to the bolt-grout interface. As for the axial response, it is useful to determine the interface shear stress before decoupling occurs. The analytical part also provides a new tool to predict the full pull-out response (in terms of axial displacement, axial load and shear stress along the embedded length) of a fully grouted rockbolt subjected to a tensile axial load. This tool is of particular interest in the case of long rockbolts, for which the shear stress is not uniformly distributed. To run this tool, the bolt radius, embedment length and Young's modulus are required, as well as the interface shear stress-slip relationship,  $\tau_b(W)$ , also referred to as bond-slip model. Such a relationship is of experimental nature and can be obtained through pull-out tests, which justifies the experimental investigation undertaken. Additionally, it is also demonstrated in this theoretical part that short embedment lengths are more accurate to deduce the  $\tau_b(W)$  relationship.

The experimental investigation has been conducted mainly at laboratory scale, in static conditions. Pull-out tests have been conducted using a new experimental bench. This bench was designed before the beginning of this thesis, but has been tuned and put into operation during the Ph.D. Three types of rockbolts (HA25 and FRP rebars and also smooth steel bars) and Flexible cablebolts have been tested. The study has been focused on rockbolts, while the main target of the pull-out tests on cablebolts has been to validate the set-up designed to prevent these tendons from unscrewing.

The experimental bench is based on the double embedment principle, that accounts for the field situation in which a grouted, unplated bolt intersects a discontinuity close to the excavation surface. The short anchorage length between the discontinuity and the excavation surface may be damaged and even lost depending on the tensile force on the bar, while the length beyond the discontinuity remains coupled. In such a case, the lower rock block will slip with respect to the bolt. The bolt equilibrium equation in this zone relates the bolt axial load with the shear stress developed at the bolt outer surface. Knowledge of the interface shear stress, and more generally, knowledge of the interface behaviour (which includes the normal and tangential directions), allows to determine the reinforcement anchoring capacity. In this context, the pull-out tests conducted have aimed at understanding which are the most important parameters that influence this anchoring capacity. The tested samples are composed of a rock sample, a grouting material, a bolt and a metallic tube grouted to the bolt to account for the longer, anchored length. The bench design is flexible enough to investigate a wide range of parameters; however, in this study, attention has been focused on the embedment length (short enough to ensure a uniform distribution of the shear stress), the confining pressure and the bolt type and profile. In the future, the effect of the rock and grout mechanical properties, the borehole wall roughness and the grout annulus thickness needs to be studied as well. A preliminary examination of the influence of the rock properties has been undertaken at the end of this thesis through the execution of two identical pull-out tests, except for the rock sample used: sandstone and granite were respectively tested<sup>1</sup>. The results, yet exploratory, clearly prove the anchoring capacity dependence on the rock stiffness, which agrees with the results found in the literature.

---

<sup>1</sup>Note that the pull-out test on the granite sample has not been described in the previous chapters because it is only a first, exploratory test.

The test results show the predominant influence of the confining pressure applied, in particular at the peak strength. In the post-peak phase, the interface damage reduces the anchoring capacity to a residual level. According to the results, there are two main contributions to the interface damage: the confining pressure (thus, friction) and the bolt profile. The higher the pressure and/or the rougher the profile, the higher the interface deterioration. With respect to the bolt profile, the results show an interesting fact: since in general the cablebolt indentations are smoother than those of rockbolts, the residual capacity provided by the former is substantially higher than that provided by the latter. As a result, in situations where great amounts of axial slip are expected and if the stability relies to some extent on grouted bolts, the use of cablebolts over rockbolts is thought to be more beneficial. Conversely, as far as the peak strength is concerned, both tendons show a similar performance in equivalent conditions.

The analysis of the laboratory results on rockbolts has been directed towards the determination of an interface behaviour model, defined by the relationships  $\tau_b(W, p_b)$  and  $\Delta u_{rb}(W, p_b)$ , in which  $\tau_b$  is the interface shear stress,  $W$  is the axial displacement,  $p_b$  is the bolt-grout interface normal pressure and  $\Delta u_{rb}$  is the radial opening. This analysis has been focused on the tests held at constant radial stiffness (HA25 and FRP rebars) because, as conducted, they provide more information than the tests carried out at constant radial pressure. In the first place, the interface pressure  $p_b$  has been calculated analytically from the pressure acting on the bladder  $p_{bl}$  and from the axial displacement  $W$ . To do so, the tests at the end of which no radial fractures were visible have been selected. The analysis of these tests is more straightforward than that of the tests in which radial cracks appear and propagate. The resemblance between the relationships  $\tau_b(W)$  and  $p_b(W)$  has proven the influence of friction, in particular after the peak stress. But since friction is not the only component to the shear stress, it has been supposed that there are two contributions: one proportional to the interface pressure and one non-proportional to it (a modified tri-linear function, similar to the classic tri-linear relationship). On this basis, a model for the shear stress has been defined. The radial opening  $\Delta u_{rb}$  has been derived from the experimental pressure data. Given that the radial opening accounts for the bolt profile, two empirical expressions have been selected to model  $\Delta u_{rb}$ , one for HA25 rebars and one for FRP rockbolts. This way, a semi-empirical method to determine the investigated relationships  $\tau_b(W, p_b)$  and  $\Delta u_{rb}(W, p_b)$  is proposed. The axial response of a long grouted rockbolt can then be inferred from the combination of this new semi-empirical method with the analytical tool previously described. On the other hand, with a view to the definition of a constitutive law, the validity of the interface model to predict the response under different boundary conditions needs to be evaluated as well. To do so, pull-out tests held at constant confinement and equipped to measure either the confining fluid volume variation or the sample outer radial displacement are required. Finally, a similar procedure needs to be accomplished for cablebolts.

Pull-out tests have also been conducted in the field, in ANDRA's URL in North-Eastern France. Due to the great embedment lengths in use and the fact that it was decided not to reach the bolts yield strength, the tests were stopped before any significant displacement occurred. Nonetheless, the experimental  $\tau_b(W)$  relationships have been derived partially from the data available using the new analytical tool. In the future, field pull-out tests might be designed according to the interface behaviour model defined for short embedment lengths. This way, the comparison between the field and the modelled results for great lengths would help evaluate the laboratory, small-scale research.

Overall, from the tests carrying out and the analysis of the results, the following conclusions and perspectives of evolution can be made.

- In the case of HA25 rockbolts and smooth bars, it may be better not to grout the metallic

tube to the bars. It has been concluded that the bolt-metallic tube assembly distorts the displacement measurements. As a result, a calibration is needed, in particular in the pre-peak phase. In addition, grouting the tube to the bolt is quite arduous and furthermore it is very difficult to ensure a proper distribution of the adhesive material along the annular space. An easy alternative to the current set-up would be to constrain the tube to the bolt by means of a barrel and wedge or an equivalent system installed on the tube. This way, the tube would not be grouted to the bolt; therefore, the elongation of the bar along this part could be easily derived from elastic considerations, because the force along the bar free length is constant and equal to the applied load. On the other hand, the accuracy of the correction introduced through the bench calibration is subjected to the proper bolt-tube grouting; hence, it would be both more practical and reliable to move to a set-up in which the tube is not grouted. In the long term, the best solution for HA25 bolts and smooth bars would be to pull the rockbolt directly, without the metallic tube. However, in the case of FRP rockbolts, the metallic tube should be grouted to the bar. As for cablebolts, in order to prevent them from untwisting in the free length, it is believed that they had better be grouted along such length. In these cases where the tube should be grouted to the tendon, the upper anchorage needs to be stiffer than in the current thesis and also well determined, through a calibration procedure similar to the one described in this manuscript.

- With respect to the measured variables during the test, the confining pressure is not enough to gain more insight into the bolt-grout interface normal behaviour. Ideally, the interface pressure  $p_b$  and opening  $\Delta u_{rb}$  should be measured; since this is not possible, either the confining fluid volume variation  $\Delta V$  or the outer radial displacement  $u_{rbl}$  can be used together with the measured pressure acting on the bladder,  $p_{bl}$ . In this thesis, only the first alternative was available, through the hydraulic oil equation of state. However, it has turned out to be less precise than needed because the pressure measurement is subjected to technical problems such as the bladder permeability at high pressures, the changes in the fluid temperature or some play between the bench parts. Therefore, if the volume variation is used to study the interface normal response, it should be measured directly by means of a pressure injector or a flow meter. Alternatively, the outer radial displacement  $u_{rbl}$  could be recorded at several points along the embedment length; the combination of  $p_{bl}$  and  $u_{rbl}$  would then lead to the determination of  $p_b$  and  $\Delta u_{rb}$ . The displacement measurement can be made by mounting cantilever strain gauged arms on the inner surface of the biaxial cell. If this solution is adopted for the current bench, it will be necessary to extend the cell in the radial direction, in order to house the measurement devices. Consequently, more quantity of confining fluid will be required, and its stiffness will be reduced. But in any case, the radial measurement will be more accurate than it is at present.
- Due to design reasons, the reaction force from the hydraulic jack is directly transferred to the top of the rock sample, which is consequently compressed to a certain extent. This fact is common to most of the pull-out benches examined through the literature review. Ideally, a pull-out test would consist in a true tensile test; that is to say, the rock sample would be grabbed by its opposite end (*i.e.*, far from the borehole) while the bolt is pulled. During this process, the reaction force from the pulling device would not be transferred to the top of the rock sample, but either to the sample opposite face or to an external surface. In the case of the sandstone rock samples used in this thesis, it would be technically difficult to successfully grab the lower part of the samples, in particular inside the biaxial cell. Further reflections are required to try to

solve this matter. Notwithstanding, the local effect caused by the hydraulic jack reaction force has been quantified. In order to eliminate this local effect, it could be proposed to use longer embedment lengths; however, it has been explained that to accurately examine the interface behaviour and to ensure a uniform distribution of the shear stress along the embedded length, short lengths should be used. Bearing all these observations in mind, a feasible solution would be to keep the current design, but to drill deeper boreholes, and to grout the bolt to the end of these holes, along a short length. This way, the local effect on top of the rock sample would not distort the test results, while at the same time, the interface could be properly investigated.

These findings and perspectives may eventually lead to a fully understood bench and measurements, from which interface behaviour models can be inferred as explained. The final goal would be then to implement these models in a numerical software; the comparison between numerical predictions and field data (convergence and extensometer measurements from a bolted excavation) would let examine the ability of such models to reproduce the reinforcement action. On the other hand, numerical simulations are useful tools to design rock reinforcement patterns, whence the importance of accurately modelling the reinforcing elements and their interaction with the rock mass.

## REFERENCES

- Al Hallak R.** 1999. Étude expérimentale et numérique du renforcement du front de taille par boulonnage dans les tunnels en terrains meubles. Ph.D. thesis. École Nationale des Ponts et Chaussées. 55
- Alejano I.,** Alonso E., Rodríguez-Dono A., et al. 2010. Estimate of support and reinforcement cost increase associated to poor blasting practices in drifting in *Proceedings of the 9<sup>th</sup> International Symposium on Rock Fragmentation by Blasting (Fragblast 9, Granada, Spain)*, edited by J.A. Sanchidrián (Taylor & Francis Group, London). pp. 731–740. 10
- ANDRA** 2007. Architecture des galeries du laboratoire période 2008-2012. Plan D PL ALS 07-0443/D. 114
- Ansell A.** 2005. Laboratory testing of a new type of energy absorbing rock bolt. *Tunnelling and Underground Space Technology*. 20: 291 - 300. 16  
[dx.doi.org/10.1016/j.tust.2004.12.001](https://doi.org/10.1016/j.tust.2004.12.001)
- Barley A.** and Windsor C. R. 2000. Recent advances in ground anchor and ground reinforcement technology with reference to the development of the art. 12, 18, 21
- Bawden W.,** Hyett A., and Lausch P. 1992. An Experimental Procedure for the *In Situ* Testing of Cable Bolts. *International Journal of Rock Mechanics and Mining Sciences & Geomechanics Abstracts*. 29: 525 - 533. 29, 31, 38, 85, 105  
[dx.doi.org/10.1016/0148-9062\(92\)92635-P](https://doi.org/10.1016/0148-9062(92)92635-P)
- Bawden W.,** Dube S., and Hyett A. J. 1994. A Laboratory Study on the Capacity of Fully Grouted Cable Bolts Subjected to Combined Axial and Lateral Loads. Tech. Rep. Department of Mining Engineering Queen's University (Canada). 6, 26  
[www.yieldpoint.com/pdf/Combined\\_Axial\\_And\\_Lateral\\_Loads\\_Report.pdf](http://www.yieldpoint.com/pdf/Combined_Axial_And_Lateral_Loads_Report.pdf)
- Bawden W.,** Moosavi M., and Hyett A. 1997. Evaluation of long cable tendon load distribution using Computer Aided Cable Load Estimation (CABLE) in *Proceedings of the 1<sup>st</sup> Asian Rock Mechanics Symposium (Environmental and Safety Concerns in Underground Construction, Seoul, South Korea)*, edited by Lee, Yang & Chung (Balkema, Rotterdam). pp. 875–881. 18, 24, 125
- Bawden W.** and Lausch P. 2000. The use of SMART cable bolt instruments toward the design optimization of underground rock support systems in *5<sup>3rd</sup> Canadian Geotechnical Conference (Montreal, Canada)*. 28
- Benmokrane B.,** Chennouf A., and Mitri H. S. 1995. Laboratory evaluation of cement-based grouts and grouted rock anchors. *International Journal of Rock Mechanics and Mining Science & Geome-*

*chanics Abstracts*. 32: 633 - 642.

[dx.doi.org/10.1016/0148-9062\(95\)00021-8](https://doi.org/10.1016/0148-9062(95)00021-8) 8, 20, 24, 36, 37, 38, 39, 41, 48, 57, 65, 72, 73, 74, 75, 96, 101

**Benmokrane R.** and Chekired M. 1996. Investigation on the load transfer of cement grouted cables bolts and their instrumentation in *Proceedings of the 2<sup>nd</sup> North American Rock Mechanics Symposium (Rock Mechanics: Tools and Techniques, Montreal, Canada)*, edited by Aubertin, Hassani & Mitri (Balkema, Rotterdam). pp. 195–202. 28

**BS 7861-1.** 1996. Strata reinforcement support system components used in coal mines. Part 1. Specification for rockbolting. 31, 33

**BS 7861-2.** 1996. Strata reinforcement support system components used in coal mines. Part 2. Specification for cable bolts. 31, 33

**Campbell R.** and Mould R. 2005. Impacts of gloving and un-mixed resin in fully encapsulated roof bolts on geotechnical design assumptions and strata control in coal mines. *International Journal of Coal Geology*. 64: 116 - 125.

[dx.doi.org/10.1016/j.coal.2005.03.009](https://doi.org/10.1016/j.coal.2005.03.009) 20

**Chen W.** and Ren F. 2008. Mechanical behavior of the bamboo-steel composite rock-bolt. Research Report 2006BAK30B02. Dunhuang Academy & Cultural Relics Protection Center of the Lanzhou University. 41, 71, 72

**Déneché D.,** Leleu A., and Beth M. 2009. Essais de traction boulons d’ancrage. Campagne octobre 2009. Rapport des essais. Tech. Rep. Sol Data (pour ANDRA). 114, 115, 191

**Dunham R.** 1976. Anchorage tests on strain-gauged resin bonded bolts. *Tunnels and Tunnelling*. pp. 73–76. 35, 36

**Durville J.,** Bidaut P., Guillemin P., et al. 2006. Essais de cisaillement sur discontinuités rocheuses armées par ancrages passifs: utilisation d’une boîte de cisaillement de grandes dimensions. *BLPC No.263-264*. pp. 8–18. 27

**Farmer I.** 1975. Stress distribution along a resin grouted rock anchor. *International Journal of Rock Mechanics and Mining Sciences & Geomechanics Abstracts*. 12: 347–351.

[dx.doi.org/10.1016/0148-9062\(75\)90168-0](https://doi.org/10.1016/0148-9062(75)90168-0) 7, 33, 34, 35, 39, 57, 64

**Fine J.** 1998. *Le soutènement des galeries minières* (Presses de l’Ecole des Mines de Paris). 13, 22

**Freeman T.** 1978. The behaviour of fully-bonded rock bolts in the Kielder experimental tunnel. *Tunnels and Tunnelling*. pp. 37–40. 6, 25

**Fuller P.** and Cox R. 1975. Mechanics of Load Transfer from Steel Tendons to Cement Based Grout in *Proceedings of the 5<sup>th</sup> Australian Conference on the Mechanics of Structures and Materials (Melbourne)*. pp. 189–203. 7, 31, 32, 36, 43, 44

**Fuller P.** 1983. Cable support in mining. A keynote lecture in *Proceedings of the International Symposium on Rock Bolting (Rock Bolting: Theory and Application in Mining and Underground Construction, Abisko, Sweden)*, edited by O. Stephansson (Balkema, Rotterdam). pp. 511–522. 26, 27

**Fuller P.,** Hume B., and Hume R. 1996. Bolt load simulation and its practical application in *Proceedings of the 2<sup>nd</sup> North American Rock Mechanics Symposium (Rock Mechanics: Tools and Techniques, Montreal, Canada)*, edited by Aubertin, Hassani & Mitri (Balkema, Rotterdam). pp. 187–193. 27

- Gagnon D.** 1996. Rock bolting - A practical review in *Proceedings of the 2<sup>nd</sup> North American Rock Mechanics Symposium (Rock Mechanics: Tools and Techniques, Montreal, Canada)*, edited by Aubertin, Hassani & Mitri (Balkema, Rotterdam). pp. 203–208. **23**
- Girard A.** 1996. Choosing a ground support system for mobile ground in *Proceedings of the 2<sup>nd</sup> North American Rock Mechanics Symposium (Rock Mechanics: Tools and Techniques, Montreal, Canada)*, edited by Aubertin, Hassani & Mitri (Balkema, Rotterdam). pp. 243–249. **15**
- Goris J.** 1990. *Report of investigation vol 9308*. chap. Laboratory evaluation of cable bolt supports, part 1: Evaluation of supports using conventional cables. **24**
- Hagan P.** 2004. Variation in load transfer of a fully encapsulated rockbolt in *Proceedings of the 23<sup>rd</sup> International Conference in Ground Control in Mining (Morgantown, USA)*. **7, 33, 49, 57, 65, 84, 88, 92, 113**
- Hoek E.** 2007. *Practical Rock Engineering*.  
[www.rocsience.com/education/hoek\\_corner](http://www.rocsience.com/education/hoek_corner) **14, 15, 21**
- Hutchinson D.** and Diederichs M. 1996. *Cablebolting in Underground Mines* (BiTech Publishers Ltd). 1st ed. **19**
- Hyett A., Bawden W., and Coulson A.** 1992a. Physical and mechanical properties of normal Portland cement pertaining to fully grouted cable bolts in *Proceedings of the International Symposium on Rock Support (Rock Support in Mining and Underground Construction, Sudbury, Canada)*, edited by P.K. Kaiser & D.R. McCreath (Balkema, Rotterdam). pp. 341–348. **20**
- Hyett A., Bawden W., and Reichert R.** 1992b. The effect of rock mass confinement on the bond strength of fully grouted cable bolts. *International Journal of Rock Mechanics and Mining Sciences & Geomechanics Abstracts*. 29: 503 - 524.  
[dx.doi.org/10.1016/0148-9062\(92\)92634-0](https://doi.org/10.1016/0148-9062(92)92634-0) **20, 31, 32, 45, 76, 96, 110**
- Hyett A. J., Bawden W. F., Macsporrán G. R., et al.** 1995. A constitutive law for bond failure of fully-grouted cable bolts using a modified hoek cell. *International Journal of Rock Mechanics and Mining Science & Geomechanics Abstracts*. 32: 11 - 36.  
[dx.doi.org/10.1016/0148-9062\(94\)00018-X](https://doi.org/10.1016/0148-9062(94)00018-X) **8, 20, 24, 41, 43, 44, 45, 46, 47, 48, 52, 54, 57, 64, 93, 105, 128**
- Hyett A. J., Moosavi M., and Bawden W. F.** 1996. Load distribution along fully grouted bolts, with emphasis on cable bolt reinforcement. *International Journal for Numerical and Analytical Methods in Geomechanics*. 20: 517–544.  
[dx.doi.org/10.1002/\(SICI\)1096-9853\(199607\)20:7<517::AID-NAG833>3.0.CO;2-L](https://doi.org/10.1002/(SICI)1096-9853(199607)20:7<517::AID-NAG833>3.0.CO;2-L) **22**
- ISRM** 1973. *Rock Characterization, Testing and Monitoring* (Pergamon Press). chap. Suggested Method for rockbolt testing (Coordinator: Franklin). **31**
- Ivanovic A.** and Neilson R. D. 2009. Modelling of debonding along the fixed anchor length. *International Journal of Rock Mechanics and Mining Sciences*. 46: 699 - 707.  
[dx.doi.org/10.1016/j.ijrmms.2008.09.008](https://doi.org/10.1016/j.ijrmms.2008.09.008) **24, 65**
- Jager A.** 1992. Two new support units for the control of rockburst damage in *Proceedings of the International Symposium on Rock Support (Rock Support in Mining and Underground Construction, Sudbury, Canada)*, edited by P.K. Kaiser & D.R. McCreath (Balkema, Rotterdam). pp. 621–631. **16**
- Jomaa M.** 2003. Modélisation par éléments finis du soutènement par boulonnage. Projet de fin d'études, MINES-ParisTech. **54**

- Kaiser P.**, Yazici S., and Nosé J. 1992. Effect of stress change on the bond strength of fully grouted cables. *International Journal of Rock Mechanics and Mining Sciences & Geomechanics Abstracts*. 29: 293 - 306.  
[dx.doi.org/10.1016/0148-9062\(92\)93662-4](https://doi.org/10.1016/0148-9062(92)93662-4) 24
- Kilic A.**, Yasar E., and Celik A. G. 2002. Effect of grout properties on the pull-out load capacity of fully grouted rock bolt. *Tunnelling and Underground Space Technology*. 17: 355 - 362.  
[dx.doi.org/10.1016/S0886-7798\(02\)00038-X](https://doi.org/10.1016/S0886-7798(02)00038-X) 20
- Kilic A.**, Yasar E., and Atis C. D. 2003. Effect of bar shape on the pull-out capacity of fully-grouted rockbolts. *Tunnelling and Underground Space Technology*. 18: 1 - 6.  
[dx.doi.org/10.1016/S0886-7798\(02\)00077-9](https://doi.org/10.1016/S0886-7798(02)00077-9) 15
- Laigle F.** 2004. Modèle Conceptuel pour le Développement de Lois de Comportement adaptées à la Conception des Ouvrages Souterrains. Ph.D. thesis. Centre d'Ingénierie Hydraulique & École Centrale de Lyon. 8, 10, 50, 58
- Langille C.**, Tannant D., and Galbraith J. 1996. Investigation of one-pass grouted support systems for use in a high stress mining environment. *CIM Bulletin*. 89: 111-116. 28
- Li C.** and Stillborg B. 1999. Analytical models for rock bolts. *International Journal of Rock Mechanics and Mining Sciences*. 36: 1013 - 1029.  
[dx.doi.org/10.1016/S1365-1609\(99\)00064-7](https://doi.org/10.1016/S1365-1609(99)00064-7) 7, 22, 30, 35, 38, 40, 64
- Li C.** 2007. A Practical Problem with Threaded Rebar Bolts in Reinforcing Largely Deformed Rock Masses. *Rock Mechanics and Rock Engineering*. 40: 519-524.  
[folk.ntnu.no/charliel/Y2007\\_RMRE\\_rebar.pdf](http://folk.ntnu.no/charliel/Y2007_RMRE_rebar.pdf) 15, 22
- Li C.** 2010a. Field Observations of Rock Bolts in High Stress Rock Masses. *Rock Mechanics and Rock Engineering*. 43: 491-496.  
[dx.doi.org/10.1007/s00603-009-0067-8](https://doi.org/10.1007/s00603-009-0067-8) 6, 22, 25, 26
- Li C. C.** 2010b. A new energy-absorbing bolt for rock support in high stress rock masses. *International Journal of Rock Mechanics and Mining Sciences*. 47: 396 - 404.  
[dx.doi.org/10.1016/j.ijrmms.2010.01.005](https://doi.org/10.1016/j.ijrmms.2010.01.005) 16
- Ludvig B.** 1983. Shear tests on rock bolts in *Proceedings of the International Symposium on Rock Bolting (Rock Bolting: Theory and Application in Mining and Underground Construction, Abisko, Sweden)*, edited by O. Stephansson Lulea University (Balkema, Rotterdam). pp. 113– 123. 6, 25
- Mark C.**, Molinda G., and Dolinar D. 2003. Analysis of roof bolt systems. 9
- Minova** 2009a. LOKSET SiS-Cartridges Type SF-L Technical Data Sheet. Minova CarboTech GmbH. 19
- Minova** 2009b. LOKSET Resin Capsules Product Data Sheet. Minova Australia. 19, 117
- Mitri H.** 2011. Evaluation of Rock Support Performance through Instrumentation and Monitoring of Bolt Axial Load in *Underground Coal Operators' Conference*. Paper 349.  
[ro.uow.edu.au/coal/349](http://ro.uow.edu.au/coal/349) 28
- Moosavi M.** and Bawden W. F. 2003. Shear strength of Portland cement grout. *Cement and Concrete Composites*. 25: 729 - 735.  
[dx.doi.org/10.1016/S0958-9465\(02\)00101-4](https://doi.org/10.1016/S0958-9465(02)00101-4) 117

- Moosavi M.**, Jafari A., and Khosravi A. 2005. Bond of cement grouted reinforcing bars under constant radial pressure. *Cement and Concrete Composites*. 27: 103 - 109.  
[dx.doi.org/10.1016/j.cemconcomp.2003.12.002](https://doi.org/10.1016/j.cemconcomp.2003.12.002) 7, 15, 20, 24, 30, 41, 47, 48, 49, 64, 101
- NF A 35 080 1.** 2010. Reinforcing steel - Weldable steel - Part 1: Bars and coils. 94
- NF EN 10080.** 2005. Steel for the reinforcement of concrete - Weldable reinforcing steel - General. 94
- NF P 94-153.** 1993. Sols: reconnaissance et essais. Essai statique de tirant d'anracement. 115
- NF P 94-242-1.** 1993. Renforcement des sols. Essai statique d'arrachement de clou soumis à un effort axial de traction. Essai à vitesse de déplacement constante. 115
- Offner C.**, Galvin J., and Fabjanczyk M. 2000. Evaluating Anchoring Mechanisms of Fully Encapsulated Rock Bolts in *Proceedings of the 19<sup>th</sup> International Conference on Ground Control in Mining (Morgantown, USA)*, edited by S.S. Peng and C. Mark. pp. 255-260. 92, 131
- Pellet F.** 1993. Résistance et déformabilité des massifs rocheux stratifiés renforcés par ancrages passifs. Ph.D. thesis. École Polytechnique Fédérale de Lausanne. 27
- R. Pakalnis D. P.** and Peter M. 1994. Glass fibre cable bolts - an alternative. *CIM Bulletin*. 87: 53-57. 24
- Rabcewicz L.** 1964. *The New Austrian Tunnelling Method (NATM)*. vol. I, II, III. 11, 28
- Reichert R.**, Bawden W. F., and Hyett A. J. 1991. Evaluation of desing bond strength for fully grouted bolts in *9<sup>3rd</sup> Annual Meeting of CIM*. 24
- Ren F.**, Yang Z., Chen J., et al. 2010. An analytical analysis of the full-range behaviour of grouted rockbolts based on a tri-linear bond-slip model. *Construction and Building Materials*. 24: 361 - 370.  
[dx.doi.org/10.1016/j.conbuildmat.2009.08.021](https://doi.org/10.1016/j.conbuildmat.2009.08.021) 8, 39, 40, 41, 57, 71, 75, 77
- Reynolds C.** 2006. Testing and standards for rock reinforcement consumables. 32, 92, 93
- Rong G.**, Zhu H., and Zhou C. 2004. Testing study on working mechanism of fully grouted bolts of thread steel and smooth steel. *Chinese Journal of Rock Mechanics and Engineering*. 23: 469-475.  
[en.cnki.com.cn/Article\\_en/CJFDTOTAL-YSLX200403022.htm](http://en.cnki.com.cn/Article_en/CJFDTOTAL-YSLX200403022.htm) 40, 41
- Saeb S.** and Amadei B. 1990. Modelling Joint Response Under Constant or Variable Normal Stiffness Boundary Conditions (Technical Note). *International Journal for Numerical and Analytical Methods in Geomechanics*. 27: 213-217.  
[dx.doi.org/10.1016/0148-9062\(90\)94330-V](https://doi.org/10.1016/0148-9062(90)94330-V) 139
- Saeb S.** and Amadei B. 1992. Modelling rock joints under shear and normal loading. *International Journal of Rock Mechanics and Mining Sciences & Geomechanics Abstracts*. 29: 267 - 278.  
[dx.doi.org/10.1016/0148-9062\(92\)93660-C](https://doi.org/10.1016/0148-9062(92)93660-C) 128
- Signer S. P.** 1990. Field Verification of Load Transfer Mechanics of Fully Grouted Roof Bolts. Tech. Rep. USBM RI9301. USA Department of Interior. 36
- Smith W.** 1993. Roof control strategies for underground coal mines. Information circular 9351 of the U.S. Bureau of Mines, page 17. 23
- Stillborg B.** 1983. Research carried out within the Swedish Mining Research Foundation in relation to cables and cable bolting in *Proceedings of the International Symposium on Rock Bolting (Rock Bolting: Theory and Application in Mining and Underground Construction, Abisko, Sweden)*, edited by O. Stephansson (Balkema, Rotterdam). pp. 571-573. 29, 110

- Stillborg** B. 1984. Experimental investigation of steel cables for rock reinforcement in hard rock. Ph.D. thesis. University of Lulea. [24](#), [43](#), [94](#)
- Stillborg** B. 1986. *Professional Users Handbook for Rock Bolting* (Trans Tech Publications). [9](#), [12](#), [14](#), [15](#), [22](#), [23](#)
- Stille** H. 1992. Keynote lecture: Rock support in theory and practice in *Proceedings of the International Symposium on Rock Support (Rock Support in Mining and Underground Construction, Sudbury, Canada)*, edited by P.K. Kaiser & D.R. McCreath (Balkema, Rotterdam). pp. 421–438. [25](#)
- Sun** X. 1984. Grouted rock bolt used in underground engineering in soft surrounding rock or in highly stressed regions in *Proceedings of the International Symposium on Rock Bolting (Rock Bolting: Theory and Application in Mining and Underground Construction, Abisko, Sweden)*, edited by O. Stephansson (Balkema, Rotterdam). pp. 93–99. [25](#)
- Tijani** M. 2008. Contribution à l'étude thermomécanique des cavités réalisées par lessivage dans des formations géologiques salines. Habilitation à diriger des recherches. Université Pierre et Marie Curie. [tel.archives-ouvertes.fr/tel-00430361](http://tel.archives-ouvertes.fr/tel-00430361) [53](#)
- Tincelin** E. and Fine J. 1991. *Memento du boulonnage* (Ecole des Mines de Paris). [15](#), [22](#), [27](#)
- Verderame** G. M., Ricci P., Carlo G. D., et al. 2009a. Cyclic bond behaviour of plain bars. Part I: Experimental investigation. *Construction and Building Materials*. 23: 3499 - 3511. [dx.doi.org/10.1016/j.conbuildmat.2009.07.002](http://dx.doi.org/10.1016/j.conbuildmat.2009.07.002) [30](#), [84](#)
- Verderame** G. M., Carlo G. D., Ricci P., et al. 2009b. Cyclic bond behaviour of plain bars. Part II: Analytical investigation. *Construction and Building Materials*. 23: 3512 - 3522. [dx.doi.org/10.1016/j.conbuildmat.2009.07.001](http://dx.doi.org/10.1016/j.conbuildmat.2009.07.001) [96](#)
- Villaescusa** E., Varden R., and Hassell R. 2008. Quantifying the performance of resin anchored rock bolts in the Australian underground hard rock mining industry. *International Journal of Rock Mechanics and Mining Sciences*. 45: 94 - 102. [dx.doi.org/10.1016/j.ijrmms.2007.03.004](http://dx.doi.org/10.1016/j.ijrmms.2007.03.004) [20](#)
- Windsor** C. and Thompson A. 1993. *Rock reinforcement- technology, testing, design and evaluation*. *Comprehensive Rock Engineering - Principles, Practice and Projects* (Pergamon Press, Oxford). vol. 4. pp. 451–484. [5](#), [12](#)
- Windsor** C. and Thompson A. 1996. Terminology in rock reinforcement practice in *Proceedings of the 2<sup>nd</sup> North American Rock Mechanics Symposium (Rock Mechanics: Tools and Techniques, Montreal, Canada)*, edited by Aubertin, Hassani & Mitri (Balkema, Rotterdam). pp. 225–232. [5](#), [11](#)
- Yazici** S. and Kaiser P. 1992. Bond strength of grouted cable bolts. *International Journal of Rock Mechanics and Mining Sciences & Geomechanics Abstracts*. 29: 279 - 292. [dx.doi.org/10.1016/0148-9062\(92\)93661-3](http://dx.doi.org/10.1016/0148-9062(92)93661-3) [8](#), [41](#), [42](#), [43](#), [45](#), [46](#)
- FLAC 2000. *Flac Version 5.0 Users Manual*. Itasca Consulting Inc. [52](#)

## A Laboratory pull-out test campaign on rockbolts

The results of all the pull-out tests conducted on rockbolts within the main laboratory experimental campaign are shown here. These results correspond to the tests compiled in table 3.7.

In each graph, the results correspond to pull-out tests conducted on the same bolt type using the same grouting material and embedment length (*i.e.*, the only parameter that changes is the confining pressure applied). The operating conditions (displacement rate, boundary conditions in the biaxial cell and use of the end plate) are also identical for the tests in each graph; however, since before the use of the end plate failure was not restricted to the bolt-grout interface, several failure modes may co-exist in some of the graphs. An overview of most of the samples is also shown. The unexpected results are commented as well.

Finally, the results are shown in terms of axial load-axial displacement and also in terms of radial outer pressure variation-axial displacement. It should be noted that, in the tests conducted without radial confinement, the measured pressure corresponds to the air pressure (*i.e.*, the confining oil was not injected in the biaxial cell).

Moreover, in some of the tests conducted at slow displacement rate, the pressure  $p_r$  was changed in the residual phase, while the axial displacement was held constant (that is to say, the hydraulic jack was not in operation). This was made to broaden the residual phase study (*i.e.*, to get more points to complete the relationship  $\tau_{\text{res}}(p_r)$ ). However, it has been not possible to exploit the results because the measured force (and, consequently, the shear stress) does not correspond to a limit (in terms of strength) value: to measure such value, it would have been necessary to re-load the bolt and to measure the corresponding force. The results are therefore not shown here.

## A.1 Pull-out tests on HA25 rockbolts

Resin grout. Operating conditions: constant outer radial stiffness  $K_{R^+}$ , displacement rate=0.84 mm/s, without end plate

1. Embedment length  $L = 130$  mm.

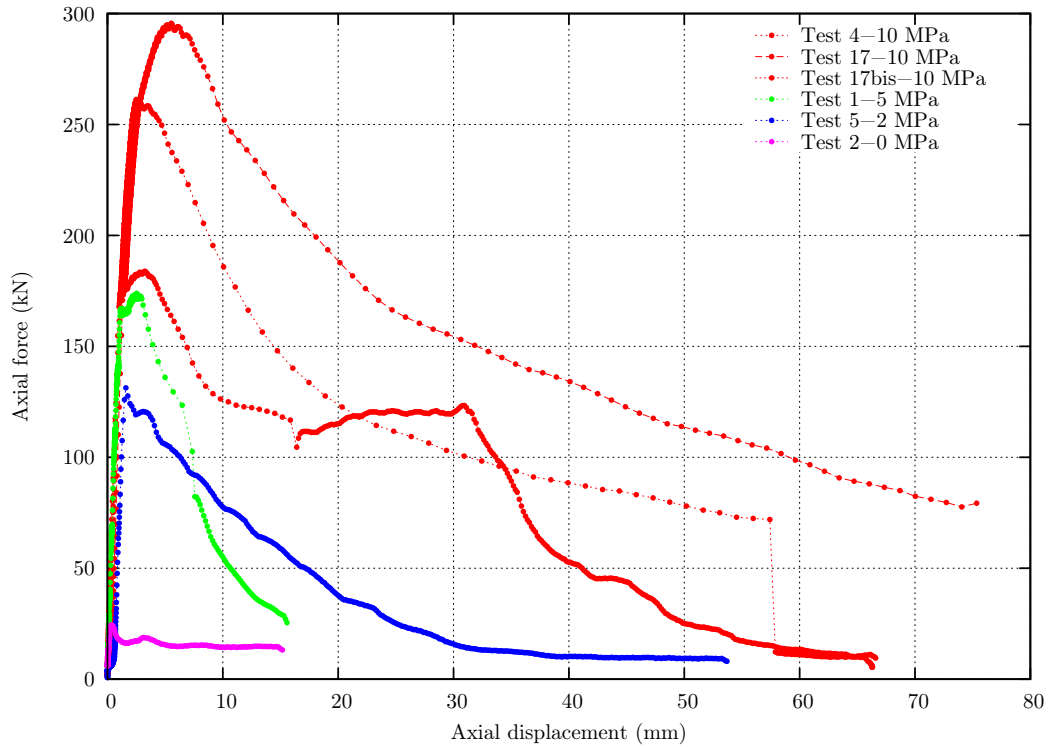


Figure A.1: Load-displacement curves.

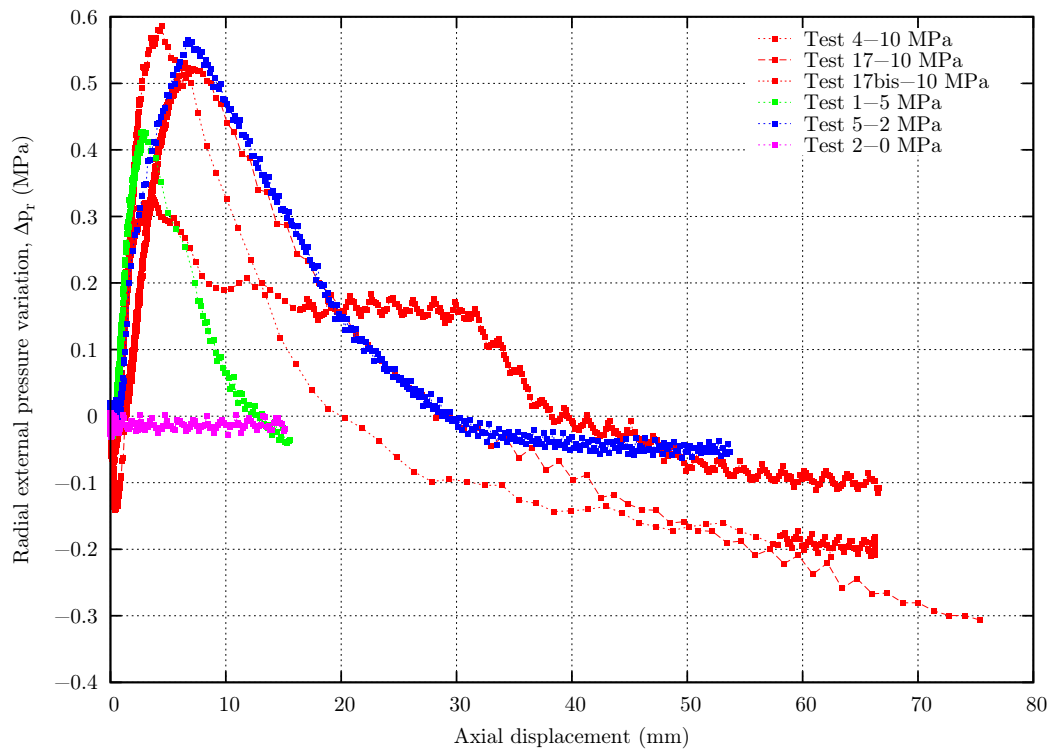


Figure A.2: Radial pressure variation-displacement curves.



**Figure A.3:** Openview of the test 4, 5 and 17bis samples, from top to bottom.

Comments: tests 1 and 2 were stopped at low values of axial displacement. In test 17bis, failure started at the grout-rock interface and switched to the bolt-grout interface after about 33 mm of axial displacement, see the lowest picture in figure A.3.

2. Embedment length  $L = 90$  mm.

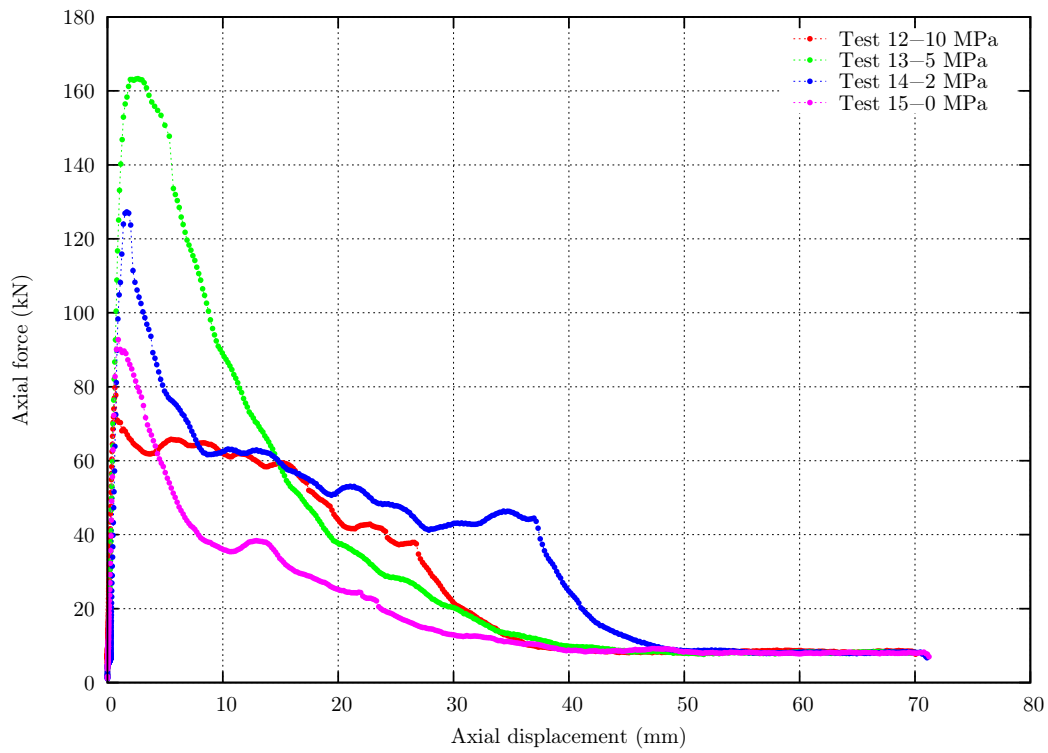


Figure A.4: Load-displacement curves.

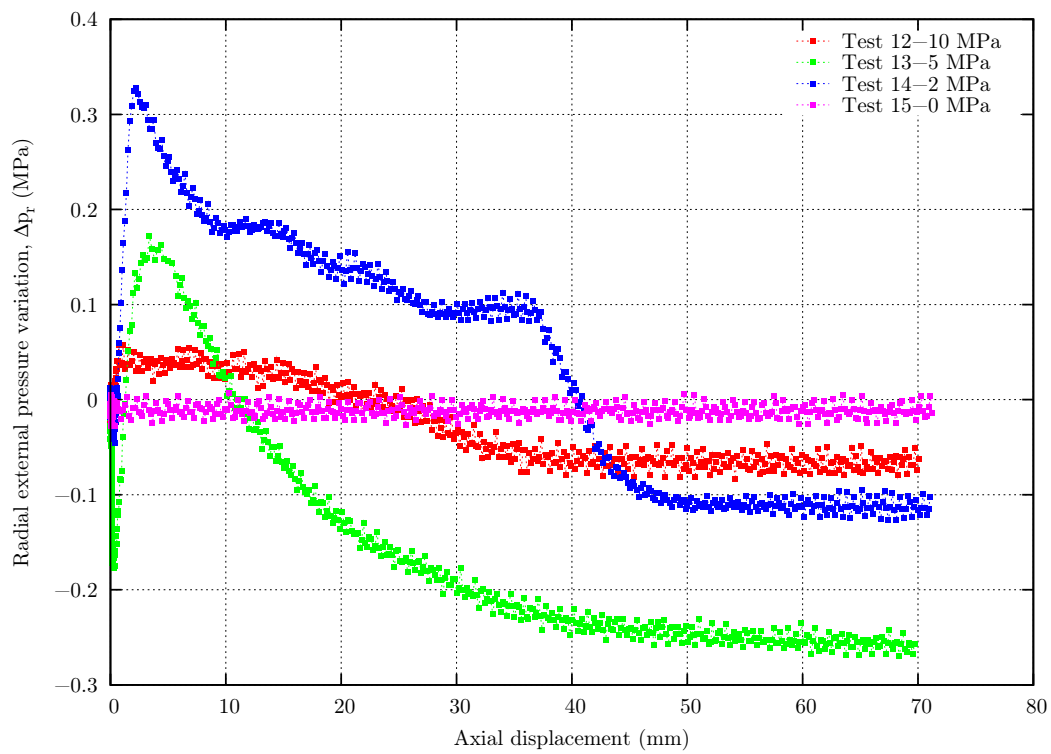


Figure A.5: Radial pressure variation-displacement curves.



**Figure A.6:** Openview of the test 13 sample.



**Figure A.7:** Openview of the tests 12, 14 and 15 samples.

Comments: in tests 12, 14 and 15, failure did not take place at the bolt-grout interface. In test 13, the resin close to the borehole collar was pulled out with the rockbolt.

3. Embedment length  $L = 150$  mm.

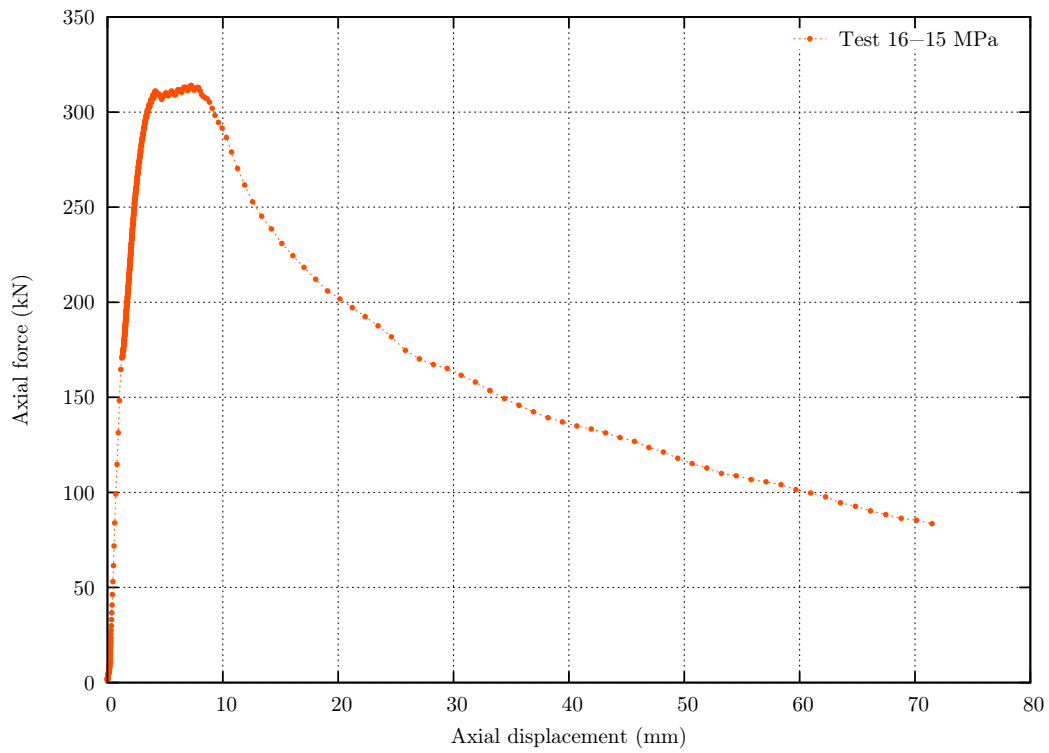


Figure A.8: Load-displacement curve.

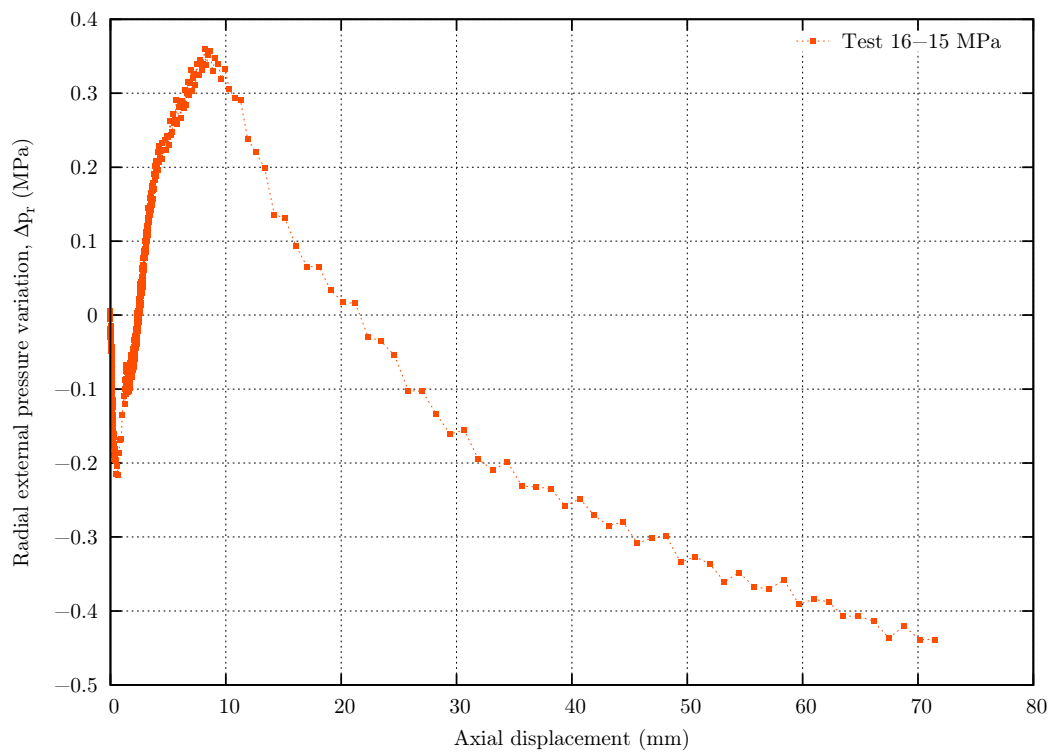
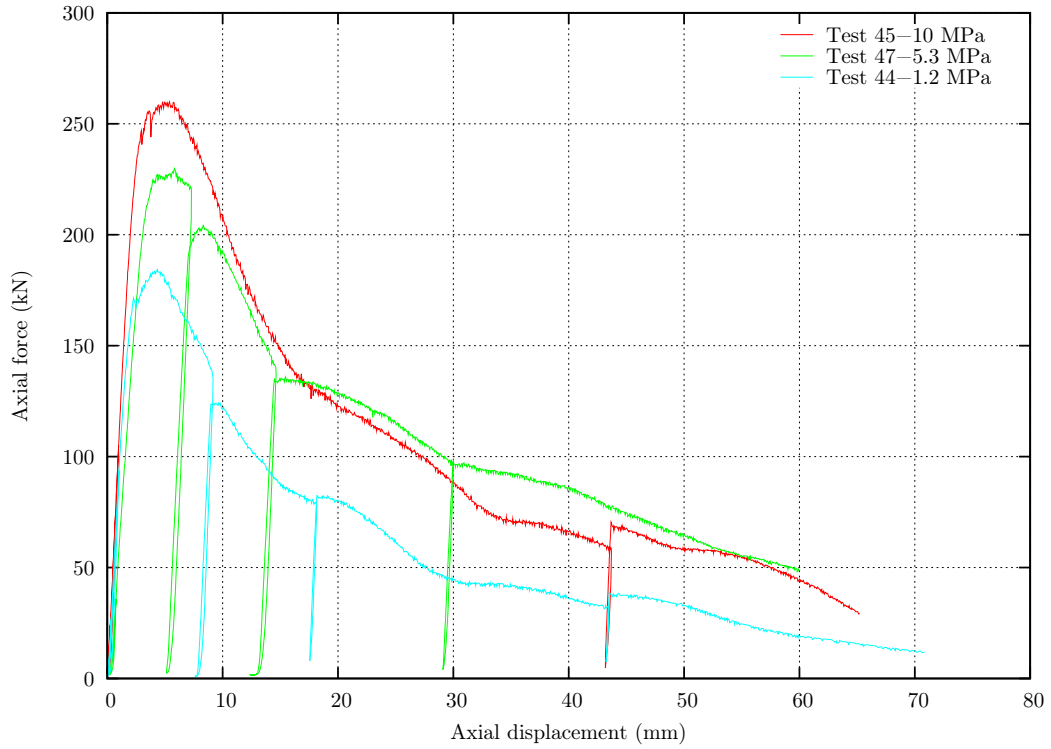


Figure A.9: Radial pressure variation-displacement curve.

**Resin grout. Operating conditions: constant outer radial stiffness  $K_{R_r^+}$ , displacement rate=0.02 mm/s, with end plate, ungrouted tube**

1. Embedment length  $L = 130$  mm.



**Figure A.10:** Load-displacement curves.

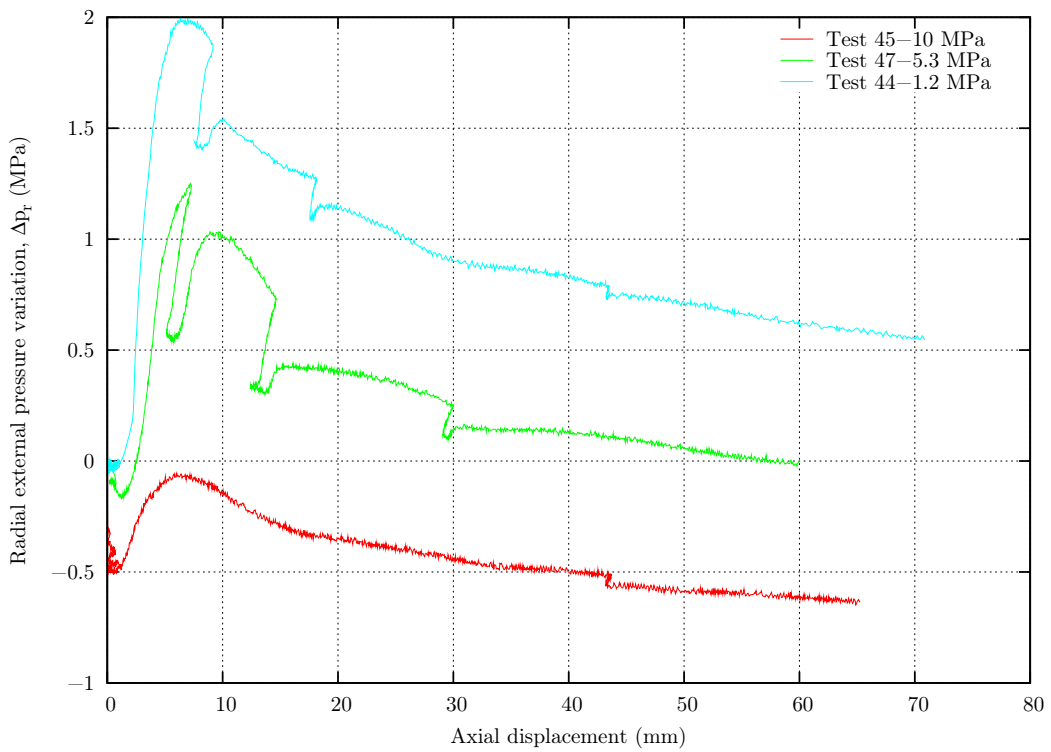


**Figure A.11:** Radial pressure variation-displacement curves.



**Figure A.12:** Openview of the tests 45, 47 and 44 samples, from left to right.

Comments: no radial fractures were identified after test 45. Additionally, in these tests the metallic tube was not grouted to the bolt. Instead, it was constrained by means of a steel 30 mm high ring welded to the rockbolt, on top of the metallic tube. The aim of these tests was to evaluate both the effect of the bolt-metallic tube assembly on the results and the viability of simplifying the samples preparation.

**Resin grout. Operating conditions: constant radial pressure  $p_r$ , displacement rate=0.02 mm/s, with end plate**

1. Embedment length  $L = 130$  mm.

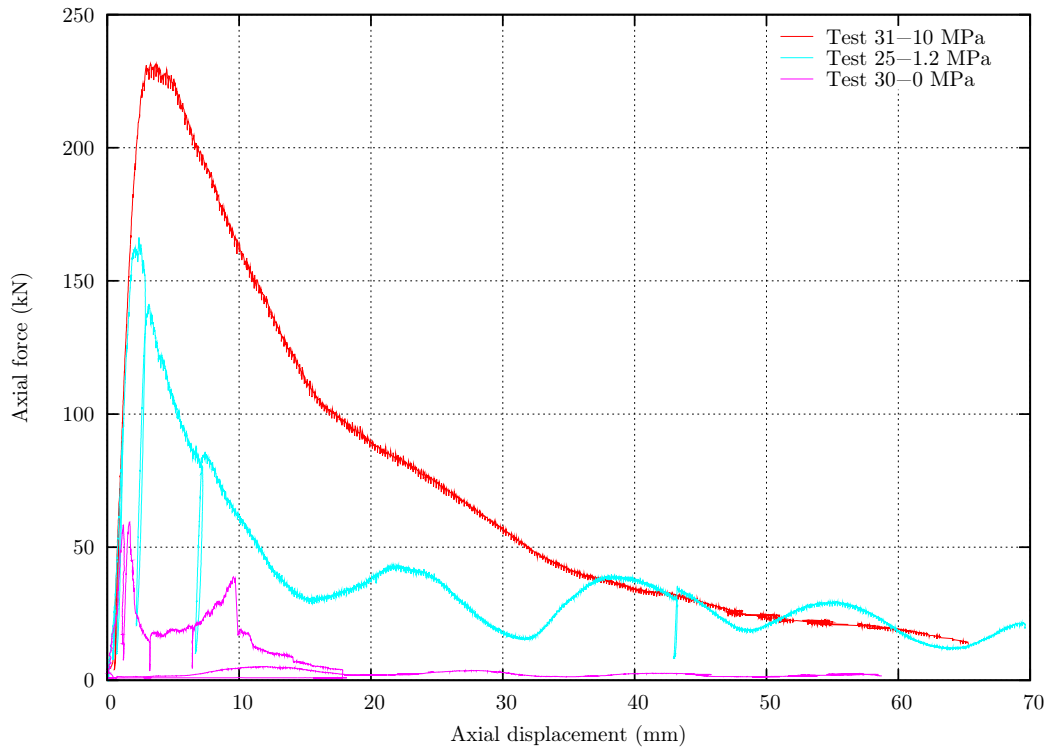


**Figure A.13:** Load-displacement curves.

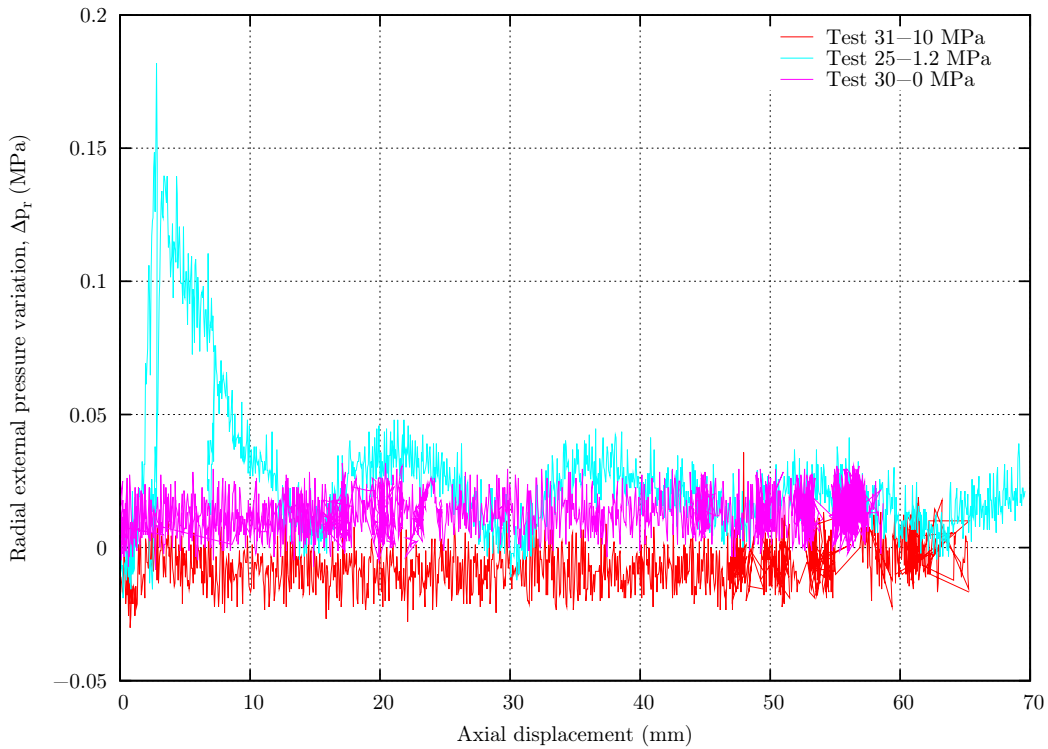


**Figure A.14:** Radial pressure variation-displacement curves.

Comments: in test 30, after about 17 mm of axial displacement, the rockbolt was forced to the initial position ( $Z = 0$ ) and the test was re-started.

2. Embedment length  $L = 90$  mm.

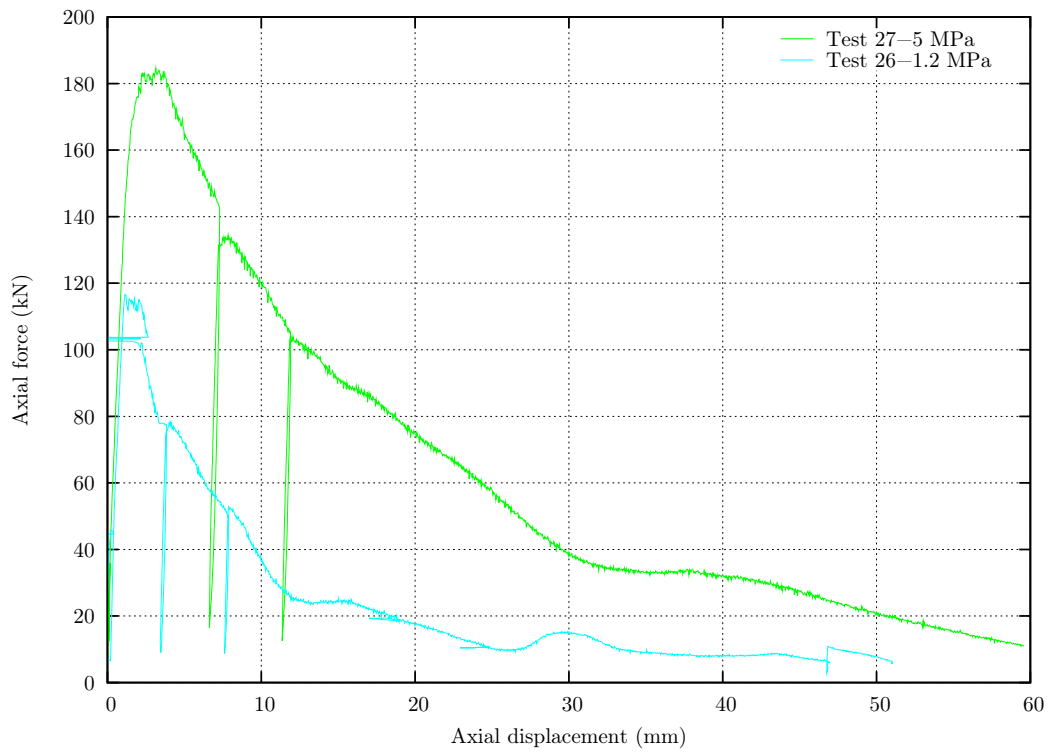


Figure A.15: Load-displacement curves.

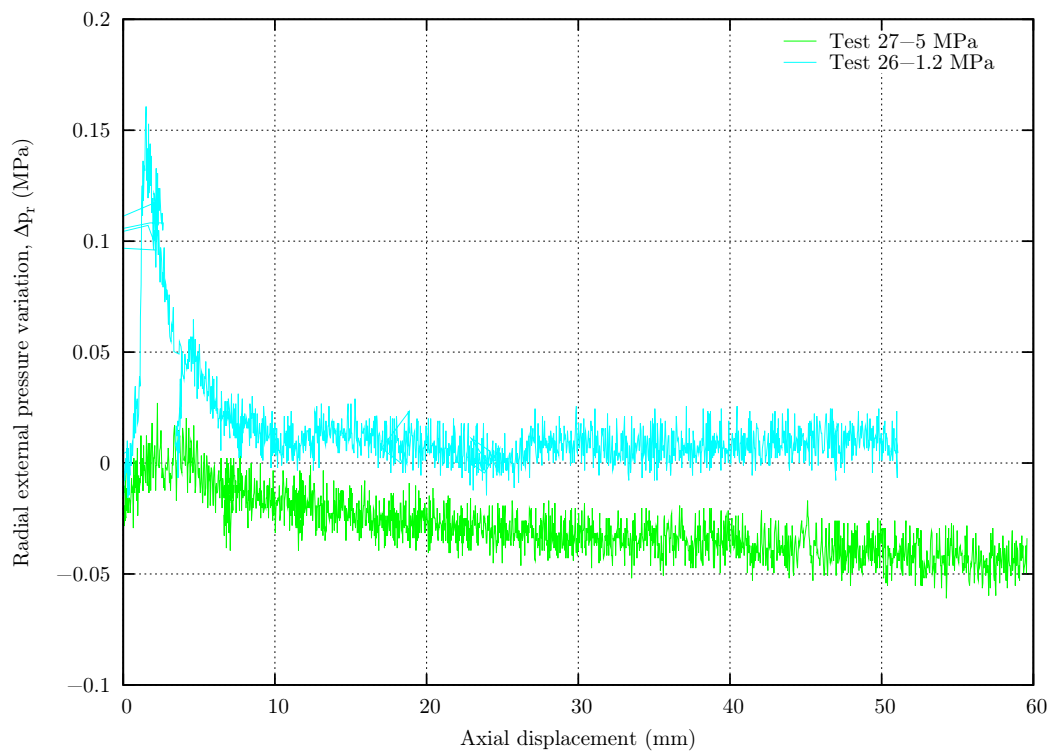
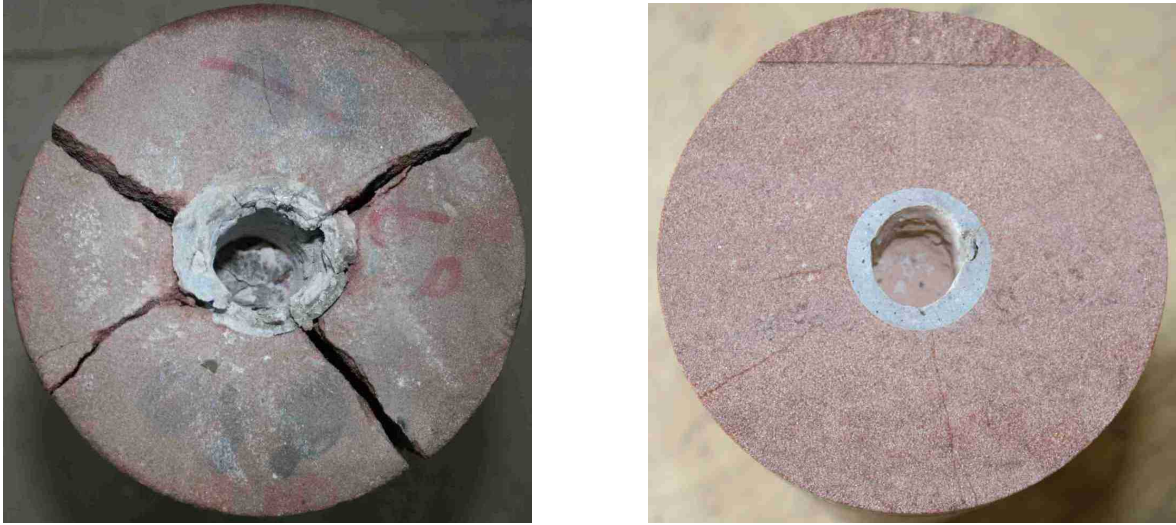


Figure A.16: Radial pressure variation-displacement curves.



**Figure A.17:** View of the tests 26 and 27 samples, from left to right.

Comments: in test 26, the LVDTs sensors recorded unexpected variations of axial displacement (some variations were also recorded in test 31). This could be due to either a malfunction of one or several sensors or the breakage of the rock sample.

Resin grout. Operating conditions: constant radial pressure  $p_r$ , displacement rate=0.02 mm/s, with end plate, ungrouted tube

1. Embedment length  $L = 130$  mm.

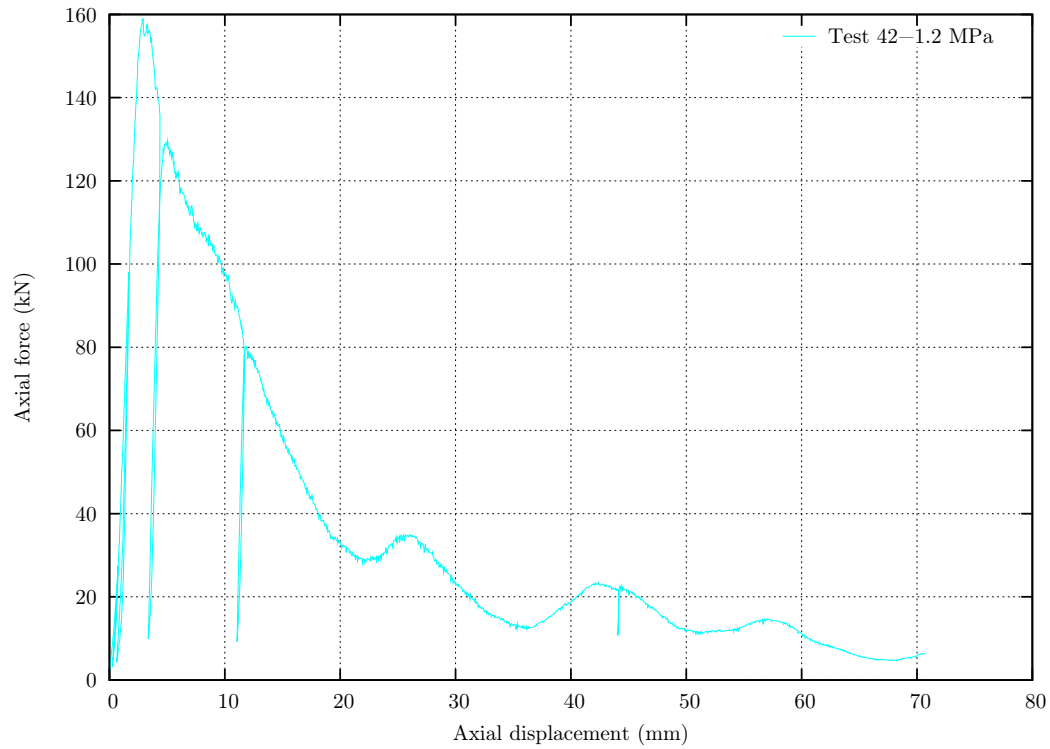


Figure A.18: Load-displacement curves.

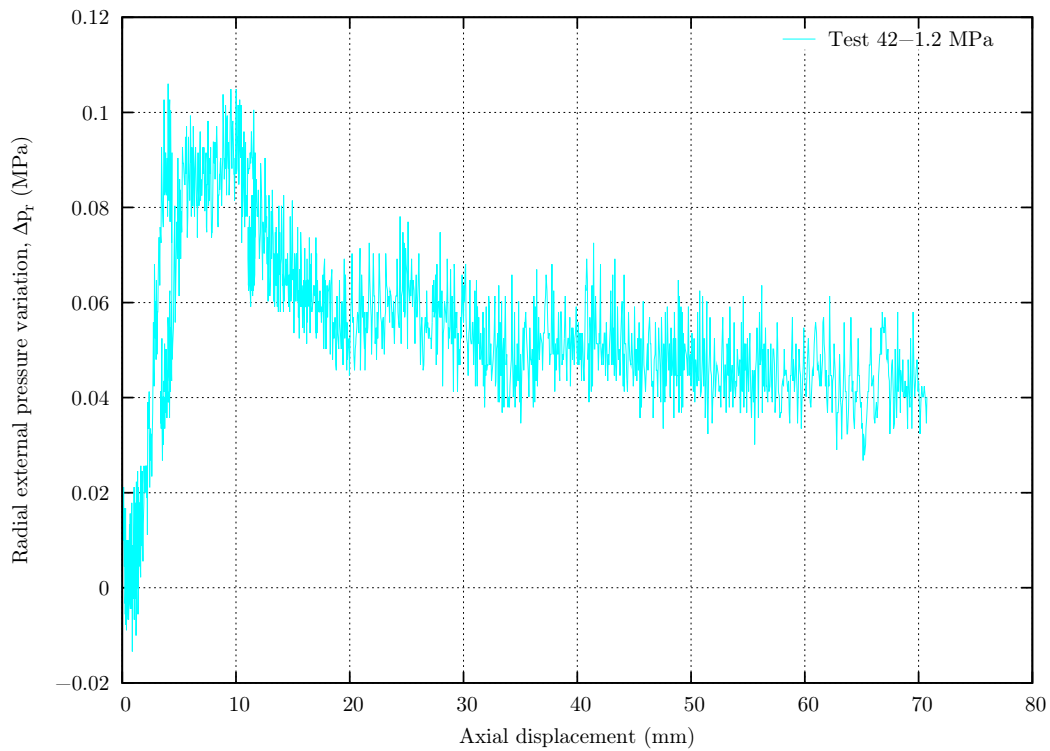


Figure A.19: Radial pressure variation-displacement curves.



**Figure A.20:** View of the test 42 sample.

Comments: in this test, the metallic tube was not grouted to the bolt (a steel ring was welded to the rebar on top of the tube). The comparison of the results, after correction of the free length elongation, with those obtained when the tube is grouted (*cf.* figure [A.13](#), test 25) corroborates the distortion introduced by the bolt-tube assembly and the need for a calibration, in particular in the pre-peak phase.

**Cementitious grouts. Operating conditions: constant outer radial stiffness  $K_{R_r^+}$ , displacement rate=0.84 mm/s, without end plate**

1. Embedment length  $L = 130$  mm.

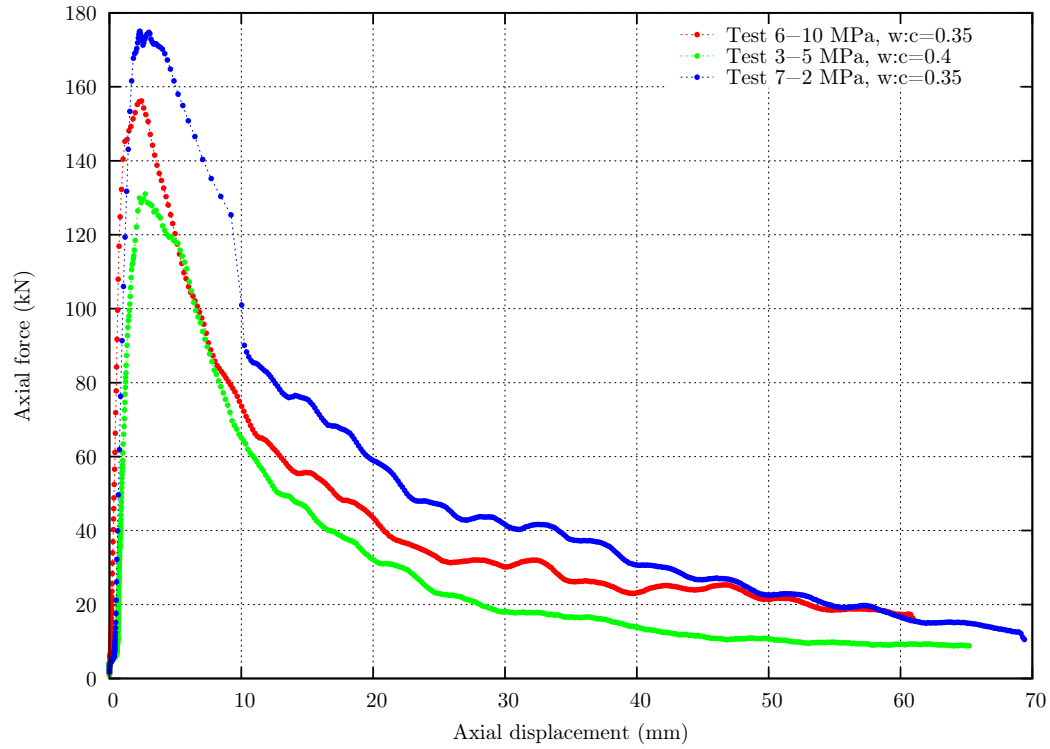


**Figure A.21:** Load-displacement curves.

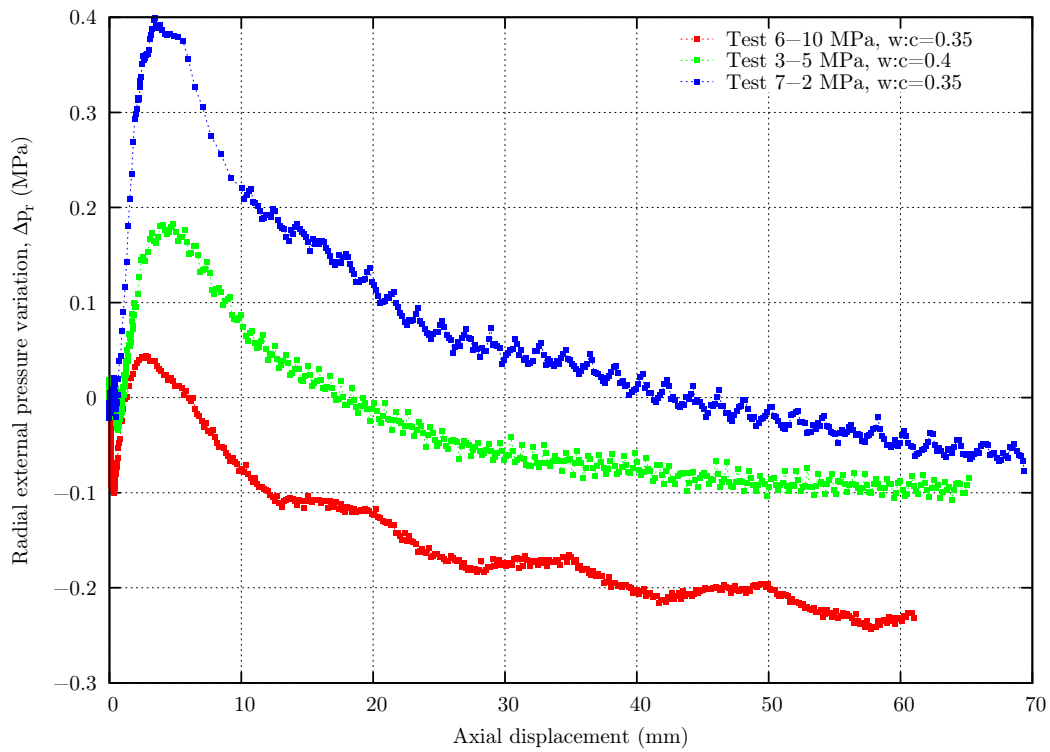


**Figure A.22:** Radial pressure variation-displacement curves.



**Figure A.23:** Openview of the tests 6, 3 and 7 samples, from top to bottom.

Comments: the peak load at  $p_r = 2$  MPa (test 7) was higher than at  $p_r = 10$  MPa (test 6). A third test is necessary to clarify these results, although they are probably related to the greater pressure increase at  $p_r = 2$  MPa.

## A.2 Pull-out tests on FRP rockbolts

Resin grout. Operating conditions: constant outer radial stiffness  $K_{R_r^+}$ , displacement rate=0.84 mm/s, without end plate

1. Embedment length  $L = 130$  mm.

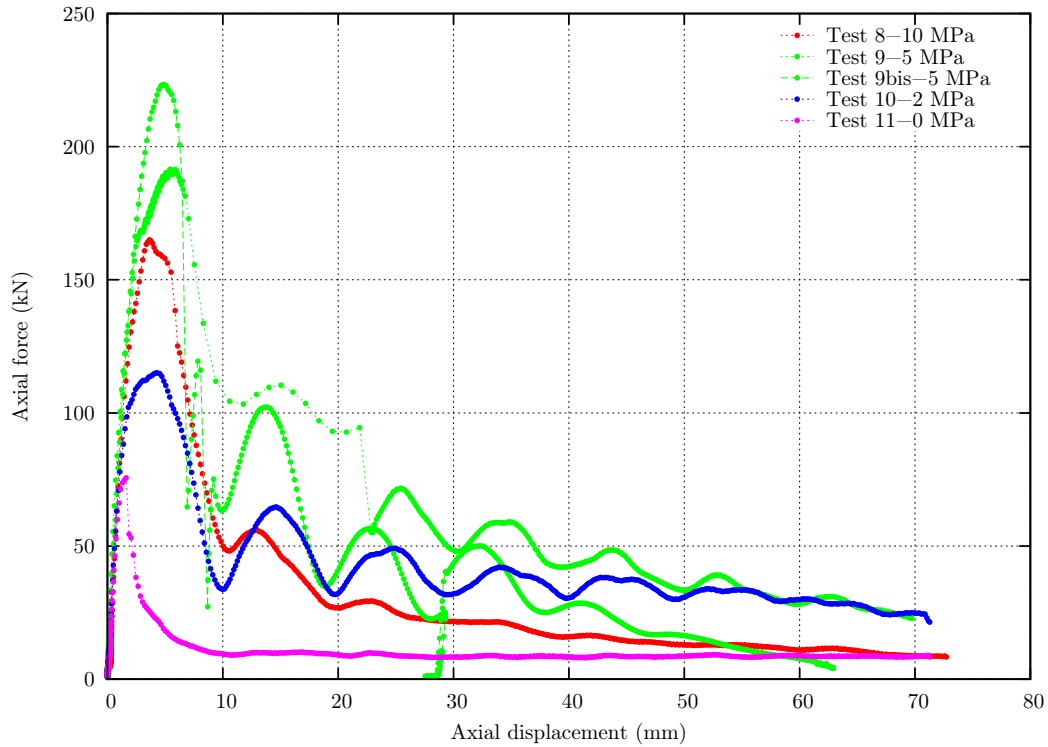


Figure A.24: Load-displacement curves.

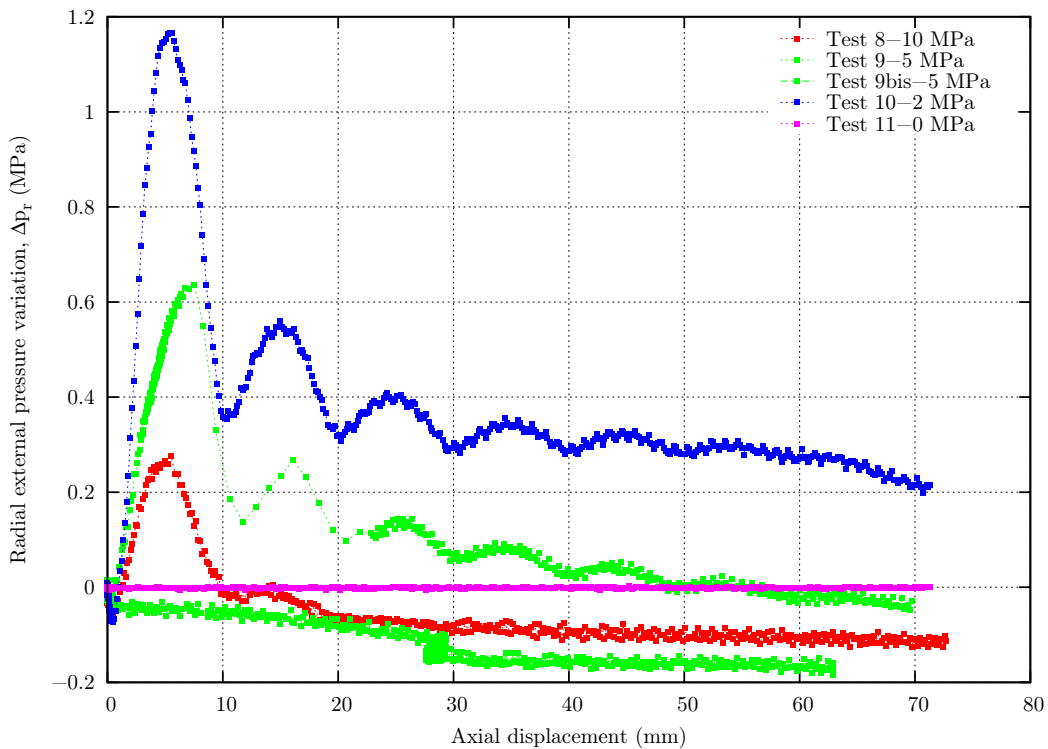
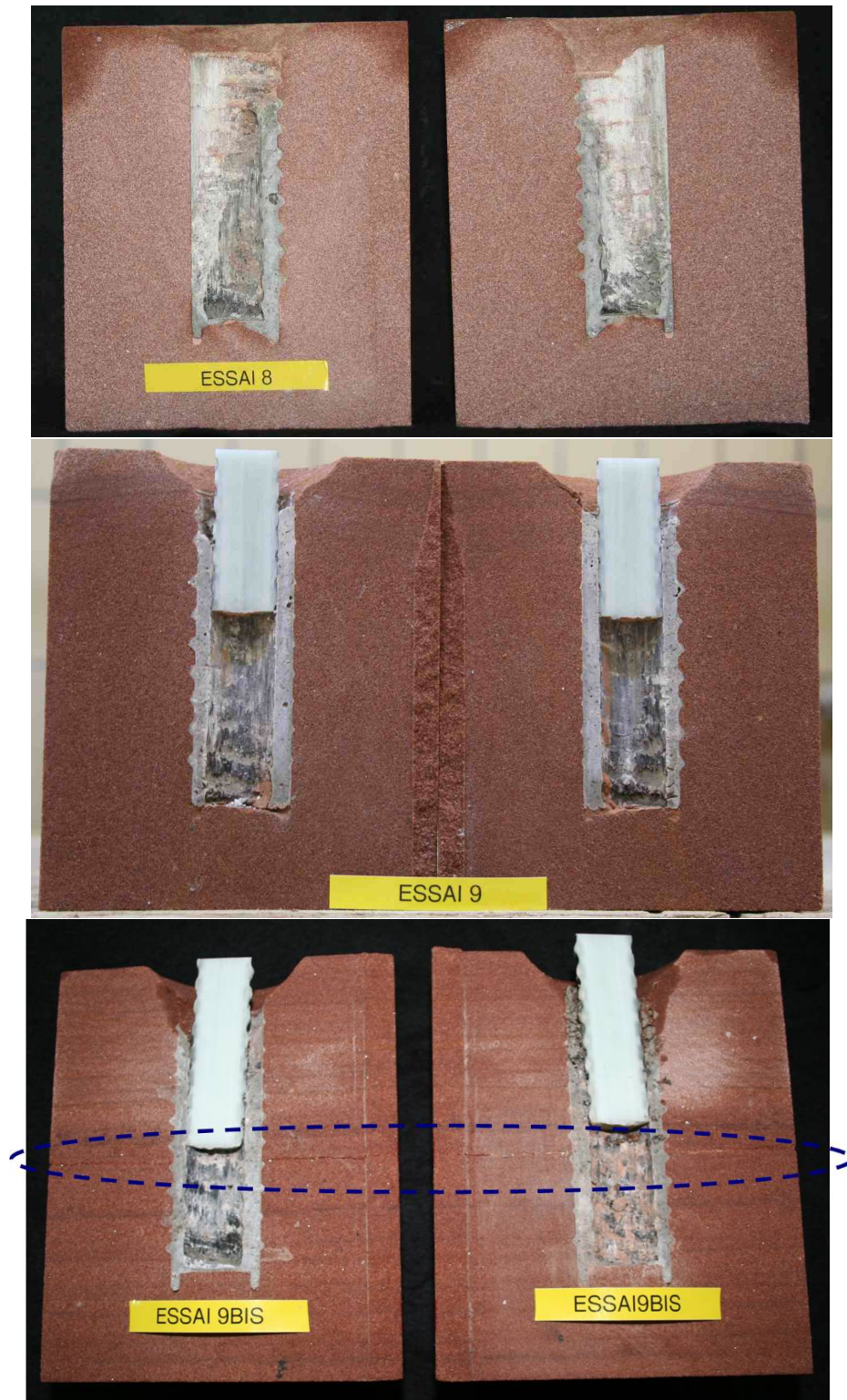


Figure A.25: Radial pressure variation-displacement curves.



**Figure A.26:** Openview of the tests 8, 9 and 9bis samples.

Comments: in test 8, part of the grout was pulled out with the rockbolt, see the uppermost picture in figure A.26. In test 9bis, the bolt external coating failed (like in the calibration tests, cf. figure 3.26). Moreover, the rock and grout annuli showed a horizontal failure plane at  $Z \approx 43$  mm as displayed in the last photo in figure A.26. These facts could explain the load drop in the load-displacement curve and the evolution of the confining pressure. Furthermore, during this test the pump was purposely discharged and recharged at  $W \approx 29$  mm.

2. Embedment length  $L = 90$  mm.

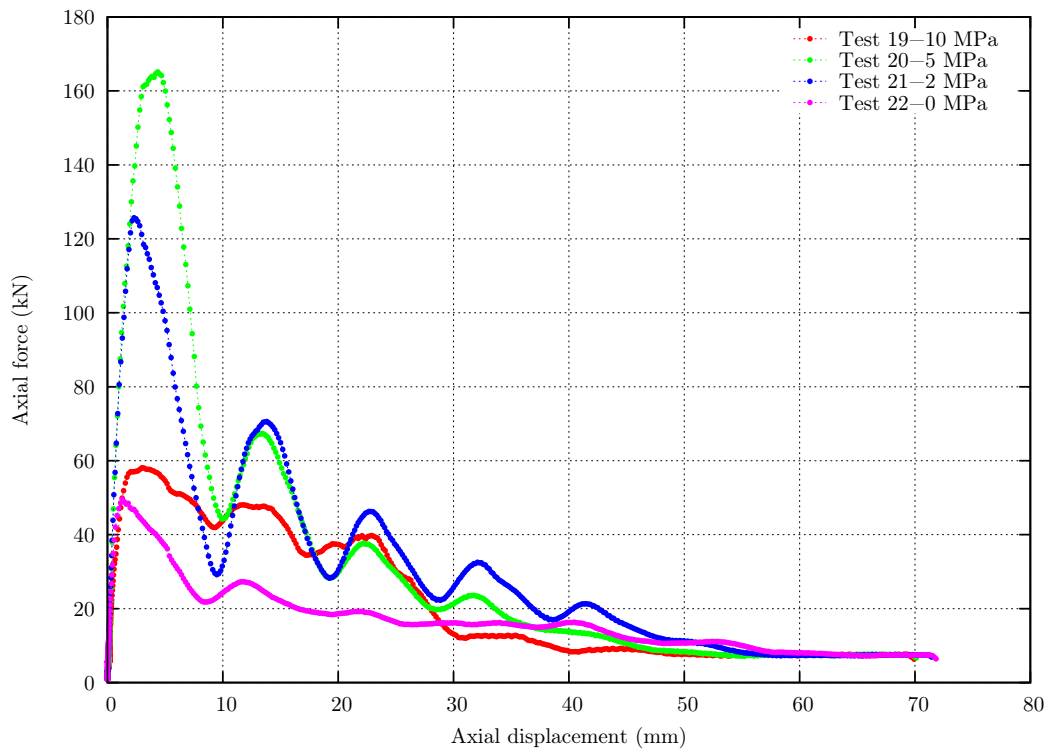


Figure A.27: Load-displacement curves.

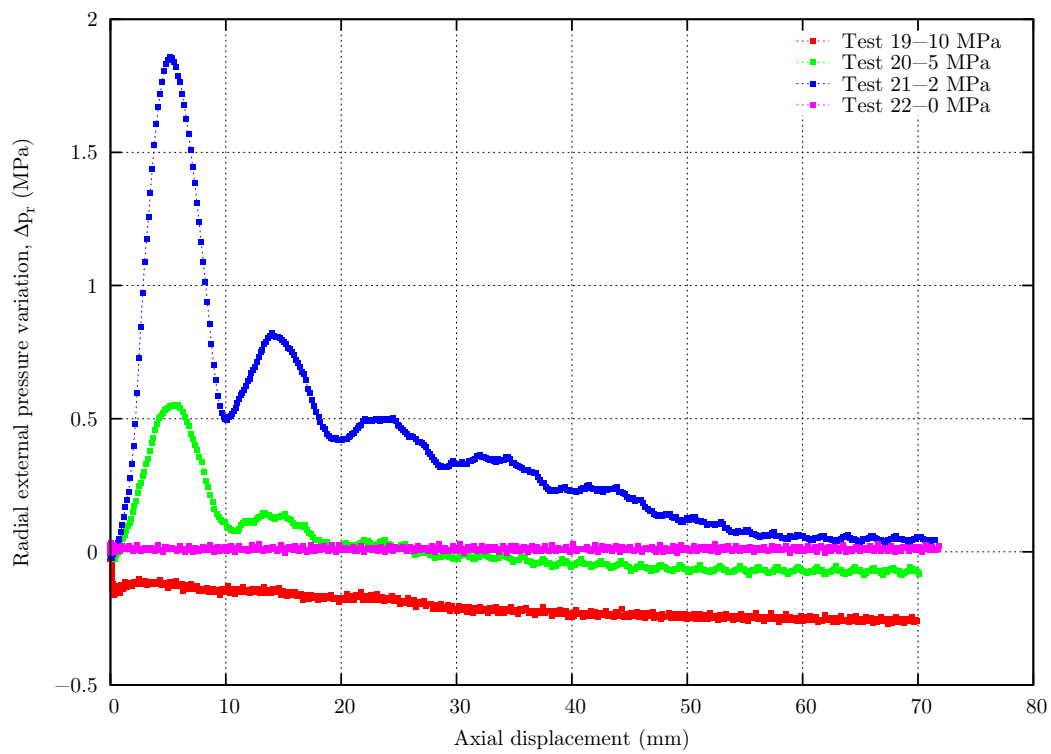


Figure A.28: Radial pressure variation-displacement curves.



Figure A.29: Openview of the test 19 sample.

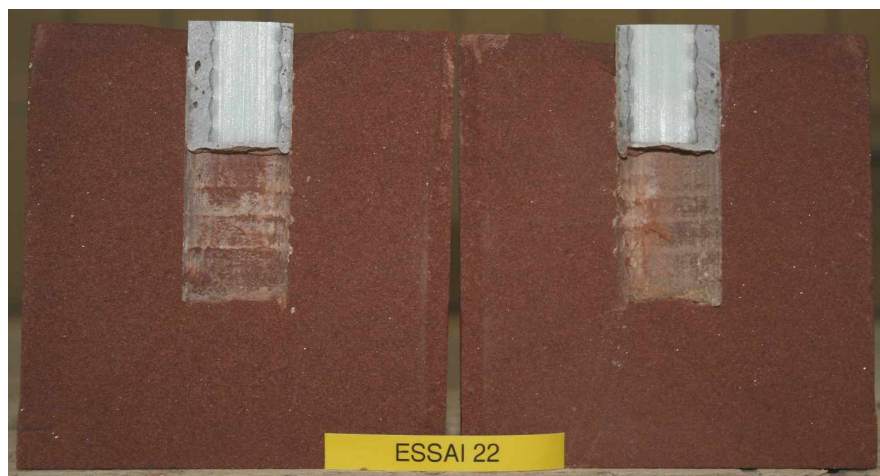
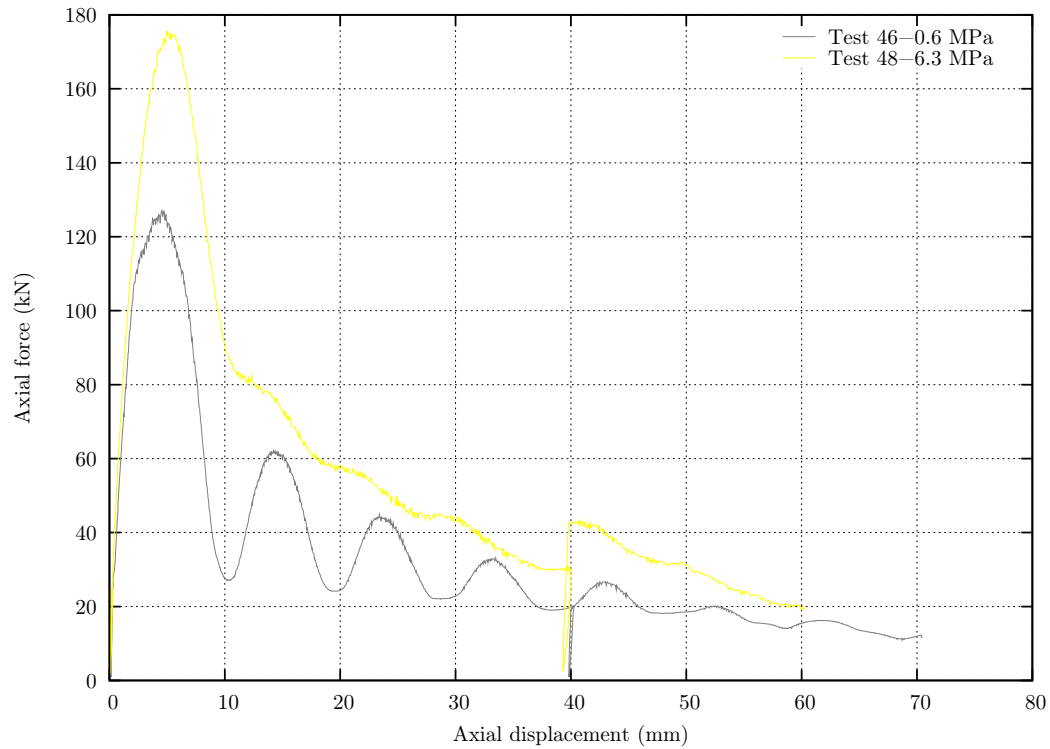


Figure A.30: Openview of the test 22 sample.

Comments: in test 19, failure did not take properly place at the bolt-grout interface. In test 22, decoupling occurred at the grout-rock interface. Tests 20 and 21 are satisfactory.

**Resin grout. Operating conditions: constant outer radial stiffness  $K_{R_r^+}$ , displacement rate=0.02 mm/s, with end plate**

1. Embedment length  $L = 90$  mm.



**Figure A.31:** Load-displacement curves.

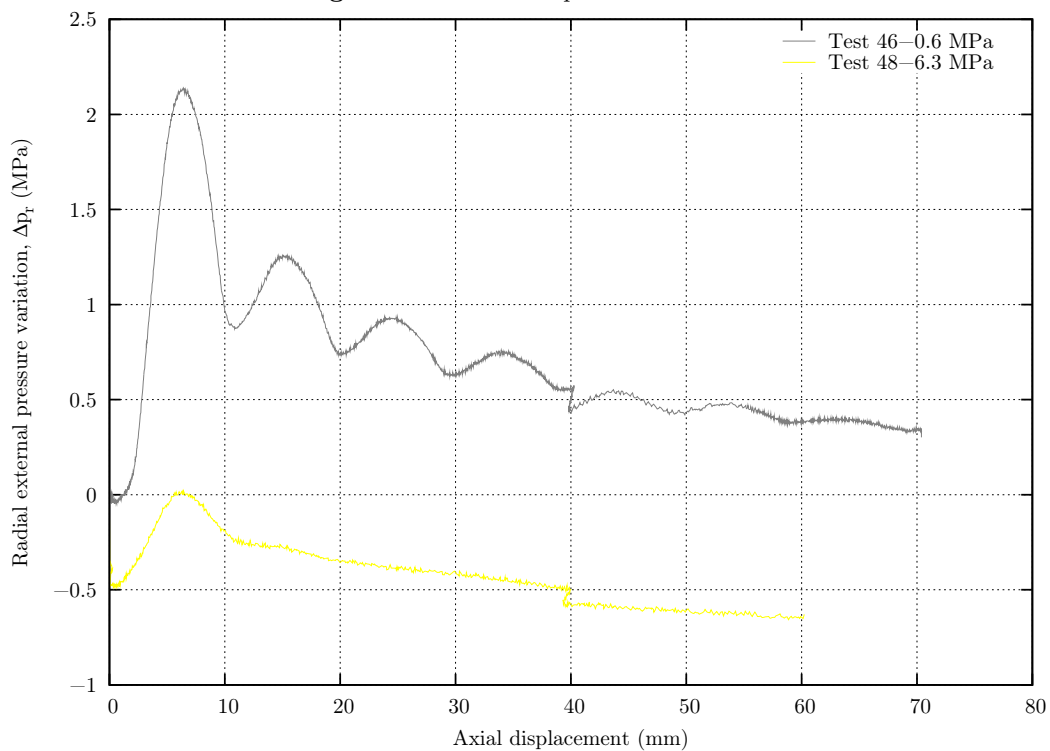


**Figure A.32:** Radial pressure variation-displacement curves.

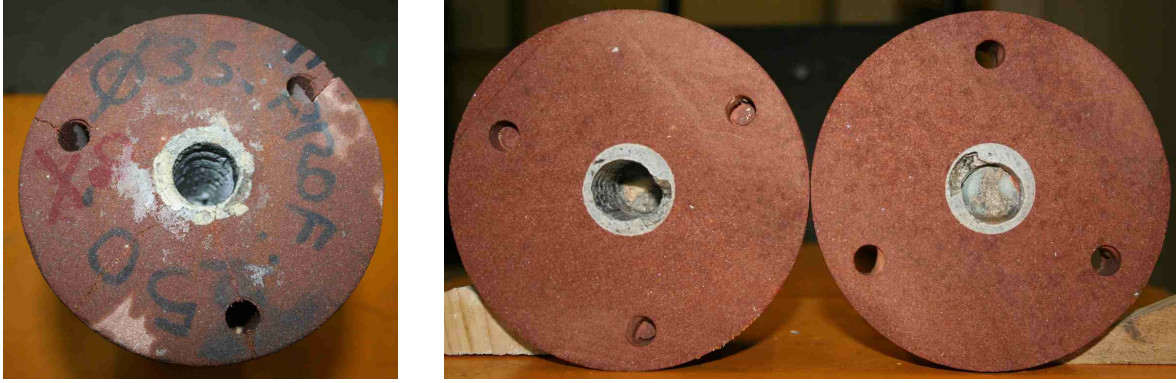


**Figure A.33:** View of the tests 46 and 48 samples, from left to right.

Comments: while the annuli were radially split after test 46, they were intact after test 48.

**Resin grout. Operating conditions: constant radial pressure  $p_r$ , displacement rate=0.02 mm/s, with end plate**

1. Embedment length  $L = 90$  mm.

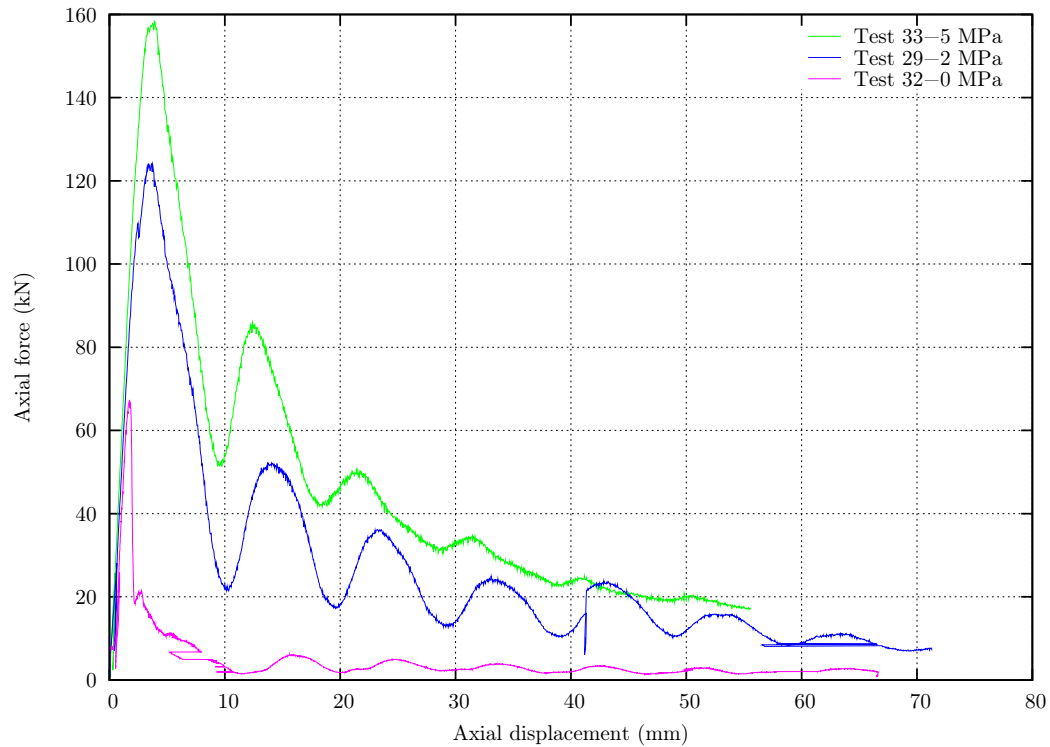


**Figure A.34:** Load-displacement curves.

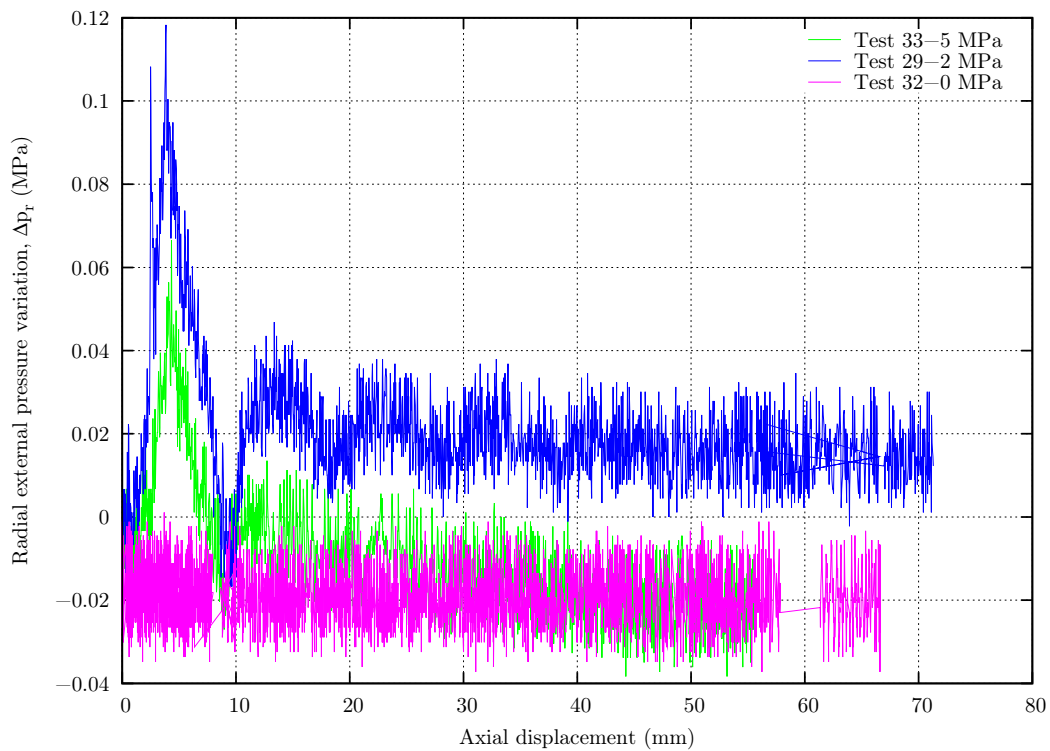


**Figure A.35:** Radial pressure variation-displacement curves.



**Figure A.36:** View of the tests 32, 29 and 33 samples, from left to right.

Comments: in test 32, the LVDTs sensors recorded unexpected variations of axial displacement. Like in test 26, this could be due to either a malfunction of such sensors or the breakage of the rock core.

**Cementitious grouts. Operating conditions: constant outer radial stiffness  $K_{R_r^+}$ , displacement rate=0.84 mm/s, without end plate**

1. Embedment length  $L = 130$  mm.

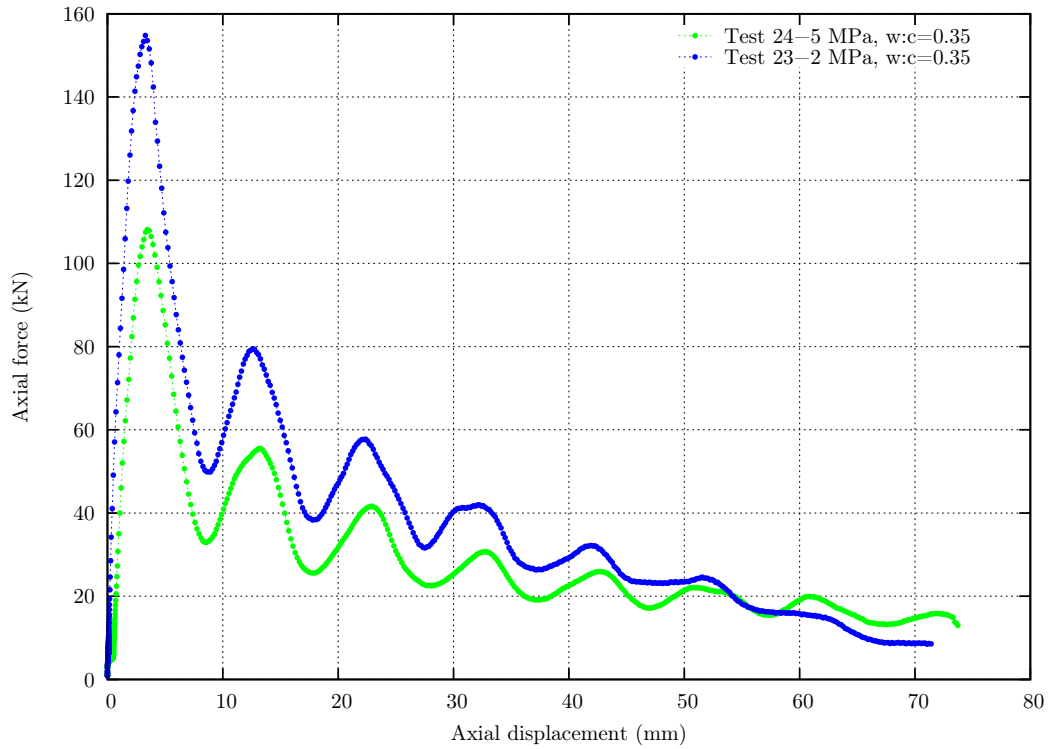


**Figure A.37:** Load-displacement curves.

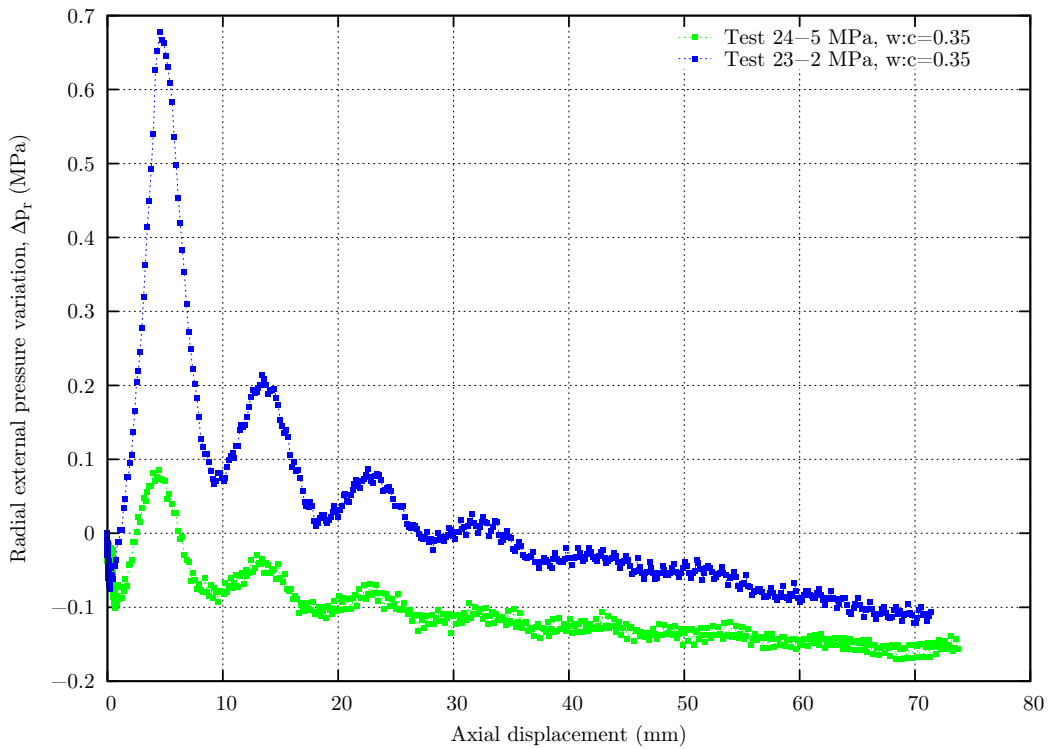


**Figure A.38:** Radial pressure variation-displacement curves.

Comments: as with HA25 bolts, the peak load at  $p_r = 2$  MPa (test 23) was higher than at  $p_r = 5$  MPa (test 24). This is probably related to the greater pressure increase at  $p_r = 2$  MPa.

**Cementitious grouts. Operating conditions: displacement rate=0.02 mm/s, without end plate. Instrumented rock samples**

1. Embedment length  $L = 130$  mm. Strain gauges at  $Z = 30$  mm, without confinement.

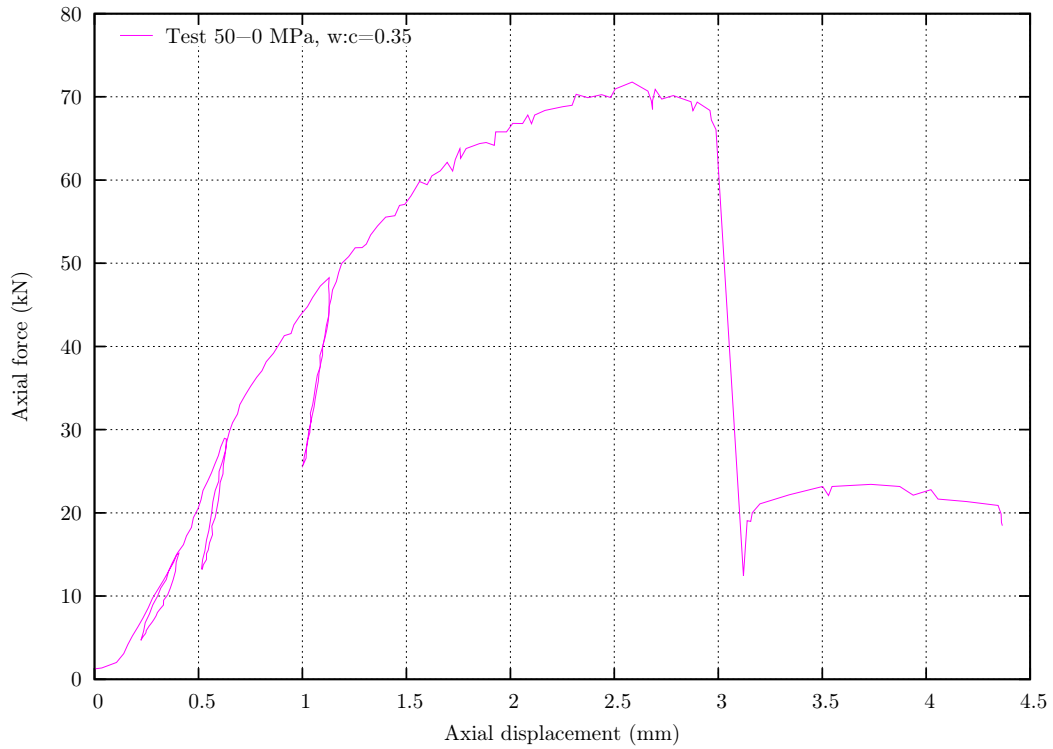


**Figure A.39:** Load-displacement curve.

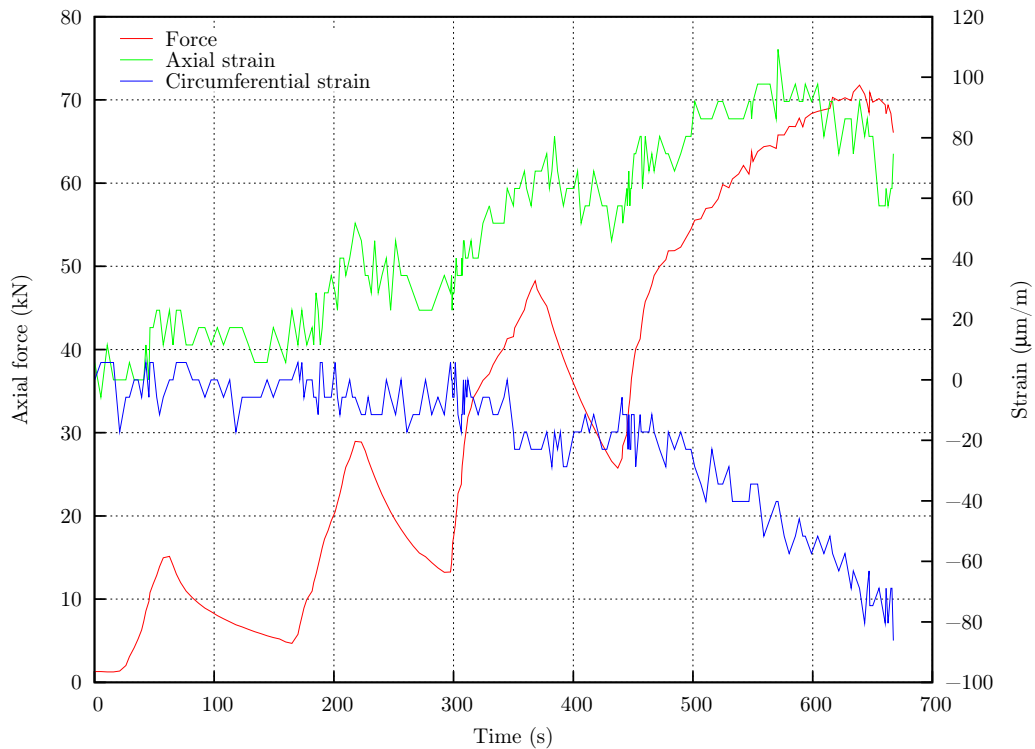


**Figure A.40:** Force and strain during the test.

2. Embedment length  $L = 90$  mm. Strain gauges at  $Z = 60$  mm, without confinement.

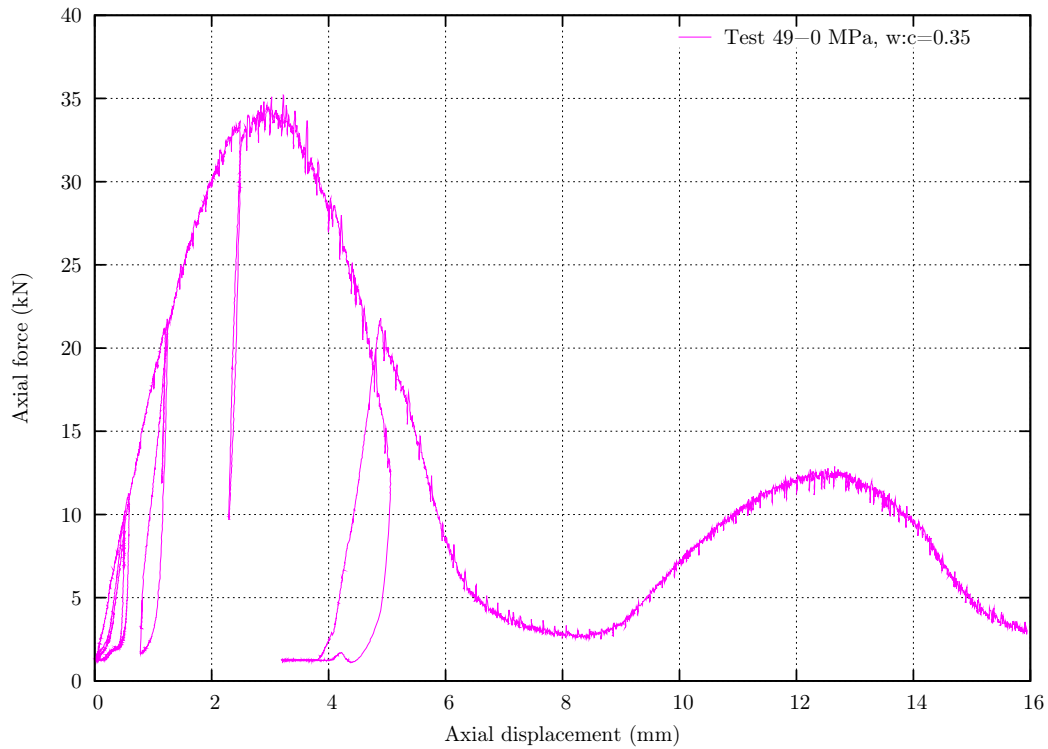


**Figure A.41:** Load-displacement curve.

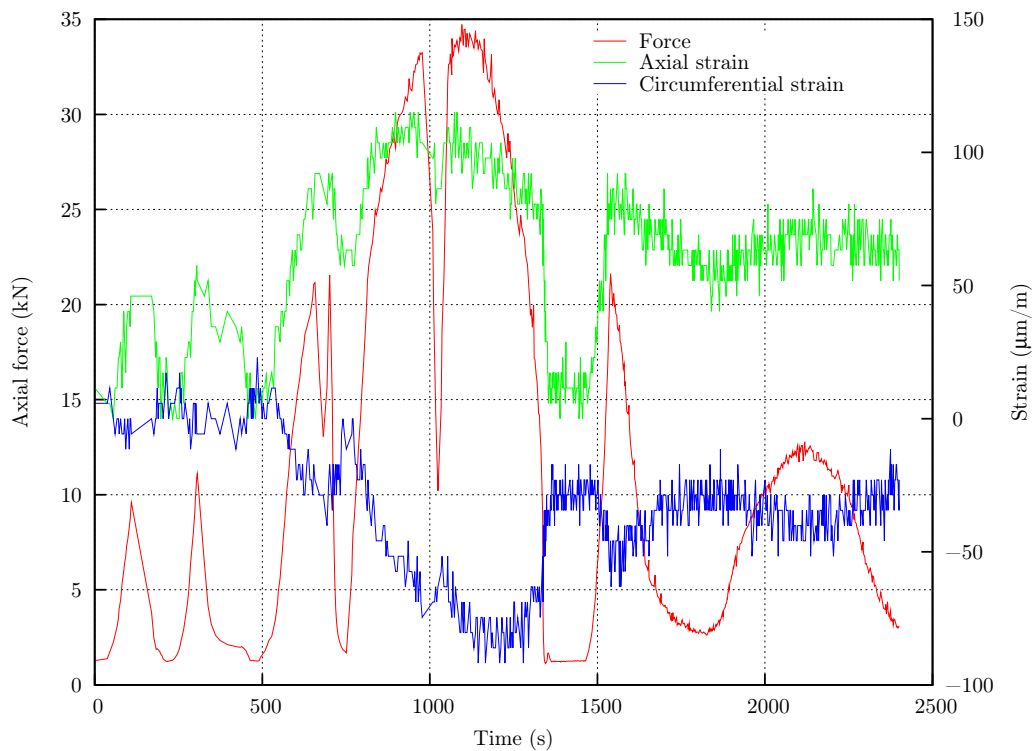


**Figure A.42:** Force and strain during the test.

Comments: two pairs of diametrically opposed axial and circumferential strain gauges were mounted on two rock samples. The embedment lengths were  $L = 90$  mm and  $L = 130$  mm. In the first case, the gauges were installed at  $Z = 60$  mm, while in the second case they were installed at  $Z = 30$  mm. The aims of these two tests were to investigate the rock sample deformation during the pull-out test and to compute the radial displacement of the rock sample,  $u_{rr}$ , through equation (2.13), in order to validate the simplified analytical approach adopted in this thesis (assumption of a generalized plane stress state). The results show very interesting facts: in the case  $L = 90$  mm, the annuli did not split radially and the measured circumferential strain was beyond the critical theoretical hoop strain to cause failure,  $\varepsilon_{\theta, \text{crit}} \approx 3 \cdot 10^{-5}$ . In the case  $L = 130$  mm, the annuli (grout and rock) fully split radially at the peak load and the strain gauges, which were closer to the borehole end, announced consistent values with respect to the analytical predictions. Figure A.43 displays both samples after the tests. From these results (in agreement with the FEM simulations), it has been concluded that the reaction force has a local, but not negligible confining effect in the vicinity of the borehole collar. On the one hand, this effect prevents the annuli from splitting when short lengths are used, but on the other hand, the simplified theoretical approach is less accurate. For longer lengths, the local effect is reduced and the theoretical predictions match the experimental data beyond the locally influenced zone.

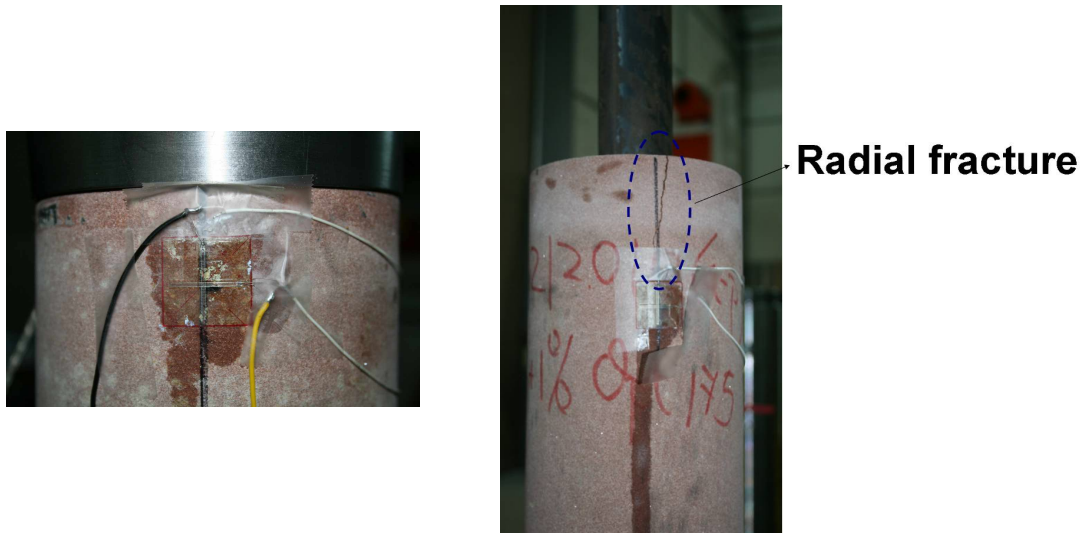


**Figure A.43:** View of the tests 49 and 50 samples, from left to right.

Finally, it should be noticed that in test 49, the displacement measurements during the loading-unloading cycles are not accurate because the LVDTs support leaned directly on the hydraulic jack; in a normal set-up, the LVDTs support and the metallic tube are interdependent.

### A.3 Pull-out tests on smooth steel bars

Resin grout. Operating conditions: constant radial pressure  $p_r$ , displacement rate=0.02 mm/s, with end plate

1. Embedment length  $L = 130$  mm.

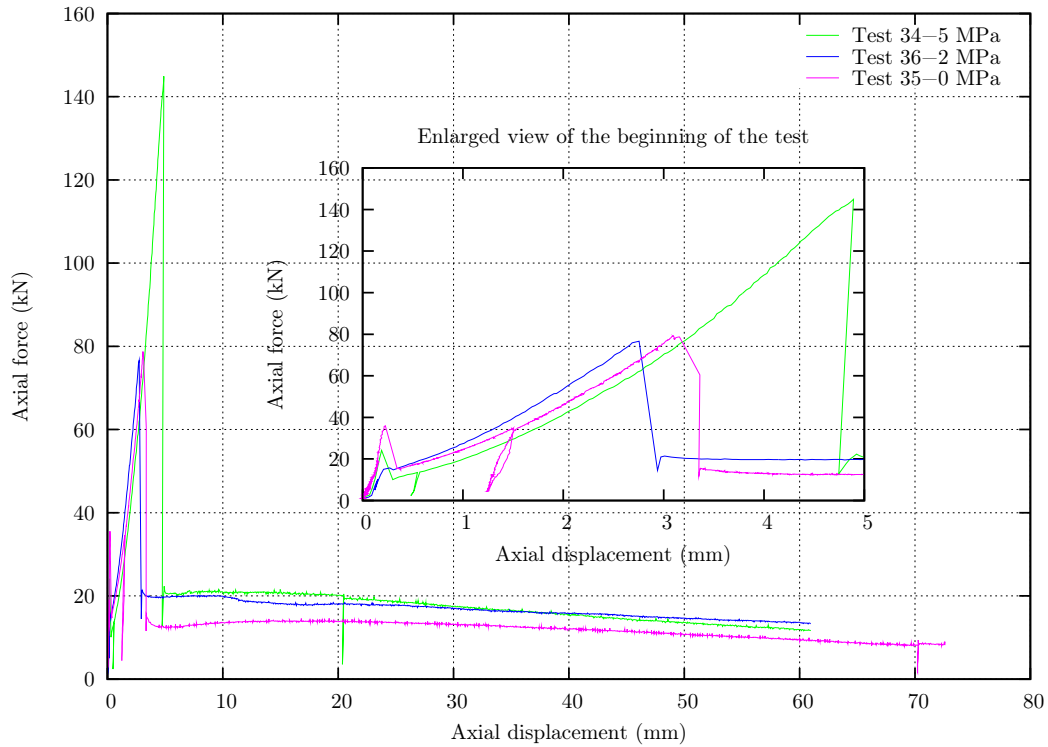


Figure A.44: Load-displacement curves.

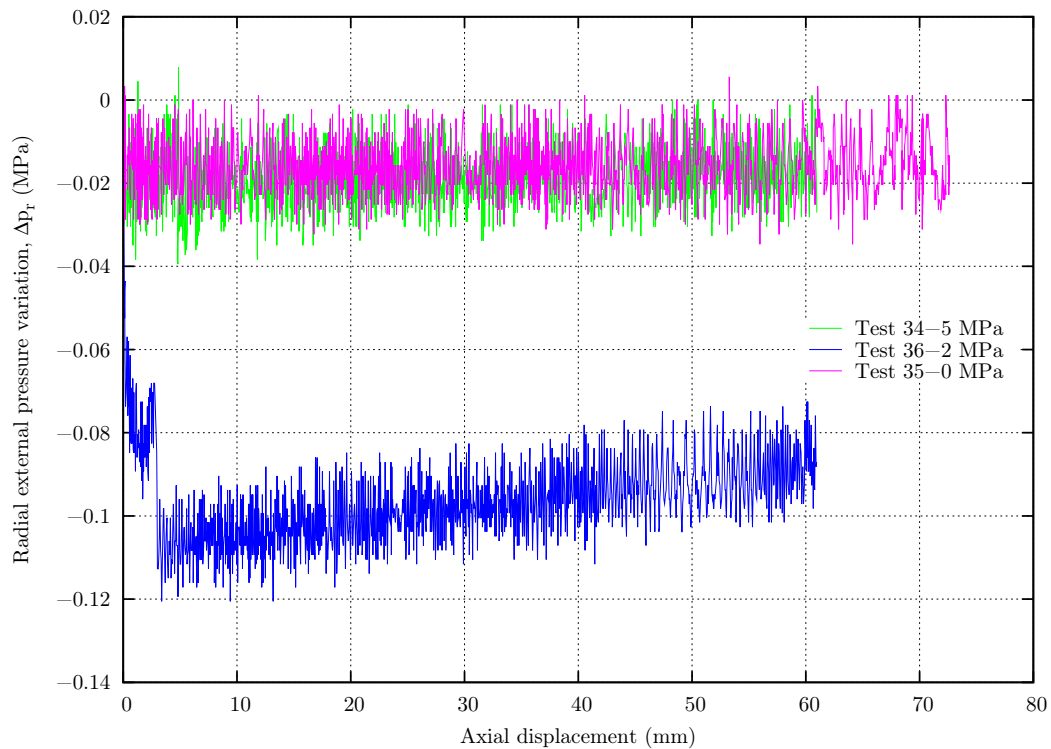
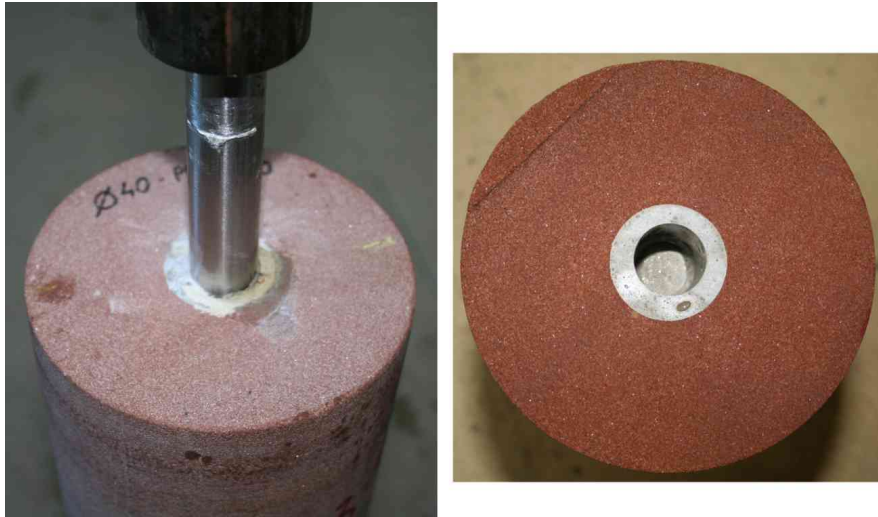


Figure A.45: Radial pressure variation-displacement curves.



**Figure A.46:** View of the test 36 sample.

Comments: all the tested samples were intact (*i.e.*, without radial fractures) after the tests.

2. Embedment length  $L = 100$  mm, bolt radius  $R_b = 10$  mm, borehole radius  $R_g = 15$  mm.

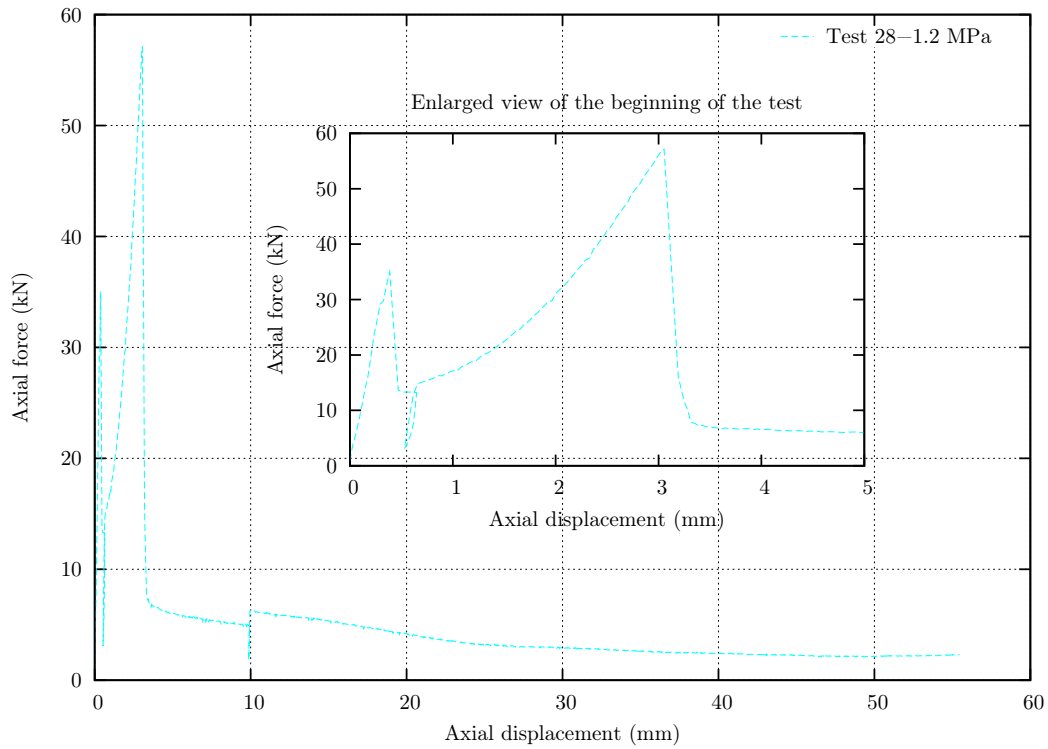


Figure A.47: Load-displacement curves.

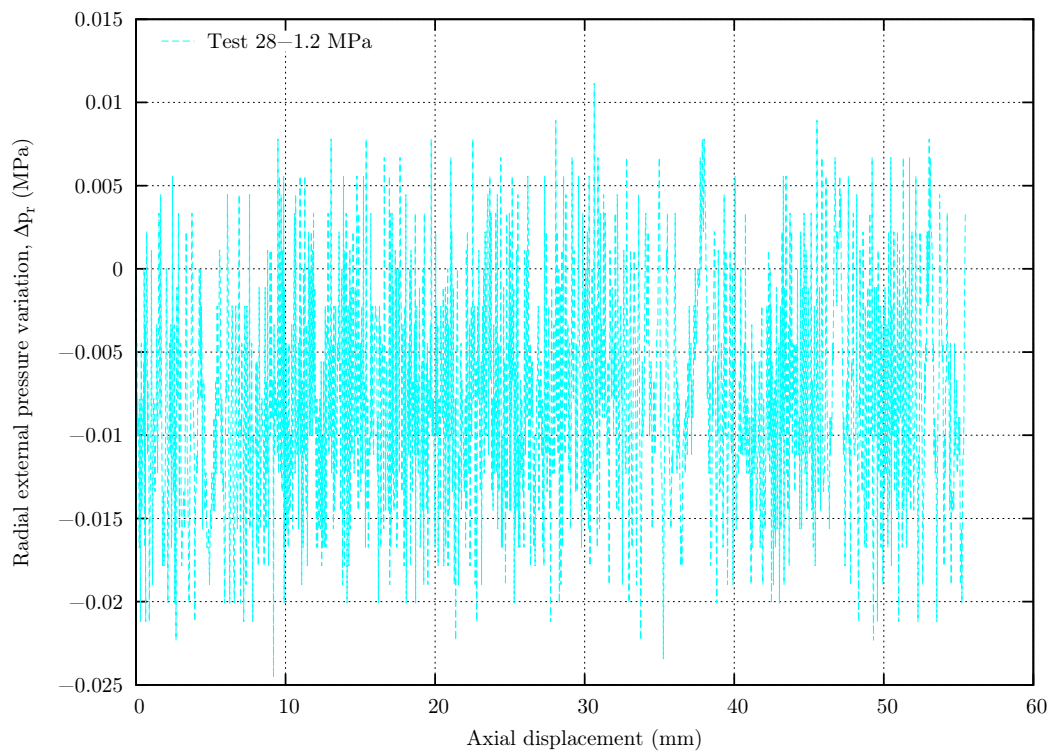
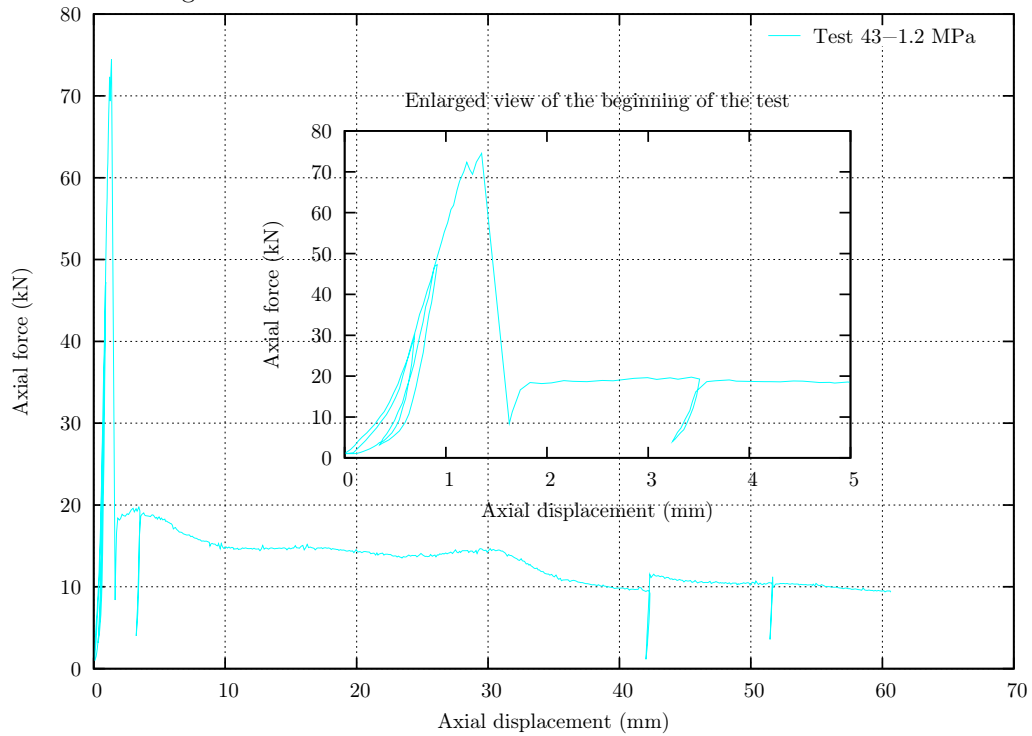


Figure A.48: Radial pressure variation-displacement curves.

**Resin grout. Operating conditions: constant radial pressure  $p_r$ , displacement rate=0.02 mm/s, with end plate, ungrouted tube**

1. Embedment length  $L = 130$  mm.



**Figure A.49:** Load-displacement curves.

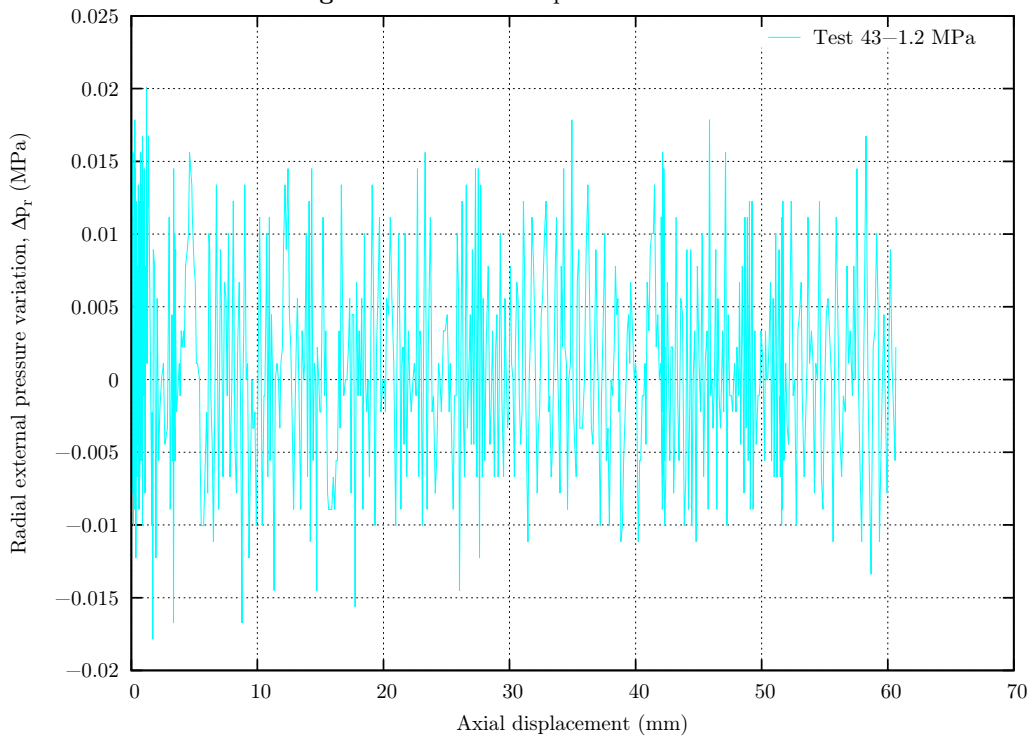


**Figure A.50:** Radial pressure variation-displacement curves.

Comments: the metallic tube was not grouted to the bar (use of a steel ring). It can be seen that the first peak of the load-displacement curves in figure A.44 (that corresponds to the decoupling process at the bar-adhesive interface inside the tube) does not take place. The peak load and the post-peak phase are comparable to those of tests 34-36, shown in figure A.44.

## **B Laboratory pull-out test campaign on cablebolts**

Five tests have been conducted on 23 mm diameter Flexible cablebolts. The principal aim of these tests is to verify the effectiveness of the designed tools to prevent the unscrewing phenomenon. All the tests have been carried out using a resin-based grout and a confining pressure  $p_r = 2.7$  MPa. As for the operating conditions, the displacement rate is 0.02 mm/s and the tests have been conducted at constant confinement. The end plate has been used in all these tests.

The first two tests are not comparable to the others because they were not conducted in equivalent conditions: in fact, these tests were executed without a barrel and wedge system installed on the metallic tube, which brought about some slip inside this tube, thereby distorting the results.

## B.1 Pull-out tests on Flexible cablebolts

1. Embedment length,  $L = 325$  mm

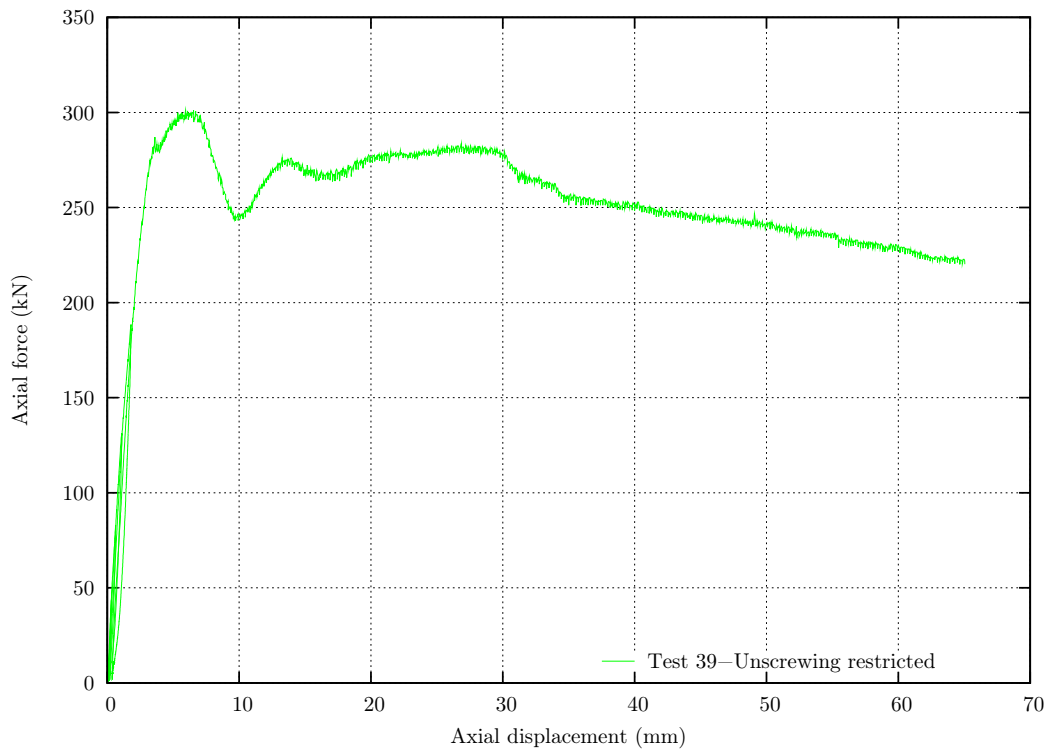


Figure B.1: Load-displacement curve.

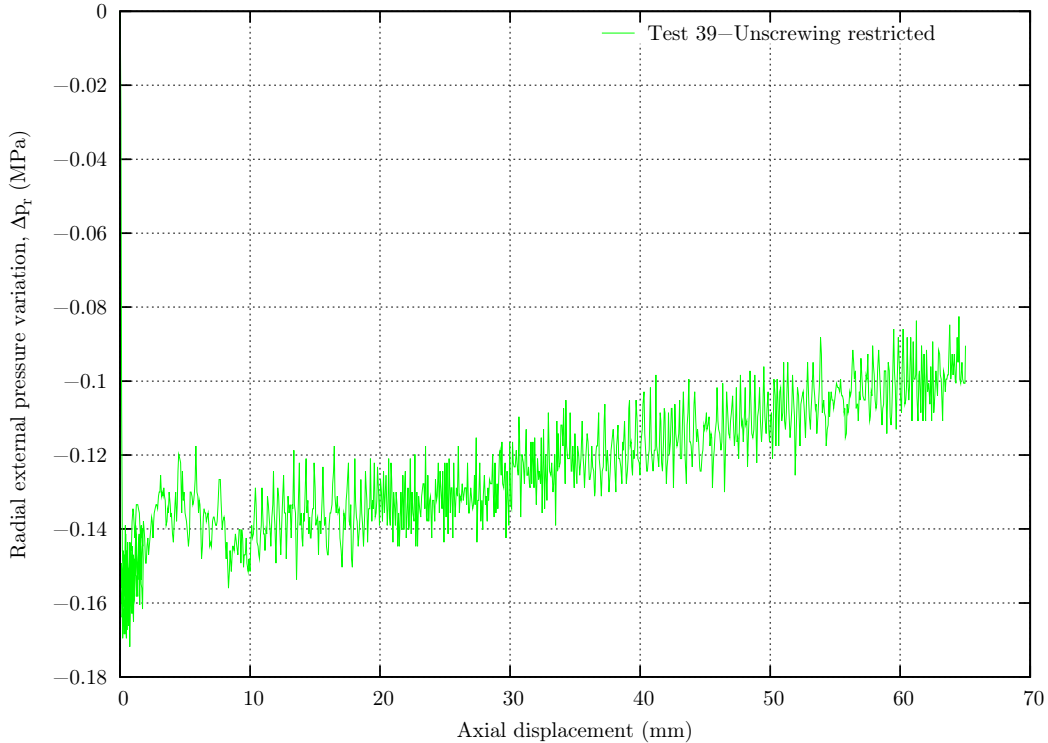
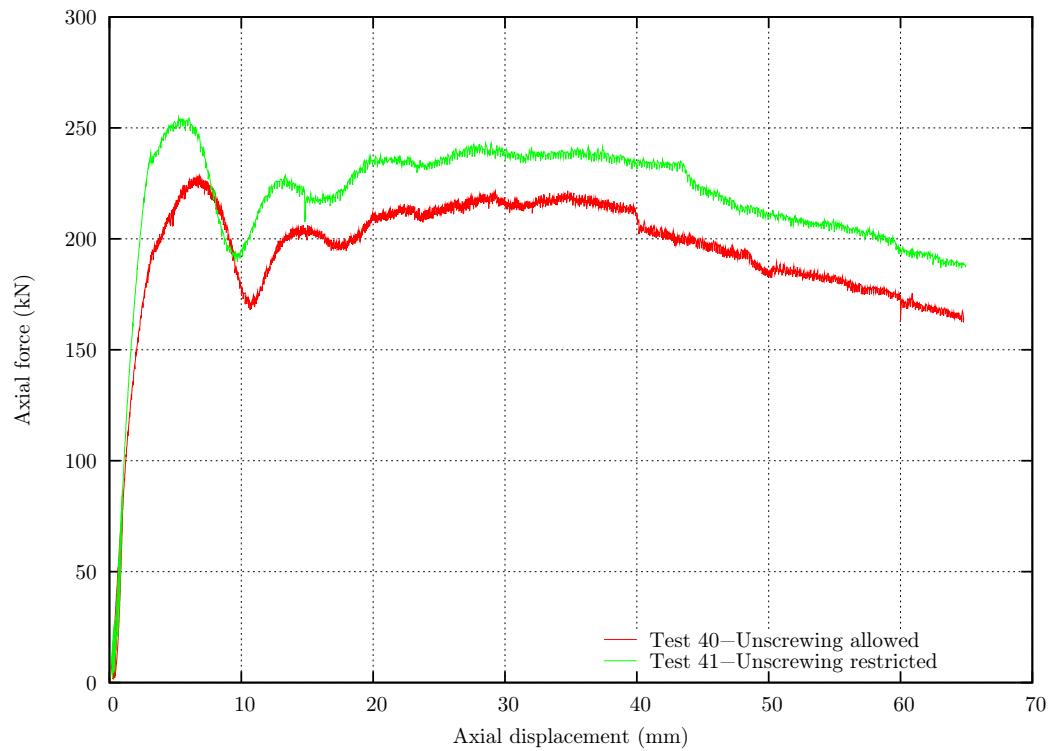
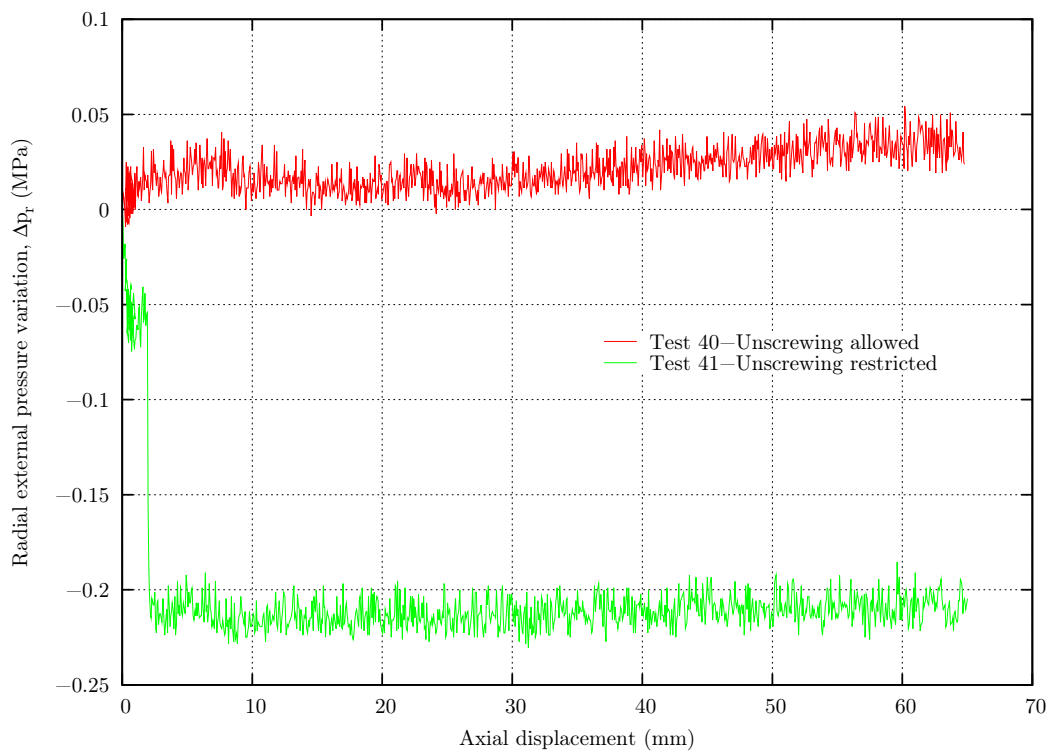


Figure B.2: Radial pressure variation-displacement curve.

Comments: a pull-out test in which unscrewing was not restricted and a test in which it was prevented were conducted, but they were carried out without the barrel and wedge system. Therefore, since the operating conditions are not the same, the results are not presented here.

2. Embedment length,  $L = 250$  mm**Figure B.3:** Load-displacement curve.**Figure B.4:** Radial pressure variation-displacement curve.

## C Field pull-out test campaign on HA25 rockbolts

The information in the following table corresponds to the pull-out tests compiled in table 3.8.

**Table 3:** Pull-out tests details (after [Dénecé2009]).

| Test ID  | Drift | Test type     | Grouting material | Embedment length (m) |
|----------|-------|---------------|-------------------|----------------------|
| HA25-02  | GT8   | Constant rate | Resin             | 3.0                  |
| HA25-03  | GT8   | Constant rate | Resin             | 3.0                  |
| HA25-02  | GAT   | Constant rate | Resin             | 2.4                  |
| HA25-04  | GAT   | Constant rate | Resin             | 2.4                  |
| HA25-05  | GT8   | Constant rate | Cement            | 3.0                  |
| HA25-09  | GT8   | Constant rate | Cement            | 3.0                  |
| HA25-06  | GAT   | Constant rate | Cement            | 2.4                  |
| HA25-07  | GAT   | Constant rate | Cement            | 2.4                  |
| HA25-10  | GAT   | Constant rate | Cement            | 2.4                  |
| HA25-13* | GAT   | Constant rate | Cement            | 2.4                  |
| HA25-01  | GT8   | Creep         | Resin             | 3.0                  |
| HA25-04  | GT8   | Creep         | Resin             | 3.0                  |
| HA25-07  | GT8   | Creep         | Resin             | 3.0                  |
| HA25-01  | GAT   | Creep         | Resin             | 2.4                  |
| HA25-03  | GAT   | Creep         | Resin             | 2.4                  |
| HA25-05  | GAT   | Creep         | Resin             | 2.4                  |
| HA25-08  | GT8   | Creep         | Cement            | 3.0                  |
| HA25-10  | GT8   | Creep         | Cement            | 3.0                  |
| HA25-06  | GT8   | Creep         | Cement            | 3.0                  |
| HA25-08  | GAT   | Creep         | Cement            | 2.4                  |
| HA25-09  | GAT   | Creep         | Cement            | 2.4                  |
| HA25-11* | GAT   | Creep         | Cement            | 2.4                  |
| HA25-12* | GAT   | Creep         | Cement            | 2.4                  |

\*: instrumented bolts





## Étude théorique et expérimentale du boulonnage à ancrage réparti sous sollicitations axiales

**Résumé :** Le boulonnage et le câblage à ancrage réparti sont deux techniques de renforcement du terrain couramment utilisées dans l'industrie minière et dans le génie civil. Au fil de cette recherche, on s'intéresse à la réponse de ces éléments sous des sollicitations axiales de traction, en régime statique. Dans ces conditions, l'expérience montre que la rupture se produit le plus fréquemment à l'interface barre-scellement *via* un processus de décohérence qui commence dès que la force sur la barre atteint une valeur limite. L'objectif est de mieux comprendre le comportement de cette interface, avant et après rupture. Premièrement, on revoit l'état de l'art afin de comprendre le travail effectué et les aspects non maîtrisés à ce jour. Deuxièmement, on décrit des outils analytiques qui permettent de comprendre la réponse d'un boulon ou d'un câble à ancrage réparti soumis à une force de traction. Ensuite, on présente les études expérimentales menées en laboratoire et *in situ*. Des essais d'arrachement ont été effectués pour déterminer les principaux facteurs qui régissent la réponse de l'interface. Finalement, on analyse les résultats des essais effectués en laboratoire sur les boulons. Après l'obtention des variables nécessaires, on propose un modèle semi-empirique d'interface, qui devra être validé par des essais complémentaires. Cette perspective et d'autres améliorations sont également présentées.

**Mots-clés :** approche analytique, boulon, câble, conditions opératoires, essai d'arrachement, interface boulon-scellement, méthode semi-empirique

## Theoretical and experimental study of fully grouted rockbolts and cablebolts under axial loads

**Abstract:** Rockbolting and cablebolting are two ground reinforcement techniques broadly used in civil and mining engineering. This research focuses on the behaviour of fully grouted bolts subjected to tensile axial loads, in static conditions. Under these circumstances, experience throughout the world proves that failure usually takes place at the bolt-grout interface *via* a decoupling process that starts if the load on the bolt exceeds a critical value. The objective is to gain more insight into the behaviour of this interface, before and after failure. First, the state-of-the-art is presented to understand the existing advances and to identify the lacking aspects. Secondly, analytical tools that help understand the response of a fully grouted bolt subjected to a tensile load are described. Then, the field and laboratory experimental campaigns are exposed. Pull-out tests have been conducted to determine the most influencing parameters on the interface behaviour. Finally, the laboratory results on rockbolts are analyzed. Once the necessary variables are obtained, a semi-empirical interface behaviour model is proposed. The further evaluation of this model and other improvements are suggested as perspectives of evolution.

**Keywords:** analytical approach, bolt-grout interface, boundary conditions, cablebolt, pull-out test, rockbolt, semi-empirical method

